

**An impulse framework for hydrodynamic force analysis:
fish propulsion, water entry of spheres, and marine propellers**

by

Brenden P. Epps

Submitted to the Department of Mechanical Engineering
in partial fulfillment of the requirements for the degree of

Doctor of Philosophy in Mechanical Engineering

at the

MASSACHUSETTS INSTITUTE OF TECHNOLOGY

February 2010

© Massachusetts Institute of Technology 2010. All rights reserved.

Author
Department of Mechanical Engineering
February 5, 2010

Certified by
Alexandra H. Techet
Associate Professor, Mechanical Engineering
Thesis Supervisor

Accepted by
David E. Hardt
Chairman, Department Committee on Graduate Students

**An impulse framework for hydrodynamic force analysis:
fish propulsion, water entry of spheres, and marine propellers**

by
Brenden P. Epps

Submitted to the Department of Mechanical Engineering
on February 5, 2010, in partial fulfillment of the
requirements for the degree of
Doctor of Philosophy in Mechanical Engineering

Abstract

This thesis presents an *impulse framework* for analyzing the hydrodynamic forces on bodies in flow. This general theoretical framework is widely applicable, and it is used to address the hydrodynamics of fish propulsion, water entry of spheres, and the off-design performance of marine propellers. These seemingly-unrelated physics problems share a key common thread: The forces on these fish, spheres, and propellers can be modeled as the sum of the reaction to the rate of change of (1) the *pressure impulse* required to set up the potential flow about the body, and (2) the *vortex impulse* required to create the vortical structures in the wake of the body.

Fish generate propulsive forces by creating and manipulating large-scale vortical structures using their body and tail. High-speed particle image velocimetry experiments show that a fish generates two vortex rings during a C-turn maneuver and that the change in momentum of the fish balances the change in *pressure impulse* plus the *vortex impulse* of these rings.

When a sphere plunges into a basin of water and creates a sub-surface air cavity in place of a vortical wake, the *vortex impulse* is zero, and the force on the sphere is given by the *pressure impulse* component. Using data from high-speed imaging experiments, a semi-empirical numerical simulation is developed herein; this numerical model shows how the presence of the cavity alters the unsteady pressure force on the sphere and modulates the dynamics of the impact event.

During steady propeller operation, the *pressure impulse* is constant, and the loads on the propeller are given by the *vortex impulse* component. To analyze these loads, a computational design and analysis tool is presented; this code suite is based on propeller lifting line theory, which is shown to be a special case of the general impulse framework of this thesis. A marine propeller is designed, built, and tested over a range of off-design operating conditions. Experimental results match the predicted performance curve for this propeller, which provides important validation data for the numerical method presented herein.

Bringing this thesis full circle, the unsteady startup of the propellor is addressed, which is analogous to the impulsive maneuvering of the swimming fish. As in the fish maneuvering problem, the propellor generates a ring-like vortical wake, and it is shown herein how the vortex impulse of these rings provides thrust for the propellor. With the perspective of the impulse framework developed in this thesis, the results of these tandem experimental investigations and numerical simulations provide deeper insight into classical fluid-dynamics theory and modern experimental hydrodynamics.

Thesis committee members:

Paul Sclavounos, Professor, Mechanical Engineering, MIT

Mark Drela, Professor, Aeronautics and Astronautics, MIT

Richard Kimball, Associate Professor, Maine Maritime Academy, Castine, ME

Thesis Supervisor: Alexandra H. Techet

Title: Associate Professor, Mechanical Engineering

Acknowledgments

There are so many people whom I wish to thank for contributing to this effort. To my loving wife Wendy, thank you for making me feel that anything is possible. I am grateful for my team of advisors whose support and guidance helped shape this work: Alex Techet, Rich Kimball, Mark Drela, and Paul Sclavounos. Thanks to my labmates and fellow students who shared in many of these projects: Tadd Truscott, Jesse Belden, Anna Shih, Jenna McKown, Jerod Ketcham, Jordan Stanway, and Rod LaFoy to name a few. Tadd, thanks for making those late nights and the extra hours in lab fun. Thanks to Leslie Regan for getting me started at MIT. And thanks to two of my undergraduate professors, Tom I-P. Shih and Glenn Sinclair, who supported my application to graduate school at MIT.

Several people supported this work financially, and their contributions are gratefully acknowledged. I am grateful for several Department of Mechanical Engineering teaching assistantships, thanks to the professors who hired me: Alex Techet (2.016 F05 and F07), John Heywood (2.006 F06), Rich Kimball (2.23 S07), Carol Livermore (2.001 F08), and Sanjay Sarma (2.003 S09). I am also grateful for a Link Foundation Doctoral Research Fellowship (S08), and for the current financial support from Robert Damus of the Project Ocean and Chryssostomos Chryssostomidis of the MIT Sea Grant College Program.

Finally, I would like to thank my family, my Lopez Street ‘family’, and my friends for their love and support. Hooray!

[THIS PAGE INTENTIONALLY LEFT BLANK]

Contents

1	Introduction	13
1.1	Fluid impulse	17
1.1.1	Example: impulse of a vortex ring	20
1.2	Impulsive forces	22
1.2.1	Vorticity field model	26
1.2.2	Impulsive force model	29
1.2.3	Incorrect derivation of the force	30
1.3	Applications in experimental hydrodynamics	32
	Bibliography	35
I	Fish propulsion	37
2	Impulse generated during unsteady maneuvering of swimming fish	39
2.1	Introduction	41
2.2	Materials and methods	44
2.3	Results and Discussion	47
2.3.1	Vortical wake structure	48
2.3.2	Maneuver kinematics	50
2.3.3	Circulation	54
2.3.4	Comparison of fluid impulse with fish impulse	56

2.4	Conclusion	60
2.5	Epilogue	63
	Bibliography	64
3	Swimming performance of a biomimetic compliant fish-like robot	67
3.1	Introduction	69
3.2	Compliant biomimetic swimming robots	72
3.3	Materials and methods	75
3.4	Results and discussion	78
3.4.1	Kinematics	78
3.4.2	Vortical wake structure	80
3.4.3	Swimming speed	85
3.4.4	Thrust	87
3.4.5	Wake width versus flapping amplitude	91
3.5	Conclusions	93
	Bibliography	97

II Methods for experimental data analysis and modeling 101

4	An error threshold criterion for singular value decomposition modes extracted from PIV data	103
4.1	Introduction	104
4.1.1	Synthesis of SVD, POD, and BOD	106
4.2	Threshold criterion	109
4.3	Materials and methods	111
4.3.1	Experimental details	111
4.3.2	Wake interrogation	113
4.3.3	Experimental PIV error	114

4.3.4	Data smoothing	115
4.4	Results and discussion	116
4.4.1	PIV wake data	116
4.4.2	Singular values	118
4.4.3	Mode shapes and amplitudes	120
4.4.4	Wake reconstruction	126
4.5	Conclusions	127
	Bibliography	129
5	A method for inferring forces from experimental position data	133
5.1	Introduction	135
5.2	Analytic example	140
5.2.1	Roughness and error scaling	144
5.2.2	Comparison between <code>csaps</code> and the present method	146
5.2.3	Predictive error	147
5.3	Automated algorithm	149
5.4	Experimental example	152
5.4.1	Application of the present spline fitting method	153
5.4.2	A check for the derivatives $s'(t)$, $s''(t)$, and $s'''(t)$	157
5.5	Conclusions	160
5.6	Appendix: non-dimensional equations	161
	Bibliography	163
6	Unsteady forces on spheres during water entry	165
6.1	Introduction	168
6.2	Materials and methods	169
6.3	Potential flow model	172
6.4	Results and discussion	181

6.4.1	PIV results	188
6.5	Effect of mass ratio	191
6.6	Summary	196
	Bibliography	197
III	Marine propulsion and energy harvesting	199
7	Off-design performance analysis of marine propellers and turbines using lifting line theory	201
7.1	Introduction	205
7.2	Propeller lifting-line formulation	206
7.3	Propeller design optimization	210
7.3.1	A modified design optimization method	215
7.3.2	Example propeller design	217
7.4	Propeller geometry	218
7.5	Off-design performance analysis	219
7.5.1	Example propeller off-design analysis	225
7.6	Non-dimensional parameters	228
7.7	Summary	229
	Bibliography	230
8	Propeller off-design performance experiments	233
8.1	Experimental setup	233
8.1.1	Calibration tests	235
8.1.2	PIV test setup	240
8.2	Propeller design	241
8.2.1	Optimized performance	242
8.2.2	Blade shape	246

8.2.3	Fabrication	249
8.3	Steady propeller performance experiments	251
8.4	Unsteady start-up experiments	255
8.4.1	Unsteady wake flow visualization	261
8.4.2	Impulsive force model	264
8.5	Summary	268
	Bibliography	270
9	Hydrokinetic turbine design and analysis	271
9.1	Turbine lifting-line representation	271
9.2	Turbine design optimization	273
9.2.1	Simple turbine optimization scheme	273
9.2.2	Improved, actuator-disk-based optimization scheme	276
9.2.3	Chord length optimization	278
9.3	Off-design performance analysis	278
9.4	Turbine off-design performance experiments	280
9.4.1	Turbine design	280
9.4.2	Steady performance experiments	285
9.5	Summary	288
	Bibliography	288
10	Summary and outlook	289
10.1	Contributions of this thesis	293
10.2	Extensions of this work	296

[THIS PAGE INTENTIONALLY LEFT BLANK]

Chapter 1

Introduction

This thesis presents an impulse framework for analyzing the hydrodynamic forces on bodies in flow. This theoretical framework is widely applicable, and it is used to address the hydrodynamics of fish propulsion, water entry of spheres, and marine propellers through both numerical modeling and experimental investigation. This thesis is motivated by the need for a theoretical framework to serve as a basis for understanding and modeling the hydrodynamic forces generated for unsteady propulsion, specifically those forces observed in an experimental context. This thesis is concerned with both biological applications, such as fish propulsion, and conventional propulsion applications, such as the design of propellers for underwater vehicles. To motivate the need for my framework, consider the following methods that one might employ to measure forces experimentally and the issues with doing so in the context of these applications.

Measuring force on a load cell

Often in model tests (e.g. measuring propeller loads in a water tunnel), the total force on a model can be measured by mounting it on a load cell instrumented with strain gauges. This approach yields accurate force readings if care is taken to account for

the effect of the mounting device on the measured loads. This approach is used in Chapter 8 to measure the thrust produced by a model propeller during steady and unsteady performance tests. However, this approach cannot be used for biological applications (e.g. inferring the forces on a fish during a rapid maneuver), nor does it give any insight into the hydrodynamics that result in the measured forces.

Inferring force from body acceleration

The force on a body is computed from its acceleration by Newton's second law

$$\mathbf{F} = m\mathbf{a} \quad (1.0.1)$$

In some applications (e.g. measuring the overall dynamics of an underwater vehicle), a body could be instrumented with accelerometers to measure acceleration directly. However, as with measuring forces using a load cell, this approach cannot be used for biological application (at least not easily), nor does it give any physical insight into the measured forces. This approach is used in Chapter 5 to determine the overall forces on a sphere falling into a basin of water, but in order to explain the nature of these forces, in Chapter 6 a numerical model is developed based on the impulse framework of this thesis.

Inferring force from pressure and viscous stress

The net force on a body could be computed by integrating the pressure and viscous stresses over the body surface

$$\mathbf{F} = \int_{S_b} \hat{\mathbf{n}} \cdot [p\mathbf{E} - \mathbf{T}] dS \quad (1.0.2)$$

where S_b is the body surface, $\hat{\mathbf{n}}$ is a unit normal vector pointing out of the fluid (into the body), p is the static pressure, \mathbf{E} is the identity tensor ('E' stands for the German

term ‘Einheitsmatrix’), and $\mathbf{T} = \mu [(\nabla \mathbf{u}) + (\nabla \mathbf{u})^\top]$ is the viscous stress tensor, where \mathbf{u} and μ are the fluid velocity and dynamic viscosity, respectively.

This approach is infeasible experimentally, especially in the case of a moving body, since it requires both (a) resolving the fluid pressure at the body surface, and (b) resolving the velocity gradients in the boundary layer at the body surface. Each of these experimental tasks is formidable, especially in the case of an unsteady flowfield with a moving body.

Practically, this approach requires performing a full-blown computational fluid dynamics (CFD) simulation. Highly-accurate immersed-boundary CFD methods do exist and have been used in several propulsion studies, such as that of a human swimmer (von Loebbecke et al, 2009) or that of a carangiform swimming fish (Borazjani and Sotiropoulos, 2008). These CFD studies yield a wealth of flowfield information that can be used to understand the dynamics of these flows. However, this approach required hundreds of CPU-hours (on current computers) and doesn’t necessarily lend itself to explaining and understanding the results of particular experiments observed in the lab.

Inferring force from control volume analysis

Neglecting buoyancy and assuming no flow through the body surface, the force on a body can be computed by applying conservation of momentum to a control volume V , which is bounded by the body surface S_b and an arbitrary exterior surface S , as shown in figure 1-1. This yields

$$\mathbf{F} = -\frac{d}{dt} \left[\int_V \rho \mathbf{u} dV \right] - \int_S \hat{\mathbf{n}} \cdot (\mathbf{u} - \mathbf{u}_s) \rho \mathbf{u} dS + \int_S \hat{\mathbf{n}} \cdot [-p \mathbf{E} + \mathbf{T}] dS \quad (1.0.3)$$

where \mathbf{u}_s is the velocity of surface S and ρ is the fluid density. Equation (1.0.3) is well known, and the three terms represent: (1) the reaction to the rate of increase

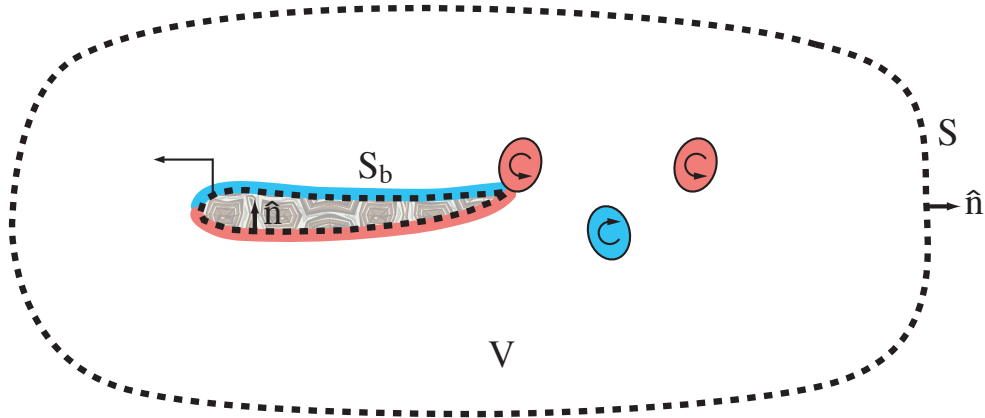


Figure 1-1: Illustration of a *finite control volume* surrounding a moving body.

of momentum in the control volume, (2) the reaction to the net flux of momentum out of the control volume, and (3) the force required to balance the net pressure and tractive forces on the fluid at the exterior control surface.

This approach is used with great success in some experiments, such as model tests with steady flow in a water tunnel. In this case, the first and third integrals in (1.0.3) are assumed to be zero, and the momentum flux is easily measured by a wake survey (i.e. using Pitot tubes to measure the fluid velocity where the wake passes through the downstream control surface).

However, for unsteady propulsion applications, evaluating (1.0.3) presents the same difficulties as evaluating (1.0.2). Namely, the entire 3D velocity field must be known, and the pressure must be known at the exterior control surface. Further, equation (1.0.3) requires computing the *rate of change* of the total fluid momentum, which can be challenging experimentally. Noca (1997) offers several alternatives to (1.0.3) that eliminate the pressure integral in favor of rates of change of integrals and integrals involving velocity gradients. Finding these temporal and spatial derivatives is challenging, because finite difference methods amplify measurement error, and derivatives of functional fits depend on the fitting parameters that may not accurately represent instantaneous flowfield behavior. Chapter 5 outlines the difficulties in

computing the derivative of a measured quantity and provides a method for doing so. Still, estimating forces from (1.0.3) is tenuous in unsteady propulsion problems, and an alternate method is desirable.

Inferring force from fluid impulse

Finally, the net force on a body is the reaction to the rate of change of fluid impulse, which can be decomposed into *vortex impulse* and *pressure impulse*

$$\mathbf{F} = -\frac{d}{dt} \left(\mathbf{I}_v + \mathbf{I}_p \right) \quad (1.0.4)$$

These components are discussed in classical texts, such as (Lamb, 1945), (Lighthill, 1986b), and (Saffman, 1995), and one purpose of this thesis is to show how both of these components contribute to the total force on the body. Before I formally derive (1.0.4), I shall introduce these two components of fluid impulse.

1.1 Fluid impulse

It is well known that any velocity field can be decomposed into rotational flow (\mathbf{u}_0) and irrotational flow ($\nabla\phi$) components

$$\mathbf{u} = \mathbf{u}_0 + \nabla\phi \quad (1.1.1)$$

where ϕ is the velocity potential, and \mathbf{u}_0 is the velocity in excess of the (irrotational) potential flow component (Saffman, 1995). Since $\nabla \times \nabla\phi = 0$ by definition, the vorticity field is given solely by the rotational flow component $\boldsymbol{\omega} \equiv \nabla \times \mathbf{u} = \nabla \times \mathbf{u}_0$. Considering these points, it follows that the total fluid impulse can also be decomposed into two components: *vortex impulse* and *pressure impulse*.

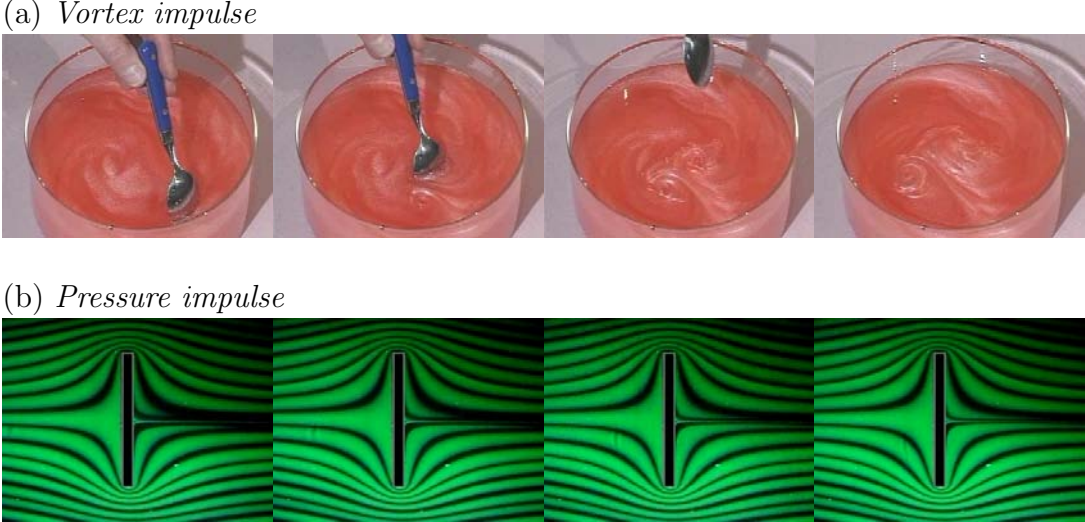


Figure 1-2: (a) Vortices shed from a spoon are visualized with Kalliroscopic fluid, illustrating *vortex impulse*; (b) Flow past a vertical plate is visualized in a Hele-Shaw cell, illustrating *pressure impulse*. Both are reproduced from (Homsy et al, 2000).

For an unbounded flow, *vortex impulse* is defined as

$$\mathbf{I}_v \equiv \frac{1}{2} \rho \int_V \mathbf{x} \times \boldsymbol{\omega} dV \quad (1.1.2)$$

where the \mathbf{x} is the position from some arbitrarily-chosen origin, and $\boldsymbol{\omega} = \boldsymbol{\omega}(\mathbf{x})$ is the vorticity field. A physical interpretation of equation (1.2.17) may be arrived at by considering the vortical flow velocity, \mathbf{u}_0 . This velocity \mathbf{u}_0 can be thought of as being ‘induced’ by the vorticity distribution, in which case the velocity at position \mathbf{x}' can be computed using Biot-Savart law

$$\mathbf{u}_0(\mathbf{x}') = \frac{1}{4\pi} \int_V \frac{(\mathbf{x} - \mathbf{x}') \times \boldsymbol{\omega}(\mathbf{x})}{|\mathbf{x} - \mathbf{x}'|^3} d\mathbf{x} \quad (1.1.3)$$

where $d\mathbf{x}$ is used here in place of dV to explicitly indicate that \mathbf{x} is the dummy variable of integration (but the integral is still taken over the entire fluid volume). Comparing (1.1.3) and (1.1.2) reveals that the vortex impulse is proportional to the

velocity induced at the origin, which is

$$\mathbf{u}_0(\mathbf{0}) = \frac{1}{4\pi} \int_V \frac{\mathbf{x} \times \boldsymbol{\omega}(\mathbf{x})}{|\mathbf{x}|^3} d\mathbf{x} \quad (1.1.4)$$

Figure 1-2a illustrates the vortex impulse imparted by the motion of a ‘flat plate’ (i.e. a spoon) normal to itself. As the spoon is drawn through the bath, the flow separates at the edges of the spoon, and a vortex pair is shed¹. The motion of this vortex pair persists long after the spoon is removed from the fluid, showing that impulse has been imparted to the fluid via the creation of these vortices. Further discussion of *vortex impulse* can be found in (Batchelor, 1967, §5.72), (Saffman, 1995, §3.2), (Lighthill, 1986b, §11.2), and (Lamb, 1945, §152).

Figure 1-2b illustrates the irrotational flow about a flat plate, characterized by no flow separation, symmetrical flow upstream and downstream of the plate, and no vorticity. In the absence of vorticity, the velocity field can be described solely using a potential function, $\mathbf{u} = \nabla\phi$. In this case, $\rho\phi$ is the *impulsive pressure* of the flow, so the impulse required to set up the potential flow is the integral of this impulsive pressure over the body surface, which is called the *pressure impulse*

$$\mathbf{I}_p \equiv \int_{S_b} \rho\phi \hat{\mathbf{n}} dS \quad (1.1.5)$$

where $\hat{\mathbf{n}}$ points out of the fluid (into the body). Further discussion of *pressure impulse* can be found in (Batchelor, 1967, §6.10), (Saffman, 1995, §4.1), (Lighthill, 1986b, §6.1), and (Lamb, 1945, §119).

¹It is well known that vortex tubes cannot end in the fluid (Saffman, 1995, §1.4), so this vortex pair either extends to the bottom of the bowl or connects, but this is besides the point.

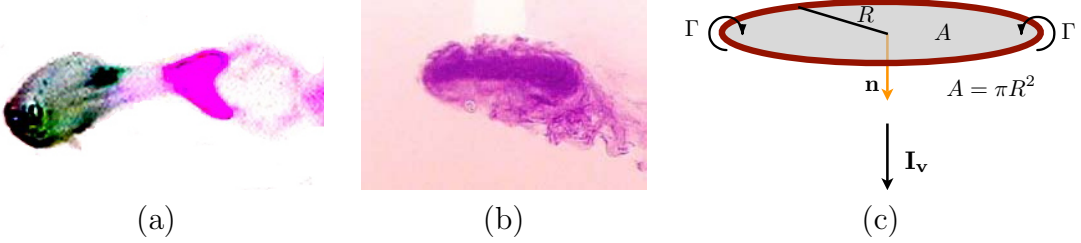


Figure 1-3: (a) Dye visualization of a live swimming fish shows the formation of a vortex ring during the initial stage of a rapid turning maneuver; (b) Dye visualization of a propeller shows the formation of a vortex ring during unsteady start from rest (reproduced from (Stettler, 2004)); (c) Illustration of a vortex ring.

1.1.1 Example: impulse of a vortex ring

The key feature of the impulsive force framework is that the fluid impulse can be modeled in such a way that the model parameters can be accurately measured in laboratory experiments. For example, consider the axisymmetric vortex ring model, in which the impulse depends solely on the circulation Γ and radius R of the ring, which can be quantified accurately in a particle image velocimetry experiment.

The vortex ring model applies well to a variety of fluid flows: For example, a live swimming fish will form a vortical wake during a rapid maneuver that resembles two distinct vortex rings (as discussed in Chapter 2); the first of these two rings is visualized with fluorescent dye in figure 1-3a. A propeller will form a vortical structure during unsteady start-up that resembles a vortex ring, as visualized by Stettler (2004) using fluorescent dye (reproduced in figure 1-3b). Ring-like vortex structures are quite prevalent in biological propulsion, and Dabiri (2009) suggests that optimal vortex ring formation should be a driving principle for biomimetic design of propulsion systems.

A vortex ring is constructed mathematically by a limiting process in which the cross-sectional area of a circular vortex filament is reduced to zero while the circulation is held constant. In this limit, the vorticity becomes zero everywhere except for on the ring, where it becomes infinite. Choosing cylindrical coordinates $\mathbf{x} = (r, \theta, x)$, the

vorticity field is represented in terms of a delta function by

$$\boldsymbol{\omega}(\mathbf{x}) = \Gamma \delta(\mathbf{x} - \mathbf{x}_r) \mathbf{e}_\theta \quad (1.1.6)$$

where Γ is the circulation, $\mathbf{x}_r = R\mathbf{e}_r + \theta\mathbf{e}_\theta$ for $0 \leq \theta \leq 2\pi$ are the coordinates defining the ring, and R is the radius of the ring, as shown in figure 1-3c.

Inserting (1.1.6) into (1.1.2) yields the *vortex impulse*

$$\mathbf{I}_v = \frac{1}{2} \rho \int_0^{2\pi} (R\mathbf{e}_r \times \Gamma\mathbf{e}_\theta) R d\theta$$

which simplifies to

$$\mathbf{I}_v = \rho \Gamma A \mathbf{n} \quad (1.1.7)$$

where $A = \pi R^2$ is the frontal area of the vortex ring. Inserting (1.1.6) into (1.1.4) yields the velocity at the center of the ring

$$\begin{aligned} \mathbf{u}_0(0) &= \frac{1}{4\pi} \int_0^{2\pi} \frac{(R\mathbf{e}_r \times \Gamma\mathbf{e}_\theta)}{R^3} R d\theta \\ &= \frac{\Gamma}{2R} \mathbf{n} \\ &= \frac{\mathbf{I}_v}{2R\rho A} \end{aligned}$$

These results are well known and can be found in many classical texts (e.g. Milne-Thomson, 1958, §10.21). A correction to (1.1.7) is given by Saffman (1995) for the case of a toroidal vortex ring (i.e. a circular vortex filament with a finite cross-sectional area), as discussed in Chapter 2.

It is important to reiterate that in this vortex ring model, the fluid impulse can be computed from experimental measurements of just Γ and R , which can be computed with a good degree of accuracy.

1.2 Impulsive forces

In this section, I formally derive equation (1.0.4), which can be used as a framework for modeling and understanding hydrodynamic forces on bodies in flow. This framework will be applied in the experimental studies described in this thesis. Equation (1.0.4) simply says that the total force on a body is the sum of two components:

- (1) the reaction to the rate of change of *vortex impulse*, associated with the creation and manipulation of vortices in the wake, and
- (2) the reaction to the rate of change of *pressure impulse*, which is required to generate the irrotational flow about the body.

The *pressure impulse force* depends linearly on the body motion and can be easily modeled for simple geometrical forms. The *vortex impulse force* depends on the non-linear dynamics of the fluid flow, but it can be estimated with knowledge of the vorticity field in the wake of the body. A unifying discussion of these two concepts is presented by Lighthill (1986a) in the context of wave loading on offshore structures, without derivation. The purpose of this section is to provide a unifying derivation of the total force on the body (1.0.4), rather than to consider the *vortex impulse* and *pressure impulse* components separately as done in Section 1.1 and in the classical fluid dynamics texts cited therein. Much of the following derivation also appears in the works of Noca (1997), Wu and Wu (1996), and Lighthill (1979). In working through the details, we will find that the definition of *vortex impulse* (1.1.2) will have to be augmented to accurately compute the force on the body.

The starting equation for the derivation is (1.0.3). I will manipulate (1.0.3) using a series of vector calculus identities and assumptions. The final impulsive force framework assumes: (1) the fluid density is constant and uniform throughout the fluid; (2) no flow through and no slip on the body surface; (3) gravitational effects can be accounted for separate from this model, (4) the fluid extends infinitely far

from the body; (5) the fluid domain is three-dimensional and is *simply connected*; (6) the Reynolds number is high, such that the vorticity field can be modeled as a vortex sheet surrounding the body plus vorticity in the wake; and (7) we either have experimental data for or we can model the entire vorticity field in the wake.

The force on a body is given by equation (1.0.3), which is reproduced here

$$\mathbf{F} = -\frac{d}{dt} \left[\int_V \rho \mathbf{u} dV \right] - \int_S \hat{\mathbf{n}} \cdot (\mathbf{u} - \mathbf{u}_s) \rho \mathbf{u} dS + \int_S \hat{\mathbf{n}} \cdot [-p \mathbf{E} + \mathbf{T}] dS \quad (1.0.3)$$

where control volume V is bounded by the body surface S_b and an arbitrary exterior surface S , as shown in figure 1-1. In general, both the body and control surfaces may move in time, so the volume may be unsteady in time. Equation (1.0.3) only assumes no flow through the body surface ($\hat{\mathbf{n}} \cdot (\mathbf{u} - \mathbf{u}_b) = 0$ on S_b , where \mathbf{u}_b is the body surface velocity) and no bulk fluid force (i.e. no gravity). Including gravity is trivial, as it simply results in the addition of a buoyancy force (by Archimedes' principle) and does not affect the arguments presented herein. In what follows, I assume that the fluid density ρ is constant and uniform throughout the fluid, but I will keep it in the formulae throughout the derivation.

To proceed, I will make use of two identities. The first is the so called *impulse-momentum identity*

$$\int_V \mathbf{u} dV = \frac{1}{2} \int_V \mathbf{x} \times \boldsymbol{\omega} dV - \frac{1}{2} \int_{S \oplus S_b} \mathbf{x} \times (\hat{\mathbf{n}} \times \mathbf{u}) dS \quad (1.2.1)$$

where \mathbf{u} is the fluid velocity, $\boldsymbol{\omega} = \nabla \times \mathbf{u}$ is the vorticity, \mathbf{x} is the position from some arbitrarily chosen origin, volume V is a simply-connected region in 3D space bounded by surfaces S and S_b , and I use the notation $\int_{S \oplus S_b} = \int_S + \int_{S_b}$ (Noca, 1997, §3.1.1; Saffman, 1995, §3.2). The second is the so called *pressure identity*

$$-\frac{1}{2} \int_{S^*} \mathbf{x} \times (\hat{\mathbf{n}} \times \nabla \phi) dS = \int_{S^*} \phi \hat{\mathbf{n}} dS \quad (1.2.2)$$

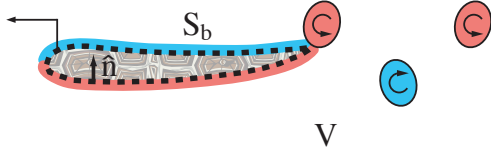


Figure 1-4: Illustration of an *infinite control volume* surrounding a moving body.

where ϕ is a single-valued scalar on surface S^* . An equation similar to (1.2.2) could be derived by setting $\mathbf{u} = \nabla\phi$ in (1.2.1), noting that $\boldsymbol{\omega} = \nabla \times (\nabla\phi) = 0$, and manipulating the left hand side by Green's theorem $\int_V \nabla\phi dV = \int_{S \oplus S_b} \phi \hat{\mathbf{n}} dS$; this results in (1.2.2) but with $S^* = S \oplus S_b$ (Saffman, 1995, §4.2). Noca (1997, §3.1.2) offers an alternate proof in which he shows that this identity holds on either surface, $S^* = S_b$ or $S^* = S$. Note that the pressure field is necessarily single-valued, so I will make use of (1.2.2) once while setting $\phi = p$.

Inserting (1.2.1) into (1.0.3) yields

$$\begin{aligned} \mathbf{F} = & -\frac{d}{dt} \left[\frac{1}{2} \rho \int_V \mathbf{x} \times \boldsymbol{\omega} dV \right] + \frac{d}{dt} \left[\frac{1}{2} \rho \int_{S_b} \mathbf{x} \times (\hat{\mathbf{n}} \times \mathbf{u}) dS \right] \\ & + \frac{d}{dt} \left[\frac{1}{2} \rho \int_S \mathbf{x} \times (\hat{\mathbf{n}} \times \mathbf{u}) dS \right] \\ & - \int_S \hat{\mathbf{n}} \cdot (\mathbf{u} - \mathbf{u}_s) \rho \mathbf{u} dS + \int_S \hat{\mathbf{n}} \cdot [-p \mathbf{E} + \mathbf{T}] dS \end{aligned} \quad (1.2.3)$$

At this point, consider the case when the vorticity is confined to a finite region surrounding the body and the exterior control surface, S , extends a great distance from both the body and surrounding vorticity. In the limit of $S \rightarrow S_\infty$, I will now show that the integrals over S_∞ cancel and that we are left with a tractable formula for the force. The following derivation follows that given in (Noca, 1997, §2.4.6).

First note that if we assume the vorticity at large distances from the body decays at most exponentially, $|\boldsymbol{\omega}| \lesssim e^{-\alpha r}$ as $r \rightarrow \infty$, then the velocity scales as $|\mathbf{u}| \lesssim r^{-3}$ in 3D space, but no analogous assumption can be made about the pressure at infinity

(Bachelor, 1967). Assuming that control surface S_∞ is fixed in space ($\mathbf{u}_s = 0$) and that viscous stresses are negligible at infinity, then

$$-\int_{S_\infty} \hat{\mathbf{n}} \cdot (\mathbf{u} - \mathbf{u}_s) \rho \mathbf{u} dS + \int_{S_\infty} \hat{\mathbf{n}} \cdot \mathbf{T} dS \sim 0,$$

and the force on the body (1.2.3) becomes

$$\begin{aligned} \mathbf{F} = & -\frac{d}{dt} \left[\frac{1}{2} \rho \int_V \mathbf{x} \times \boldsymbol{\omega} dV \right] + \frac{d}{dt} \left[\frac{1}{2} \rho \int_{S_b} \mathbf{x} \times (\hat{\mathbf{n}} \times \mathbf{u}) dS \right] \\ & + \frac{d}{dt} \left[\frac{1}{2} \rho \int_{S_\infty} \mathbf{x} \times (\hat{\mathbf{n}} \times \mathbf{u}) dS \right] \\ & - \int_{S_\infty} p \hat{\mathbf{n}} dS \end{aligned} \quad (1.2.4)$$

Since the exterior control surface S_∞ is fixed, the time derivative in the third term can be evaluated readily. This term can then be manipulated using the Navier-Stokes equations $\rho \frac{\partial \mathbf{u}}{\partial t} = -\nabla p - \rho \nabla \cdot (\mathbf{u} \mathbf{u}) + \nabla \cdot \mathbf{T}$, which yields

$$\begin{aligned} \frac{d}{dt} \left[\frac{1}{2} \rho \int_{S_\infty} \mathbf{x} \times (\hat{\mathbf{n}} \times \mathbf{u}) dS \right] &= \frac{1}{2} \int_{S_\infty} \mathbf{x} \times (\hat{\mathbf{n}} \times [\rho \frac{\partial \mathbf{u}}{\partial t}]) dS \\ &= \frac{1}{2} \int_{S_\infty} \mathbf{x} \times (\hat{\mathbf{n}} \times [-\nabla p - \rho \nabla \cdot (\mathbf{u} \mathbf{u}) + \nabla \cdot \mathbf{T}]) dS \end{aligned}$$

The integrals of the inertial and viscous terms again are zero:

$$\frac{1}{2} \int_{S_\infty} \mathbf{x} \times (\hat{\mathbf{n}} \times [-\rho \nabla \cdot (\mathbf{u} \mathbf{u}) + \nabla \cdot \mathbf{T}]) dS \sim 0.$$

The integral of the pressure term is evaluated using the *pressure identity*:

$$\frac{1}{2} \int_{S_\infty} \mathbf{x} \times (\hat{\mathbf{n}} \times [-\nabla p]) dS = \int_{S_\infty} p \hat{\mathbf{n}} dS.$$

Thus, I have shown:

$$\frac{d}{dt} \left[\frac{1}{2} \rho \int_{S_\infty} \mathbf{x} \times (\hat{\mathbf{n}} \times \mathbf{u}) dS \right] = \int_{S_\infty} p \hat{\mathbf{n}} dS, \quad (1.2.5)$$

so the last two terms in (1.2.4) cancel, and the net force on the body becomes

$$\mathbf{F} = -\frac{d}{dt} \left[\frac{1}{2} \rho \int_V \mathbf{x} \times \boldsymbol{\omega} dV \right] + \frac{d}{dt} \left[\frac{1}{2} \rho \int_{S_b} \mathbf{x} \times (\hat{\mathbf{n}} \times \mathbf{u}) dS \right] \quad (1.2.6)$$

Noca (1997) ends his discussion of unbounded flows at this point and continues to derive the analogous equation for a finite-sized control volume. I proceed with the infinite-fluid case.

Since the no-slip condition holds for real viscous fluids, the fluid velocity at the body surface is given by the surface velocity $\mathbf{u} = \mathbf{u}_b$ on S_b

$$\mathbf{F} = -\frac{d}{dt} \left[\frac{1}{2} \rho \int_V \mathbf{x} \times \boldsymbol{\omega} dV \right] + \frac{d}{dt} \left[\frac{1}{2} \rho \int_{S_b} \mathbf{x} \times (\hat{\mathbf{n}} \times \mathbf{u}_b) dS \right] \quad (1.2.7)$$

Equation (1.2.7) requires knowledge of the entire vorticity field, including the boundary layer. It is impractical with the resolution of current digital cameras to simultaneously capture both the small scales of the boundary layer and the large scales of the overall flowfield. Thus, I continue by modeling the vorticity field.

1.2.1 Vorticity field model

To proceed, we must revisit the velocity field decomposition $\mathbf{u} = \mathbf{u}_0 + \nabla\phi$, and we must make precise the definitions of each of the two components for flow about a body immersed in an infinite 3D fluid domain. Following Lighthill (1986b, §6.3, §11.2), ϕ is defined as the *simple velocity potential*, which is a solution of Laplace's equation, $\nabla^2\phi = 0$, with the following boundary conditions

$$\hat{\mathbf{n}} \cdot (\mathbf{u}_b - \nabla\phi) = 0, \quad \text{on } S_b, \quad (1.2.8)$$

$$\phi \rightarrow 0, \quad \text{as } r \rightarrow \infty$$

It is important to note that even for a lifting surface such as a wing, the simple potential flow represents the flow past the body *without circulation*. The no-through-flow boundary condition on S_b does not require the tangential component of the fluid velocity to equal the body surface velocity, and this gives rise to the notion of a vortex sheet on the body surface of strength $[\hat{\mathbf{n}} \times (\mathbf{u}_b - \nabla\phi)]$. This vortex sheet represents the portion of the vorticity in the boundary layer that rectifies the difference between the true body velocity and the simple potential flow velocity.

The rotational flow component \mathbf{u}_0 is defined as satisfying the so called *zero boundary conditions*, which are appropriate for a *body instantaneously at rest*

$$\mathbf{u}_0 = 0, \quad \text{on } S_b, \quad (1.2.9)$$

$$\mathbf{u}_0 \rightarrow 0, \quad \text{as } r \rightarrow \infty$$

That is, \mathbf{u}_0 represents the velocity field that would immediately be induced by the vorticity distribution if the body were instantaneously brought to rest.

In general, the rotational flow may further be decomposed as $\mathbf{u}_0 = \mathbf{u}_1 + \nabla\Phi_0$, where \mathbf{u}_1 is uniquely determined by the vorticity distribution via the Biot-Savart law (1.1.3). The velocity potential Φ_0 is required to negate any flow through S_b that may be induced by the vorticity field. Interestingly, since the vorticity field is (assumed to be) confined to a finite region of space, the far-field velocity can be expressed as a velocity potential $\mathbf{u}_0 \rightarrow \nabla\phi_0$, whence $\mathbf{u}_1 \rightarrow 0$ and $\Phi_0 \rightarrow \phi_0$ in the far field. Further, by defining $\Phi_0 = 0$ on S_b and $\Phi_0 \rightarrow \phi_0$ in the far field, one can construct the irrotational velocity field required to satisfy the no-slip condition (1.2.9), since the gradient of Φ_0 along the surface would be zero by this definition. More importantly, since $\Phi_0 = 0$ on S_b , the *pressure impulse* is exactly *zero* for the rotational flow component.

I can now define the *additional vorticity*

$$\boldsymbol{\omega}_a \equiv \nabla \times \mathbf{u} = \nabla \times \mathbf{u}_0 = \nabla \times \mathbf{u}_1 \quad (1.2.10)$$

which is now understood to represent all of the vorticity in the flow in addition to the vortex sheet on the body surface. For bluff bodies, $\boldsymbol{\omega}_a$ is simply that in the boundary layer (which produces no net circulation) and that shed into the wake. For wing-like bodies such as propellers and fish fins, $\boldsymbol{\omega}_a$ also includes the portion of the vorticity in the boundary layer that generates circulation, so for a wing-like body, the additional vorticity can be modeled as a *vortex lattice* that represents both the *bound vorticity* as well as the associated *trailing vorticity* in the wake.

It is clear from boundary conditions (1.2.8) and (1.2.9) that in order to satisfy the no-slip condition for the total flow, $\mathbf{u} = \mathbf{u}_b$ on S_b , the total vorticity field must include the vortex sheet on the body surface as well as the additional vorticity

$$\boldsymbol{\omega} = \left[\hat{\mathbf{n}} \times (\mathbf{u}_b - \nabla\phi) \right] \delta(\mathbf{x} - \mathbf{x}_b) + \boldsymbol{\omega}_a \quad (1.2.11)$$

where $\delta(\cdot)$ is the Dirac delta function. It should be noted that this equation is exact in that it accurately reflects the velocity field decomposition discussed above, and no approximations have been made to this point.

The advantage of representing the velocity field as in equation (1.1.1) and the vorticity field as in (1.2.11) is that the *additional vorticity* in the boundary layer can be well approximated in typical experimental hydrodynamics problems. Typically for the high-Reynolds-number fluid flows observed in hydrodynamics experiments, vorticity is confined to a thin boundary layer surrounding the body and to a well-defined wake. For streamlined bodies such as fish, the velocity at the edge of the boundary layer is well approximated from the simple potential flow velocity $\nabla\phi$ (Schlichting, 1987), so the vortex sheet model well approximates the actual boundary layer vorticity, and the additional vorticity in the boundary layer can be neglected. Thus, for streamlined bodies, the additional vorticity can be approximated as that in the wake, which can be quantified using particle image velocimetry. For lifting surfaces such as propeller blades, the additional vorticity in the boundary layer that does not produce circulation is still well approximated by the vortex sheet, so the additional vorticity in the boundary layer can be approximated as just the *bound vorticity* that generates circulation about the wing; this bound vorticity can be inferred from a survey of the trailing vortex system in the wake. Thus, it is reasonable in experimental hydrodynamics to ignore the boundary layer completely and focus experimental efforts on quantifying the additional vorticity shed into the wake.

1.2.2 Impulsive force model

Inserting (1.2.11) into (1.2.7) yields

$$\mathbf{F} = -\frac{d}{dt} \left[\frac{1}{2} \rho \int_V \mathbf{x} \times \boldsymbol{\omega}_a dV \right] + \frac{d}{dt} \left[\frac{1}{2} \rho \int_{S_b} \mathbf{x} \times (\hat{\mathbf{n}} \times \nabla \phi) dS \right] \quad (1.2.12)$$

The second term in equation (1.2.12) can be manipulated by employing the *pressure identity* on S_b . Therefore, the final form of the impulse framework for the force on a body immersed in an infinite fluid flow is

$$\mathbf{F} = -\frac{d}{dt} \left[\frac{1}{2} \rho \int_V \mathbf{x} \times \boldsymbol{\omega}_a dV \right] - \frac{d}{dt} \left[\int_{S_b} \rho \phi \hat{\mathbf{n}} dS \right] \quad (1.2.13)$$

More compactly, the total force can be written as the reaction to the rate of change of total impulse in the fluid

$$\mathbf{F} = \mathbf{F}_v + \mathbf{F}_p \quad (1.2.14)$$

$$\mathbf{F}_v = -\frac{d\mathbf{I}_v}{dt} \quad (1.2.15)$$

$$\mathbf{F}_p = -\frac{d\mathbf{I}_p}{dt} \quad (1.2.16)$$

where the *vortex impulse* and *pressure impulse* are

$$\mathbf{I}_v \equiv \frac{1}{2} \rho \int_V \mathbf{x} \times \boldsymbol{\omega}_a dV \quad (1.2.17)$$

$$\mathbf{I}_p \equiv \int_{S_b} \rho \phi \hat{\mathbf{n}} dS \quad (1.2.18)$$

Note that the *vortex impulse* (1.1.2) has been redefined in (1.2.17) in terms of the *additional vorticity*, $\boldsymbol{\omega}_a$, to properly account for the presence of the body. Also note that in steady flow scenarios $\mathbf{F}_p = 0$, but $\mathbf{F}_v \neq 0$, since vorticity is continually shed into the wake, continually increasing the vortex impulse. In unsteady flow scenarios, both \mathbf{F}_p and \mathbf{F}_v are non-zero and contribute to the total force on the body.

Equation (1.2.14) represents a compact, yet quite general and useful representation of the force on a body in flow. This model is valid in cases where the vorticity is confined to a thin boundary layer and to observable vortical structures in the wake, such as a swimming fish or a propeller. The *vortex impulse force*, \mathbf{F}_v , can be estimated by characterizing the wake of the body using current particle image velocimetry techniques. This typically involves modeling the vortical structures observed in the experiment (say as toroidal vortex rings as in the case of a maneuvering fish). The *pressure impulse force*, \mathbf{F}_p , is simply the *added mass* force on the body (Newman, 1977), which depends solely on the geometry and motion of the body, so it can readily be estimated. Since we have developed an equation for the force in terms of the vorticity in the wake (which is easy to characterize using particle image velocimetry) and the velocity potential (which is easy to model for standard geometrical shapes), we have a useful equation that can be applied to analyze and explain experimental results or can be applied as a basis for efficient numerical simulations.

1.2.3 Incorrect derivation of the force

It may be tempting, yet incorrect, to try to derive equation (1.2.13) directly from a statement of the total change in momentum of the fluid, as in

$$\tilde{\mathbf{F}} = -\frac{d}{dt} \left[\int_V \rho \mathbf{u} dV \right] \quad (1.2.19)$$

where the tilde is used to indicate that this force is incorrect. To proceed, one might insert the velocity field decomposition $\mathbf{u} = \mathbf{u}_0 + \nabla\phi$ discussed in Section 1.2.1 into (1.2.19) and apply the *impulse-momentum identity* (1.2.1) to each component. Since $\mathbf{u}_0 = 0$ on S_b by (1.2.9), the rotational flow momentum is

$$\int_V \rho \mathbf{u}_0 dV = \frac{1}{2} \rho \int_V \mathbf{x} \times \boldsymbol{\omega}_a dV - \frac{1}{2} \rho \int_{S_\infty} \mathbf{x} \times (\hat{\mathbf{n}} \times \mathbf{u}_0) dS \quad (1.2.20)$$

Note that the integral over the exterior bounding surface cannot be assumed to be zero, and (1.2.5) shows that in fact it is non-zero.

Since $\nabla \times \nabla\phi = 0$ identically, the simple potential flow momentum is

$$\begin{aligned}\int_V \rho(\nabla\phi) dV &= -\frac{1}{2} \rho \int_{S_b} \mathbf{x} \times (\hat{\mathbf{n}} \times \nabla\phi) dS - \frac{1}{2} \rho \int_{S_\infty} \mathbf{x} \times (\hat{\mathbf{n}} \times \nabla\phi) dS \\ &= \int_{S_b} \rho\phi \hat{\mathbf{n}} dS - \frac{1}{2} \rho \int_{S_\infty} \mathbf{x} \times (\hat{\mathbf{n}} \times \nabla\phi) dS\end{aligned}\quad (1.2.21)$$

where again the component on the exterior bounding surface cannot be ignored. This presentation ignored the effect of the vortex sheet on the body surface; if it were properly accounted for, the volume integral of the vorticity field (i.e. the vortex sheet) would cancel the body surface integral of $\hat{\mathbf{n}} \times \mathbf{u}_b$ anyway (as in deriving (1.2.12)), yielding the result shown in equation (1.2.21).

Inserting (1.2.20) and (1.2.21) into (1.2.19) and combining the integrals on S_∞ yields the result

$$\begin{aligned}\tilde{\mathbf{F}} &= -\frac{d}{dt} \left[\frac{1}{2} \rho \int_V \mathbf{x} \times \boldsymbol{\omega}_a dV \right] - \frac{d}{dt} \left[\int_{S_b} \rho\phi \hat{\mathbf{n}} dS \right] \\ &\quad + \frac{d}{dt} \left[\frac{1}{2} \rho \int_{S_\infty} \mathbf{x} \times (\hat{\mathbf{n}} \times \mathbf{u}) dS \right]\end{aligned}\quad (1.2.22)$$

This is the same force as given in the impulse force model (1.2.13), with the addition of the surface integral over S_∞ . Had the pressure term in (1.0.3) been included from the outset,

$$-\int_{S_\infty} p \hat{\mathbf{n}} dS$$

the surface integrals over S_∞ would cancel by (1.2.5), and the correct result (1.2.13) would be recovered.

1.3 Applications in experimental hydrodynamics

The impulse framework presented herein is applicable to a wide range of experimental hydrodynamics problems, since typically Reynolds numbers are large and wakes contain well-defined vortical structures. These wakes can be characterized using particle image velocimetry (PIV) and modeled using classical vortex dynamics and potential flow theory. In this thesis, I apply my impulse framework to several experimental hydrodynamics problems and show new facets of the framework in each application. This thesis makes important contributions in three key areas: (I) propulsion and maneuvering of fish; (II) numerical and analytical methods for experiments, with application to the water entry of spheres; and (III) design and analysis of marine propellers and hydrokinetic turbines.

Fish generate propulsive forces by creating and manipulating large-scale vortical structures using their body and tail. Using time-resolved PIV with live fish (in Chapter 2), I show the formation of distinct vortex rings at multiple stages of a maneuver. These vortex rings impart an impulse change to the animal, allowing it to turn, fast-start, and escape from predators. Modeling the impulse using classical vortex dynamics theory, I show how the framework of this thesis can be used to analyze fast-starting and turning maneuvers by fish. Extending this work with live fish (in Chapter 3), I present experiments with a biomimetic, compliant robot fish. This chapter shows that the swimming speed of the robot scales with the size and strength of its wake, and it explains why operating away from the intended design flapping frequency produces non-optimal body vibrations and a vortical wake with high lateral force and reduced thrust. Using my results to optimize the kinematics of fish-like robots could increase their swimming efficiency and maneuvering ability.

In Chapter 4, I further examine the dynamics of a swimming fish's wake using singular value decomposition (SVD). Although the results were not surprising -- that the dynamic modes of the fish's wake, which is reverse Kármán street, resemble those

of a regular Kármán street created by flow past a circular cylinder -- this study raised an important question: How does experimental error affect the results of the SVD? Chapter 4 shows that experimental error tends to corrupt higher SVD modes, in which the root mean square data value is smaller than the measurement error. Using this result, I derive a threshold criterion that can be used as a rough limit of the validity of SVD modes extracted from experimental data. My threshold criterion is of practical importance to the experimental community, since it governs the applicability of SVD to experimental data, which inevitably contain measurement error.

Experimental measurement error makes even the simple task of finding the instantaneous derivatives of time-series data quite challenging. Chapters 5 and 6 were motivated by example; in order to determine the unsteady forces on a sphere using a high-speed image sequence, one needs to determine the acceleration from digitized position data. Since instantaneous derivatives can be predicted using a smoothing spline (which yields analytic derivatives that follow the local trends in the data), I present (in Chapter 5) a novel and robust method for choosing the best spline fit and, hence, the best prediction of the desired derivatives. The water entry of hydrophobic spheres is actually one hydrodynamics problem with no wake, since an air cavity is formed behind the sphere during water entry. As a result, the vortex impulse force on the sphere is taken to be zero, and the flow is modeled as potential flow. In Chapter 6, I show that the pressure impulse force acting on the body is, in fact, the net pressure force, with the pressure evaluated using unsteady Bernoulli's equation. For a sphere immersed in an infinite fluid, this is the added mass force, as will be discussed. To analyze the forces on the sphere during water entry, I present a semi-empirical potential flow model, which accounts for the pressure impulse force on the sphere. My potential flow model represents the cavity as series of ring sources, and it shows that the instantaneous forces on the falling sphere are modulated by the evolution of the cavity shape during growth and collapse of the sub-surface air cavity.

While the sphere problem is a case in which the vortex impulse force is zero and the total force is simply the pressure impulse force, the steady operation of a marine propeller affords the opposite scenario. Here, the pressure impulse force is zero due to steady operation, and the total force on the propeller is given by the vortex impulse force. In Chapter 7, I apply the impulse framework of this thesis to derive propeller lifting line theory, which is the mathematical basis for a method of design and analysis of marine propellers and horizontal axis turbines. Using this applied theoretical framework, I develop an off-design performance analysis method, which allows for rapid estimation of the performance curve for a marine propeller. I have implemented my method in **OPENPROP**, a suite of open-sourced computer codes for the rapid design and analysis of marine propellers and hydrokinetic turbines, as will be discussed.

In Chapter 8, I present validation data for my propeller off-design performance method. I use **OPENPROP** to design a propeller for use in water tunnel tests. In a series of tests, I show that the performance curve predicted using my vortex-impulse method matches well with experimental data for a wide range of the operational profile. In this chapter, I also investigate the unsteady start-up of this propeller and use PIV to characterize the unsteady vortical wake generated by the propeller. Modeling the initial wake as an axisymmetric vortex ring (analogous to the maneuvering fish), I derive an estimate of the thrust produced by the propeller during this impulsive startup event.

In Chapter 9, I show that since vortex impulse reverses with a sign change in the vorticity, propeller lifting line theory can also be applied to the design of hydrokinetic turbines, the marine analog of wind turbines. In this chapter, I present the design, construction, and off-design performance tests for a hydrokinetic turbine, using the same experimental apparatus as the propeller tests. Finally, I summarize the contributions of this thesis and offer perspective and outlook in Chapter 10.

Bibliography

- Abbott IH, von Doenhoff AE (1959) Theory of Wing Sections. Dover.
- Bachelor G (1967) An Introduction to Fluid Dynamics. Cambridge Univ. Press.
- Borazjani I, Sotiropoulos F (2008) “Numerical investigation of the hydrodynamics of carangiform swimming in the transitional and inertial flow regimes,” Journal of Experimental Biology **211**:1541–1558.
- Dabiri J (2009) “Optimal vortex formation as a unifying principle in biological propulsion,” Annual Review of Fluid Mechanics **41**:17–33.
- Homsy G, Aref H, Breuer K, Hochgreb S, Koseff J, Munson BR, Powell K, Robertson C, Thoroddsen S (2000) Multimedia Fluid Mechanics DVD. Cambridge Univ. Press.
- Lamb H (1945) Hydrodynamics. Dover Publications.
- Lighthill J (1979) “Waves and hydrodynamic loading,” In: Proceedings of the Second International Conference on the Behaviour of Off-Shore Structures, London.
- Lighthill J (1986a) “Fundamentals concerning wave loading on offshore structures,” Journal of Fluid Mechanics **173**:667–681.
- Lighthill J (1986b) An Informal Introduction to Theoretical Fluid Mechanics. Clarendon Press.
- Milne-Thomson L (1958) Theoretical Aerodynamics. Dover Publications.
- Newman J (1977) Marine Hydrodynamics. MIT Press.
- Noca F (1997) On the evaluation of time-dependent fluid-dynamic forces on bluff bodies. PhD thesis, California Institute of Technology.
- Saffman P (1995) Vortex Dynamics. Cambridge University Press.
- Schlichting H (1987) Boundary Layer Theory. McGraw Hill.

Stettler J (2004) Steady and unsteady dynamics of an azimuthing podded propulsor related to vehicle maneuvering. PhD thesis, MIT.

von Loebbecke A, Mittal R, Fish F, Mark R (2009) “Propulsive efficiency of the underwater dolphin kick in humans,” J. Biomechanical Eng. **131**(5)

Wu J, Wu J (1996) “Vorticity dynamics on boundaries,” Advances in Applied Mechanics **32**:119–275.

Part I

Fish propulsion

[THIS PAGE INTENTIONALLY LEFT BLANK]

Chapter 2

Impulse generated during unsteady maneuvering of swimming fish

In this chapter, we consider the impulsive maneuvering of live swimming fish, and we use the framework developed in Chapter 1 to analyze the impulse imparted to the fish during the maneuver. In these experiments, we characterize the vortical wake generated by the fish using high-speed particle image velocimetry (PIV). The two vortical structures observed are modeled as toroidal vortex rings, which each have impulse (directed normal to the plane of the ring) of magnitude

$$|\mathbf{I}_v| = \rho \Gamma A \left(1 + \frac{3}{4} \frac{a}{A} \right) \quad (2.0.1)$$

where Γ is the circulation of the vortex, $A = \frac{\pi D^2}{4}$ is the frontal area of the ring, D is the major diameter (core to core), $a = \frac{\pi d^2}{4}$ is the cross-sectional area of the torus, and d is the wire diameter of the torus (Saffman 1995, p. 199).

Applying the framework developed in Chapter 1, we have that the total force on the fish is given by equations (1.2.14), (1.2.15), and (1.2.16), which are reproduced

here

$$\mathbf{F} = \mathbf{F}_v + \mathbf{F}_p \quad (1.2.14)$$

$$\mathbf{F}_v = -\frac{d\mathbf{I}_v}{dt} = -\frac{d}{dt} \left[\frac{1}{2} \rho \int_V \mathbf{x} \times \boldsymbol{\omega}_a dV \right] \quad (1.2.15)$$

$$\mathbf{F}_p = -\frac{d\mathbf{I}_p}{dt} = -\frac{d}{dt} \left[\int_{S_b} \rho \phi \hat{\mathbf{n}} dS \right] \quad (1.2.16)$$

The total change in momentum of the fish from the start to the end of the maneuver is given by integrating the total force acting on the fish during the maneuver

$$m_{\text{fish}} \Delta \mathbf{V}_{\text{fish}} = \int_{t_{\text{start}}}^{t_{\text{end}}} \mathbf{F} dt = \int_{t_{\text{start}}}^{t_{\text{end}}} \mathbf{F}_v dt + \int_{t_{\text{start}}}^{t_{\text{end}}} \mathbf{F}_p dt \quad (2.0.2)$$

In the ‘C’-turn maneuvers discussed herein, the fish enters and exits the turn moving straight ahead, so the time-integral of the pressure impulse force is the net change in *added impulse* of the fluid: $\int_{t_{\text{start}}}^{t_{\text{end}}} \mathbf{F}_p dt = -m_a \Delta \mathbf{V}_{\text{fish}}$, where m_a is the *added mass* of the fluid about the fish for straight-ahead swimming (Newman, 1977). Since $\int_{t_{\text{start}}}^{t_{\text{end}}} \mathbf{F}_v dt = -\Delta \mathbf{I}_v$ by the fundamental theorem of calculus, we arrive at an impulse balance between the fish and fluid for the maneuver

$$(m_{\text{fish}} + m_a) \Delta \mathbf{V}_{\text{fish}} = -\Delta \mathbf{I}_v \quad (2.0.3)$$

Equation (2.0.3) simply states that the net change in momentum of the fish balances the net change of impulse of the fluid. In summary, by characterizing the strength and geometry of the vortices in the wake of the fish using high-speed PIV, we can verify that the change in momentum of the fish is accurately predicted by the vortex impulse framework.

In this chapter, the relationship between the maneuvering kinematics of a Giant Danio (*Danio aequipinnatus*) and the resulting vortical wake is investigated for a rapid, ‘C’-start maneuver using fully time-resolved (500 Hz) Particle Image

Velocimetry (PIV). PIV illuminates the two distinct vortices formed during the turn. The fish body rotation is facilitated by the initial, or ‘maneuvering’ vortex formation, and the final fish velocity is augmented by the strength of the second, ‘propulsive’ vortex. Results confirm that the axisymmetric vortex ring model is reasonable to use in calculating the hydrodynamic impulse acting on the fish. The total linear momentum change of the fish from its initial swimming trajectory to its final swimming trajectory is balanced by the vector sum of the impulses of *both* vortex rings. The timing of vortex formation is uniquely synchronized with the fish motion, and the choreography of the maneuver is addressed in the context of the resulting hydrodynamic forces.

The following text previously appeared in:

B.P. Epps and A.H. Techet (2007) “Impulse generated during unsteady maneuvering of swimming fish,” Experiments in Fluids **43**:691-700.

2.1 Introduction

When it comes to maneuvering performance, fish can swim circles around underwater vehicles. A conventional, propeller-driven underwater vehicle turns by sweeping a circular arc, about ten vehicle lengths in diameter, and this requires about fifteen times the amount of time it would take to cruise forward one vehicle length. In contrast, a fish, such as the Giant Danio (*Danio aequipinnatus*), can turn in a space that is approximately one third of its body length and requires only about half the time it takes to swim one body length. This performance is enhanced by the well-choreographed formation and control of large-scale wake vortices by the fish body and fins.

Maneuvers and fast-starts are defined classically as either ‘C’ or ‘S’ types. Typically, three stages of each maneuver are considered: in stage one (the preparatory stage) a straight swimming fish bends into a C or S shape; in stage two (the propulsive stage) the fish sweeps its tail in the reverse direction; and in the final, variable stage, the fish exits the turn either swimming straight ahead or coasting (Weihs, 1973; Webb, 1978). Classical hydrodynamic analyses by Lighthill (1971) and Weihs (1972) assert that as the body bends, unsteady (added mass) forces oppose this motion and apply a net angular moment on the fish, thus turning the body. When the fish whips its tail aft to straighten its body, it generates a propulsive force parallel to the direction of the anterior portion of the fish body.

In fast-starting maneuvers, the fish is essentially stationary at the onset of the turn and exits the maneuver with a non-zero velocity. This is in contrast to the case where a fish has an initial non-zero forward velocity and then turns to swim along another trajectory. When the fish has an initial forward velocity, turning can be initiated by simply reorienting the head or tail to achieve a lifting force which causes a moment on the body. Blake and Chan (2006) offer physical models to describe these two cases in the context of powered versus unpowered turns.

Researchers use qualitative and quantitative experimental techniques to better understand fish maneuvering performance (e.g. Weihs (1972); Harper and Blake (1990); Wolfgang et al (1999)). An excellent review of the kinematics and performance of fast-starting is presented by Domenici and Blake (1997). Research on the maneuvering of fish-like swimming mechanisms also extends to the robotic realm, from biomimetic studies with robotic fish (e.g. Triantafyllou et al (2000) and Bandyopadhyay (2002)) to simple flapping foils and fins (e.g. Freymouth (1988); Albhorn et al (1991, 1997); Tobias (2006)).

Flow visualization helps researchers studying live fish better understand the overall vortical wake structure. McCutchen (1977) presents shadograph images of

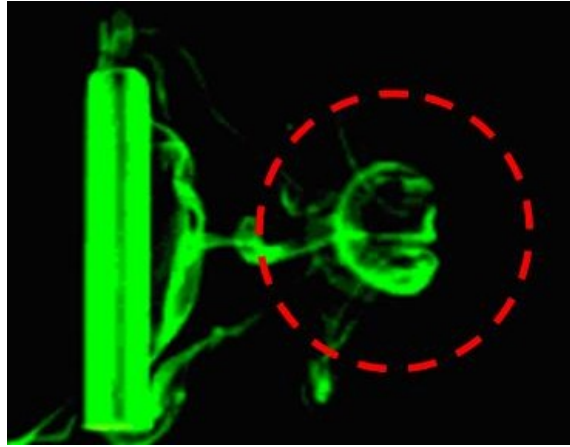


Figure 2-1: Dye visualization of a foil that has flapped once to the right on the page and back to the position shown in a continuous motion, as viewed from behind the trailing edge. The foil is a NACA0030 with 2:1 aspect ratio. The flap took 3.2 sec and had a maximum heave of approximately one chord length, maximum angle of attack of 20° , and 0° phase shift between heave and pitch. Courtesy, Tobias (2006).

a maneuvering Zebra Danio (*Brachydanio rerio*) which show two wakes generated during burst-and-coast swimming maneuvers, and he suggests that these wakes may be modeled as vortex rings. Müller et al (1999) and Wolfgang et al (1999) use particle imaging velocimetry (PIV), both at 30 Hz or less, to quantitatively visualize the wake of maneuvering Zebra and Giant Danio, respectively. Müller et al (1999) present a very thorough analysis of the maneuvering wake, as well. In addition to the PIV results, Wolfgang et al (1999) presented a panel method numerical simulation of a maneuvering fish, showing good agreement with the experiments.

Dye visualization experiments by Tobias (2006) show that for a simple double flap motion of a NACA 0030 foil, with a 2:1 aspect ratio, a single vortex ring could be formed (see figure 2-1). Tip and trailing edge vortices are shed in a horseshoe shape that eventually pinches off into a single, discrete vortex ring. Similar looking vortex rings are reported in the wake of swimming fish by McCutchen (1977), in his shadowgraphs of maneuvering fish, and also by Drucker and Lauder (1999) through PIV experiments on steady swimming fish.

Modeling the wake of a maneuvering fish as a simple vortex ring makes the analysis straightforward; an algebraic expression predicts impulse of the ring. Thus, by inspecting the wake generated by a maneuvering fish, one can deduce the impulse imparted on the body during the maneuver.

Since the typical maneuver time of the Giant Danio is less than one half of one second, it is desirable to revisit the problem of the maneuvering fish with high-speed PIV capable of frame rates over 100 Hz. Thus fully time-resolved PIV is used here to illustrate the vortical evolution and circulation as a function of time over the duration of the maneuver. ‘C’ starts and turns are investigated to capture the instantaneous flow field with enhanced spacial and temporal resolution over prior published results. Using the simple vortex ring model, the circulation and impulse is calculated for each vortex generated by the fish. The overall body kinematics and momentum through the turn are compared with the vortex evolution and impulses to develop an enhanced understanding of fish maneuvering.

2.2 Materials and methods

The experimental study with maneuvering fish was performed using the Giant Danio (*Danio aequipinnatus*) in a small tank, in which the fish were allowed to swim freely. The four fish ranged in length from 5.0 to 7.5 cm and mass from 1.6 to 5.6 grams. Results presented herein are for a larger adult fish that had a mass of 4.3 g and had an overall length, height, and beam of 7.4, 1.9 and 0.83 cm, respectively. The fish were constrained to swim in a 15.6 cm × 12.5 cm working area, with 8 cm deep water. The maneuvers considered were those in response to visual and auditory stimuli; a slender rod was introduced into the aquarium near the wall and tapped the floor of the tank, triggering an evasive maneuver.

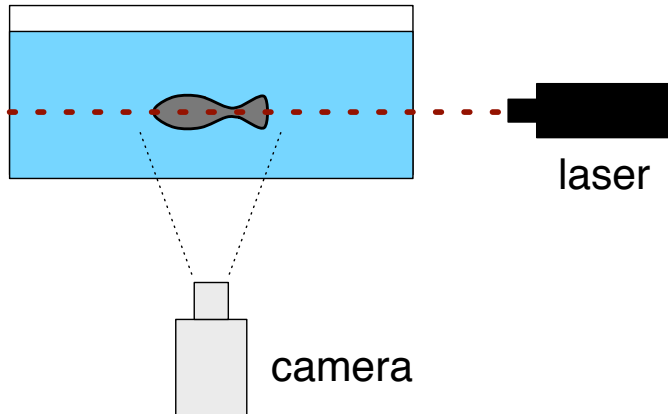


Figure 2-2: Experimental PIV setup used for maneuvering studies. The high speed camera viewed up through the bottom of a glass aquarium, and the laser sheet was oriented horizontally at the midplane of the fish.

The flow features were characterized using a high-speed implementation of particle imaging velocimetry (PIV) (Raffel et al, 2002). The tank was seeded with silver coated, neutrally buoyant, hollow glass spheres (average diameter 93 μm). The particles were illuminated using a low-powered, near-IR diode laser. The Lasiris Magnum diode laser produced a maximum output of 500 mW at 810 nm, and was fitted with optics to produce a 10° fan of light. The horizontal light sheet was imaged using an IDT XS-3 CCD camera with an 85 mm Nikkon lens which viewed up from the bottom of the tank (see figure 2-2). The high-speed camera imaged at 500 frames per second (fps), yielding a time-step between frames of 0.002 s. The image resolution was 1260 x 1024 pixels and the field of view was 15.33 cm x 12.46 cm, giving a 82.2 px/cm zoom. The laser sheet was positioned 3.5 cm from the bottom of the tank. Many runs were performed, but only those where the fish was positioned such that the light sheet was at its mid-plane (i.e. approximately along the lateral line of the fish) were processed. Since the fish were allowed to swim freely, it was a significant challenge to ensure that the light sheet illuminated the mid-plane of the body. Luckily, however, the fish did not actively try to elude the near-IR light sheet as they typically do with green lasers.

The time-series of particle images were processed using the LaVision DaVis 7.1 software package. A multi-pass, cross-correlation processing algorithm, with a final interrogation window size of 32×32 pixels and 50% overlap was used for processing all of the images. The output was a velocity field of 79×64 vectors, with approximately 38 vectors along the length of the fish body. The velocity field was postprocessed in Matlab to determine vorticity and circulation, as well as the body trajectory.

Circulation of each vortex was computed by evaluating Stokes theorem numerically

$$\Gamma = \sum_{i,j} \omega_{(i,j)} \delta A \quad (2.2.1)$$

where $\omega_{(i,j)}$ is the curl of the velocity field at point (i,j) , and $\delta A = (16 \text{ px})^2 = 0.0379 \text{ cm}^2$ was the area of each interrogation window. The circulation computed depends on the area defined to be the vortex: the more area considered, the higher the total circulation. Gharib et al (1998) overcome this by defining the vortex to reside within an isovorticity line of some fixed level. To calculate the circulation of the vortices in the fish wake presented herein, an isovorticity line equivalent to 25% of the maximum vorticity is chosen for each vortex. Given our field of view and PIV spatial resolution, this percentage yielded the most accurate and repeatable results.

Figure 2-3 is an example of the circulation calculated as a function of percentage of the maximum vorticity considered. These data were computed for the first vortex formed by the fish during its maneuver, 0.120 seconds after the start of the turn, corresponding to the fifth frame of figure 2-5. The plot shows that, as the vorticity threshold decreases towards 5% of the maximum vorticity in that vortex, the circulation steadily increases, but beyond the 5% level, the circulation blows up, due to summing low-level vorticity over a large area of the ambient fluid. For this example, the 25% vorticity threshold level yields a circulation of $22.8 \text{ cm}^2/\text{s}$, whereas using a threshold of 5% would yield $26.0 \text{ cm}^2/\text{s}$, or approximately 14% more circulation.

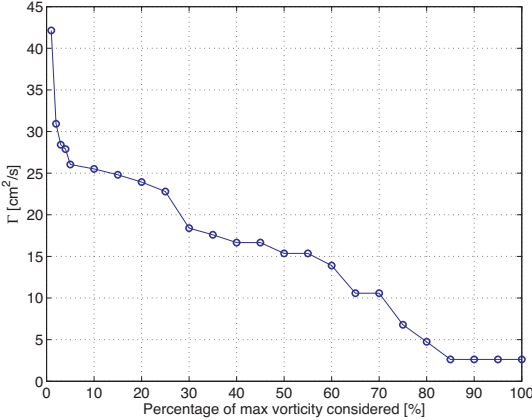


Figure 2-3: Plot of circulation computed by Stokes theorem (equation 8.1.8) versus the threshold percentage of the maximum vorticity used to bound the vortex, for vortex 1A at time $t = 0.120$ s, as shown in figure 2-5. For reference, the values at 1, 5, and 25% are 53.1, 23.2, and $20.0\text{ cm}^2/\text{s}$, respectively.

Using a threshold of 1% yields $53.1\text{ cm}^2/\text{s}$, a 129% difference from a baseline 5% threshold level, which introduces unacceptable error. Using a 25% vorticity threshold admittedly introduces a 10-15% uncertainty on circulation calculations, but it limits the region of interest to the vortices formed by the fish. For figure 2-5, only vorticity levels greater than 10 1/s have been shown, which is consistent with the 25% vorticity threshold used in all circulation calculations.

2.3 Results and Discussion

This section focuses on a representative C-start maneuver, in which the fish makes a 105° clockwise turn in 0.25 seconds. In this powered turn, the fish is barely moving at the onset, but increases its speed ten-fold by the end of the maneuver. The kinematics, vortex circulation, and timing will be discussed.

An overview of this C-start is presented in figure 2-4. Here, mid-line body traces of the fish at 0.012 s intervals (every 6th frame) are shown. These mid-lines are determined manually by inspecting the fish body position in the PIV image sequence.

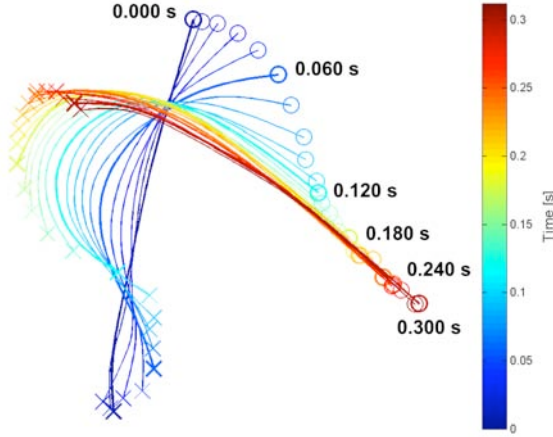


Figure 2-4: Body midline tracings of a 105° single-bend C-start. The head is marked by an “o” and the tail by “x”. The colorbar is offered to help discern the beginning of the turn from the end; the darkest blue trajectory represents the initial body position, and the darkest red line shows the final body mid-line at the end of the turn.

Initially, the fish is moving towards the top of the frame with a velocity of 1.4 cm/s (0.18 L/s). The body proceeds to coil up into a C shape over the first 0.1 seconds of the maneuver. Then the tail rapidly reverses direction and sweeps aft (to the left and upwards in figure 2-4), before the fish extends straight along its new trajectory at time 0.25 s. The final velocity of the fish is 14.6 cm/s (1.98 L/s).

2.3.1 Vortical wake structure

An overview of the vortex formation throughout the maneuver is presented in figure 2-5. This figure shows twelve instantaneous vorticity fields, which were calculated from their respective velocity fields, as determined by the PIV algorithm. The images shown are 15 frames (0.030 s) apart. The vorticity contours are overlayed on digitized projections of the fish’s body determined from the image sequence.

Figure 2-5 shows the formation of four distinct vortices during the maneuver, as well as a patch of vorticity which appeared to pinch off from the third vortex. In the axisymmetric vortex ring model, it is assumed that the two pairs of opposite-signed vortices are each the cross-section of a toroidal-shaped vortex ring. To facilitate

discussion of the two rings, these vortices are labeled vortex 1 and vortex 2. Further, the first side of each ring shed is labeled side A, and the second, side B. Without 3D imaging, it is unclear what role the small patch of vorticity between the two rings plays in the overall wake structure. Thus, the following is a discussion of the generation of vortices 1A, 1B, 2A, and 2B only.

The sequence shown in figure 2-5 begins at the onset of the maneuver. Over the first 30 frames (0.060 s), a strong vortex pair develops at the tail, as the tail pushes against the fluid. The clockwise (blue) side, vortex 1A, is shed first, at time $t = 0.036$ s, followed by vortex 1B, which is shed at $t = 0.092$ s. This first vortex pair is configured in a jet-like arrangement; its impulse is a result of the net forcing by the fish on the water at that location. The inertia of the fluid resists the motion of the fish, and a vortex ring is generated. The reaction force, acting on the caudal peduncle and tail, far from the fish center of mass, applies a clockwise moment on the fish, which augments the anterior body rotation as the fish curls up into the C shape. Henceforth, vortex 1 is referred to as the ‘maneuvering vortex’.

As the fish body flexes into a ‘C’ shape, it draws its head and tail together, pushing and pulling the surrounding fluid and thus, imparting circulation into the flow around the body. Eventually, body-bound vorticity is shed into the wake in a second vortex pair; we refer to vortex two as the ‘propulsive vortex’. Vortex 2A is shed first at $t = 0.150$ s, and vortex 2B, the clockwise side, is shed subsequently at $t = 0.250$ s, between the ninth and tenth PIV frames shown in figure 2-5. This counter-rotating vortex pair also resembles a jet, indicating again a net force by the fish on the fluid at that location. The reaction thrust is in the direction of the fish’s final trajectory, which serves to stop the body rotation and to propel the fish forward.

Since the fish body is reflective and textured, the PIV software can track the body using its cross-correlation algorithm, just as it can track other particles in the fluid. By the body boundary conditions, the velocity field should be continuous and

smooth along the body. Given a smooth and continuous velocity field, its curl can be computed; this is equivalent to the vorticity of a fluid particle or equivalent to twice the rotation rate of a discrete portion of the fish body. For the image sequence used herein, considering all the frames, a continuous velocity field is evident except in the shadow regions. Calculations of vorticity for the time series show that body rotation is ‘shed’ into the fluid during the maneuver in a continuous fashion.

It is useful to note that the laser illuminates the fluid from the left in the PIV images, such that data in the shadow to the right of the fish must be considered with care. Most notably, vortex 2B (labeled in figure 2-5) appears out of the shadow region, just prior to time $t = 0.180$ s, as the fish body moves out of the way from obstructing the laser sheet. Despite being unable to image the formation of vortex 2B, the entire vortex is in full view by the time it is shed, so the calculation of its impulse is still possible.

2.3.2 Maneuver kinematics

The kinematics of the fish motion are now compared with the timing of vortex shedding. From the fish position data presented in figure 2-4, the velocity of the head, caudal peduncle, and tail tip are calculated for each time step in both the local body-tangent (V_{\parallel}) and body-normal (V_{\perp}) directions. For each body location, the tangential direction is defined positive towards the head, and the normal direction is defined positive towards the center of the C-shape.

Figure 2-6 shows several kinematic parameters plotted over the duration of the maneuver; the time at which each vortex is shed from the tail is indicated by the dashed vertical lines. The angular velocity (θ') and acceleration (θ'') of the anterior body, taken from the head to one third of the body length, are shown in figures 2-6(a) and 2-6(b). The body-tangent (V_{\parallel}) and body-normal (V_{\perp}) velocities of the head, caudal peduncle, and tail are shown in figures 2-6(c) - (f).

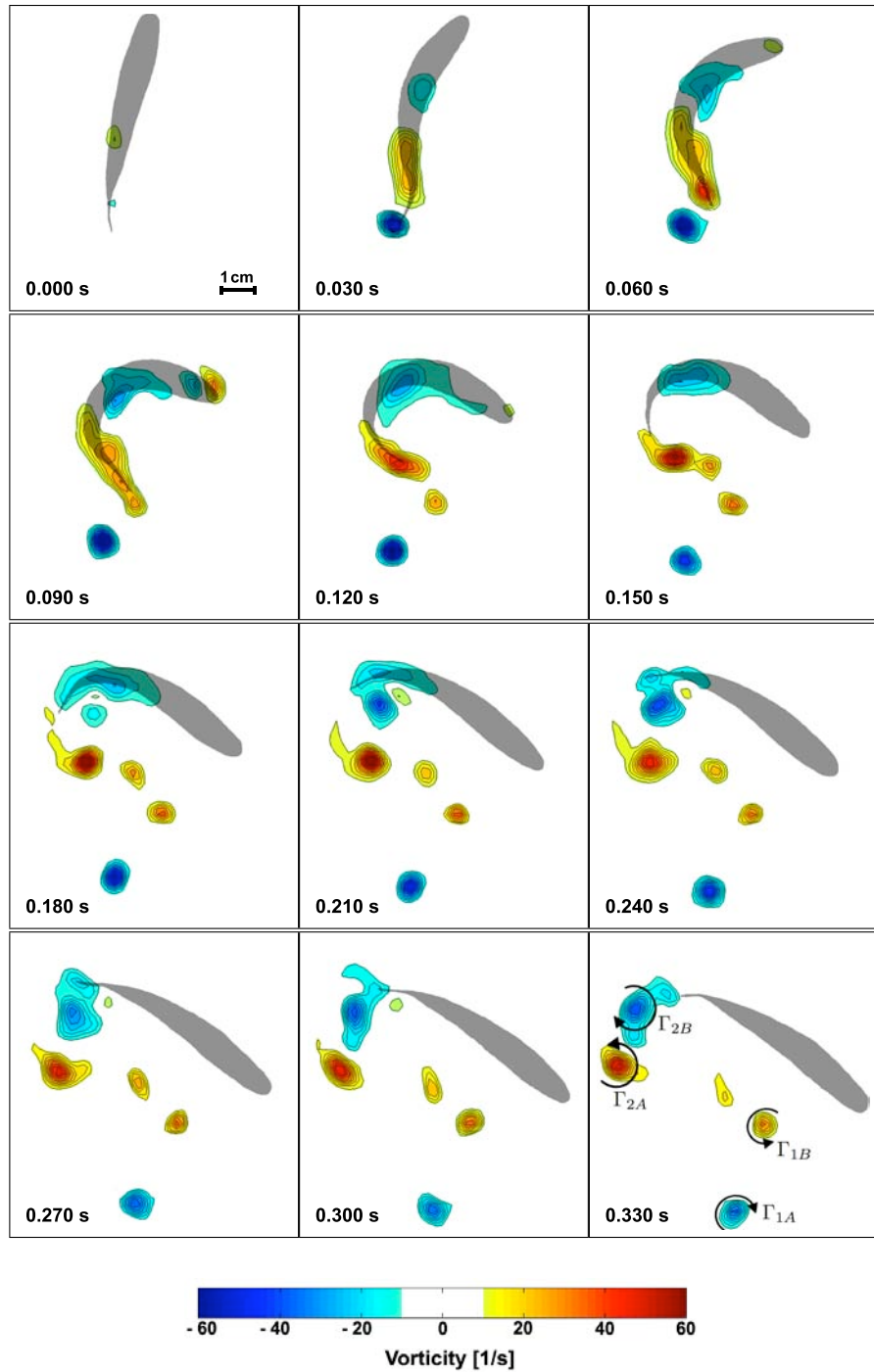


Figure 2-5: Sequence of instantaneous vorticity fields determined using PIV for a 105° C-start. Every 15th frame is presented ($\Delta t = 0.030$ s). Anticlockwise (positive) vorticity is shown in red and clockwise (negative) in blue. Ambient vorticity of less than 10 1/s has been removed for clarity. The four vortices shed during the maneuver are labeled Γ_{1A} , Γ_{1B} , Γ_{2A} , and Γ_{2B} .

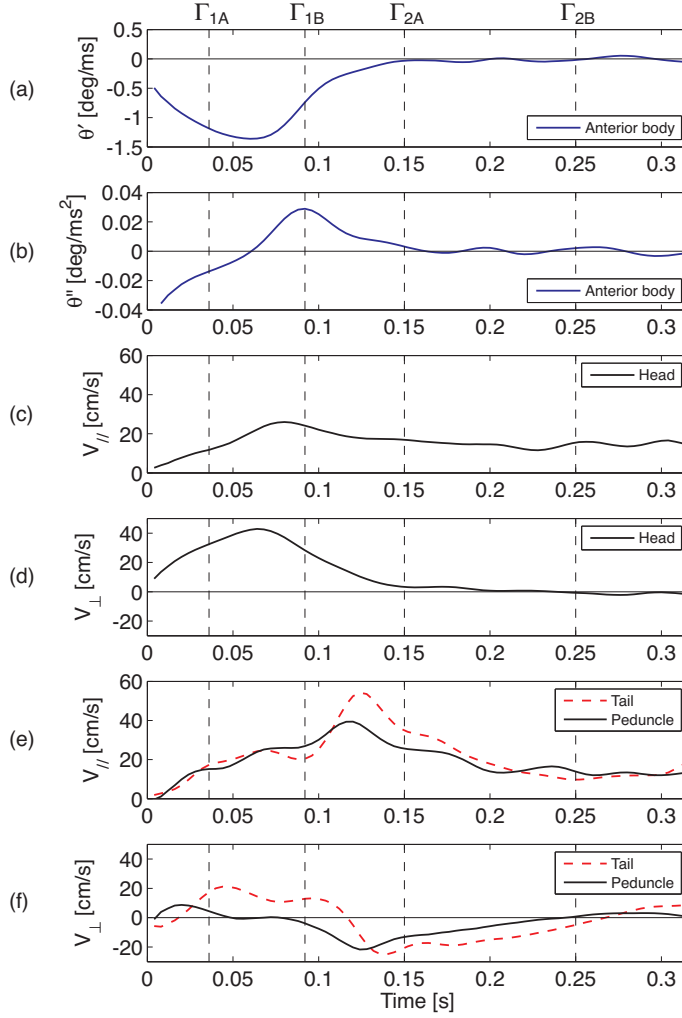


Figure 2-6: Kinematic analysis of the maneuver: (a) Anterior body (head to 1/3 of length) angular velocity, θ' (positive anticlockwise), (b) Anterior body angular acceleration, θ'' , (c) Body-tangential head velocity, V_{\parallel} , (d) Body-normal head velocity, V_{\perp} , (e) Body-tangential tail and caudal peduncle velocities, V_{\parallel} , and (f) Body-normal tail and caudal peduncle velocities, V_{\perp} . All body-tangential (V_{\parallel}) and body-normal (V_{\perp}) velocities are in local coordinate systems for each body part. Body-tangential is instantaneously tangent to the midline at the body part, positive towards the head. Body-normal is positive towards the inside of the C-shape. Dashed lines show times when vortices are shed.

The timing of both anterior body rotation and of vortex shedding closely follows the body-normal motion of the caudal peduncle. This makes sense, because added mass forcing on the peduncle, far from the center of mass, applies a moment on the flexed fish body. This moment, carried through the body by the fish musculature,

acts to turn the anterior portion of the fish. Wolfgang et al (1999) show that vorticity is shed at the caudal peduncle and manipulated by the tail fin. Thus, it is reasonable that the shedding of vortices would follow the motion of the caudal peduncle perpendicular to itself.

Figure 2-6 shows that for stage one of the maneuver, the rotation of the anterior body follows the body-normal velocity of the caudal peduncle. The angular velocity (θ') of the anterior body increases monotonically in the clockwise (negative) sense while the body-normal velocity (V_{\perp}) of the caudal peduncle is positive (i.e. as the fish coils up into the C-shape). Angular velocity reaches its maximum at time 0.060 s, as the caudal peduncle reverses direction. At this time, the angular acceleration changes from negative to positive and the body-normal velocity of the caudal peduncle is zero.

The timing does not synchronize as well for stage two of the maneuver. This is because the fish does not recoil from the C-shape in the same manner as it forms it. Instead, the posterior of the fish unrolls, as the anterior portion rotates and progresses forwards (see figure 2-4). Thus, the negative body-normal peduncle and tail velocities serve to both stop the anterior body rotation as well as provide forward thrust.

A similar correlation between the body-normal motion of the caudal peduncle and the timing of vortex shedding is seen. Vortex 1A is shed at 0.036 s, just prior to the time when the body-normal velocity of the caudal peduncle reaches zero. For a short time, the body-normal velocity at the caudal peduncle remains zero; the motion of the peduncle is tangential only as it traverses the face of what will be the maneuvering vortex. Vortex 1B is shed at 0.092 s, as the caudal peduncle body-normal velocity becomes negative. A patch of secondary vorticity forms as the fish sweeps its tail through the middle portion of the turn. Between times 0.10 and 0.15 s, the motions of the tail and peduncle are predominantly tangential as they follow their paths from the points of release of vortex 1B to 2A. The timing of vortex shedding in stage two does not quite synchronize with the motion of the caudal peduncle. Vortex 2A is shed

at 0.150 s, while the peduncle is still unrolling and has negative body-normal velocity. However, vortex 2B is shed when the body-normal velocity of the caudal peduncle again reaches zero at time 0.250 s. At this point the fish has finished forming the second vortex pair, which results in the final forward motion of the fish along its new trajectory.

2.3.3 Circulation

The circulation of the vortices over time is presented here in the context of the maneuvering choreography. The circulation of each vortex is evaluated using Stokes theorem with a 25% vorticity threshold, as discussed in Section 2.2. Figure 2-7 shows the evolution of circulation in each of the four vortices over time as well as the rotation of the fish body. When determining the circulation and body rotation, a digitized projection of the fish is overlaid on the vorticity field, such that vorticity can be identified as body-bound or free. Only vorticity that is free from the body is considered in the circulation of the vortices. Body-bound ‘vorticity’ is integrated and reported as ‘body rotation’.

In maneuvers when the fish has little to no initial forward velocity, such as this one, the predominant forcing on the fluid can be evidenced in topological flow changes. For the maneuvering fish discussed herein, the rotation of the posterior body and subsequent tail motions act to create vortices 1B and 2A. After vortex 2A is shed at time 0.150 s, the anticlockwise body rotation goes to zero. The sum of the circulations of vortices 1B and 2A at time $t = 0.150$ seconds is $13.2 + 47.9 = 61.1 \text{ cm}^2/\text{s}$.

As the fish coils up into the C-shape, three distinct regions of circulation appear: clockwise vortex 1A, posterior body anticlockwise rotation, and anterior body clockwise rotation. Despite the three dimensionality of our flow, at $t = 0.056$ s, the total circulation is almost zero: $\Gamma_{tot} = -23.7 + 60.2 - 33.9 = 2.6 \text{ cm}^2/\text{s}$. The total circulation is computed at each time step. The average and standard deviation

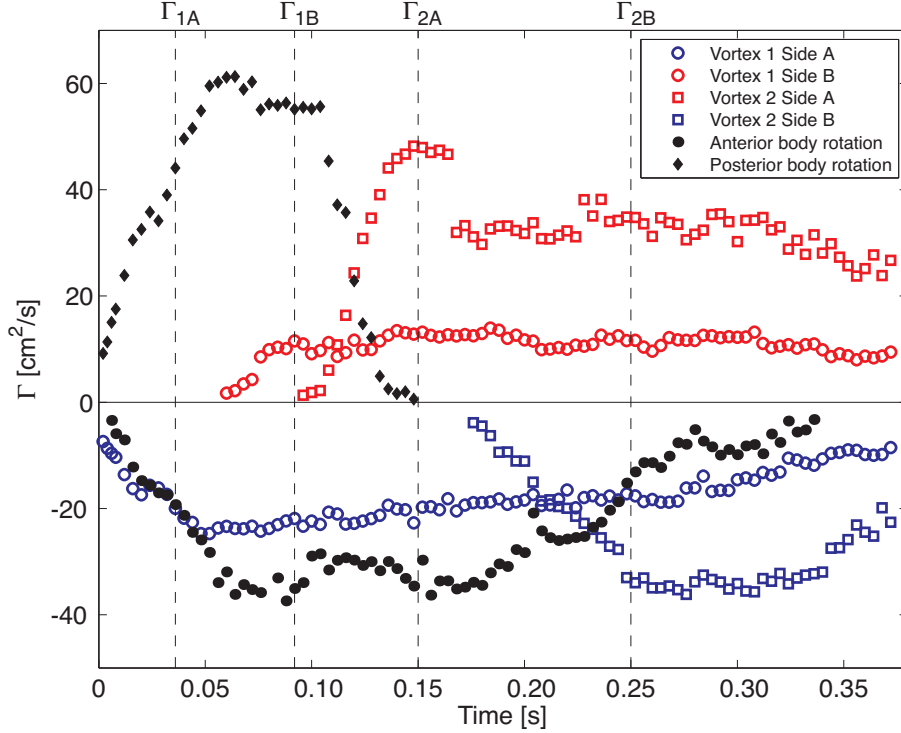


Figure 2-7: Circulation as a function of time for each vortex formed during the maneuver, computed using equation 8.1.8 with a 25% threshold. Counterclockwise (positive) circulation is represented by the red markers for both vortex one and two; clockwise (negative) circulation is indicated in blue. The closed, black circles ‘•’ and diamonds ‘♦’ represent the body rotation generated by the anterior and posterior fish body, respectively. Dashed lines show times when vortices are shed.

of the total instantaneous circulations were 9.4 and $6.2 \text{ cm}^2/\text{s}$, respectively. Vorticity that may have formed at the fish’s nose, could not be imaged due to laser setup.

The circulation data in figure 2-7 support the vortex ring wake model. Vortex rings have the same circulation at any azimuthal position, so a counter-rotating pair made by taking a cross-section should have equal and opposite circulation. Indeed, the two vortex pairs (1A and 1B) and (2A and 2B) exhibit excellent symmetry in both size and circulation over the duration of the turn. The two traces of circulation over time in figure 2-7 match quite well and reinforce the assertion by researchers such as McCutchen (1977) and Drucker and Lauder (1999) that the vortex ring model is quite applicable in fish maneuvering. At the conclusion of the maneuver ($t = 0.250 \text{ s}$), the

circulations of vortices 1A and 1B are $\Gamma = -18.8$ and $12.2 \text{ cm}^2/\text{s}$, and the circulations of vortices 2A and 2B are $\Gamma = 33.8$ and $-34.6 \text{ cm}^2/\text{s}$, respectively.

The uncertainty in these circulation computations is on the order of 15% and comes from three main sources of error: vorticity thresholding, sampling error, and PIV error. The predominant source of error is in the thresholding used to define the vortex. Since the vortex ring model assumes that all circulation is concentrated at or near the core of the vortex ring, counting vorticity far from the core is not appropriate. Thus, choosing the level at which to threshold is a balancing act between including all of the points that constitute the vortex, but not including points far from the centroid. For the example discussed in Section 2.2, a 14% error resulted from thresholding at the 25% level as opposed to the 5% level, but a 129% was prevented error by not summing large areas of low-level vorticity unrelated to the maneuver.

The second source of error comes from the limited sample size available for circulation calculations. The circulation is computed in Matlab by identifying the vortex core, and then running an algorithm which searches for all neighboring points which meet the threshold requirement. To assess repeatability, the authors performed this computation multiple times on any given frame and were always able to repeat their results to within 5% variation. Finally, error in the PIV velocity field, which propagates through circulation computations, is also a factor in the overall error. As an example, consider the circulation of vortex 2A, plotted over time in figure 2-7 (red squares). From time 0.25 to 0.30 seconds, Γ_{2A} should be approximately constant, but it has a mean value of $33.3 \text{ cm}^2/\text{s}$ and standard deviation of $1.8 \text{ cm}^2/\text{s}$. Error in circulation due to PIV error is on the order of 5%.

2.3.4 Comparison of fluid impulse with fish impulse

To better understand how the fluid impulse balances the fish's change in momentum, classical vortex dynamics theory is used. For a vortex ring moving steadily ahead,

the impulse (in the axial direction, normal to the plane of the vortex) has magnitude

$$I_0 = \rho \Gamma \frac{\pi D^2}{4} \quad (2.3.1)$$

where Γ is the circulation and D is the diameter from core to core. For a toroid, then the additional impulse associated with the thickness of the vortex core is

$$I_1 = \rho \Gamma \frac{\pi D^2}{4} \left[\frac{3}{4} \frac{d^2}{D^2} \right] \quad (2.3.2)$$

where d is the diameter of the vortex core (Saffman, 1995).

Figure 2-7 shows that the circulation of the vortices decreases after they are released from the body. Consequently, the circulation of each vortex must be evaluated immediately after it is shed. In other words, the circulation of vortex 1 must be computed immediately after it is shed, several time-steps before vortex 2 is shed. To compute the values listed in table 3.2, the circulation is averaged over the four time-steps following the shedding of each side of each vortex. Thus, the values listed in table 3.2 average out any small variations in time (or measurement) or differences between the two sides of the vortex ring.

The added impulse (added mass times velocity) of a vortex ring is (Dabiri, 2005)

$$I_a = \rho c_{11} \frac{\pi D^2}{4} S U_v \quad (2.3.3)$$

where c_{11} is the added mass coefficient, S is the diameter of the vortex ring in the direction of propagation, and U_v is the velocity of propagation of the ring. Dabiri (2005) reports $c_{11} = 0.72$ for a mechanically generated vortex ring. If added impulse is considered, then the total impulse of a vortex ring becomes

$$\mathbf{I}_v = (I_0 + I_1 + I_a) \mathbf{e}_z \quad (2.3.4)$$

where \mathbf{e}_z is the axial direction in which the impulse acts.

Table 2.1: Table of vortex quantities for the maneuvering and propulsive vortex rings: circulation, Γ ; vortex ring diameter, D ; vortex core diameter, d ; vortex ring axial diameter, S ; vortex ring propagation speed, U_v ; impulse of a concentrated vortex ring, I_0 ; impulse associated with a finite core diameter, I_1 ; added mass impulse, I_a ; total impulse, I_v ; angle the impulse makes with the positive x-axis (to the right on the page, in a lab-fixed Cartesian reference frame), β ; maximum wake velocity, U ; and time to form the vortex, t .

	'maneuvering' vortex	'propulsive' vortex	
Γ (eq. 8.1.8)	17	34	[cm ² /s]
D	1.40	1.84	[cm]
d	0.84	1.03	[cm]
S	1.26	1.66	[cm]
U_v	13.5	14.2	[cm/s]
I_0 (eq. 2.3.1)	25	91	[gcm/s]
I_1 (eq. 2.3.2)	7	21	[gcm/s]
I_a (eq. 2.3.3)	19	45	[gcm/s]
I_v (eq. 2.3.4)	51	157	[gcm/s]
β	-27	167	[deg]
U	16.7	20.0	[cm/s]
t	0.092	0.250	[s]

The results of the wake analyses are presented in table 3.2. Determining the longitudinal vortex diameter (S) via the procedure outlined in Dabiri (2005) proves quite challenging, due to the three-dimensionality of the fish wake. The vortex ring axial diameter is $S \approx 0.9D$ for both vortices over a range of frames. All magnitudes of the impulse (I_0 , I_1 , and I_a) are tabulated, and they all act along the same line. The angle this impulse vector makes with the positive x-axis (to the right on the page in a lab-fixed cartesian reference frame) is given by β .

The vector sum of the impulse of the two vortex rings should balance the net change in linear momentum of the fish (i.e. the impulse applied to the fluid should be equal and opposite to that applied to the fish)

$$\mathbf{I}_f = (m + m_{11})\Delta\mathbf{V} \quad (2.3.5)$$

Table 2.2: Impulse comparison: fluid impulse assuming concentrated vortex rings, I_0 ; fluid impulse assuming finite core diameter rings, $I_0 + I_1$; fluid impulse using the total impulse, I_v ; angle the fluid impulse makes with the positive x-axis (to the right on the page, in a lab-fixed cartesian reference frame), β ; fish impulse using the lower bound for added mass, $I_{f,l}$; fish impulse using the upper bound for added mass, $I_{f,u}$; angle the fish impulse makes with the positive x-axis, α . All fluid impulse values are the magnitude of the vector sum of the impulses of the two ring vortices.

Fluid impulse		
I_0	66	[gcm/s]
β	172	[deg]
Fish impulse		
$I_{f,l}$	65	[gcm/s]
$I_{f,u}$	78	[gcm/s]
α	-47	[deg]
$180 - \alpha$	133	[deg]
I_v	108	[gcm/s]
β	174	[deg]

where $m = 4.3$ g and m_{11} are the fish mass and added mass, and \mathbf{V} is the change in swimming velocity of the fish. The fish initial and final swimming velocities are computed manually by locating a morphological feature of the fish in images five frames apart and computing $\Delta V_x = 10.3$ cm/s and $\Delta V_y = -10.9$ cm/s. Since only the initial and final stages of the turn are considered (when there is no longer any body rotation), the added mass is calculated for a fish moving straight ahead without undulation. A lower bound for m_{11} can be made by assuming the fish is a rigid slender body of revolution, for which the ratio of the added mass to the mass of a neutrally buoyant body is $\frac{m_{11}}{m_f} = (\frac{r}{l})^2 \ln(\frac{r}{l})$, where r is the maximum body radius, and l is the body length (Newman, 1977). Taking r to be the half-breadth of the fish, the added mass is 0.9% of the fish mass. An upper bound for m_{11} is 20% of the fish mass, which was the value found by Webb (1982) for fast-starts of trout. Webb (1982) also reports that other researchers have found values for m_{11} in-between 1% and 20%.

To balance the overall change in momentum of the fish, one must account for *both* the propulsive and maneuvering vortices. The impulse of the individual vortices is

listed in table 3.2, and the net impulse on the fluid and on the fish is reported in table 2.2. For perfect agreement, the magnitudes of the impulses should be equal, and the angle β should equal 180° minus α . For this trial, the magnitude of the change in momentum of the fish was between 65 and 78 gcm/s. If the ‘maneuvering’ vortex is ignored in the momentum balance, then the resulting fluid impulse would be greater than 91 gcm/s (I_0 , listed in table 3.2), which is an overestimation of the magnitude. Further, if the maneuvering vortex was not generated during stage 1, the fish would be unable to effectively generate body rotation, since the moment on the fish would be negligible.

There is not perfect alignment in the direction of fluid and fish impulses (see table 2.2). Since the line of action of the fish impulse was -47° , the fluid impulse should act at 133° from the horizontal. However for this trial, the fluid impulse acts approximately 172° from the horizontal. This discrepancy is most likely due to the curvature of the fish body over the duration of the turn. When the fish has non-zero forward swimming speed, curvature allows the body to act as a lifting surface (i.e. a rudder) to steer the fish through the water. A steady-moving, cambered hydrofoil experiences a moment about its quarter-chord, even though it does not shed trailing edge vorticity. Similarly, the fish will change its swimming direction without any measurable effect on the circulation imparted to the wake.

2.4 Conclusion

This chapter presents fully time-resolved PIV data, with high spatial resolution, for a maneuvering fish. The Giant Danio used in these experiments performs a 105° ‘C’-maneuver during which it generates two distinct vortex rings, indicated by counter-rotating pairs of vortices. The data presented for the circulation of each shed vortex, over time, show good symmetry in the vortex pairs, confirming our assertion that each

vortex pair can be treated as a ring, similar to that formed by the foil in figure 1. This is clearly a three-dimensional problem, warranting further investigation using three-dimensional flow measurement techniques such as stereo PIV (e.g. (Sakakibara et al, 2004)). However, the trade-offs between resolving three-dimensional effects and the rapid time scales of the maneuver make a case for both high speed and 3D flow measurement techniques.

Fish are clearly adapted as graceful swimmers with an excellent capacity for rapid-maneuvering. Through the combination of PIV visualizations (fig. 2-5) and kinematic data (fig. 2-6), it is shown that the formation and shedding of the vortices corresponds well with the motions of the caudal peduncle. This is in agreement with Wolfgang et al (1999) who showed that for a swimming Giant Danio, vorticity is shed at the caudal peduncle and is manipulated by the tail fin.

Several researchers have sought to determine a robust starting point for stage two of a maneuver. As detailed in Domenici and Blake (1997), the transition from stage one to stage two has been defined in several ways: (a) the change in direction of tail motion (i.e. V_{\perp} of the peduncle becoming negative) (Webb, 1978), (b) the change in turning direction of the anterior body midline (from clockwise to anticlockwise in our case) (Domenici and Blake, 1997), (c) the onset of forward propulsion (Foreman and Eaton, 1993), and (d) the onset of contralateral electromyographic signal (Jayne and Lauder, 1993). Note that these four definitions are not necessarily synonymous. In our data, the change in direction of the caudal peduncle motion (a) occurs at $t \approx 0.08$ s, whereas the change in turning direction of the anterior body midline (b) does not happen until $t = 0.150$ s, and the head body-parallel velocity is non-zero (c) at the start of the maneuver.

An alternate, or perhaps even synonymous, definition to those above may arise if the timing of vorticity generation in the fish wake is considered. When the first vortex has been fully shed (i.e. vortex 1B is released from the tail), the fish is no

longer putting energy into the turning phase of the maneuver (stage one), nor into the maneuvering vortex. For the case presented here, vortex 1B is shed at time $t = 0.092$ s, just moments after the change in direction of the caudal peduncle lateral motion, which occurs at $t = 0.078$ s. At this time the peduncle region is moving in a predominately tangential direction, and the tail is just beginning to change directions. The timing of vortex shedding used to determine the transition from stage 1 to stage 2 correlates well with the definition of transition suggested by Webb (1978). The current assessment of the vortex wake does not necessarily agree with criteria (b) by Domenici and Blake (1991) or (c) by Foreman and Eaton (1993), and without EMG data, and cannot compare with (d) by (Jayne and Lauder, 1993).

Taking into account solely the linear momentum of the fish into and out of the turn, it has been shown that the net impulse of the *two* vortex rings is close to the total change in momentum of the fish. In this particular maneuver, the initial velocity is quite low, and thus the fish body is not able to use its initial forward momentum to significantly aid in the turn. Were the fish moving at a sufficiently high initial velocity, such that slight changes in body orientation away from the forward motion could generate a lifting force on either the anterior or posterior sections of the body and thus a turning moment, the need for this ‘maneuvering’ vortex might be lessened. The transitions between maneuvering stages become important when only considering one of the vortices or certain segments of the turn. Here, the question arises as to which parts of the turn should be considered when determining scaling laws: should the entire turn be considered (using both the maneuvering and propulsive vortex), or only the formation of the final vortex ring?

Triantafyllou et al (2005) suggests that a scaling law can be determined using the time to develop a full vortex ring as the principal parameter controlling rapid maneuvering and fast-starting, in a similar fashion to the Strouhal law for steadily flapping foils and the formation number in impulsively-started jets by Gharib et al

(1998). In order to determine scaling laws for maneuvering fish, considering the maneuver from stage one through stage three taking into account only the linear momentum of the fish's body at the beginning and end of the turn, there will be cases where both the first 'maneuvering' vortex jet as well as the second 'propulsive' vortex jet may need to be considered in order to balance the total change in momentum of the fish. There may also be cases where the first vortex is negligible or non-existent due to the initial conditions of the turn.

2.5 Epilogue

In preparing the manuscript reprinted above, I reported the *added impulse* of each vortex ring, I_a , in table 3.2. However, it should be noted that these data are **not** relevant in the momentum balance with the fish. The theoretical framework presented in Chapter 1 postulates that the fluid impulse of interest is that due to the vorticity in the wake. Specifically, equation (1.2.17) defines the impulse in the wake as

$$\mathbf{I}_v = \frac{1}{2} \rho \int_V \mathbf{x} \times \boldsymbol{\omega}_a dV \quad (1.2.17)$$

For a thin-cored toroidal vortex ring, this evaluates to equation (2.0.1) (see Saffman 1995, p. 199), which can be written as

$$|\mathbf{I}| = \rho \Gamma \frac{\pi D^2}{4} \left(1 + \frac{3}{4} \frac{d^2}{D^2} \right) = I_0 + I_1 \quad (2.5.1)$$

Note that this result does not include the added impulse, I_a . The data in table 2.2 show that the change in momentum of the fish ($\mathbf{I}_f = (m + m_{11})\Delta\mathbf{V}$) agrees well with $-(\mathbf{I}_0 + \mathbf{I}_1)$, as expected. However, the inclusion of added impulse, $-(\mathbf{I}_0 + \mathbf{I}_1 + \mathbf{I}_a)$, results in an over-prediction of the momentum change.

Bibliography

- Albhorn B, Harper DG, Blake RW, Ahlborn D, Cam M (1991) “Fish without footprints,” Journal of Theoretical Biology **148**:521–533.
- Albhorn B, Chapman S, Stafford R, Blake RW, Harper DG (1997) “Experimental simulation of the thrust pahses of fast-start swimming fish,” Journal of Experimental Biology **200**:2301–2312.
- Bandyopadhyay P (2002) “Maneuvering hydrodynamics of fish and small underwater vehicles,” Integrative and Comparative Biology **42**:102–117.
- Blake RW, Chan KHS (2006) “Models of the turning and fast-starting swimming dynamics of aquatic vertebrates,” Journal of Fish Biology **69**:1824–1836.
- Dabiri JO (2005) “On the estimation of swimming and flying forces from wake measurements,” Journal of Experimental Biology **208**:3519–3532.
- Domenici P, Blake RW (1991) “The kinematics and performance of the escape response in the angelfish (*pterophyllum eimekei*),” Journal of Experimental Biology **156**:187–205.
- Domenici P, Blake RW (1997) “The kinematics and performance of fish fast-start swimming,” Journal of Experimental Biology **200**:1165-1178.
- Drucker EG, Lauder GV (1999) “Locomotor forces on a swimming fish: three-dimensional vortex wake dynamics quantified using digital particle image velocimetry,” Journal of Experimental Biology **202**:2393–2412.
- Foreman MB, Eaton RC (1993) “The direction change concept for reticulospinal control of goldfish escape,” Journal of Neuroscience **13**:4101–4133.
- Freymouth P (1988) “Propulsive vortical signature of plunging and pitching airfoils,” AIAA Journal **26**:881–883.

Gharib M, Rambod E, Shariff K (1998) “A universal time scale for vortex ring formation,” Journal of Fluid Mechanics **360**:121–140.

Harper DG, Blake RW (1990) “Fast-starts of rainbow trout (*salmo gairdneri*) and northern pike (*esox lucius*) during escapes,” Journal of Experimental Biology **148**:128–155.

Jayne BC, Lauder GV (1993) “Red and white muscle activity and kinematics of the escape response of bluegill sunfish during swimming,” Journal of Comparative Physiology A **173**:495–508.

Lighthill M (1971) “Large-amplitude elongated-body theory of fish locomotion,” Proceedings of the Royal Society of London B **179**:125–138.

McCutchen CW (1977) “Froude propulsive efficiency of a small fish, measured by wake visualization,” In: Pedley T (ed) Scale Effects in Animal Locomotion Academic Press, chap. 22, pp. 339–363.

Müller UK, Stamhuis EJ, Videler JJ (1999) “Hydrodynamics of unsteady fish swimming and the effects of body size: Comparing the flow fields of fish larva and adults,” Journal of Experimental Biology **203**:193–206

Newman J (1977) Marine Hydrodynamics MIT Press.

Raffel M, Willert C, Kompenhans J (2002) Particle Image Velocimetry: A Practical Guide Springer, New York.

Saffman P (1995) Vortex Dynamics Cambridge University Press.

Sakakibara J, Nakagawa M, Yoshida M (2004) “Stereo-PIV study of flow around a maneuvering fish,” Experiments in Fluids **36**:282–293.

Tobias D (2006) Kinematics and vortical wake patterns of rapidly maneuvering fish and flapping foils Bachelor’s thesis, MIT.

Triantafyllou MS, Triantafyllou GS, Yue DKP (2000) “Hydrodynamics of fish-like swimming,” Annual Review of Fluid Mechanics **32**:33–53.

Triantafyllou M, Hover F, Techet A, Yue D (2005) “Review of hydrodynamic scaling laws in aquatic locomotion and fishlike swimming,” Applied Mechanics Review **58**(4):226–237.

Webb P (1978) “Fast-start performance and body form in seven species of teleost fish,” Journal of Experimental Biology **74**:211–226.

Webb PW (1982) “Fast-start resistance of trout,” Journal of Experimental Biology **96**:93–106.

Weihs D (1972) “A hydynamical analysis of fish turning manoeuvres,” Proceedings of the Royal Society of London B **182**:59–72.

Weihs D (1973) “The mechanism of rapid starting of slender fish,” Biorheology **10**:343–350.

Wolfgang M, Anderson J, Grosenbaugh M, Yue D, Triantafyllou M (1999) “Near-body flow dynamics in swimming fish,” Journal of Experimental Biology **202**:2303–2327.

Chapter 3

Swimming performance of a biomimetic compliant fish-like robot

Continuing our work in fish propulsion, we now consider steady swimming. For a free-swimming fish, the instantaneous total force on the animal is unsteady in time, due to the unsteady body undulations and vortex shedding. However, the time-averaged total force must be zero for a fish swimming at constant speed:

$$\langle \mathbf{F} \rangle \equiv \frac{1}{\Delta t} \int_t^{t+\Delta t} \mathbf{F} dt = 0 \quad (3.0.1)$$

where Δt is the period of tail flapping. Therefore, the time-averaged *pressure impulse force* must balance that of the *vortex impulse force*, since

$$\langle \mathbf{F} \rangle = \langle \mathbf{F}_v \rangle + \langle \mathbf{F}_p \rangle = 0 \quad (3.0.2)$$

In the spirit of the vortex impulse framework, we investigate the time-averaged vortex impulse force on the animal

$$\langle \mathbf{F}_v \rangle \equiv \left\langle -\frac{d}{dt} \left[\frac{1}{2} \rho \int_V \mathbf{x} \times \boldsymbol{\omega}_a dV \right] \right\rangle \quad (3.0.3)$$

Thus, by examining the wake, we can infer the vortex and pressure impulse forces on the steadily-swimming fish.

Using particle image velocimetry, we can characterize the geometry and strength of the vortices shed by the swimming fish. In lieu of evaluating (3.0.3) directly, we can model the wake generated by the swimming fish as a series of interconnected vortex loops, and we can approximate $\langle \mathbf{F}_v \rangle$ using classical vortex dynamics theory. Kármán and Burgers (1935) consider the drag on a 2D rigid wing moving at constant speed. Since the wing is rigid and translates uniformly, $\langle \mathbf{F}_p \rangle = 0$ in their model. They model the wake a great distance behind the wing as an infinite double-row of counter-rotating vortices, configured such that it induces a net flow towards the body. With the direction of the circulation reversed, the wake becomes thrust-generating, and the time-average thrust per unit depth is

$$\langle F_v \rangle / b = (\rho \frac{w}{\ell}) U \Gamma + \rho \left(\frac{w}{\ell} \tanh \frac{\pi w}{\ell} - \frac{1}{2\pi} \right) \frac{1}{\ell} \Gamma^2 \quad (3.0.4)$$

where ρ is the fluid density, w is the wake width, ℓ is the streamwise spacing of the vortices, U is the speed of the wing (or fish), and Γ is the circulation of the vortices. Fitting with the theme of this thesis, equation (3.0.4) estimates the force on the body from the strength and geometry of its wake.

In this chapter, I use digital particle image velocimetry and fluorescent dye visualization to characterize the performance of fish-like swimming robots. During nominal swimming, these robots produce a ‘V’-shaped double wake, with two reverse-Kármán streets in the far wake. The Reynolds number based on swimming speed

and body length is approximately 7500, and the Strouhal number based on flapping frequency, flapping amplitude, and swimming speed is 0.86.

It is found that swimming speed scales with the strength and geometry of a *composite wake*, which is constructed by freezing each vortex at the location of its centroid at the time of shedding. Specifically, I find that swimming speed scales linearly with vortex circulation. Also, swimming speed scales linearly with flapping frequency and the width of the composite wake. The thrust produced by the swimming robot is estimated using the above vortex impulse model, and I find satisfactory agreement between this estimate and measurements made during static load tests. These results suggest that it might be of interest in future CFD studies to examine the wake impulse and the fitness of this impulsive force model.

The following text previously appeared in:

B.P. Epps, P. Valdivia y Alvarado, K. Youcef-Toumi, and A.H. Techet (2009) “Swimming performance of a biomimetic compliant fish-like robot,” Experiments in Fluids **47**:927-939.

3.1 Introduction

Fish have attracted the interest of researchers because they have superior swimming ability compared to man-made devices. The understanding of fish swimming dynamics has benefited from significant advances from both theoretical and experimental studies. In particular, Lighthill’s *Note on the swimming of slender fish* (Lighthill, 1960) renewed interest in the theoretical understanding of the physical

principles that enable fish swimming. Subsequent refinements of Lighthill's slender body theory (Wu, 1971; Newman, 1973; Lighthill, 1975; Childress, 1981), research into the dynamics of laminar wakes (Triantafyllou et al, 1986; Karniadakis and Triantafyllou, 1989) and flapping foils (Streitlien and Triantafyllou, 1998), and recent experimental studies (Triantafyllou and Triantafyllou, 1995; Techet et al, 2003) have further contributed to clarify both the kinematics of body motion and the resultant fluid dynamics that enable fish to swim.

Fish that swim by undulating their bodies produce a body wave that travels downstream with phase speed greater than the fish's swimming speed. These kinematics are typically classified by the amplitude envelope of the body undulations and wavelength of the propulsive body wave (Sfakiotakis et al, 1999). Herein, we consider carangiform swimming, which typically has a wavelength of about one body-length and an amplitude envelope which increases in magnitude from nose to tail (Wardle et al, 1995). Reviews of fish swimming are given in (Videler, 1993; Triantafyllou et al, 2000; Fish and Lauder, 2006).

Carangiform swimmers generate propulsive forces by generating and manipulating large-scale vortical structures using their body and tail (Wolfgang et al, 1999; Liao et al, 2003). These structures are similar to those generated by flapping foils. M.S. Triantafyllou et. al. (1991) showed that the wake dynamics of flapping foils are dominated by the Strouhal number, $St = \frac{fA}{U}$, where f is the flapping frequency, U is the forward speed, and A is the width of the wake. They suggest that optimal efficiency is achieved for $0.25 < St < 0.35$. Further, G.S. Triantafyllou et. al. (1993) observed that indeed, many live fish swim in this range of Strouhal numbers. Anderson et. al. (1998) use particle image velocimetry to show that the wake generated by a flapping foil in this Strouhal number range is a reverse Kármán street.

One critical assumption made in (Triantafyllou et al, 1991) is that the wake width, A , is "taken to be equal to the maximum excursion of the foil's trailing edge." This

assumption pervades the fish swimming literature, but herein, we show that the wake dynamics and resulting forces on our swimming robot depend on the width of the wake and not necessarily on the flapping amplitude (see Section 3.4.5).

The understanding of fish swimming has in turn motivated efforts to replicate such performance. In particular, several fish-mimicking devices (Bandyopadhyay, 2005; Anderson and Chhabra, 2002; Yu et al, 2004) and devices that exploit fish-like swimming techniques (Lauder et al, 2007; Bandyopadhyay et al, 1997; Garner et al, 2000; Licht et al, 2004) have been proposed and tested. Traditionally, body and fin motions on robots have been implemented using complex mechanisms which employ several discrete, stiff components. As a result, several actuators are required, along with sophisticated controls. Valdivia y Alvarado and Youcef-Toumi (2003, 2005, 2006) have proposed alternative biomimetic devices based on continuous compliant viscoelastic bodies. The resulting devices are simpler and more robust and can potentially replicate more naturally the required fish motions.

In order to test the capabilities of these new devices, it is natural to look at their swimming performance. In this paper, we focus on carangiform-type swimming, and we present flow visualization studies of prototypes built using our design methodology (Valdivia y Alvarado and Youcef-Toumi, 2008). Dye visualization and particle image velocimetry (PIV) are used to characterize the wake behind a swimming robot. The geometry and strength of the wake are used to estimate the thrust produced during steady swimming, and the results are compared to static thrust measurements.

The remainder of the paper is composed of four sections. Section 3.2 briefly describes the approach used to design and build the swimming robots. Section 3.3 describes the robots used and the flow visualization experiments. Section 3.4 discusses the experimental results. Finally, section 4.5 summarizes our conclusions.

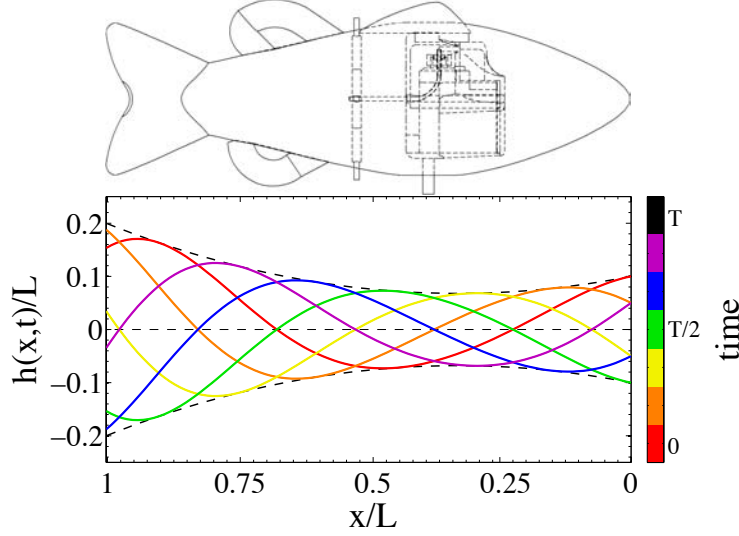


Figure 3-1: Carangiform swimmer target kinematics (at the design flapping frequency, $f_d = 2$ Hz): lateral deflection, $h(x, t)$, is plotted versus distance from the nose, x , for six time steps over one flapping cycle.

3.2 Compliant biomimetic swimming robots

Unlike traditional discrete robots, compliant robots are made of a continuous flexible body whose material distribution is such that a minimum set of input forces can exploit resultant modes of vibration for locomotion (Valdivia y Alvarado and Youcef-Toumi, 2006, 2008). In the case of fish swimming, the design and synthesis process is summarized as follows:

- The desired swimming mode is chosen from a range of classical swimmers, (e.g. anguilliform, carangiform, or thunniform). Reviews of fish swimming characteristics can be found in (Lighthill, 1975) and (Videler, 1993). Based on the desired mode shape, the design-intent body motions are identified (see fig. 3-1). For the carangiform mode, studied herein, the spine motions are given by

$$h(x, t; f) = \frac{1}{2}y(x; f) \cos(2\pi ft - kx) \quad (3.2.1)$$

where f [Hz] is the tail-beat frequency, $y(x; f)$ is the peak-to-peak amplitude of

body lateral deflection at a distance x from the nose (which, for a carangiform swimmer, is different for each frequency), $k = 2\pi/0.9L$ is the wavenumber, and L is the body length. These target body motions, are shown in figure 3-1.

The design-intent flapping frequency is also selected in this step. For the robots studied herein, the design-frequency is $f_d = 2.7$ Hz. The robotic fish are able to swim at other flapping frequencies, though typically with reduced performance.

- b) The body geometry, including fin shape and placement, is dictated by the selected swimming mode. The top panel of figure 3-2 is a schematic of the carangiform-type swimmers studied herein.
- c) The material and actuation distributions are found by solving the governing equation for body dynamics, given the desired kinematics (3.2.1). The body dynamics are governed by a modified Bernoulli-Euler beam equation (Valdivia y Alvarado, 2007)

$$(m + m_a) \frac{\partial^2 h}{\partial t^2} = \frac{\partial^2}{\partial x^2} \left(M(x, t) - EI \frac{\partial^2 h}{\partial x^2} - \mu I \frac{\partial^3 h}{\partial t \partial x^2} \right) \quad (3.2.2)$$

where $m(x)$ and $m_a(x)$ are the mass and added mass per unit length of an infinitesimal section of the body at position x , $I(x)$ is the section moment of inertia, and $E(x)$ and $\mu(x)$ are the material elasticity and viscosity, respectively. The servomotor is commanded by a square-wave input signal and applies a concentrated moment at position $x = a$. This actuation can be approximated with a sine wave and delta function:

$$M(x, t) \approx M_0 \delta(x - a) \sin(2\pi f_d t) \quad (3.2.3)$$

Using equations (3.2.2) and (3.2.3), the material properties, E and μ , as well as the actuator moment, M_0 , and position, a , are determined, which result in the target kinematics (3.2.1).

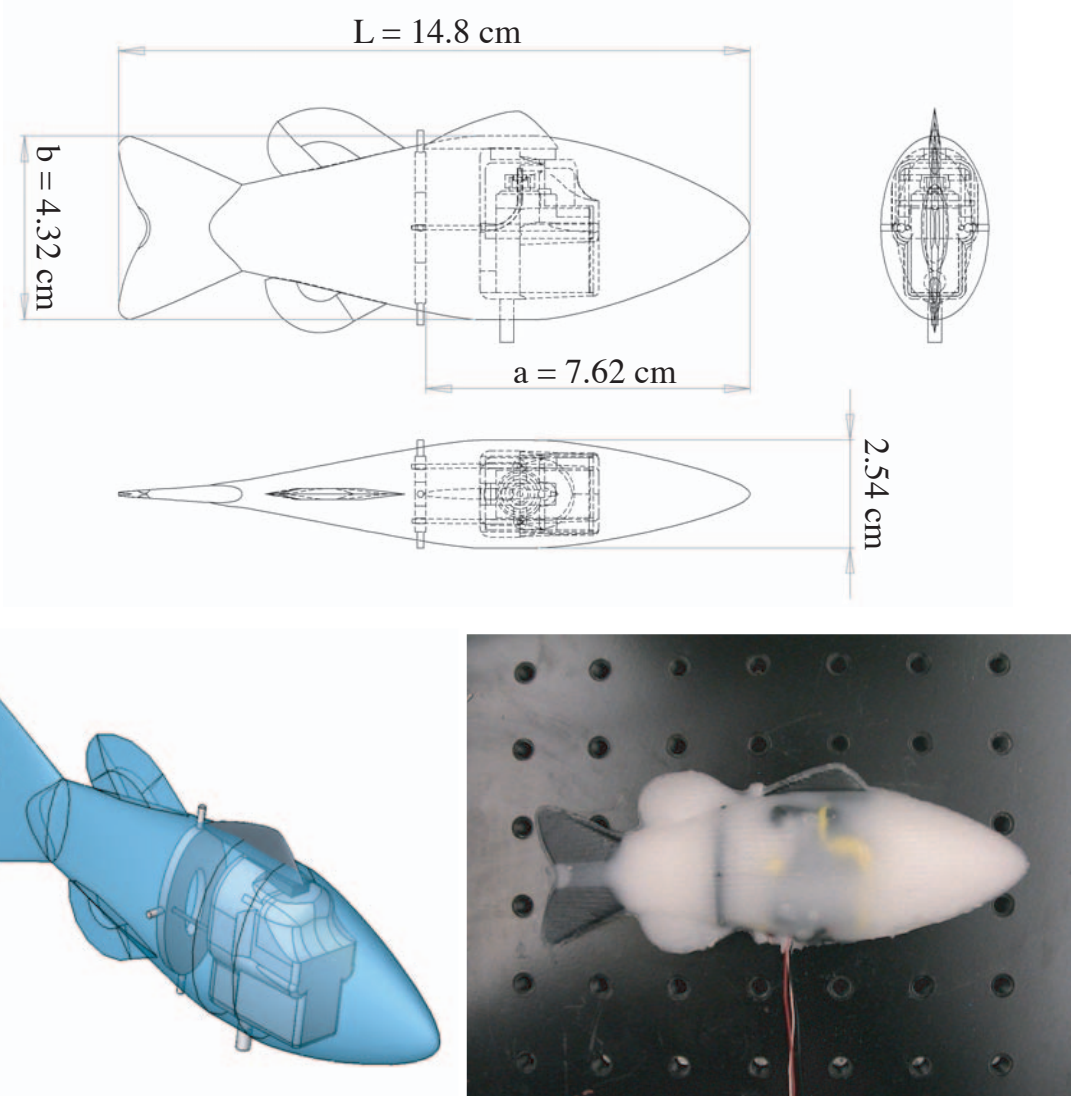


Figure 3-2: The carangiform swimming robot used in the PIV experiments consists of a compliant body with an embedded actuator. Power and control signal are carried by umbilical cord (Valdivia y Alvarado, 2007). (top) schematic, (left) isometric view, (right) robot A.

- d) The prototype's body is cast using silicone and urethane gel compounds matching the desired material properties.

This approach yields simple and robust devices. Further discussion regarding this design process is detailed in (Valdivia y Alvarado, 2007).

3.3 Materials and methods

Two nearly-identical prototypes, robots A and B, were used for the flow visualization experiments. They were designed to mimic the swimming motions and performance of carangiform swimmers. The body form based on these desired motions is shown in figure 3-2.

The two prototypes have a body length from snout to tail tip of $L = 14.8$ cm, are composed of elastomer materials of average elasticity $E = 97835$ Pa and viscosity $\mu = 92.3$ Pa·s, and are powered by single servomotor. The servomotor applies a moment $M_0 = 0.1$ Nm to a plate located at a distance $a = 7.6$ cm from the prototype's snout. The prototypes have a body mass of 68 grams and are close to neutral buoyancy. The two robots were identical in design and differed only due to construction. Robot B was slightly tail-heavy, whereas robot A swam at nearly level trim. The flow features of robot A were characterized using high-speed particle image velocimetry (PIV). Unfortunately, robot A was retired at the conclusion of the PIV experiments due to mechanical failure (after over one hundred hours of swimming), so robot B was used to qualitatively illustrate the wake using dye visualization.

Quantitative measurements were made using high-speed particle image velocimetry (PIV) (Raffel et al, 2002). The robotic fish was allowed to swim freely in a tank seeded with $93\ \mu\text{m}$ particles. A horizontal laser sheet was positioned such that it was at the fish mid-plane. A high-speed camera imaged from below at 100 fps, yielding a time-step between frames of 0.01 s. Image resolution was 1260×1024 pixels, and the field of view was 16.6 cm x 13.5 cm, giving a 75.9 px/cm zoom.

A time-series of PIV images were captured for each of three trials at selected flapping frequencies between 1 and 4 Hz. Flapping frequency, f , tail flapping amplitude, H , and spine location, $h(x, t)$, were determined from these raw images. The time-series of particle images were then processed using the LaVision DaVis 7.1 software package. The output was a velocity field of 79×64 vectors, with

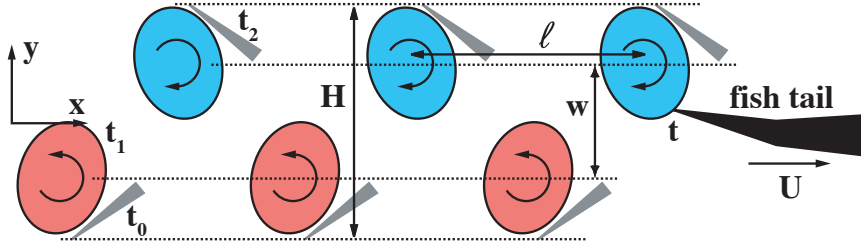


Figure 3-3: Composite wake used to compute wake geometry. The locations of tail maximum excursions and vortex centroids are recorded for three flapping cycles. Wake width, w , streamwise spacing (i.e. stride length), ℓ , flapping amplitude, H , and swimming speed, U , are computed from the composite wake.

approximately 70 vectors along the length of the fish body. The data were post-processed in Matlab to determine vorticity, circulation, and wake geometry.

The procedure used to determine vortex circulation and wake geometry is similar to that used by Streitlien and Triantafyllou (1998) in the study of flapping foils. Namely, we form a *composite wake* from three or more tail flap cycles by freezing each vortex in its shed position, and we make measurements on the composite wake (see figure 3-3). This composite wake allows us to use 2D classical vortex dynamics theory to predict the forces on the fish (3.4.4). While this model ignores three-dimensional effects, we show in Section 3.4.4 that it does successfully predict the swimming performance of the fish. Streitlien and Triantafyllou (1998) define a vortex as a simply-connected region of same-signed vorticity which is above some threshold. In this experiment we used a threshold of 4 s^{-1} , which is approximately 10% of the maximum vorticity level for many trials. The circulation, Γ , and centroid of the vorticity constituting each discrete vortex, (x_c, y_c) , is computed by evaluating the zeroth and first moments of the vorticity, ω , respectively

$$\Gamma = \sum \omega \delta A, \quad x_c = \frac{1}{\Gamma} \sum x \omega \delta A, \quad y_c = \frac{1}{\Gamma} \sum y \omega \delta A \quad (3.3.1)$$

where the summation is performed over the field points constituting the vortex, and $\delta A = (16 \text{ px})^2 = 0.044 \text{ cm}^2$ is the box size. Equation (8.1.8) is evaluated in five time-steps about vortex shedding, and the mean values are used to form the composite wake (this time-average smoothes out any small fluctuations in the PIV data). The lateral width, w , and streamwise spacing (i.e. stride length), ℓ , are computed from the composite wake, and the circulation, Γ , is the mean of the magnitudes of all vortex circulations. Streitlien and Triantafyllou (1998) reported acceptable agreement between the measured thrust of a flapping foil and that computed using this procedure with equation (3.4.3).

Swimming speed is defined as

$$U = f\ell \quad (3.3.2)$$

where f is the flapping frequency, which is identical to the vortex shedding frequency. Swimming speed computed using equation (3.3.2) was, for all trials, within 3% of the value calculated by inspecting the movement of a feature of the body in several frames.

Qualitative flow visualization was performed using dye. A fluorescent dye mixture was painted onto the caudal fin and allowed to shed freely into the flow as the robot swam. The mixture consisted of fluorescein dye, polyvinyl acetate (adhesive), dimethicone (viscous thickener), butylene glycol (hygroscopic substance and solubilizer), and other solubilizers. The dye was illuminated using incandescent flood lamps fitted with blue cinema gels and imaged using a video camera at 30 fps. Images were post processed by performing a band-pass filter on the light intensity levels, and by inverting the color spectrum (so the green dye appears magenta in the images herein).

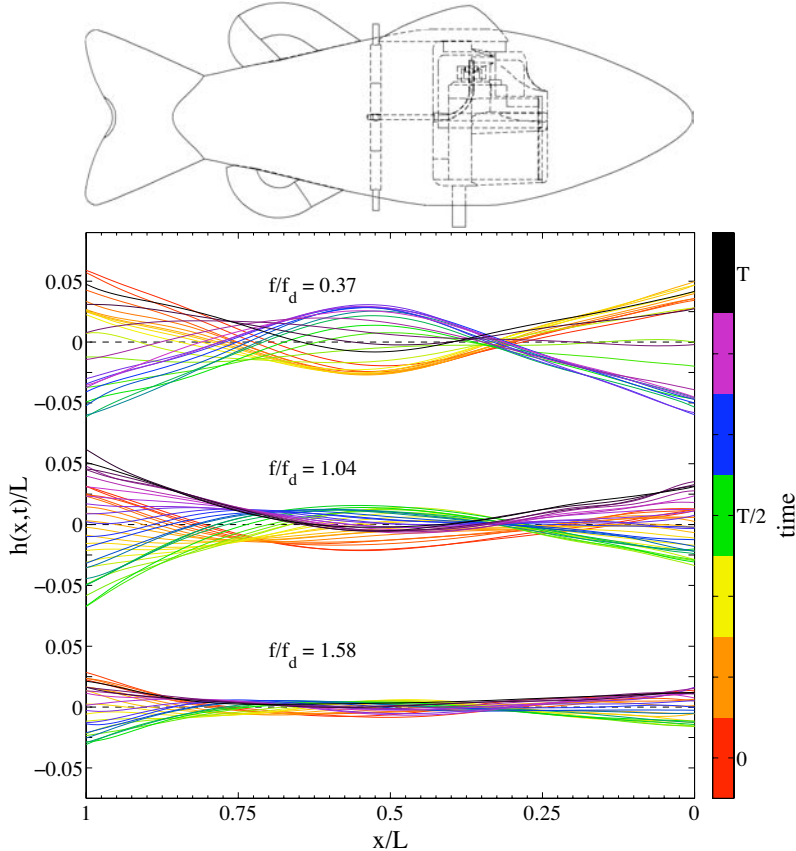


Figure 3-4: Spline positions (measured from the raw PIV images) illustrate the kinematics of one flapping cycle in the low-frequency ($f/f_d = 0.37$), nominal ($f/f_d = 1.04$), and high-frequency flapping ($f/f_d = 1.58$) regimes. In the nominal case, the kinematics resemble carangiform swimming, whereas in the low- and high-frequency flapping cases, the kinematics are altered. The time-step between body tracings is 0.04 s in the $f/f_d = 0.37$ case and 0.01 s in the other two cases. The aspect ratio of the axes is 2:1.

3.4 Results and discussion

3.4.1 Kinematics

Just as with a simple mass-spring system, the swimming robot behaves differently when actuated at frequencies much less than, in tune with, or much greater than its natural frequency. The robot and surrounding fluid can be conceptualized as a simple mass-spring system, with the bending stiffness of the body playing the

roll of the spring and the servomotor playing the roll of the forcing function (see Valdivia y Alvarado (2007) for more discussion). In this way, we can classify the kinematics of the robot into one of three swimming regimes.

Figure 3-4 illustrates the three swimming regimes of the robotic fish: ‘low-frequency’ ($f/f_d \leq 0.37$), ‘nominal’ ($0.56 \leq f/f_d \leq 1.11$), and ‘high-frequency’ ($1.30 \leq f/f_d$) flapping¹. In all swimming trials, the actuator applies the same moment to the fish body when triggered. The only parameter changed between trials is the actuation frequency. The kinematics at each flapping frequency are slightly different, but these three groupings classify the behavior sufficiently.

The *low-frequency* flapping regime (e.g. figure 3-4, $f/f_d = 0.37$) can be characterized as a ‘flap and coast’ mode. In this regime, the actuation frequency is much less than the ‘natural frequency’ of the robot, and the tail tracks the forcing from the servomotor. Since the servomotor is commanded by a square wave signal, the tail motion also resembles a square wave, but with rounded corners. Physically speaking, the caudal fin pauses at the end of each tail stroke, waiting for the actuator to begin the next stroke. In figure 3-4, several nearly-overlapping spine positions illustrate the period of time spent coasting, while the few tracings in-between illustrate the period of time spent actively flapping.

In the *nominal frequency* flapping regime (e.g. figure 3-4, $f/f_d = 1.04$), the kinematics resemble the target carangiform swimming kinematics. The target kinematics (shown in figure 3-1) are a traveling wave from nose to tail, with all parts of the body involved in undulation. During nominal swimming, the motion of the tail is out of phase with the mid-body, and a traveling wave propagates down the rear half of the fish with each tail stroke. The wavelength of this traveling wave is approximately 0.9 L, which is the target.

¹The listed minimum and maximum flapping frequencies that bound each regime correspond to frequencies tested in the PIV experiments. The precise frequencies that bound the regimes were not determined.

Another interesting feature illustrated by the figure 3-4, $f/f_d = 0.37$ and 1.04 cases is the ‘rigid-body’ mode of vibration of the system, due to the umbilical hanging below the robot. In this mode, the robot acts as a lumped mass on the umbilical, which acts as a spring. Note two nearly identical spine position curves, offset by one another by about $0.02 L$ in figure 3-4, $f/f_d = 1.04$. These tracings correspond to the start and end of the flapping cycle. The robot does not swim straight along its trajectory; rather, it sways side to side as it moves forward. The center of mass traces a sine wave about the swimming trajectory.

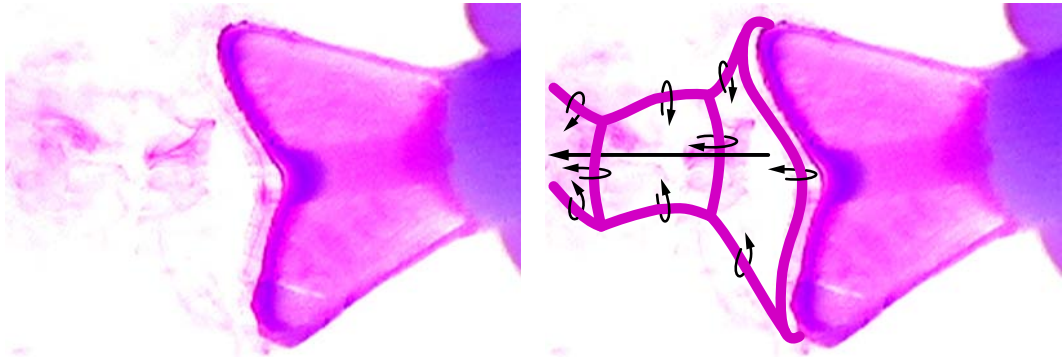
In the *high-frequency* regime (e.g. figure 3-4, $f/f_d = 1.58$), the servomotor actuates at frequencies much greater than the design-intent frequency, and the body deflections are greatly reduced. In this regime, the kinematics are quite different from the target kinematics. The middle half of the body remains nearly still, while the head and tail flap in sync with one another. The caudal fin nearly pivots about the caudal peduncle, and very little of the body is involved in a propulsive traveling wave.

Kinematic errors are mainly due to the limitations in fabricating the required material distributions found through the design methodology. The modulus of elasticity and viscosity are required to be continuous functions of body positions, $E(x)$ and $\mu(x)$. However, current manufacturing techniques do not allow true anisotropy; we approximate it by casting the bodies picewise with slightly different materials (Valdivia y Alvarado, 2007). Nevertheless, the robotic fish is able to swim in a wide range of actuation frequencies beyond its design-intent flapping frequency.

3.4.2 Vortical wake structure

In the analysis of the vortical wake created by the swimming robot, it will be helpful to refer to the wake in one of three ways. First, the ‘near wake’ is defined as the most recent two vortices which have been shed from the tail. The ‘far wake’ constitutes all other vortices beyond the near wake. Finally, the ‘composite wake’, as defined in

(a) nominal swimming ($f/f_d = 1.0$)



(b) Low-frequency swimming ($f/f_d = 0.37$)

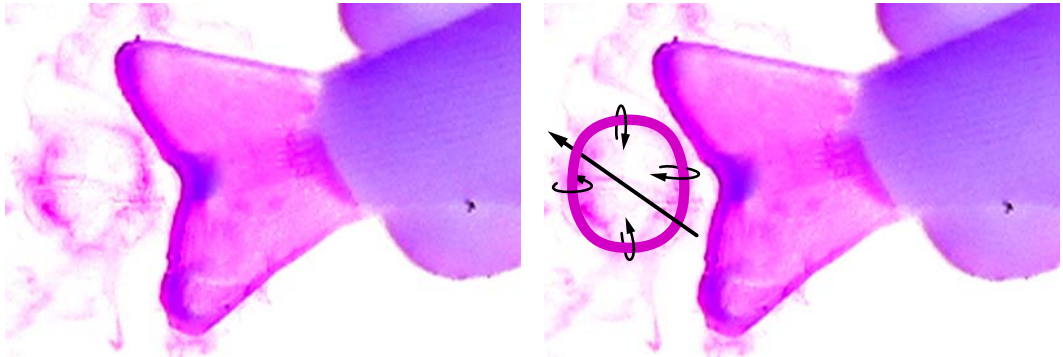


Figure 3-5: Vortical wake structure, visualized using dye. (a) During nominal swimming, the carangiform swimmer produces a series of interconnected vortex loops. (b) In the low-frequency regime, the tail pauses between strokes, and the vortices do not interlace. The images are *not* synched in time. The Reynolds numbers for these trials, based on swimming speed and body length, are approximately 7500 and 3000, respectively. (See animations 5a and 5b online.)

Section 3.3, is constructed by freezing the vortices in their centroidal locations at the time they were shed. The configuration of the near wake (e.g. single- vs. double-vortex street, drag- vs. thrust-type wake) is the same as that of the composite wake, although the geometry is slightly different due to the motion of the vortex system during the period of time between vortex shedding events.

A snapshot of the wake visualized using fluorescent dye is presented in figure 3-5. The Reynolds number is quite high ($Re = UL/\nu \approx 7500$ in figure 3-5a), so the dye mixes quite rapidly, and only the near wake can be visualized.

During *nominal* swimming (figure 3-5a), the *near wake* of the robot resembles the classic series of interconnected vortex loops observed in swimming studies with live fish, e.g. (Tytell and Lauder, 2004; Nauen and Lauder, 2002). In the horizontal mid-plane of the robot, where PIV measurements were made, this near wake appears as two vortices shed per flapping cycle. The *composite wake* is a 2D reverse Kármán jet wake. This type of composite wake was observed in all trials with a flapping frequency greater than or equal to 0.56 times the design frequency.

During *low-frequency* swimming (figure 3-5b), the robots form a ring-like vortex structure with each stroke of the tail. In the horizontal PIV plane, each 3D ring appears as a pair of 2D vortices, with two vortex pairs shed per flapping cycle.

Figures 3-6 and 3-7 present a PIV time-series of vorticity fields for the nominal and low-frequency swimming regimes, respectively. The high-frequency regime is not shown, since these vorticity fields are similar to the nominal regime, but have reduced wake width and vortex circulation. Vorticity contours are overlaid on digitized projections of the robot's body determined from the PIV image sequence. Ambient vorticity of less than 4 s^{-1} has been removed for clarity.

During *nominal* swimming cases, the robot's wake resembles a 'V'-shape (see figure 3-6). Two alternating-signed vortices are shed per cycle into the near wake in a reverse-Kármán street configuration (e.g. vortices 4 and 5 in the 3T/4 image). Each vortex shed into the near wake splits roughly in half as it proceeds into the far wake (e.g. vortex 3), and the far wake resembles two reverse-Kármán streets which form a 'V'-shape (see the 3T/4 image). This type of double-wake has been observed in the study of a pitching flat plate (Buchholz and Smits, 2006). A 'V'-shaped double-wake was also observed in a CFD study by Borazjani and Sotiropoulos (2008) for a carangiform swimmer at similar Re and St_H . Their study indicates that the vortex splitting process is quite complex, and it would be interesting to investigate this phenomena further using CFD in conjunction with 3D PIV.

nominal swimming ($f/f_d = 1.0$, $St_H = 0.86$, $St_w = 0.54$)

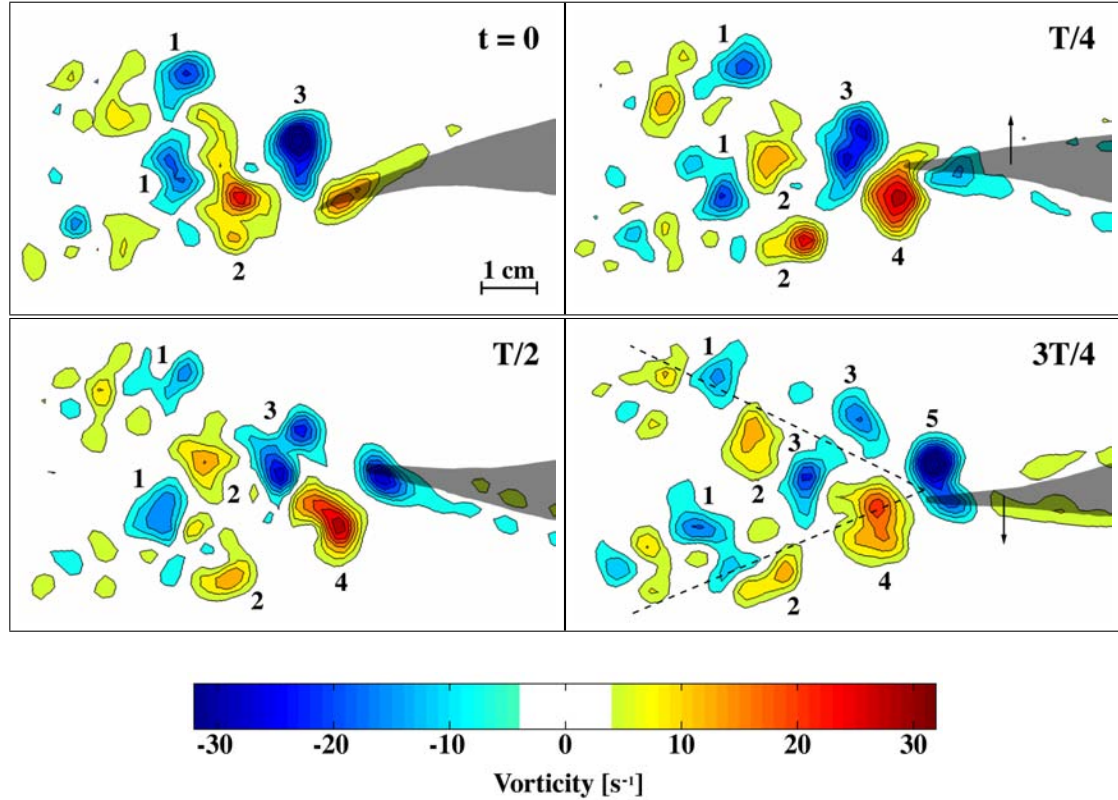


Figure 3-6: Sequence of instantaneous vorticity fields determined using PIV. During *nominal* swimming ($f/f_d = 1.0$), the robot forms a ‘V’-shaped double reverse Kármán jet wake. Numbers indicate patches of vorticity shed continuously from the caudal fin. Arrows indicate direction of tail motion. Every 1/4 period is shown. Anticlockwise (positive) vorticity is shown in red and clockwise (negative) in blue. Digitized projections of the robot’s tail are shown in gray. (See animation 6 online.)

low-frequency swimming ($f/f_d = 0.37$, $St_H = 0.82$)

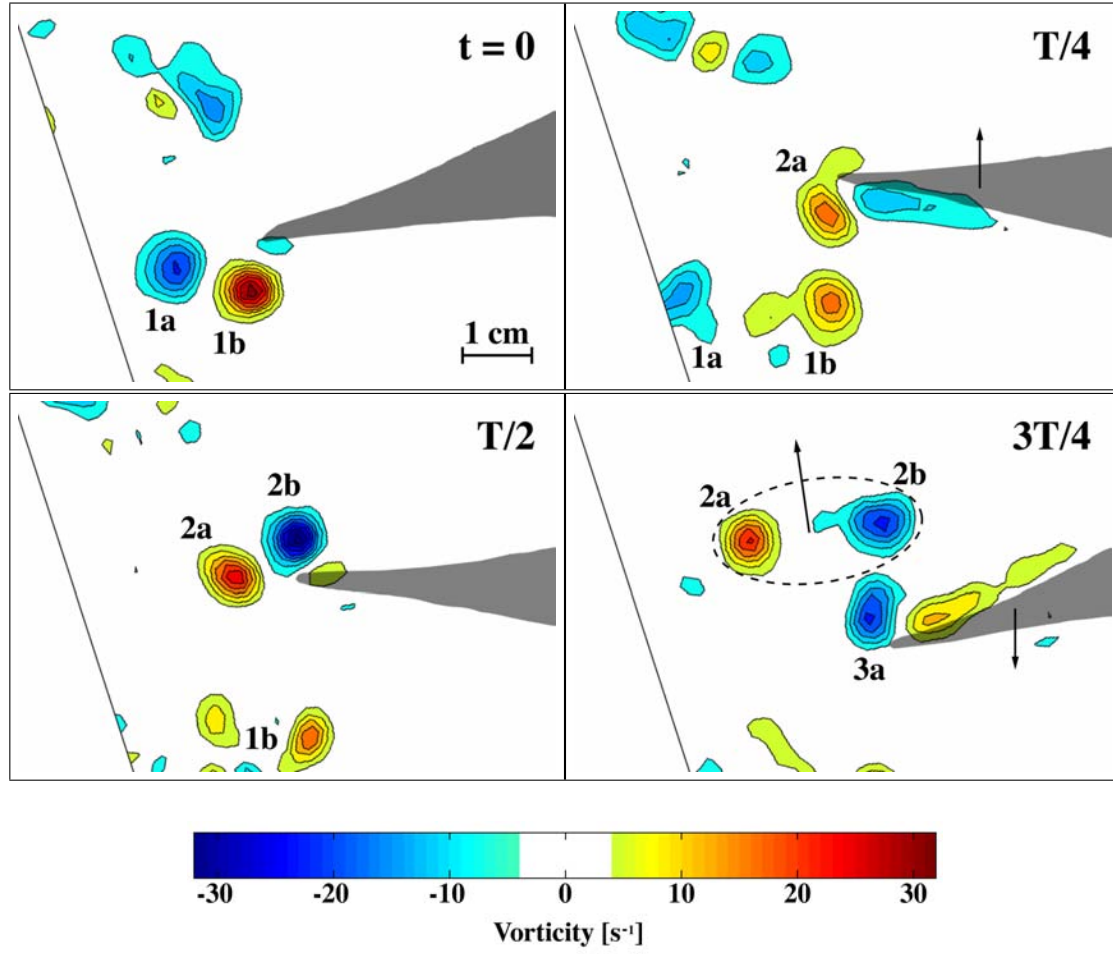


Figure 3-7: Sequence of instantaneous vorticity fields determined using PIV. During *low-frequency* swimming, the tail pauses between strokes, and two vortex pairs are shed per flapping cycle. Figure information is same as figure 3-6. The solid line indicates the edge of the field of view. (See animation 7 online.)

In the *low-frequency* flapping regime (figure 3-7), the caudal fin pauses at the end of each stroke, waiting for the actuator to begin the next stroke. With each start of a tail stroke, the caudal fin sheds a starting vortex (e.g. vortex 2a in the $T/4$ image). When the tail pauses at the end of the stroke, an ending vortex is shed (e.g. vortex 2b in the $T/2$ image). The two vortices pair to form a ring-like structure, as shown by the dye visualization. The impulse of the vortex pair acts at a near 70-deg angle to the swimming direction, and the fish pays with reduced swimming speed.

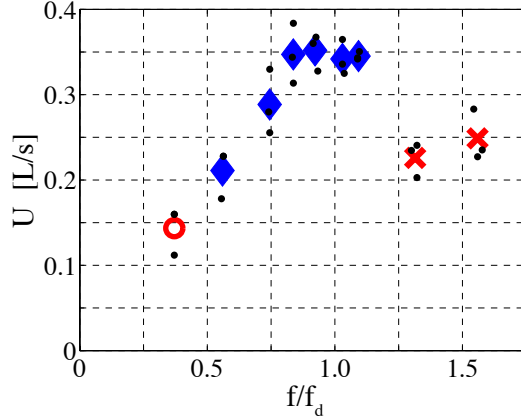


Figure 3-8: Swimming speed, U [L/s], versus flapping frequency normalized by the design frequency, f/f_d . Swimming speed reaches a maximum at frequencies near the design frequency. Values from individual trials are marked with ‘•’, and average values for each flapping frequency are marked with the ‘○’, ‘♦’, and ‘×’ symbols. These symbols denote the low-frequency, nominal, and high-frequency regimes, respectively.

3.4.3 Swimming speed

In this paper, we concern ourselves with the robot’s swimming speed and the dynamics of its thrust production. In this section, we present measured data from the PIV trials, and in the next section, we present a physical model which explains the robot’s thrust production in accord with these experimental results.

Figure 3-8 shows the robot’s swimming speed versus tail flapping frequency for all PIV trials. The data are partitioned into the three swimming regimes: low-frequency ($f/f_d \leq 0.37$), nominal ($0.56 \leq f/f_d \leq 1.11$), and high-frequency ($1.30 \leq f/f_d$) flapping, denoted by the ‘○’, ‘♦’, and ‘×’ symbols, respectively. The three regimes are distinguished by the kinematics of the robot, as discussed in Section 3.4.1 and illustrated in figure 3-4. As expected, the robot swims fastest near its deign frequency.

The swimming speed of the robot tested in this study is about one quarter to one fifth of the speed of live fish (other robots have attained up to one third the speed of live fish speed (Valdivia y Alvarado, 2007)). For flapping frequencies in the range of $0.5 \leq f/f_d \leq 0.8$, figure 3-8 shows that swimming speed is linearly proportional

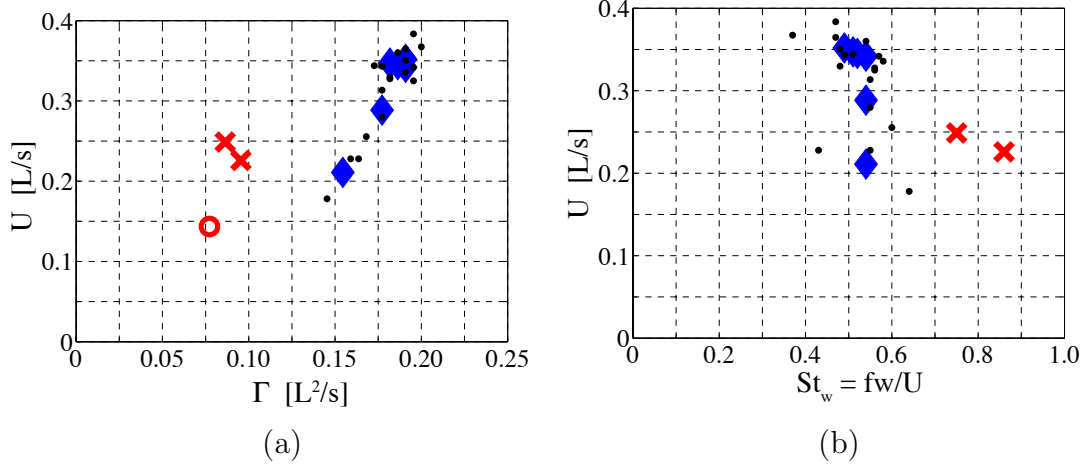


Figure 3-9: (a) Swimming speed is linearly proportional to vortex circulation, with a constant of proportionality of 3.5 [L/s]/[L²/s]. (b) The Strouhal number defined using wake width, $St_w = fw/U$, is nearly 0.52 for many swimming trials, regardless of swimming speed. Legend same as figure 3-8. Strouhal number, as defined in equation (3.4.2), does not apply for the low-frequency flapping regime, so these data are not shown.

to tail beat frequency. This constant of proportionality is 0.15 [L/s]/[Hz], about one quarter of the 0.59 [L/s]/[Hz] reported for live fish (Videler, 1993). Swimming speed plateaus at approximately 0.35 L/s over a range of frequencies near the design frequency; again, this is between one quarter and one fifth of the speed of live fish swimming at those tail-beat frequencies (Videler, 1993).

Two interesting results, shown in figure 3-9, give insight into the thrust production by the fish. First, for the nominal swimming regime cases (marked by ‘♦’), the swimming speed is linearly proportional to the average circulation of the vortices shed into the wake (see figure 3-9a).

$$U \sim \Gamma \quad (\text{during nominal swimming}) \quad (3.4.1)$$

The constant of proportionality is 3.5 [L/s]/[L²/s]. Thus, the swimming speed is proportional to the strength of the vortical wake. One may note that a line fit through these data would intercept the circulation axis at about 0.1 L²/s. This is

not necessarily alarming, because it would be expected that the relationship between circulation and swimming speed would change for very low speeds (i.e. low Reynolds number swimming).

Second, the Strouhal number, defined using the wake width² as follows,

$$St_w = \frac{fw}{U} \approx 0.52 \quad (\text{during nominal swimming}) \quad (3.4.2)$$

is nearly constant in the nominal swimming cases, with an average value of 0.52 and standard deviation of 0.021 (see figure 3-9b). Strouhal number is a measure of ‘hydrodynamic performance’; the lower the value, the faster the fish swims for a given input flapping frequency and wake width. Triantafyllou et. al. have suggested that the optimal range of Strouhal numbers for fish swimming is between 0.25 and 0.35 (Triantafyllou et al, 1991; Triantafyllou and Triantafyllou, 1995), which corresponds to as much as twice the swimming speed for a live fish exerting the same hydrodynamic input as the robot.

Strouhal number, defined in this way, also describes the geometry of the composite wake. One may rewrite the Strouhal number as $St_w = w/\ell$, since $U = f\ell$ by definition. Thus, the data in figure 3-9b show that the geometry of the composite wake is nearly constant for the nominal swimming cases.

3.4.4 Thrust

The time-averaged *total* force (net thrust and drag) on a steadily-moving object is zero. In this section, we attempt to quantify the amount of thrust which must be produced in order to balance viscous friction drag during steady swimming.

Since the thrust produced by the swimming robot scales by ρU^2 , swimming speed is a proximal measure of thrust production. The data in figure 3-9 show that the

²Recall, ‘wake width’ is defined as the lateral distance between vortex centroids, across the composite wake.

thrust produced by the swimming fish is related to the strength and geometry of the vortical wake. Thrust can be related to the strength and geometry of the wake by classical vortex dynamics theory (von Kármán and Burgers, 1935).

Kármán and Burgers (1935) computed the drag on a 2D body producing a regular vortex street (i.e. a drag wake), and Streitlien noted that for a thrust wake, their analysis could be carried through with the signs of the force and circulation reversed (Streitlien and Triantafyllou, 1998). This yields the average thrust per unit depth

$$T/b = (\rho \frac{w}{\ell}) U \Gamma + \rho (\frac{w}{\ell} \tanh \frac{\pi w}{\ell} - \frac{1}{2\pi}) \frac{1}{\ell} \Gamma^2 \quad (3.4.3)$$

where ρ is the fluid density, w is the wake width, ℓ is the streamwise spacing of the vortices, U is the average swimming speed, and Γ is the circulation of the vortices. This model assumes point vortices immersed in inviscid flow, thus ignoring viscous drag on the body. To estimate the thrust produced by the robot, T , we multiply the right hand side of (3.4.3) by the tail breadth, b .

$$T = (\rho b St_w) U \Gamma + \rho b (St_w \tanh(\pi St_w) - \frac{1}{2\pi}) \frac{1}{\ell} \Gamma^2 \quad (3.4.4)$$

Simple manipulation of (3.4.4) shows that if $St_w = w/\ell \approx \text{constant}$ and $1/\ell \approx \text{constant}$, as in the nominal swimming cases, then (3.4.4) predicts that $U \sim \Gamma$. The largest value of $1/\ell$ for the nominal swimming cases was only 20% more than the smallest value, whereas the spread in Γ^2 was 100%; thus, Γ^2 has about five times the effect on thrust than $1/\ell$ does, and the assumption that $1/\ell \approx \text{constant}$ is valid. Since thrust scales by ρU^2 , equation (3.4.4) can be rewritten as

$$c_1 U^2 + c_2 U \Gamma + c_3 \Gamma^2 = 0$$

where $c_1 = T/\rho U^2$, $c_2 = -b St_w$, and $c_3 = -b (St_w \tanh(\pi St_w) - \frac{1}{2\pi}) \frac{1}{\ell}$ are constants.

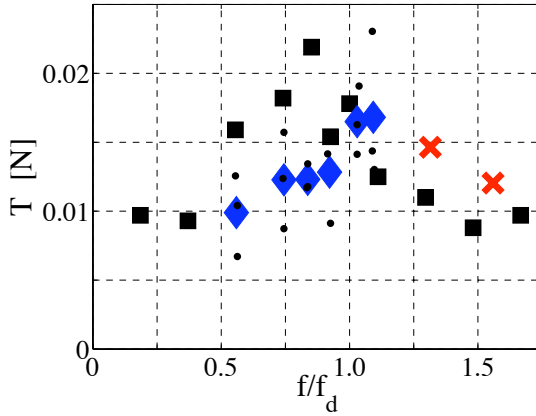


Figure 3-10: Thrust estimated by (3.4.4) is in agreement with that measured during static thrust trials ('■') (Valdivia y Alvarado, 2007). (Legend same as figure 3-8.)

This equation can be solved by the quadratic formula to yield the prediction

$$U = \frac{-c_2 + \sqrt{c_2^2 - 4c_1c_3}}{2c_1} \Gamma$$

$$U \sim \Gamma \quad (\text{given } St_w \text{ and } 1/\ell \text{ are constant}) \quad (3.4.5)$$

The data in figure 3-9a show that swimming speed is indeed linearly proportional to vortex circulation for the nominal swimming cases, when the Strouhal number and stride length are nearly constant. It is interesting to note that the model does not predict that St_w should be constant, just that if it is, then swimming speed is linearly proportional to circulation.

The thrust predicted by (3.4.4) is in acceptable agreement with static thrust measurements from (Valdivia y Alvarado, 2007), as shown in figure 3-10. During the static thrust tests, the body was clamped to a load cell and held in place, so the dynamics of the body were slightly altered. Therefore, the discrepancy between static thrust measurements and free-swimming thrust estimation is to be expected.

Equation (3.4.4) can be non-dimensionalized by swimming speed and the wetted area of the fish ($A = 64 \text{ cm}^2$) in the usual manner to yield the thrust coefficient,

$C_T = T/\frac{1}{2}\rho U^2 A$, which ranged between 1 and 3.5 for most trials. Streitlien reported a thrust coefficient of 1.1 for a foil flapping with Strouhal number of 0.5, which is comparable to our results.

Vortex impulse scaling

The assertion that thrust scales by the square of the circulation can also be made by inspecting the impulse added to the vortical wake structure during each flapping cycle. Impulse analysis has been successfully used by the authors in the context of fish maneuvering (Epps and Techet, 2007) and by other researchers studying the swimming of live fish, e.g. (Tytell and Lauder, 2004; Nauen and Lauder, 2002).

Using the model of a fish wake being a chain of interconnected vortex loops, the average thrust is given by $T = If \cos(\theta)$, where I is the impulse of a vortex loop, f is the shedding frequency (which is equivalent to the tail flapping frequency), and $\pi - \theta$ is the angle that the impulse vector makes with the swimming direction. Vortex impulse scales by $I \sim \rho\Gamma A_v$, where A_v is the frontal area of the vortex. Further, the circulation scales by $\Gamma \sim VD$, where V is the velocity of the fluid at the center of the vortex, and D is the diameter. These scaling formulae are exact for a vortex ring and yield satisfactory prediction of the impulse acting on a maneuvering fish (Epps and Techet, 2007).

To apply these scaling arguments to the wake of a swimming fish, we make three further assertions. First, the effective speed of the fluid in a vortex loop scales by $V \sim fw$, where w is the wake width. Second, the vortex diameter scales by the breadth of the caudal fin, $D \sim b$. Finally, the projected area of a vortex loop in the swimming direction scales by $A_v \cos(\theta) \sim wb$.

Thus, the thrust scales by $T \sim \rho f^2 w^2 b^2$, and the circulation in each vortex loop scales by $\Gamma \sim fwb$. This implies $U \sim \Gamma$ and $U \sim fw$, which is in agreement with the vortex dynamics model given above and the data in figure 3-9.

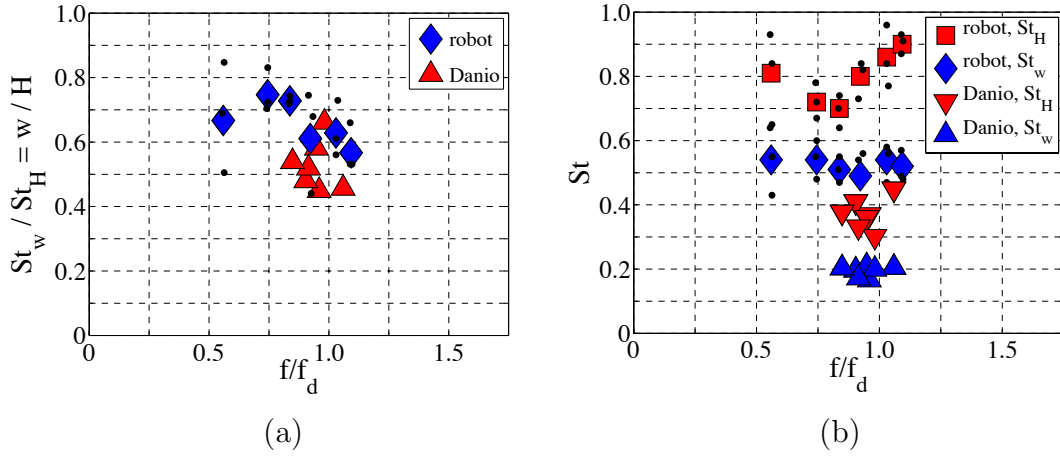


Figure 3-11: (a) The robot’s wake width is between 50 - 80% of its flapping amplitude for most ‘nominal swimming’ trials, since the centroid of the vorticity shed during each tail flap is located inboard of the point of maximum excursion of the tail tip. The wake width of a live Giant Danio is also less than the fish’s flapping amplitude. (b) Strouhal number of the robot, defined using wake width ($St_w = fw/U$, ‘♦’, same data as in figure 3-9b), is nearly constant for many flapping frequencies (mean = 0.52, standard deviation = 0.021), whereas Strouhal number defined using flapping amplitude ($St_H = fH/U$, ‘■’) is not (mean = 0.80, std. = 0.078). The same result holds for the live Giant Danio (‘▼’, ‘▲’).

3.4.5 Wake width versus flapping amplitude

Strouhal number is often defined in fish swimming literature using the tail flapping amplitude, rather than the wake width, by

$$St_H = \frac{fH}{U} \quad (3.4.6)$$

This is convenient to do for experiments where the wake width is not quantified (e.g. taking images of swimming kinematics in sync with muscle activity measurements), but this definition may be misleading hydrodynamically.

In our experiments with the swimming robot, the wake width was typically between 50% and 80% of the flapping amplitude (see figure 3-11a). This is reflected in variations in St_H . The St_H data for the ‘nominal swimming’ cases had a mean of 0.80 and standard deviation of 0.078, whereas the St_w data had mean 0.52 and

standard deviation 0.021 (as shown in figure 3-11b). To make a fair comparison of these standard deviations, one must scale them by their respective mean, $\frac{\text{std(St)}}{\text{mean(St)}}$. The scaled standard deviation of St_w is $\frac{0.021}{0.52} = 0.04$, whereas the scaled standard deviation of St_H is $\frac{0.078}{0.80} = 0.10$, which is more than twice that of St_w . Relative to St_w , St_H shows large variation in the nominal swimming regime cases, which implies that swimming speed is *not* proportional to flapping amplitude but, instead, scales with wake width.

To investigate if the wake width of a live swimming fish is also less than the fish's tail flapping amplitude, the PIV experiment was repeated with a Giant Danio (*Danio aequipinnatus*). The specimen had a length, width, breadth (tail height), and mass of 9.89 cm, 1.14 cm, 1.89 cm, and 6.3 grams, respectively. In the seven trials shown in figure 3-11, the fish's wake width was between 45% and 60% of its flapping amplitude. The St_w data for the live swimming fish had a mean of 0.19 and a standard deviation of 0.017, whereas the St_H data had a mean of 0.37 and a standard deviation of 0.049. Interestingly, the scaled standard deviation of St_w is $\frac{0.017}{0.19} = 0.09$, whereas the scaled standard deviation of St_H is $\frac{0.049}{0.37} = 0.13$, which is about 1.5 times larger than that of St_w . This suggests that for the live fish, as well as the robot, the swimming speed scales by the width of the composite wake, not by flapping amplitude.

Why is the wake width less than the tail flapping amplitude? Recall, a vortex is defined herein as a simply connected region of same-signed vorticity. The location of the vortex, which determines the wake width, is the centroid of this vorticity (see figure 3-3). Each vortex begins to shed as the tail reaches the point of maximum excursion. However, same-signed vorticity is shed over much of the return flap towards the centerline of the swimming trajectory. The total amount of same-signed vorticity is not shed until the tail is approximately on center. Since vorticity is smeared between the point of maximum excursion and the centerline, its centroid is closer to the centerline than the point of maximum tail excursion is.

Strouhal number based on flapping amplitude is, however, indicative of the robot's 'kinematic performance'. For given tail flapping kinematics (i.e. amplitude and frequency), a lower St_H indicates a faster swimming speed. In our experiment with the swimming robot, we can not dictate flapping amplitude. The only parameter which can be changed is servomotor actuation frequency (i.e. tail-beat frequency). The servomotor applies the same moment on the tail, regardless of the commanded frequency, and the tail flapping amplitude and swimming speed are a result of the fluid-body dynamics. Figure 3-11b shows a minimum St_H (i.e. maximum performance) at a flapping frequency of 0.84 times the design frequency.

3.5 Conclusions

Experiments on a robotic fish designed in (Valdivia y Alvarado, 2007) show that it swims at about one quarter of the speed of a live fish.

The robot's wake resembles a 'V'-shaped double reverse-Kármán street during nominal and high-frequency swimming. Each vortex shed into the near wake splits roughly in half as it progresses into the far wake. This 'V'-shaped double-wake is consistent with the CFD results of Borazjani and Sotiropoulos (2008). They suggest that there is a critical value of St_H over which a double wake occurs. In our trials with the swimming Giant Danio, the live fish produced a single thrust wake. While the Reynolds numbers of both the fish and robot were similar (≈ 7500), the average Strouhal number of the fish and robot were $St_H = 0.4$ and 0.8 , respectively. Although the body shape and kinematics are quite different between the fish and robot, our results seem to support those of the CFD analysis. Unfortunately, the vortex spacing (and thus St_w) was not reported in the CFD analysis, so no comparisons can be made regarding composite wake geometry versus overall wake structure.

The data in figures 3-9 and 3-11 show that swimming speed depends on the

strength (Γ) and geometry (St_w) of the composite wake for *both* the live fish and the robot. Further, these data show that swimming speed does not depend directly on St_H , which is a gross feature of the kinematics. Thus, the thrust produced by the swimming fish can be thought of as a result of the vortex dynamics, rather than the kinematics alone. The swimming kinematics serve to create the vortical wake, which is the signature of how much thrust was produced. The quantity $St_w/St_H = w/H$ can be thought of as a ‘kinematic efficiency’. Inefficiencies in the kinematics result in a wake which produces less thrust, and thus, a slower swimming speed.

For example, the effect of body wavenumber was investigated in (Müller et al, 2002). They show that the body wave must be in sync with the timing when the tail reaches its maximum excursion, or else the circulation traveling down the body is not shed when the tail is at its maximum lateral position. This reduces the wake width for a given flapping amplitude, thus providing less thrust and a slower swimming speed than could otherwise be attained.

To the authors’ knowledge, there exist very limited published data that report vortex centroid location, in addition to circulation, swimming speed, and tail-beat frequency. Nauen and Lauder report flapping frequency and circulation for two swimming speeds, but they do not report wake width (Nauen and Lauder, 2002). Note that the data reported therein are averages of measurements made in physical dimensions (e.g. cm^2/s for circulation) between multiple fish of different lengths, all swimming at the same non-dimensional speed (e.g lengths per second). Since the averages were done on the measurements in physical dimensions, variations in these quantities due to the size difference in the fish are lost. Roughly though, assuming the average fork length of their fish was 24 cm, their results for the swimming mackerel (*Scomber japonicus*) indicate that the ratio of swimming speed to circulation changed less than 10% between the two swimming speeds, which is roughly in agreement with the $U \sim \Gamma$ result reported herein.

We suggest a vortex dynamics framework for fish swimming analysis: examine the strength and geometry of the composite wake to infer thrust produced by the fish. Within this framework, old questions remain. Namely, how does body shape affect the wake? To which kinematic parameters is the wake most sensitive (e.g. H/L , k , $y(x)$)? Examining high-fidelity changes to kinematic parameters and body shapes should be done computationally, where the effects of controlled changes in each parameter can be tested.

It is also expected that this framework is only valid within a range of moderate Reynolds numbers, say $O(10^2 - 10^4)$, where viscous effects are such that discrete vortical structures coalesce in the wake. At lower Re , vorticity is present in much of the fluid, and discrete structures may not exist. At higher Re , vorticity shed from the body in the form of vortex sheets may take a ‘long time’ to coalesce, and the approximation of a composite wake formed by freezing time would no longer be physically meaningful. Reynolds number effects and limitations would be another useful focus of future work.

Appendix: tabulated experimental results

[SEE TABLES NEXT PAGE]

Table 3.1: Table of measured quantities: normalized flapping frequency f/f_d ; flapping frequency, f ; swimming speed, U ; tail flapping amplitude, H ; composite wake width, w ; composite wake streamwise vortex spacing, ℓ ; and average vortex circulation, Γ .

Specimen	f/f_d []	f [Hz]	U [cm/s]	H [cm]	w [cm]	ℓ [cm]	Γ [cm 2 /s]
RoboFish	0.37	1.00	2.13	1.73	n/a	n/a	17
	0.56	1.51	3.13	1.65	1.10	2.16	34
	0.74	2.01	4.28	1.54	1.15	2.33	39
	0.84	2.26	5.15	1.58	1.15	2.40	40
	0.92	2.49	5.22	1.67	1.02	2.20	42
	1.03	2.78	5.07	1.56	0.98	1.96	42
	1.09	2.95	5.12	1.57	0.89	1.82	41
	1.31	3.55	3.35	0.86	0.81	1.00	21
	1.56	4.21	3.69	0.60	0.66	0.91	19
Giant Danio	0.85	2.29	7.76	1.28	0.69	3.39	9.1
	0.90	2.44	7.32	1.23	0.59	3.00	10.7
	0.95	2.56	9.65	1.36	0.79	3.77	13.3
	1.06	2.86	8.78	1.38	0.63	3.07	10.8

Table 3.2: Table of computed performance parameters: normalized flapping frequency f/f_d ; thrust, T (eq. 3.4.4); thrust coefficient, $C_T = T/\frac{1}{2}\rho U^2 A$; Strouhal number, $St_w = fw/U$; Strouhal number, $St_H = fH/U$; and Reynolds number, $Re = UL/\nu$.

Specimen	f/f_d []	St_w []	St_H []	Re []	T [N*10 $^{-5}$]	C_T []
RoboFish	0.37	n/a	0.82	3167	n/a	n/a
	0.56	0.54	0.81	4644	989	3.44
	0.74	0.54	0.72	6344	1228	2.27
	0.84	0.51	0.70	7634	1231	1.50
	0.92	0.49	0.80	7738	1283	1.51
	1.03	0.54	0.86	7521	1650	2.04
	1.09	0.52	0.90	7595	1681	2.01
	1.31	0.86	0.91	4970	1464	4.24
	1.56	0.75	0.70	5471	1205	2.75
Giant Danio	0.85	0.20	0.38	7678	27	0.023
	0.90	0.20	0.41	7240	29	0.027
	0.95	0.21	0.36	9545	51	0.028
	1.06	0.21	0.45	8684	36	0.024

Bibliography

- Anderson J, Streitlien K, Barrett D, Triantafyllou M (1998) “Oscillating foils of high propulsive efficiency,” *Journal of Fluid Mechanics* **360**:41–72.
- Anderson JM, Chhabra NK (2002) “Maneuvering and stability performance of a robotic tuna,” *Integrative and Comparative Biology* **42**:118–126.
- Bandyopadhyay P, Donnelly MJ, Nedderman WH, Castano JM (1997) “A dual flapping foil maneuvering device for low-speed rigid bodies,” In: *Third Int. Symp. Performance Enhancement for Marine Vehicles* Newport, RI.
- Bandyopadhyay PR (2005) “Trends in biorobotic autonomous undersea vehicles,” *IEEE Journal of Oceanic Engineering* **30**(1):109–139.
- Borazjani I, Sotiropoulos F (2008) “Numerical investigation of the hydrodynamics of carangiform swimming in the transitional and inertial flow regimes,” *Journal of Experimental Biology* **211**:1541–1558.
- Buchholz J, Smits A (2006) “On the evolution of the wake structure produced by a low-aspect-ratio pitching panel,” *Journal of Fluid Mechanics* **546**:433–443.
- Childress S (1981) *Mechanics of Swimming and Flying* Cambridge University Press.
- Epps BP, Techet AH (2007) “Impulse generated during unsteady maneuvering of swimming fish,” *Experiments in Fluids* **43**:691–700.
- Fish FE, Lauder GV (2006) “Passive and active flow control by swimming fishes and mammals,” *Annual Review of Fluid Mechanics* **38**:193–224.
- Garner LJ, Wilson LN, Lagoudas DC, Rediniotis OK (2000) “Development of a shape memory alloy actuated biomimetic vehicle,” *Smart Material Structures* **9**:673–683.
- Karniadakis GE, Triantafyllou GS (1989) “Frequency selection and asymptotic states in laminar wakes,” *Journal of Fluid Mechanics* **199**:441–469.

Lauder GV, Anderson EJ, Tangorra J, Madden PGA (2007) “Fish biorobotics: kinematics and hydrodynamics of self-propulsion,” Journal of Experimental Biology **210**:2767–2780.

Liao JC, Beal DN, Lauder GV, Triantafyllou MS (2003) “Fish exploiting vortices decrease muscle activity,” Science **302**:1566–1569.

Licht S, Polidoro V, Flores M, Hover FS, Triantafyllou MS (2004) “Design and projected performance of a flapping foil AUV,” IEEE Journal of Oceanic Engineering **29**(3):786–794.

Lighthill MJ (1960) “Note on swimming of slender fish,” Journal of Fluid Mechanics **9**:305–317.

Lighthill MJ (1975) Mathematical Biofluidynamics Society for Industrial and Applied Mathematics, Philadelphia, PA.

Müller UK, Stamhuis EJ, Videler JJ (2002) “Riding the waves: the role of the body wave in undulatory fish swimming,” Integrative and Comparative Biology **42**(5):981–987.

Nauen JC, Lauder GV (2002) “Hydrodynamics of caudal fin locomotion by chub mackerel (*scomber japonicus*),” Journal of Experimental Biology **205**:1709–1724.

Newman JN (1973) “The force on a slender fish-like body,” Journal of Fluid Mechanics **58**:689–702.

Raffel M, Willert C, Kompenhans J (2002) Particle Image Velocimetry: A Practical Guide Springer, New York.

Sfakiotakis M, Lane DM, Davies JBC (1999) “Review of fish swimming modes for aquatic locomotion,” IEEE Journal of Oceanic Engineering **24**(2):237–252.

Streitlien K, Triantafyllou GS (1998) “On thrust estimates for flapping foils,” Journal of Fluids and Structures **12**:47–55.

Techet AH, Hover FS, Triantafyllou MS (2003) “Separation and turbulence control in biomimetic flows,” Flow Turbulence and Combustion **71**:105–118.

Triantafyllou G, Triantafyllou M, Chryssostomidis C (1986) “On the formation of vortex streets behind stationary cylinders,” Journal of Fluid Mechanics **170**:461–477.

Triantafyllou G, Triantafyllou M, Grosenbaugh M (1993) “Optimal thrust development in oscillating foils with application to fish propulsion,” Journal of Fluids and Structures **7**:205–224.

Triantafyllou M, Triantafyllou G (1995) “An efficient swimming machine,” Scientific American **272**(3):64–70.

Triantafyllou M, Triantafyllou G, Gopalkrishnan R (1991) “Wake mechanics for thrust generation in oscillating foils,” Physics of Fluids A **3**:2835–2837.

Triantafyllou MS, Triantafyllou GS, Yue DKP (2000) “Hydrodynamics of fish-like swimming,” Annual Review of Fluid Mechanics **32**:33–53.

Tytell ED, Lauder GV (2004) “The hydrodynamics of eel swimming I: wake structure,” Journal of Experimental Biology **207**:1825–1841.

Valdivia y Alvarado P (2007) Design of biomimetic compliant devices for locomotion in liquid environments PhD thesis, MIT.

Valdivia y Alvarado P, Youcef-Toumi K (2003) “Modeling and design methodology for an efficient underwater propulsion system,” In: Proc. IASTED International Conference on Robotics and Applications Salzburg, Austria.

Valdivia y Alvarado P, Youcef-Toumi K (2005) “Performance of machines with flexible bodies designed for biomimetic locomotion in liquid environments,” In: IEEE International Conference on Robotics and Automation Barcelona, Spain.

Valdivia y Alvarado P, Youcef-Toumi K (2006) “Design of machines with compliant bodies for biomimetic locomotion in liquid environments,” ASME Journal of Dynamics Systems Measurement and Control **128**:3–13.

Valdivia y Alvarado P, Youcef-Toumi K (2008) “On the design of compliant biomimetic fish-like devices,” in press.

Videler J (1993) Fish Swimming Chapman and Hall, London.

von Kármán T, Burgers JM (1935) Aerodynamic Theory, vol II: General Aerodynamic Theory - Perfect Fluids. Springer, Berlin, Germany.

Wardle CS, Videler JJ, Altringham JD (1995) “Tuning in to fish swimming waves: body form, swimming mode, and muscle function,” Journal of Experimental Biology **198**:1629–1636.

Wolfgang M, Anderson J, Grosenbaugh M, Yue D, Triantafyllou M (1999) “Near-body flow dynamics in swimming fish,” Journal of Experimental Biology **202**:2303–2327.

Wu TY (1971) “Hydromechanics of swimming propulsion, part 1: swimming of a two-dimensional flexible plate at variable forward speeds in an inviscid fluid,” Journal of Fluid Mechanics **46**:337–355.

Yu J, Tan M, Wang S, Chen E (2004) “Development of a biomimetics robotic fish and its control algorithm,” IEEE Transactions on Systems, Man, and Cybernetics-Part B: Cybernetics **34**(4).

Part II

Methods for experimental data analysis and modeling

[THIS PAGE INTENTIONALLY LEFT BLANK]

Chapter 4

An error threshold criterion for singular value decomposition modes extracted from PIV data

To better understand the dynamics of fish swimming, we turn our attention now to the energetics of the fish's wake. In this chapter, I use *singular value decomposition* (SVD) to analyze experimental velocity field data of the wake behind a swimming fish. This decomposition reveals that the four most-energetic modes of the fish's wake (which is a reverse Kármán street) resemble those of a regular Kármán street created in the wake of a circular cylinder, as expected. However, this study also revealed that lower-energy modes are corrupted by experimental measurement error.

This study raised an interesting question: how does measurement error affect the results of the singular value decomposition? Namely, what modes are most affected by the presence of measurement error in the data? In this chapter, I find that higher-order modes, which capture less of the kinetic energy of the flowfield data, are corrupted by measurement error. I propose a threshold criterion that can be used to determine if a SVD mode extracted from experimental data is valid or not.

Singular value decomposition (SVD) is often used as a tool to analyze *particle image velocimetry* (PIV) data. However, experimental error tends to corrupt higher SVD modes, in which the root mean square velocity value is smaller than the experimental error. Therefore, I suggest that the threshold criterion, $s_k > \sqrt{DT}\epsilon$, can be used as a rough limit of the validity of SVD modes extracted from experimental data (where s_k is the singular value of mode k , D and T are the number of data sites and time steps, respectively, and ϵ is the root mean square PIV error). By synthesizing the relationship between the general SVD procedure and its two special cases -- *biorthogonal decomposition* (BOD) and *proper orthogonal decomposition* (POD) -- I show that the criterion can be used to assess modes extracted by either BOD or POD. I apply the threshold criterion to PIV data of the wake behind a live swimming Giant Danio (*Danio aequipinnatus*). The biorthogonal decomposition of the fish wake, which is a reverse-Kármán street, reveals that the first four modes are similar to the modes of a regular Kármán street created in the wake of a stationary cylinder and that higher modes are corrupted by experimental error.

The following text previously appeared in:

B.P. Epps and A.H. Techet (2010) “An error threshold criterion for singular value decomposition modes extracted from PIV data,” Experiments in Fluids **48**:355-367.

4.1 Introduction

Singular value decomposition (SVD) is a well-known mathematical tool that can be used to decompose an ensemble of velocity field data into spatio-temporal modes that may reveal coherent flow structures (Gentle, 1998). Two special cases of the general SVD procedure are used in experimental fluid dynamics: *Proper orthogonal*

decomposition (POD) is used if the data are *un-correlated* in time (as in a turbulent flow) (Holmes et al, 1996, 1997; Berkooz et al, 1993), and *biorthogonal decomposition* (BOD) is used if the data are *correlated* in time (as in a laminar flow) (Aubry, 1991; Aubry et al, 1991).

Several recent experimental studies have employed POD or BOD to analyze particle image velocimetry (PIV) velocity field data: For example, POD was performed on PIV data of flow past a backward-facing step (Kostas et al, 2005), past a half-cylinder (Santa Cruz et al, 2005), in an internal combustion engine (Fogleman et al, 2004), and through an annular jet (Patte-Rouland et al, 2001). BOD was used to analyze PIV data of flow through a model of the human voice box (Neubauer and Zhang, 2007), and BOD also was applied to experimental hot-wire anemometry velocity data in the study of the boundary layer on a rotating disc (Aubry et al, 1994). Recently, PIV-derived POD modes were used as a basis for direct numerical simulations of the flow past a circular cylinder by Ma et al (2003). However, Ma notes, “the higher modes obtained from [POD of PIV velocity data] are noisy...”, and they employ a numerical method to work around these corrupted modes.

Aside from Ma’s work, this previous research has given little consideration as to how *experimental error* affects the results of POD or BOD. In theory, large-scale flow structures are captured by the lower decomposition modes, whereas small-scale flow structures are captured in higher modes. In practice, experimental PIV error may dominate higher modes, rendering them corrupted by noise. Typical sources of experimental error in PIV can include poor seeding density, high velocity gradients, and out of plane particle motion (Raffel et al, 2002).

Herein, we derive a threshold criterion that can be used to assess if the magnitude of a decomposition mode is above the noise of the measurement. Modes that do not meet the criterion have a root mean square (RMS) velocity value that is less than the RMS measurement error. It is important to assess whether or not a mode meets

our threshold criterion before it is interpreted physically (as in the above studies) or used as an input to a numerical simulation (as in (Ma et al, 2003)), because modes that do not meet the threshold may represent measurement error, not the physical flow phenomena of interest. We apply our threshold criterion to the decomposition of PIV data of the wake behind a live swimming Giant Danio (*Danio aequipinnatus*). In our experiment, the flow evolves gradually between each frame of the high-speed PIV image sequence, so the measurements are correlated in time, and we employ the biorthogonal decomposition procedure. Generally, a mid-plane slice of a carangiform swimming fish wake resembles a reverse Kármán street, which generates thrust to propel the animal (Borazjani and Sotiropoulos, 2008; Epps et al, 2009). BOD of the fish wake reveals that the first four modes are similar to the modes of a regular Kármán street created by a stationary cylinder (Ma et al, 2000, 2003) and that higher modes are corrupted by experimental error.

In order to show that our error threshold criterion, which we develop for the general case of SVD, can be used to assess modes extracted by either BOD or POD, we present a brief synthesis of the relationship between SVD, BOD, and POD. We then proceed by deriving the error criterion and applying it to the experimental data from the swimming Danio.

4.1.1 Synthesis of SVD, POD, and BOD

Here we briefly synthesize the mathematical relationship between SVD and its special cases, BOD and POD, in order to show that our error threshold criterion can be used to assess modes extracted by either BOD or POD, thus making it widely applicable to a range of experimental studies. The *singular value decomposition* (SVD) of a size $[T, D]$ data matrix, \mathbf{X} , is

$$\mathbf{X} = \mathbf{u} \cdot \mathbf{s} \cdot \mathbf{v}^T \quad (4.1.1)$$

where: T and D are the number of time steps and data sites, respectively; matrices \mathbf{u} , \mathbf{s} , and \mathbf{v} are size $[T, T]$, $[T, D]$, $[D, D]$, respectively; \mathbf{u} contains the temporal eigenfunctions of \mathbf{X} ; \mathbf{v} contains the spatial eigenfunctions of \mathbf{X} ; and \mathbf{s} contains the singular values. That is, the SVD results in T *modes* (assuming $D > T$, which is typical of PIV data), each consisting of a time-varying amplitude, a singular value (which represents the magnitude of the mode), and a spatial mode shape. The first few modes capture the primary dynamics of the flow, and small perturbations are captured in the higher SVD modes (Holmes et al, 1996).

Many additional definitions are required. Consider mode k : Its singular value is $s_k \equiv \mathbf{s}(k, k)$ (note, all off-diagonal terms in \mathbf{s} are zero). Its time-varying amplitude is given by the k^{th} column of \mathbf{u} , namely $\mathbf{u}(1 : T, k)$. Its spatial mode shape is given by the k^{th} column of \mathbf{v} , namely $\mathbf{v}(1 : D, k)$. The mode k data matrix is given by $\mathbf{X}_k = \mathbf{u}(1 : T, k) \cdot \mathbf{s}(k, k) \cdot \mathbf{v}(1 : D, k)^T$, which is in accord with (4.1.1) and is size $[T, D]$. By definition, each column of \mathbf{u} and \mathbf{v} is normalized such that its ℓ^2 -norm is unity. That is, $\sqrt{\sum_{i=1}^T \mathbf{u}(i, k)^2} \equiv 1$ and $\sqrt{\sum_{j=1}^D \mathbf{v}(j, k)^2} \equiv 1$. Thus, the magnitude of the mode is captured by its singular value. Also by definition, $\mathbf{u}^T \cdot \mathbf{u} = \mathbf{I}$ and $\mathbf{v}^T \cdot \mathbf{v} = \mathbf{I}$, where \mathbf{I} is the identity matrix (Holmes et al, 1996).

SVD of temporally-correlated data (BOD)

Consider first, the case when the T realizations of data are *correlated* in time, as in the present work. The method is to perform an SVD and then to analyze both the spatial modes, \mathbf{v} , and temporal modes, \mathbf{u} , for coherent structures and temporal regularities. In fluid dynamics, this method is referred to as the *biorthogonal decomposition* (BOD) (Aubry, 1991; Aubry et al, 1991), and in other disciplines, the method of empirical orthogonal functions. In summary, BOD and SVD are mathematically synonymous.

SVD of temporally-uncorrelated data (POD)

Consider now, the case when the T realizations of data are *uncorrelated* in time, as in a turbulent flow experiment. The method then is to perform an SVD and analyze the spatial modes, as scaled by their singular values:

$$\mathbf{Y} = \mathbf{s} \cdot \mathbf{v}^T \quad (4.1.2)$$

Since there is no correlation in time, the temporal eigenfunction matrix, \mathbf{u} , has no physical meaning and is discarded. In fluid dynamics, this method is referred to as the *proper orthogonal decomposition* (POD) (Holmes et al, 1996, 1997; Berkooz et al, 1993) or the method of snapshots or method of strobos (Sirovich, 1987). In other disciplines, this procedure is also known as the Karhunen-Loève transform, principal components analysis, or method of empirical eigenfunctions.

The POD procedure is often presented as something distinct from SVD, but the following analysis shows that POD and SVD are actually equivalent, as implied by (4.1.2). The actual POD procedure is as follows: First, one forms the *matrix of observed covariance between time steps*, $\mathbf{R}_T = \mathbf{X} \cdot \mathbf{X}^T$ (where \mathbf{R}_T is size $[T, T]$). Next, one solves the *eigenvalue problem* $(\mathbf{R}_T) \cdot \mathbf{u} = \mathbf{u} \cdot \mathbf{s}_T^2$, which yields the size $[T, T]$ eigenvector matrix \mathbf{u} (which is identical to the SVD temporal amplitude matrix) and the size $[T, T]$ eigenvalue matrix, \mathbf{s}_T^2 (which contains the squares of the T singular values of \mathbf{X} . That is, $\mathbf{s}_T^2 = \mathbf{s} \cdot \mathbf{s}^T$). Finally, one finds the POD modes, \mathbf{Y} , by *projecting the eigenvectors onto the data set* by $\mathbf{Y} = \mathbf{u}^T \cdot \mathbf{X}$. Using (4.1.1), this POD procedure is equivalent to $\mathbf{Y} = \mathbf{u}^T \cdot \mathbf{u} \cdot \mathbf{s} \cdot \mathbf{v}^T = \mathbf{s} \cdot \mathbf{v}^T$, as given in the SVD-based POD procedure (4.1.2) above. In summary, the POD procedure is equivalent to performing an SVD and discarding the temporal modes.

We have synthesized the BOD and POD procedures and shown that they both rely on the umbrella mathematical tool, the SVD. Thus, the threshold criterion developed

in the following section to assess the validity of SVD modes can be applied to either POD or BOD analyses. In Section 4.4, we apply the threshold criterion to the BOD analysis of experimental PIV data of the wake behind a swimming fish.

4.2 Threshold criterion

We now present a threshold criterion for rejecting SVD modes obtained from experimental PIV data. The criterion that determines if the magnitude of a mode is larger than the experimental error can be stated in three mathematically-equivalent ways:

- (i) the *root mean square* (RMS) velocity of the mode is larger than the RMS PIV measurement error,
- (ii) the *signal to noise ratio* is greater than unity,
- (iii) the *kinetic energy* of the mode is greater than the kinetic energy of a hypothetical spatio-temporal velocity field, with normally-distributed velocities that have zero-mean and a standard deviation equal to the RMS PIV measurement error.

To derive the criterion, first note that the velocity for mode k at time-step i and measurement site j is $\mathbf{X}_k(i, j) \equiv \mathbf{u}(i, k)\mathbf{s}(k, k)\mathbf{v}(j, k)$. Thus, the root mean square (*RMS*) velocity of mode k is

$$\begin{aligned} RMS_k &= \sqrt{\frac{1}{DT} \sum_{i=1}^T \sum_{j=1}^D (\mathbf{u}(i, k)\mathbf{s}(k, k)\mathbf{v}(j, k))^2} \\ &= \frac{\mathbf{s}(k, k)}{\sqrt{DT}} \cdot \sqrt{\sum_{i=1}^T \mathbf{u}(i, k)^2} \cdot \sqrt{\sum_{j=1}^D \mathbf{v}(j, k)^2} \\ &= \frac{s_k}{\sqrt{DT}} \end{aligned}$$

Suppose that the PIV velocity data has root mean square error of ϵ . Then (i) requires that the *threshold criterion*

$$s_k > \sqrt{DT} \cdot \epsilon \quad (4.2.1)$$

be met for the magnitude of the mode to be larger than the experimental error. If (4.2.1) is not satisfied, then the magnitude of the mode is less than the measurement error, and the mode will be, as Ma et al (2003) says, “noisy”, since it may be dominated by random PIV measurement error.

Our threshold criterion can also be viewed in terms of a *signal to noise ratio*. From this viewpoint, the singular value is a measure of the signal content of the mode; modes which do not satisfy (4.2.1) have low signal content and may be dominated by noise. The signal to noise ratio of mode k is, by definition, $SNR_k \equiv \left[\frac{RMS_k}{\epsilon} \right]^2 = \frac{s_k^2}{DT\epsilon^2}$. Statement (ii) requires that $SNR_k > 1$, which is mathematically equivalent to (4.2.1).

A third way to view our threshold criterion is in terms of *kinetic energy*. The total kinetic energy (per unit density of fluid) of mode k is the sum of the kinetic energy of each of the D velocity values over all T -time-steps, which works out to be $KE_k = \frac{1}{2}s_k^2$. The kinetic energy of a *hypothetical error velocity field* with normally-distributed velocities with zero mean and standard deviation, ϵ , is $\frac{1}{2}\epsilon^2 DT$ (Venturi, 2006) (this kinetic energy is also recovered in the hypothetical scenario of all velocities equal to ϵ). Criterion (iii) requires $\frac{1}{2}s_k^2 > \frac{1}{2}\epsilon^2 DT$, which implies (4.2.1).

We suggest that the threshold criterion (4.2.1) be used as a rough limit of the validity of SVD modes extracted from experimental PIV data. Modes that do not satisfy (4.2.1) should be considered artifacts of the noise in the measurement and disregarded. Since we showed in Section 4.1.1 that both the BOD and POD procedures are equivalent to SVD, this threshold criterion applies to both BOD and POD analyses.

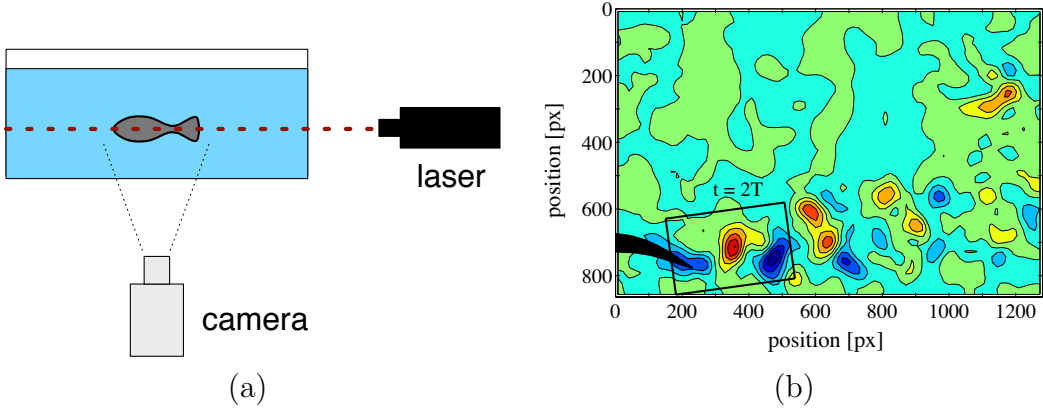


Figure 4-1: (a) Experimental PIV setup used for swimming study. The high-speed camera viewed up through the bottom of a glass aquarium, and the laser sheet was oriented horizontally at the mid-plane of the fish. (b) Qualitative illustration of the vorticity field in the last timestep. Clockwise vorticity are shown in blue, and counterclockwise vorticity are shown in red. The fish tail is shown in black. The fish swam from right to left at nearly-constant speed and made two nearly-identical tail flaps.

4.3 Materials and methods

4.3.1 Experimental details

To test the threshold criterion (4.2.1), we analyzed experimental data from a study with swimming fish (Epps et al, 2009). In this experiment, a Giant Danio (*Danio aequipinnatus*) was allowed to swim freely in a 15 cm by 30 cm tank, with 10 cm deep water. The flow features were characterized using high-speed PIV (Raffel et al, 2002). The tank was seeded with silver coated, neutrally buoyant, hollow glass spheres (average diameter 93 μm). The particles were illuminated using a low-powered, near-IR diode laser. The Lasiris Magnum diode laser produced a maximum output of 500 mW at 810 nm, and was fitted with optics to produce a 10° fan of light. The horizontal light sheet was imaged using an IDT XS-3 CCD camera with an 85 mm Nikkon lens, which viewed up from the bottom of the tank, as illustrated in figure 4-1a. The high-speed camera captured 8-bit-depth images at 100 frame/s, with a resolution of 1280 \times 864 pixels. The field of view was 19.94 \times 13.46 cm, giving a 64.2 px/cm zoom.

The time-series of particle images were processed using the multi-pass cross-correlation algorithm in the LaVision DaVis 7.2 software package. In the first pass, interrogation windows at the same location in each of two successive PIV images were cross-correlated to give an estimate of the particle displacements in that window. In the second pass, the window from the second image was centered at the displacement position estimated in the first pass, increasing the accuracy of the cross-correlation. Further details of the algorithm can be found in the DaVis product manual. In this experiment, we performed the first pass with 64×64 px interrogation windows and the second pass with 32×32 px windows, with 50% overlap in adjacent windows for higher resolution velocity fields. The output were velocity fields of 80×54 vectors, with approximately 40 vectors along the length of the fish body. For this time-series data, the time step between velocity fields was the same as the time between PIV image frames, Δt . All data post-processing -- including wake interrogation, data smoothing, and the BOD analysis -- was performed in MATLAB.

Each time the fish swam steadily through the field of view with the laser at its mid-plane, a time-series of images was saved. Results presented herein are for an adult fish (which had an overall length of $L = 9.89$ cm) swimming steadily at a speed of $U = 9.49$ cm/s = 0.96 L/s, which corresponds to a Reynolds number of $Re = UL/\nu = 9300$. Three successive tail beats were observed $T = 38$ frames apart, yielding a constant flapping frequency of $f = 2.6$ Hz. The average tail flap amplitude was $H = 1.38$ cm = 0.14 L, which corresponds to a Strouhal number of $St = fH/U = 0.37$.

In this particular case, the fish made two nearly-identical tail flaps, so these data were selected for the example BOD analysis presented herein. The tail flaps were biased to the lower end of the page, resulting in an asymmetric wake. The wake is qualitatively illustrated in figure 4-1b, where instantaneous vorticity contours show that its configuration is a reverse Kármán street.

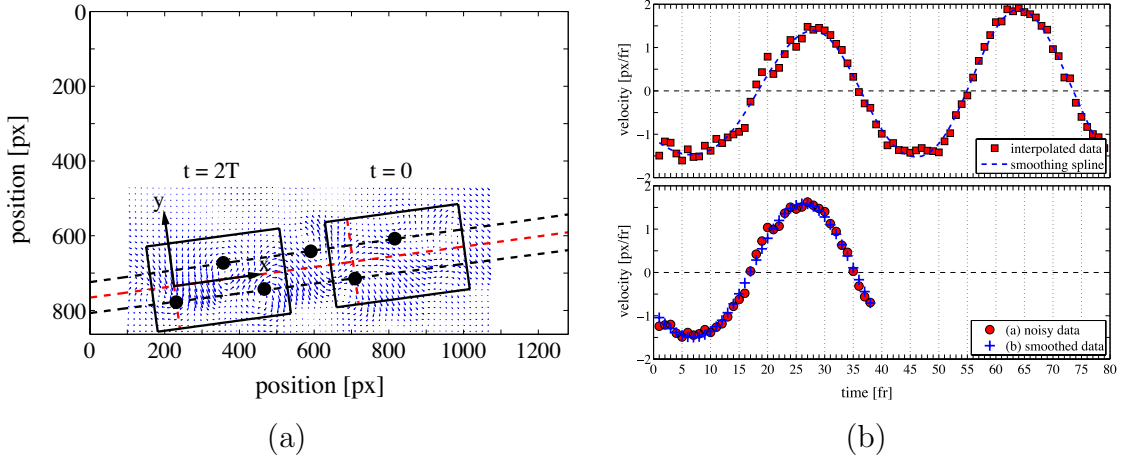


Figure 4-2: Illustration of data processing: (a) Wake interpolation schematic: tail maximum excursion positions, ‘•’; swimming trajectory, ‘--’; and outline of wake interpolation grid, ‘—’. The period of tail flapping is $T = 38$ frames. (b) Data smoothing: interpolated PIV data, ‘■’, are phase-averaged to yield the “noisy” data, ‘•’; smoothing spline values, ‘--’, are phase-averaged to yield the “smoothed” data, ‘+’. The data shown are $V_y(x \approx S_L, y \approx 0)(t)$.

4.3.2 Wake interrogation

Technically, the BOD does not require the spatial location of each measurement to have a ‘fixed identity’ (i.e. a fixed location relative to the fish). However, to facilitate interpretation of the BOD modes, and to be able to compare them to the modes of a regular Kármán street formed behind a stationary cylinder computed by Ma et al (2003), we must interrogate the wake in a body-fixed reference frame.

Outlines of the first and last wake interrogation grid are shown in figure 4-2a. The fish trajectory was determined by locating the position of the caudal fin fork at each extrema in tail lateral excursion and fitting straight lines via least squares through these points, with the average of these two fits giving the centerline of the trajectory. The origin ($x = 0$) locations of the grids for the first and last timesteps were located by perpendicularly projecting the tail extrema positions onto the trajectory centerline, as shown. Intermediate wake grids were equispaced along the trajectory, which yielded a body-fixed interpolation, since the fish swam at steady speed. Interpolation was

performed using the MATLAB command `griddata(...,'cubic')`, which performs a triangle-based cubic interpolation (MathWorks, 2009). The raw PIV velocity field was cropped (as shown in figure 4-2a) in order to expedite the interpolation procedure, which does not use data far away from the interpolation sites anyway. These interpolated wake data were projected into the wake coordinate system to find wake-aligned velocity components, V_x and V_y . The translation velocity of the wake grid was ignored in the interpolation procedure, since it is constant and would, therefore, be removed prior to BOD anyway. By interpolating on a moving grid, we ‘collected’ PIV data in a body-fixed reference frame.

4.3.3 Experimental PIV error

The two primary sources of PIV measurement error are the loss of in-plane particle pairs and error due to large velocity gradients. Other factors, such as particle image diameter and particle image displacement have lesser effects (Raffel et al, 2002; Melling, 1997). Adequate seeding density (~ 15 particles per interrogation window) and a high frame rate can mitigate the loss of in-plane particle pairs, but PIV velocity measurement error due to velocity gradients persist. In our experiment with the Danio, the “noisy” data had an RMS velocity gradient of 0.02 [(px/frame)/px], which corresponds to an RMS PIV velocity error of approximately

$$\epsilon \approx 0.1 \text{ [px/frame]} \quad (4.3.1)$$

according to Raffel et al (2002). In the present experiment, the number of data sites is $D = 1776$, and the number of timesteps is $T = 38$; therefore, the threshold singular value (4.2.1) is

$$s_k > \sqrt{1776 \cdot 38} \cdot 0.1 \text{ [px/frame]} = 26.0 \text{ [px/frame]} \quad (4.3.2)$$

Note that by definition, singular values contain the units of the original data. Since we presently consider a decomposition of velocity fields, the units of the singular values are [px/frame]. We chose to not normalize the singular values (say, by the swimming speed), since it is easier to compare singular values to PIV error using the raw units.

4.3.4 Data smoothing

In order to assess the effect of measurement error on the BOD, we must compare the interpolated PIV data to a set of data in which the error has been removed. In the high-speed PIV experiment, the flow appears to evolve smoothly to the naked eye, but -- presumably due to measurement error -- the PIV measurements deviate from otherwise smooth trajectories. To find the trajectory of each measurement, we fit a smoothing spline to these data using the automated method presented in Chapter 5. For example, figure 4-2b shows the transverse velocity at approximately one stride-length downstream of the tail, $V_y(S_L, 0)(t)$, where noisy PIV data follow the trajectory fit by the smoothing spline.

In the “noisy” and “smoothed” data sets presented herein, each trajectory is phase averaged, as shown in figure 4-2b. Phase averaging eliminates minor transient differences between the flapping cycles and allows us to perform BOD on one flapping cycle worth of data. (The authors have also performed BOD without phase averaging and find that the first two BOD modes are nearly identical to those of the phase-averaged data, confirming quantitatively that the flow is periodic.) Finally, the “error” data set presented herein was constructed by taking the difference between the “noisy” and “smoothed” data. For each data set (“noisy”, “smoothed”, and “error”) a time-series of velocity fields capturing one flapping cycle was input to the BOD analysis.

4.4 Results and discussion

4.4.1 PIV wake data

The “noisy”, “smoothed”, and “error” time-series of wake data are shown in figure 4-3. Since the translation velocity of the wake grid was ignored in the data interpolation, these vectors represent deviation from the free-stream in this body-fixed reference frame. The “noisy” and “smoothed” time-series both resemble a reverse Kármán street, which is the well-known wake structure of a carangiform swimming fish (Nauen and Lauder, 2002; Borazjani and Sotiropoulos, 2008). The velocity and vorticity “error” data have much smaller magnitudes than the “noisy” data, and they appear random, indicating that they are in fact random PIV measurement error.

The fish swam with nearly constant speed, but had a bias in its kick towards the bottom of the image. Thus, the vortices on the bottom side of the wake have higher vorticity levels than those on the top, and all vortices drift in the negative y direction as they convect downstream (due to self-induction of the wake).

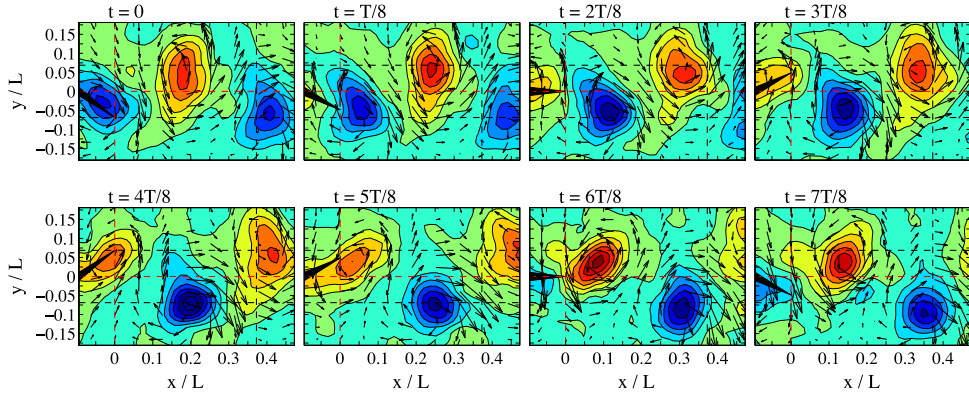
The time-average of these $\vec{V}(x, y, t)$ velocity data is

$$\vec{V}^{\text{avg}}(x, y) = \frac{1}{T} \sum_{i=1}^T \vec{V}(x, y, t_i) \quad (4.4.1)$$

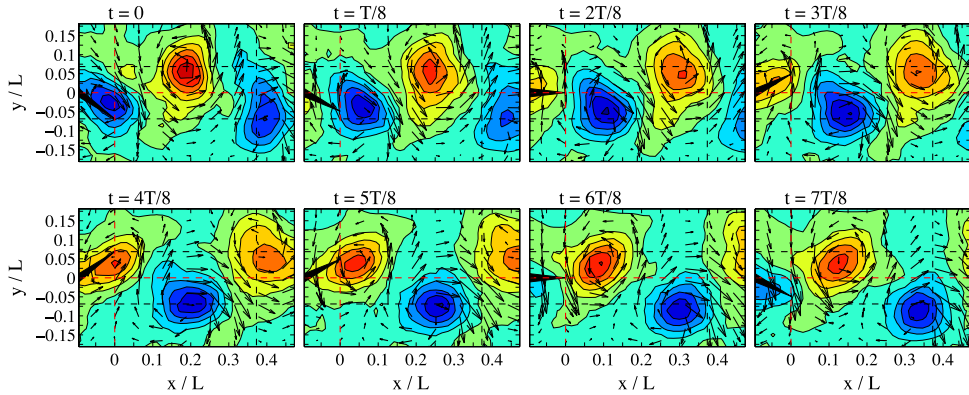
The time-averaged wake is a jet which grows in both magnitude and breadth as it progresses downstream, as shown in figure 4-4a. The maximum streamwise velocity occurs at approximately one stride length downstream of the tail flapping plane.

The time-averaged “error” data are shown in figure 4-4b. All velocity values are nearly zero; the mean “error” velocity is 0.001 [px/frame]. For comparison, the mean velocity value of the “smoothed” data is 0.19 [px/frame], nearly two hundred times greater than the mean “error” velocity value. Figure 4-4 indicates that the error data is random noise and that the signal to noise ratio of our measurements is quite high.

(a) Noisy data



(b) Smoothed data



(c) Error data

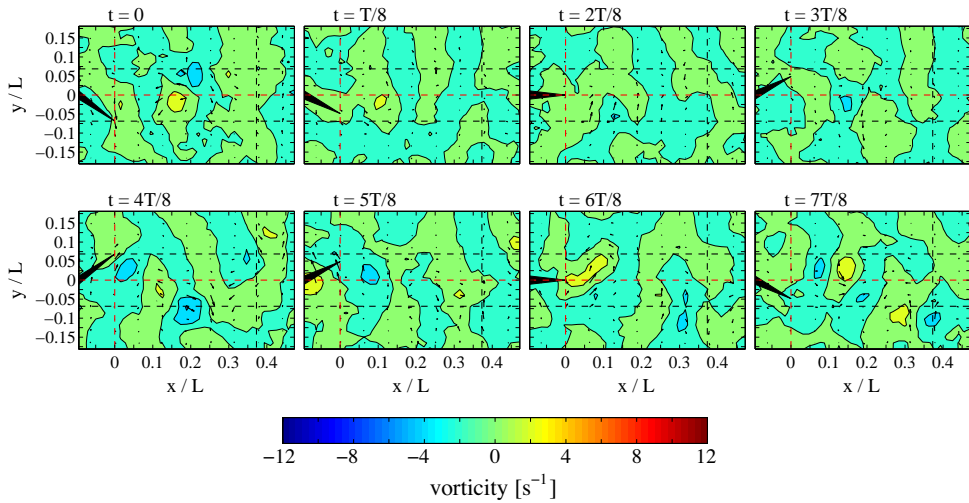


Figure 4-3: Filmstrips of velocity field data input to the BOD analysis. Points of interest: swimming centerline, $y = 0$; tail flap envelope, $y = \pm 0.07 L$; tail flap plane, $x = 0$; and stride length, $x = 0.37 L$.

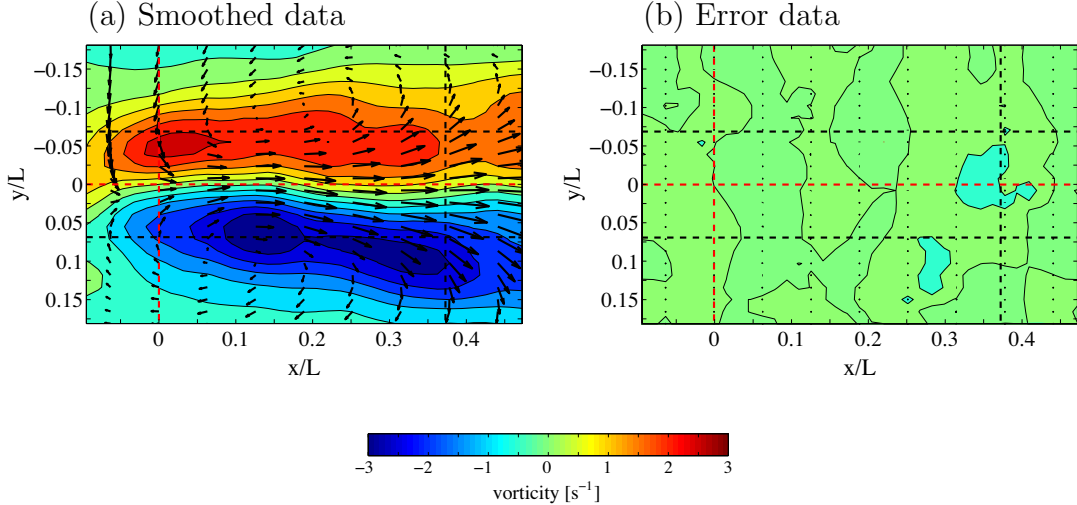


Figure 4-4: Time-averaged wake velocity and vorticity fields. The time-average of the “smoothed” and “noisy” data are nearly identical, so the time-averaged “noisy” data is not shown. The time-averaged fields for the “error” data are nearly zero. The vector scale and vorticity colormap are the same for both figures.

4.4.2 Singular values

We now present the results of the biorthogonal decomposition (BOD) of the “noisy”, “smoothed”, and “error” data sets. In order to perform the BOD, the velocity component data (which each are of size $[N = 37, M = 24, T = 38]$) are formatted into matrix \mathbf{X} , which is size $[T = 38, D = 2MN = 1776]$. Each column of \mathbf{X} contains the T measurements made at a particular data site, less their time-averaged value, which was computed using (4.4.1). The BOD was performed using the MATLAB command `svd` (MathWorks, 2009).

Figure 4-5a shows the singular values of the BOD modes, as well as a dashed line showing our *threshold criterion* (4.3.2), which is $s_k > \sqrt{DT} \cdot \epsilon = 26.0$ [px/frame]. For both the “noisy” and the “smoothed” data, singular values 1 and 2 are approximately three times the error threshold and also three times larger than the next singular values. This implies that modes 1 and 2 capture most of the flow dynamics (i.e. they contain most of the kinetic energy). Singular values 3 and 4 are nearly equal to our

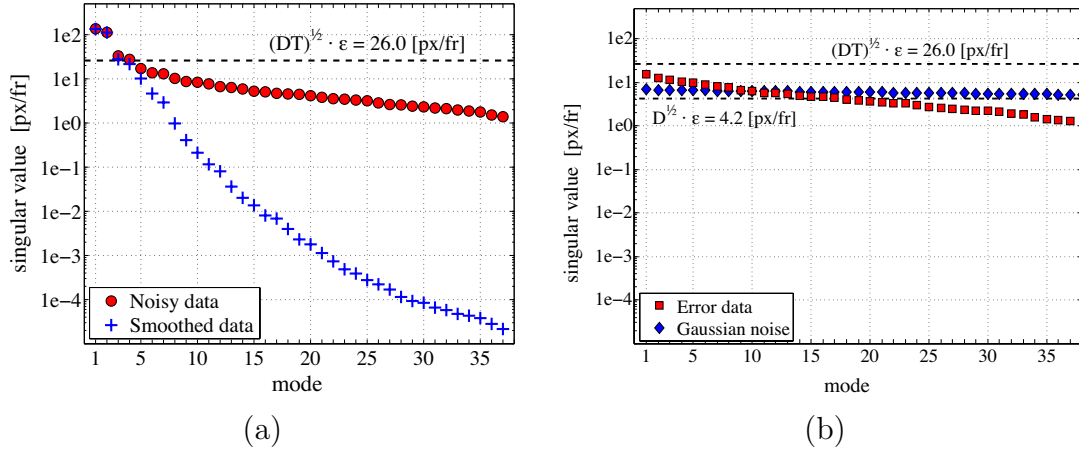


Figure 4-5: (a) BOD singular values for the “noisy” data, ‘●’, and “smoothed” data, ‘+’. The dashed line represents the PIV error criterion (4.2.1); modes 5-38 should be ignored, since their singular values are less than this threshold. (b) Singular values of the “error” data, ‘■’, and singular values of a size $[T, D]$ matrix of Gaussian random numbers with standard deviation $\mu = 0.14$ [px/frame], ‘♦’. The dashed line represents the PIV error criterion (4.2.1), and the dash-dotted line represents the expected singular values of a size $[T, D]$ matrix of Gaussian random numbers with standard deviation, $\epsilon = 0.1$ [px/frame].

error threshold criterion. In both the “noisy” and “smoothed” cases, singular values 5-38 are lower than the threshold; these modes may be contaminated by measurement noise.

Note that we do not imply that modes 5-38 only contain noise. Rather they must contain some of the signal, but since their magnitude is so small (and so little signal is left for them to capture), they are most likely dominated by measurement noise. Likewise, mode 1 must contain some measurement noise, but this is likely a small fraction of the signal content in this mode.

The singular values of the “error” data, shown in figure 4-5b, are all less than our threshold criterion, which indicates that the “error” data does not contain appreciable signal content. In addition, these singular values span only one order of magnitude; that is, compared to the singular values of the “smoothed” data, the singular values of the “error” data are nearly constant.

To appreciate this fact, consider a size $[T, D]$ random data matrix, \mathbf{X}_{rand} , populated by normally-distributed random numbers with zero mean and standard deviation, ϵ . Since there is no coherent signal in such a matrix, all T singular values will be equal (assuming $D \gg T \gg 1$). To find their value, s_{rand} , note that the total kinetic energy of the data is $\frac{1}{2} \sum_{i=1}^T \sum_{j=1}^D \mathbf{X}_{\text{rand}}(i, j)^2 = \frac{1}{2}\epsilon^2 DT$ and also is given by $\sum_{k=1}^T \frac{1}{2}s_k^2 = \frac{1}{2}Ts_{\text{rand}}^2$. Therefore,

$$s_{\text{rand}} = \sqrt{DT}\epsilon \quad (4.4.2)$$

(which is clearly less than the threshold, $\sqrt{DT}\epsilon$). Many of the singular values of the “error” data are approximately $\sqrt{D} \cdot \epsilon = 4.2$ [px/frame], which supports the claim that these data are random noise.

One may argue that $s_k > \sqrt{D}\epsilon$ should be the error threshold criterion, instead of (4.2.1). However, since (4.4.2) is the limit of no signal, it seems that modes for which $\sqrt{D}\epsilon < s_k < \sqrt{DT}\epsilon$ may still have significant noise content. Hence, (4.2.1) is our suggested threshold criterion.

The RMS of the “error” velocity data actually is $\mu = 0.14$ [px/frame], which is slightly higher than the estimated RMS PIV error of $\epsilon \approx 0.1$ [px/frame]. In hindsight, finding the RMS of the “error” velocity values may be a more accurate way of estimating PIV error than the arguments offered in section 4.3.3. Nevertheless, the results presented herein hold whether $\epsilon \approx 0.1$ or 0.14 is used. For reference, the (nearly-constant) singular values of a size $[T, D]$ matrix of Gaussian random numbers with standard deviation, $\mu = 0.14$ [px/frame], are shown in figure 4-5b.

4.4.3 Mode shapes and amplitudes

Figures 4-6, 4-7, and 4-8 show BOD modes 1-10 for the “noisy”, “smoothed”, and “error” data, respectively. Each BOD mode consists of a normalized temporal

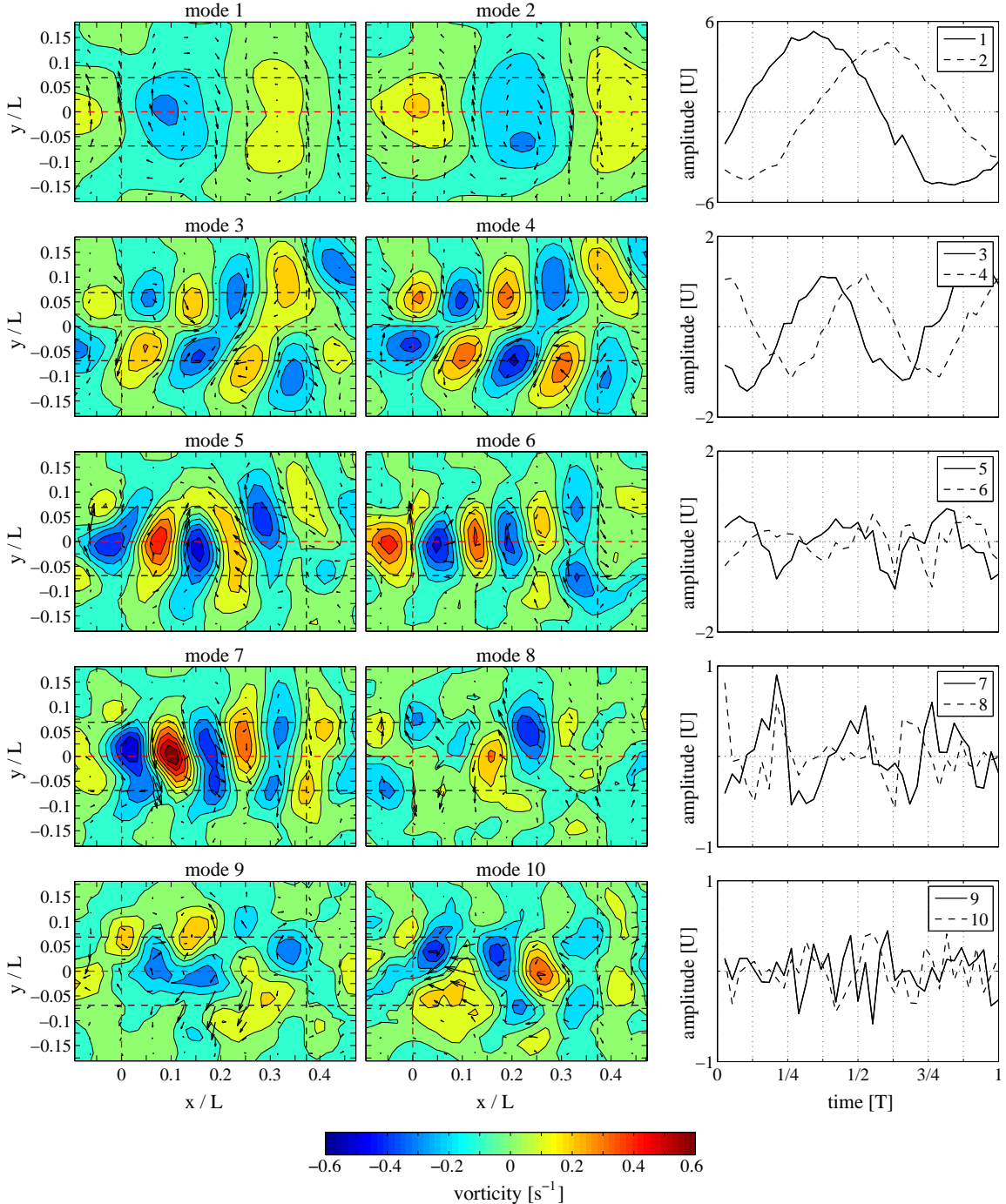


Figure 4-6: BOD modes 1 - 10 for the “noisy” data. Vorticity fields shown were computed from BOD velocity mode shapes; amplitudes shown were scaled by their respective singular values.

amplitude, normalized velocity field mode shape, and a singular value. In figures 4-6-4-8, vorticity fields are shown, which were computed from the modal velocity fields;

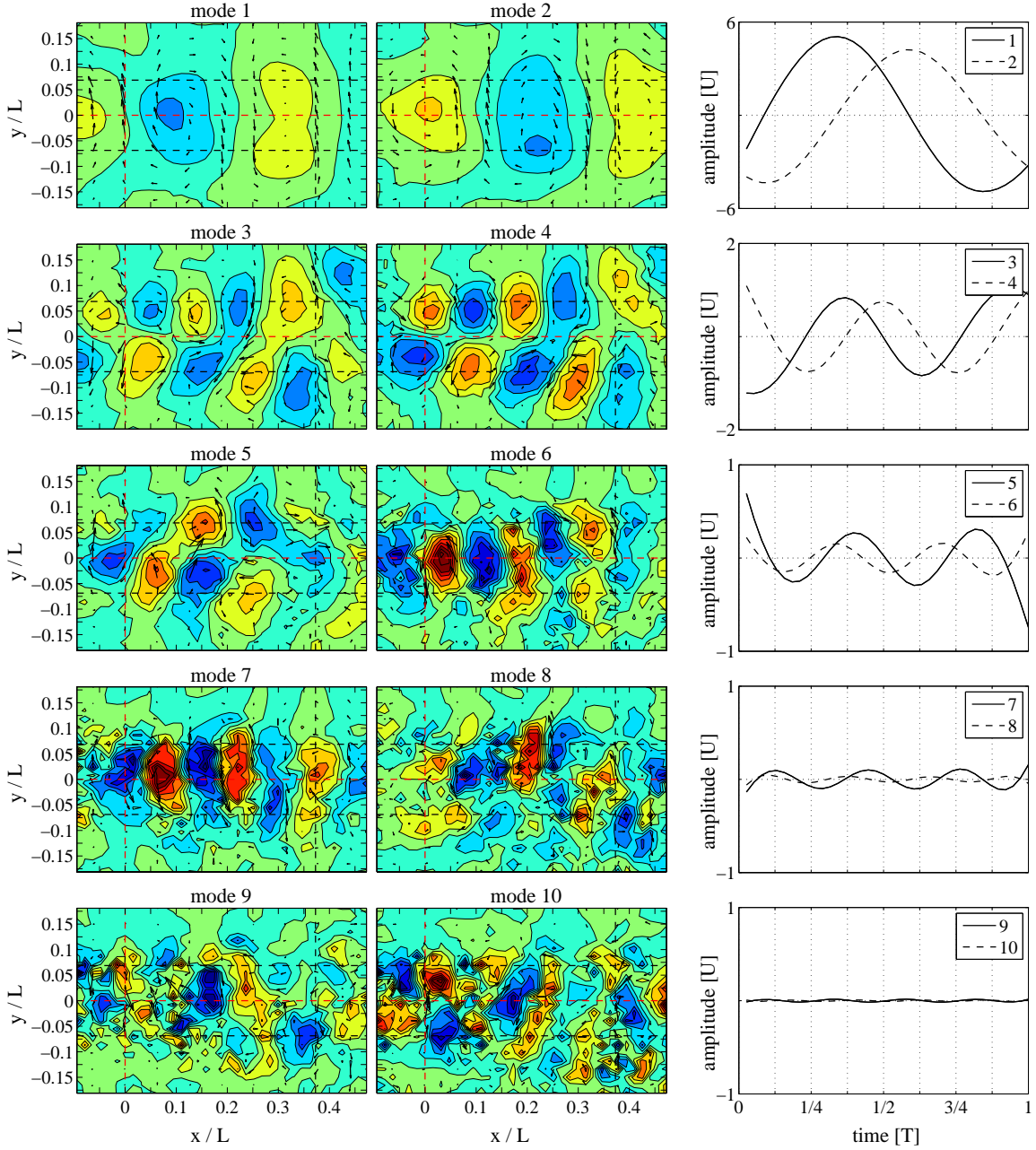


Figure 4-7: BOD modes 1 - 10 for the “smoothed” data. The vector scale and vorticity colormap are the same as figure 4-6.

also, the temporal amplitudes shown are scaled by their respective singular values, in order to show the magnitude of each mode explicitly.

Consider first the BOD amplitudes of the “noisy” data, shown in figure 4-6. Amplitudes 1 and 2 are approximately sinusoidal, which is expected since the tail

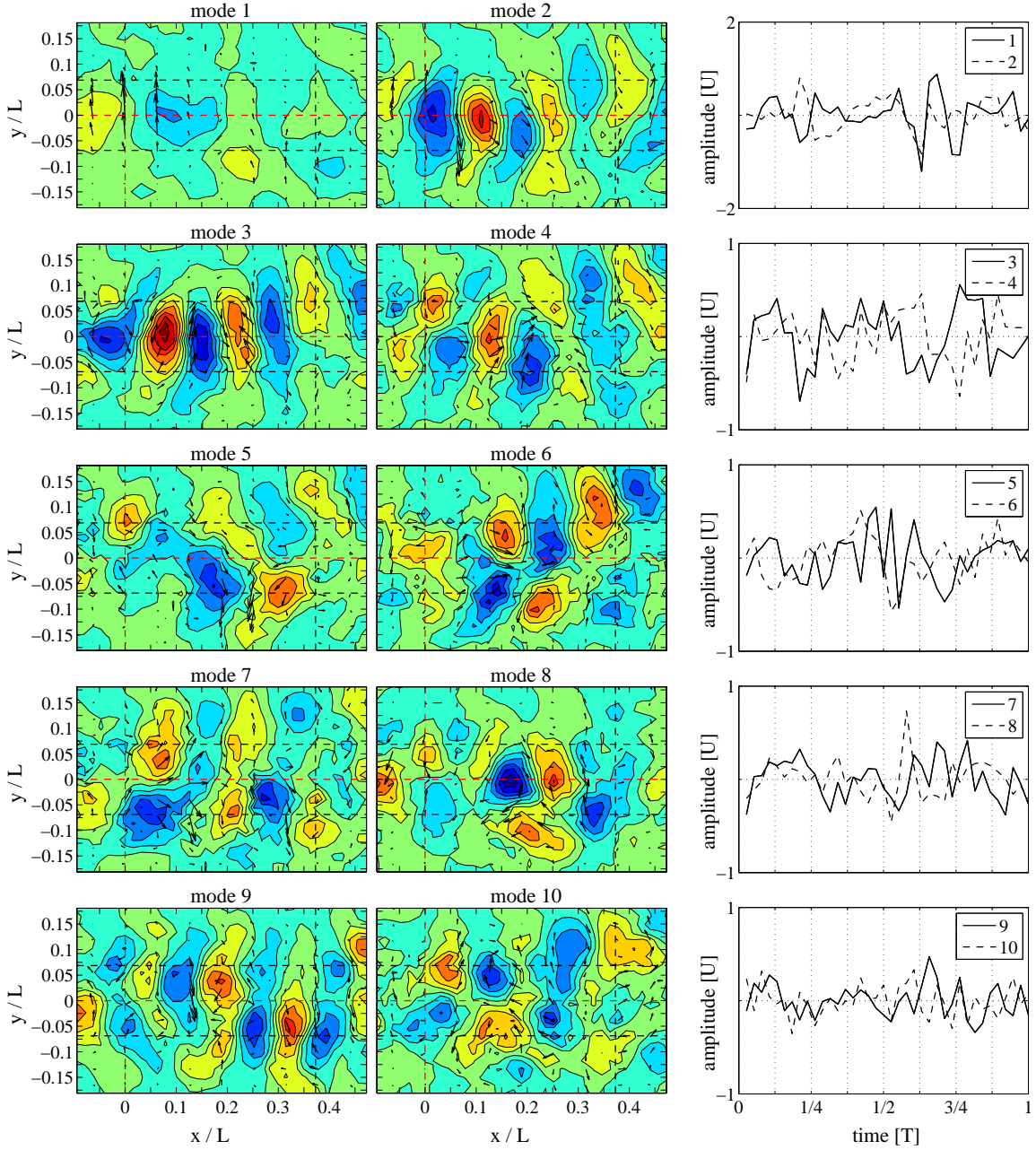


Figure 4-8: BOD modes 1 - 10 for the “error” data show no coherent signal content. The vector scale and vorticity colormap are the same as figure 4-6.

motion (and thus, the fluid forcing) was approximately sinusoidal. Because the flow is periodic, we expect the BOD modes appear in pairs, similar to the sine and cosine modes of a Fourier decomposition. Indeed, BOD amplitudes 1 and 2 have frequencies of approximately the tail flapping frequency, f , and amplitudes 3 and 4

have frequencies of approximately $2f$. However, BOD amplitudes 5 and higher (5+) are quite noisy and do not appear sinusoidal.

In sync with the temporal-frequency doubling of the amplitudes, vorticity fields 1-4 also display a spatial-frequency doubling. Vorticity fields 1 and 2 display one clockwise and one anticlockwise vorticity patch within the first stride length downstream of the tail; in other words, modes 1 and 2 have the same spatial frequency as the original data, which resembled a reverse Kármán street (see figure 4-3). Modes 3 and 4 contain two cycles of vorticity within the stride length, which corresponds to twice the spatial frequency of the original data. Modes 5+ again break the mould; they do not repeat the pattern of frequency-doubling that we would expect in a Fourier decomposition.

Modes 5+ should be ignored: Both their temporal amplitudes and their spatial mode shapes do not show the expected frequency doubling observed in prior modes; instead, these modes appear noisy and random. According to our error threshold criterion (4.2.1), modes 5+ have a magnitude lower than the PIV measurement error and should be ignored, since they may be contaminated by measurement noise. Amplitudes 5+ shown in figure 4-6 do not evolve smoothly in time, as this flow appears to the naked eye. Vorticity fields 8-10 show no coherent structures. Although vorticity fields 5-7 appear to contain a coherent pattern of vortical patches, these could be due to some actual dynamics of the flow or could very well be indicative of some systematic PIV error which appears more often in regions of high shear along the centerline of the wake. In any case, modes 5+ should be considered contaminated by measurement noise and ignored in data reconstructions or further dynamic analyses.

One might be concerned about whether the PIV spatial resolution is fine enough to resolve the small vortical structures expected to appear in modes 5 and higher. If modes 5 and 6 did contain information about the flow, then it would be expected that their spatial frequencies would be three times that of modes 1 and 2 (i.e. six vortices per stride length). Thus, the diameter of the vortices expected to appear in

modes 5 and 6 would be $d = 0.37 \text{ L}/6 = 0.06 \text{ L}$. The PIV spatial resolution was $16 \text{ px} = 0.025 \text{ L}$, which should be fine enough to resolve these vortices. However, modes 5 and 6 do not show such a vortical pattern.

One final point of interest in figure 4-6 is that the general form of vorticity fields 1 and 2 is similar to that of the decomposition of a Kármán street formed in the wake behind a circular cylinder (Ma et al, 2000). This is expected, since the fish wake is a reverse Kármán street.

Consider now the amplitudes of the temporally-smoothed data, shown in fig 4-7. In the processing of these data, the trajectory of each data site (e.g. $V_y(S_L, 0)(t)$) was smoothed in time by fitting a smoothing spline to the data; thus, the temporal fluctuation of each data site was removed, but no spatial smoothing was performed. As a result, the BOD amplitudes shown in figure 4-6 evolve quite smoothly in time, whereas the vorticity fields contain the noise of this data set.

All amplitudes approximate sinusoids: amplitudes 1 and 2 have frequency, f ; 3 and 4, $2f$; 5 and 6, $3f$; and so on, which is in agreement with the expected Fourier result. However, only vorticity fields 1-4 display the expected spatial frequencies. As with the “noisy” data, “smoothed” data modes 5-7 do not display the expected spatial frequency, and modes 8-10 show no coherent pattern.

Finally, the BOD modes of the “error” data are shown in figure 4-8. None of the temporal amplitude signals show a coherent pattern. Spatial modes 2 and 3 of the “error” data have alternating vortical patches along the centerline of the swimming trajectory, similar to spatial modes 5-7 of the “noisy” data. This implies that the PIV error that corrupted “noisy” modes 5-7 is being captured by “error” modes 2 and 3. The other “error” mode shapes appear to be random noise, indicating that “error” data is primarily random measurement error.

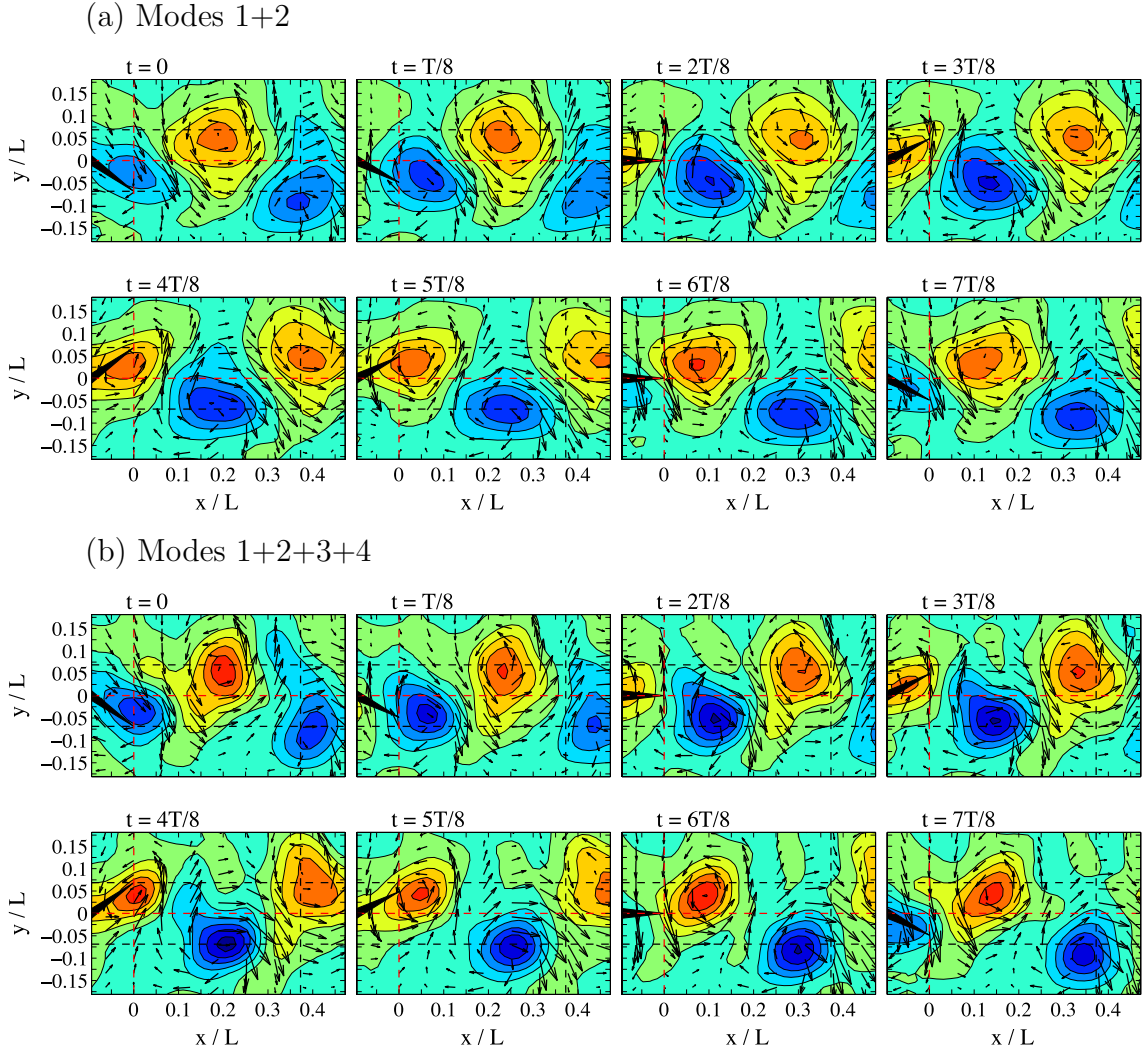


Figure 4-9: BOD low-order reconstructions of the “noisy” data. The vector scale and vorticity colormap are the same as figure 4-3.

4.4.4 Wake reconstruction

Since the present PIV experiment is only capable of resolving the first four BOD modes, one may ask if these modes are sufficient to reconstruct the fish wake. In general, one constructs a rank r approximation of \mathbf{X} (called a *Galerkin approximation*) by summing the first r BOD modes, $\mathbf{X}^{(r)} = \sum_{k=1}^r \mathbf{X}_k = \mathbf{u}(1 : T, 1 : r) \cdot \mathbf{s}(1 : r, 1 : r) \cdot \mathbf{v}(1 : D, 1 : r)^T$. The original data matrix \mathbf{X} can be recovered by summing all T modes, $\mathbf{X} = \sum_{k=1}^T \mathbf{X}_k$, which is just a restatement of (4.1.1).

Only the first two BOD modes are needed in order to reconstruct the vortex street behind the swimming fish. Since the mode 1 and 2 amplitudes are shifted temporally and their vorticity fields are shifted spatially, modes 1 and 2 can represent the formation and convection of vortices into the wake behind the fish, as shown in figure 4-9a. This is expected, since other researchers have found that only modes 1 and 2 are needed to reconstruct the (regular) Kármán street behind a circular cylinder (Ma et al, 2000). These modes capture 90.7% of the kinetic energy of the “noisy” time-series of data.

Figure 4-9b illustrates that modes 3 and 4 add further detail to the shape and strength of the vortices in the reconstructed wakes. Since modes 1 through 4 capture 96.1% of the kinetic energy of the original velocity fields (i.e. they contain most of the signal content), many of the snapshots shown in figure 4-9b look virtually identical to the original “noisy” data (shown in figure 4-3a). The inclusion of modes 6-10 in the reconstruction (not shown) yields even better agreement with the “noisy” data, but since the signal strength of modes 5 through 10 is significantly lower than our error threshold criterion, we anticipate that these modes only serve to reintroduce the PIV error back into the reconstructed solution.

4.5 Conclusions

In this work, we developed a threshold criterion (4.2.1) for rejecting singular value decomposition modes. This threshold criterion can be interpreted in three ways:

- (i) the *root mean square* (RMS) velocity of the mode is larger than the RMS PIV measurement error,
- (ii) the *signal to noise ratio* is greater than unity,
- (iii) the *kinetic energy* of the mode is greater than the kinetic energy of a hypothetical spatio-temporal velocity field, with normally-distributed velocities that have zero-mean and a standard deviation equal to the RMS PIV measurement error.

Further, we showed that since both biorthogonal decomposition (BOD) and proper orthogonal decomposition (POD) are rooted in the SVD, this threshold criterion applies to both types of analyses.

Herein, we performed a BOD analysis of 2D PIV data of a fish wake. We obtained ‘body-position-invariant’ velocity fields by interpolating the PIV data on a grid that translated with the swimming fish. We have shown that the first two BOD modes can represent the fish wake, which is a reverse Kármán street. Modes three and four add detail to the wake, whereas modes five and higher add little additional information and contain much of the measurement noise. As expected, only the first four modes obtained from our experimental data had magnitudes that met the threshold criterion. We found that smoothing our PIV data using smoothing splines has little effect on these first four BOD modes. However, since the smoothing removes PIV error, the magnitude of higher BOD modes was reduced.

Some parallels can be drawn between the present analysis and the results presented by Ma et al (2003) regarding the POD modes of a cylinder wake, which is a regular Kármán street. They compare POD modes extracted from (noisy) PIV “experimental” data to those extracted from (precise) direct numerical simulation “DNS” data. (Unfortunately, they do not report the number of velocity vectors in their experiment nor do they report the units of their singular values, so we can not verify if our threshold criterion (4.2.1) is valid in their case.) Similar to our results, Ma finds that the “experimental” data eigenmodes 1-4 were acceptable, but modes 5 and higher were corrupted by measurement error. In both our “noisy” data and Ma’s “experimental” data, the singular values of modes five and higher (5+) are clustered within one order of magnitude, whereas for our “smoothed” data and Ma’s “DNS data”, these singular values span six orders of magnitude. Since a matrix of random data has constant singular values, we assert that in comparison to the singular values of our “smoothed” and Ma’s “DNS” modes 5+, the singular values for our “noisy”

and Ma's "experimental" modes 5+ were relatively constant, indicating that these modes are capturing the experimental error.

These points taken together indicate that Kármán streets can be represented adequately with two to four BOD modes, and that experimental error must be very precisely controlled if higher modes are desired.

Bibliography

Aubry N (1991) "On the hidden beauty of the proper orthogonal decomposition," Theoretical and Computational Fluid Dynamics **2**:339–352.

Aubry N, Guyonnet R, Lima R (1991) "Spatiotemporal analysis of complex signals: Theory and applications," Journal of Statistical Physics **64**(3/4):683–739.

Aubry N, Chauve MP, Guyonnet R (1994) "Transition to turbulence on a rotating flat disk," Physics of Fluids **6**(8):2800.

Berkooz G, Holmes P, Lumley JL (1993) "The proper orthogonal decomposition in the analysis of turbulent flows," Annual Review of Fluid Mechanics **25**:539–575.

Borazjani I, Sotiropoulos F (2008) "Numerical investigation of the hydrodynamics of carangiform swimming in the transitional and inertial flow regimes," Journal of Experimental Biology **211**:1541–1558.

Epps BP, Valdivia y Alvarado P, Yousef-Toumi K, Techet AH (2009) "Swimming performance of a biomimetic compliant fish-like robot," Experiments in Fluids **47**:927–939.

Fogleman M, Lumley J, Rempfer D, Haworth D (2004) "Application of the proper orthogonal decomposition to data sets of internal combustion engine flows," Journal of Turbulence **5**(23).

Gentle JE (1998) Numerical Linear Algebra for Applications in Statistics Springer.

Holmes P, Lumley JL, Berkooz G (1996) Turbulence, Coherent Structures, Dynamic Systems, and Symmetry Cambridge University Press.

Holmes PJ, Lumley JL, Berkooz G, Mattingly JC, Wittenberg RW (1997) “Low-dimensional models of coherent structures in turbulence,” Physics Reports **287**:337–384.

Kostas J, Soria J, Chong MS (2005) “A comparison between snapshot POD analysis of PIV velocity and vorticity data,” Experiments in Fluids **38**:146–160.

Ma X, Karamanos GS, Karniadakis GE (2000) “Dynamics and low-dimensionality of a turbulent near wake,” Journal of Fluid Mechanics **410**:29–65.

Ma X, Karniadakis GE, Park H, Gharib M (2003) “DPIV-driven flow simulation: a new computational paradigm,” Proceedings of the Royal Society of London A **459**:547–565.

Melling A (1997) “Tracer particles and seeding for particle image velocimetry,” Measurement Science and Technology **8**:1406–1416.

Nauen JC, Lauder GV (2002) “Hydrodynamics of caudal fin locomotion by chub mackerel (*scomber japonicus*),” Journal of Experimental Biology **205**:1709–1724.

Neubauer J, Zhang Z (2007) “Coherent structures of the near field flow in a self-oscillating physical model of the vocal folds,” Journal of the Acoustical Society of America **121**(2):1102–1118.

Patte-Rouland B, Lalizel G, Moreau J, Rouland E (2001) “Flow analysis of an annular jet by particle image velocimetry and proper orthogonal decomposition,” Measurement Science and Technology **12**:1404–1412.

Raffel M, Willert C, Kompenhans J (2002) Particle Image Velocimetry: A Practical Guide Springer, New York.

Santa Cruz A, David L, Pecheux J, Texier A (2005) “Characterization by proper-orthogonal-decomposition of the passive controlled wake flow downstream of a half cylinder,” Experiments in Fluids **39**:730–742.

Sirovich L (1987) “Turbulence and the dynamics of coherent structures, part 1: Coherent structures, part 2: Symmetries and transformations, part 3: Dynamics and scaling,” Quarterly of Applied Mathematics **45**:561–590.

The MathWorks (2009) <http://www.mathworks.com>

Venturi D (2006) “On proper orthogonal decomposition of randomly perturbed fields with applications to flow past a cylinder and natural convection over a horizontal plate,” Journal of Fluid Mechanics **559**:215–254.

[THIS PAGE INTENTIONALLY LEFT BLANK]

Chapter 5

A method for inferring forces from experimental position data

This thesis focuses on applications of a theoretical framework for estimating fluid dynamic forces. However, in some experiments, we need not estimate the forces at all, because the net force on a body is given from its mass and acceleration by Newton's second law: $\mathbf{F} = m\mathbf{a}$. If we can determine the acceleration experimentally, then we know the net force on the body.

Measuring the acceleration directly (using accelerometers) is not possible in some experiments: For example, strapping an accelerometer to a small fish is not feasible. However, it is possible to take high-speed video of the fish and interrogate its position in each time step, $y(t)$. Then the physics problem of finding the net force simply distills to the numerical problem of finding the second derivative of the measured position data, $a(t) = \frac{d^2y}{dt^2}$.

Although finding a derivative might seem like a simple task, doing so for experimental data is not trivial, because the data inevitably contains measurement error. Consider measured position data $\tilde{y}(t) = y(t) + O(\epsilon)$, where $y(t)$ was the true position, and $O(\epsilon)$ is the order of magnitude of the measurement error. It is well

known that finite difference formulae amplify measurement error

$$a(t) = \frac{\Delta \left(\frac{\Delta(y+O(\epsilon))}{\Delta t} \right)}{\Delta t} = \frac{d^2y}{dt^2} + O\left(\frac{\epsilon}{(\Delta t)^2}\right)$$

so they can not be used. Rather, one must fit an analytic function to the data.

Typically, an experimentalist would choose (somewhat arbitrarily) a functional form (e.g. a cubic polynomial) and use least squares regression to determine the fitting parameters (the four cubic polynomial coefficients) that best fit the entire data set. Inherent in this method are two problems: (1) the true function $y(t)$ may not actually be of the chosen functional form, and (2) the function does not truly capture local trends in the data, since the fitting parameters are chosen by a best fit to the entire data set. I have circumvented both of these issues by developing a novel method by which to fit a *smoothing spline* to measured data. My methodology allows the experimentalist to find the best fit smoothing spline, which does not presume any functional form, captures local trends in the data, and allows one to analytically compute the desired derivatives.

In this chapter and the next, I consider the hydrodynamic forces acting on a billiard ball as it falls into a basin of water. This chapter details the spline fitting procedure that uses measured position data to infer the total force on a sphere, falling freely under gravity into an undisturbed water surface. Chapter 6 presents a potential flow model to explain these observed forces.

The spline fitting method presented in this chapter has been used by the author in other studies as well. The automated spline fitting procedure was used in Chapter 4 to fit splines to smooth the PIV velocity data of the fish wake, and the manual spline fitting procedure was used to find the angular velocity and acceleration of a propeller (from angular position data) during unsteady start-up experiments, as will be discussed in Chapter 8.

In this chapter, I show how instantaneous derivatives of high-resolution, high-precision experimental data can be accurately evaluated by fitting the data with a *smoothing spline*. This chapter presents a novel and robust method for choosing the best spline fit and, hence, the best prediction of the derivatives.

Typically, a smoothing spline is fit by choosing the value of a *smoothing parameter* that controls the tradeoff between *error* to the data and *roughness* of the spline. This method can yield an unsatisfactory fit, however, because the roughness of the fitted spline is extremely sensitive to the choice of smoothing parameter. An alternate fitting method is to choose an *error tolerance* and to find the spline with the least roughness possible, given that the error must be less than or equal to this tolerance.

In this chapter, we systematically explore the relationship between error tolerance and the minimum possible roughness of smoothing splines. I find that there exists a *critical error tolerance*, corresponding to the spline that has the minimum possible error to the data, without also having roughness due to the noise in the data. I present an automated method to find this critical error tolerance and show, using both an analytic example and a canonical experimental example, that this in fact yields the best spline fit.

5.1 Introduction

Finding the rate of change of a measured quantity is a ubiquitous experimental task. The present work is motivated by the canonical physics problem of finding the *velocity* (rate of change of position) and *acceleration* (rate of change of velocity) of a sphere falling into a basin of water. Other examples abound. From fluid mechanics, consider computing a spatial *velocity gradient* = $\frac{d(\text{velocity})}{d(\text{position})}$ in order to determine the shear stress on a body, given experimental velocity field data. From solid mechanics,

consider determining the *strain rate* = $\frac{d(\text{strain})}{d(\text{time})}$ of a material during a crash impact test, given strain data measured at several times during the experiment. From image processing, consider finding the *curvature* (i.e. second spatial derivative) of a feature found using standard edge detection algorithms on a digital image. In all these cases, experimentalists desire the derivative of a measured quantity.

This chapter presents a method to determine derivatives of experimental data. My method applies to data that is highly-resolved and has small experimental error (the need for these restrictions will be made apparent in Section 5.2.1). Consider a general set of experimental measurements

$$\tilde{y}_i = y(t_i) + \tilde{\epsilon}_i \quad (5.1.1)$$

made at times, t_i ($i = 1, \dots, N$), where $y(t_i)$ is the true value of some smoothly-changing quantity and $\tilde{\epsilon}_i$ is the measurement error¹. The goal of the present work is to examine experimental $\tilde{y}(t_i)$ data and to best approximate the true function it represents, as well as its first few derivatives

$$y(t), \frac{dy(t)}{dt}, \frac{d^2y(t)}{dt^2}, \frac{d^3y(t)}{dt^3}$$

Typically in experimental research, the true function is either unknown or too complex to be represented by a simple parameterized model (e.g. a single polynomial with unknown coefficients). In this case, the appropriate way to represent the unknown function is with a *smoothing spline*. This spline does not require any knowledge about the true function (aside from assuming that it is piecewise continuous and smooth), and derivatives of this spline can be computed exactly.

¹Assume for all examples herein that the time at which each measurement took place was itself measured exactly. Also note, the curve fitting procedure described herein is not restricted to functions of time. Since ‘rate of change’ semantically implies ‘in time’, examples in which time is the independent variable are given herein.

A smoothing spline can be formed by a piecewise polynomial of degree n , with $n - 1$ continuous derivatives at each break point. Typically, cubic ($n = 3$) or quintic ($n = 5$) polynomials are used. A particular spline, $s(t)$, can be characterized by its *error*

$$\check{E}(s) = \int_{t_1}^{t_N} |\tilde{y}_i - s(t_i)|^2 dt \quad (5.1.2)$$

and *roughness*, which is defined for cubic and quintic splines as follows

$$R_2(s) = \int_{t_1}^{t_N} \left| \frac{d^2 s}{dt^2} \right|^2 dt \quad (\text{cubic spline}) \quad (5.1.3)$$

$$R_3(s) = \int_{t_1}^{t_N} \left| \frac{d^3 s}{dt^3} \right|^2 dt \quad (\text{quintic spline}) \quad (5.1.4)$$

Further background on the mathematical formulation of smoothing splines and their application to measured data can be found in references (de Boor, 1978; Silverman, 1985; Wahba, 1990).

In the vast majority of the smoothing spline literature, researchers try to find the ‘best’ smoothing spline fit by minimizing the quantity

$$J(s) = p\check{E}(s) + (1 - p)R(s) \quad (5.1.5)$$

where the *smoothing parameter*, p , controls the amount of smoothing. Various procedures aimed at finding the optimum smoothing parameter can be found in (Wahba and Wold, 1975; Craven and Wahba, 1979; Chung, 1980; Wecker and Ansley, 1983; Kohn and Ansley, 1987; Pope and Gadh, 1988; Hurvich and Simonoff, 1998; Wood, 2000; Teanby, 2007). Note that p must be chosen a-priori. If you pick $p = 1$, then minimizing $J(s)$ requires minimizing $\check{E}(s)$, which happens when the spline passes through every data point. If you pick $p = 0$, then minimizing $J(s)$ requires minimizing $R(s)$; roughness is zero for a cubic spline that is composed of linear segments (and

zero for a quintic spline composed of quadratic segments). For any $p \in [0, 1]$, there exists a unique spline that minimizes $J(s)$ (de Boor, 1978). Let us call this problem of identifying the best p and minimizing $J(s)$ the ‘de Boor formulation’.

Several researchers have developed numerical procedures to identify the ‘best’ smoothing parameter, p , for a given data set (see above references). However, to the author’s knowledge, only one of the codes developed therein has been implemented and made freely-available for use in MATLAB, which is widely-used for experimental data post-processing and analysis.

One of de Boor’s codes is implemented in the MATLAB function `csaps`(t, \tilde{y}), which attempts to choose the optimum p and then determine the spline which minimizes $J(s)$. The solution of the de Boor problem in `csaps` requires solving a linear system of equations whose coefficient matrix has the form $p \cdot \mathbf{A} + (1 - p) \cdot \mathbf{B}$, where the matrices \mathbf{A} and \mathbf{B} depend on the data. The default value of the smoothing parameter in `csaps` is chosen such that $p \cdot \text{trace}(\mathbf{A}) = (1 - p) \cdot \text{trace}(\mathbf{B})$ (where the `trace` of a matrix is the sum of its diagonal elements) (de Boor, 2008). This ad-hoc method for selecting p often results in inadequate smoothing.

This chapter is motivated by the inadequate smoothing of `csaps` and the lack of any alternative readily-available for use in MATLAB. The implementation of the method described herein has been done in MATLAB, but the methodology can be implemented in any programming language.

My approach to the spline fitting problem follows Reinsch (Reinsch, 1967): I choose an *error tolerance*, E , and find the spline with the least roughness, given that the error must be less than or equal to this error tolerance:

$$\text{minimize } R(s) \tag{5.1.6}$$

$$\text{requiring } \check{E}(s) \leq E \tag{5.1.7}$$

One can show that this roughness minimization problem, hereafter referred to as the ‘Reinsch formulation’, is equivalent to minimizing $J(s)$ in the above ‘de Boor formulation’ (de Boor, 1978). Note that $E = 0$ in the Reinsch formulation is equivalent to $p = 1$ in the de Boor formulation, and $E \rightarrow \infty$ in the Reinsch formulation is equivalent to $p = 0$ in the de Boor formulation. An implementation of the Riensch formulation is available in MATLAB; the function `spaps`(t, \tilde{y}, E) returns the smoothing spline, $s(t)$, that has the least roughness possible, given that the error must be less than or equal to the given tolerance, E . The problem now is to choose the ‘best’ error tolerance, E , for a given data set.

The Reinsch problem, as implemented in `spaps`, provides a relationship between minimum roughness and error tolerance, $R(E)$. One could evaluate `spaps`(t, \tilde{y}, E) for several values of the error tolerance and compute the roughness of each resulting spline. In doing so, one would generate an ‘efficient frontier’ of smoothing splines that are viable candidates for the best fit. For any given error tolerance, splines exist with more roughness than the one on the $R(E)$ frontier, but these are undesirable.

I find that there exists a critical error tolerance, E_{cr} , which can be used to identify the ‘best fit’ spline. For error tolerances greater than E_{cr} , a spline fit to noisy data will still be smooth. For error tolerances less than E_{cr} , the minimum-roughness spline is still very rough, since it must follow very closely to the error-ridden data points.

In this chapter, I present a method for selecting the ‘best’ smoothing spline by identifying the critical error tolerance on the $R(E)$ frontier. This ‘best’ spline fit is the one that most closely follows the true function, $y(t)$; it has the minimum error possible and as much of the true roughness of $y(t)$ as possible, without capturing any roughness due to the noise in the data.

The remainder of this chapter is parsed into four sections: In the following section, I use an analytical example to present the $R(E)$ frontier and show how to use this frontier to manually select the best smoothing spline. I discuss how the $R(E)$ frontier

scales with measurement error, and I also compare the spline fit by my method to the spline fit by `csaps`. In Section 5.3, I describe an algorithm that automates my method to find the best smoothing spline for a given data set. In Section 5.4, I apply my spline fitting method to the canonical experimental example of evaluating the forces on a billiard ball falling into a basin of water. Finally, in Section 5.5, I summarize my conclusions.

5.2 Analytic example

In this section, I consider an analytic spline fitting example, and I show that there exists an *efficient frontier* of spline roughness versus error tolerance. I then show how the shape of this frontier allows one to determine the best smoothing spline fit for a given data set. In Section 5.2.1, I show how the shape of this frontier scales with measurement error. In sections 5.2.2 and 5.2.3, I compare the spline fit using my method to that fit by `csaps`. Since the true function is known in this example, I can compare my spline fits to the true function.

Consider noisy ‘‘experimental’’ data constructed using the function $y(t) = e^{-t} \cdot \sin(t)$ and normally-distributed ‘‘measurement error’’ (which can be generated in MATLAB using `randn`) with zero mean and standard deviation, ϵ . That is,

$$\tilde{y}(t_i) = e^{-t_i} \cdot \sin(t_i) + \mathcal{N}(0, \epsilon^2) \quad (5.2.1)$$

with $t_i = i \cdot \Delta t$ and $i = 1 \dots N$. These data are shown in figure 5-1a, with $\epsilon = 10^{-2}$, $\Delta t = 10^{-2}$, and $N = 10^3$.

By solving the ‘Reinsch problem’ (i.e. evaluating `spaps`(t, \tilde{y}, E)) for several error tolerances and then evaluating the roughness, R , of each output spline, one finds that there exists an *efficient frontier* of R vs. E for least-roughness smoothing splines. Two such frontiers are shown in figure 5-1b, one corresponding to quintic splines fit

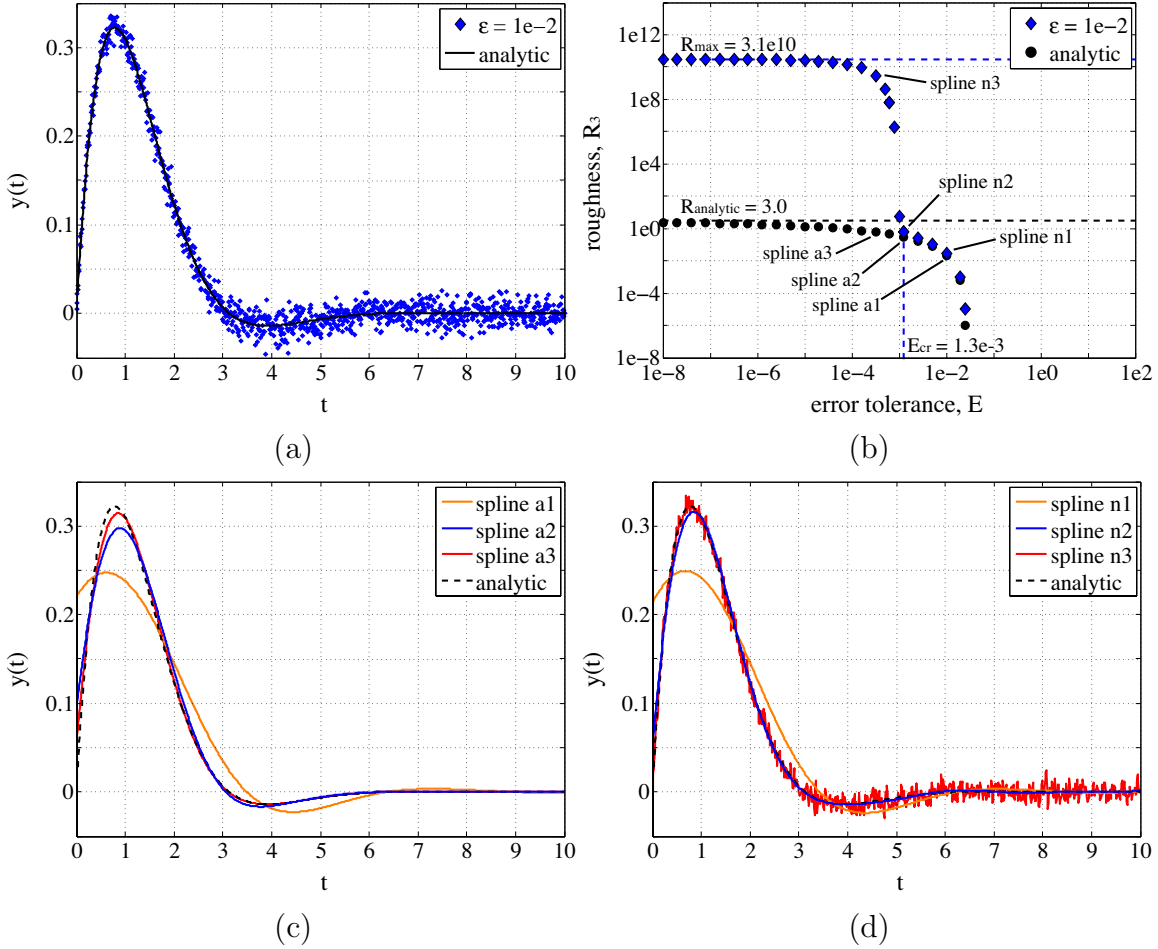


Figure 5-1: (a) Example analytic function $y(t) = e^{-t} \cdot \sin(t)$ and noisy ‘data’ $\tilde{y}(t) = y(t) + \mathcal{N}(0, \epsilon^2)$ with $\epsilon = 10^{-2}$. (b) Roughness, R_3 , versus error tolerance, E , of quintic splines found by solving the Reinsch problem. Note: each point represents a particular spline fit. The roughnesses of the spline fits to the analytic data, ‘●’, asymptotically reach the analytically-computed roughness of $y(t)$, whereas the roughnesses of the spline fits to the noisy data, ‘♦’, follow this trend for E larger than a *critical error tolerance*, E_{cr} , but increase several orders of magnitude for $E < E_{\text{cr}}$. (c) Selected splines fit to the analytic data. (d) Selected splines fit to the noisy data. Spline n2 is the fit with the smallest error tolerance that still mimics its corresponding spline fit to the analytic data.

to the noisy $\epsilon = 10^{-2}$ data (‘♦’), and one corresponding to quintic splines fit to the analytic $y(t_i)$ data (‘●’). One striking feature of the $\epsilon = 10^{-2}$ frontier is the kink at $E = 1.3 \times 10^{-3}$.

I define a *critical error tolerance*, E_{cr} ($= 1.3 \times 10^{-3}$ in this example), as the error

tolerance at this kink, for which the $R(E)$ frontier has its maximum positive curvature. This error tolerance partitions two of three interesting regions of the $R(E)$ frontiers, namely $E > 2.5 \times 10^{-2}$ (in this example), $E_{\text{cr}} < E < 2.5 \times 10^{-2}$, and $E < E_{\text{cr}}$. For $E > 2.5 \times 10^{-2}$, roughness is zero since the smoothing spline is allowed such a large error that it can be composed of segments which have no roughness.

As E is decreased from 2.5×10^{-2} to E_{cr} , the resulting smoothing splines are required to pass more closely to the given data. In doing so, each successive spline captures more of the roughness of the true function. This is illustrated by splines a1 and a2 in figure 5-1c and splines n1 and n2 in figure 5-1d. Note the similarity between the spline fits to the analytic data versus the noisy data; splines a1 and n1 look virtually identical, and splines a2 and n2 look quite similar as well. Thus, when error tolerances are chosen to be larger than the critical error tolerance, E_{cr} , a spline fit to noisy data is quite comparable to a spline fit to the analytic data.

For error tolerances less than the critical value (i.e. $E < E_{\text{cr}}$), a smoothing spline fit to noisy data is now required to follow the data so closely that the measurement error is captured by the smoothing spline. In other words, the spline is not permitted enough error tolerance to ignore the measurement error. Consequently, many wiggles are introduced into the spline fit, and the roughness increases by ten orders of magnitude over a relatively small range of E . Splines a3 and n3 (shown in figures 5-1c and 5-1d) were computed for an error tolerance just less than that of E_{cr} . Note that spline a3 follows the analytic $y(t)$ function more closely than spline a2, whereas spline n3 is quite noisy, because it is attempting to follow the noisy data.

Smoothing spline n2, as well as its first three derivatives, are compared to the analytic function in figure 5-2. The spline fit itself lays nearly on top of the analytic function in figure 5-2a, and the first two derivatives are also quite accurate. The second derivative does not capture the nature of the analytic function near time $t = 0$, because the third derivative of the analytic function is non-zero at that time,

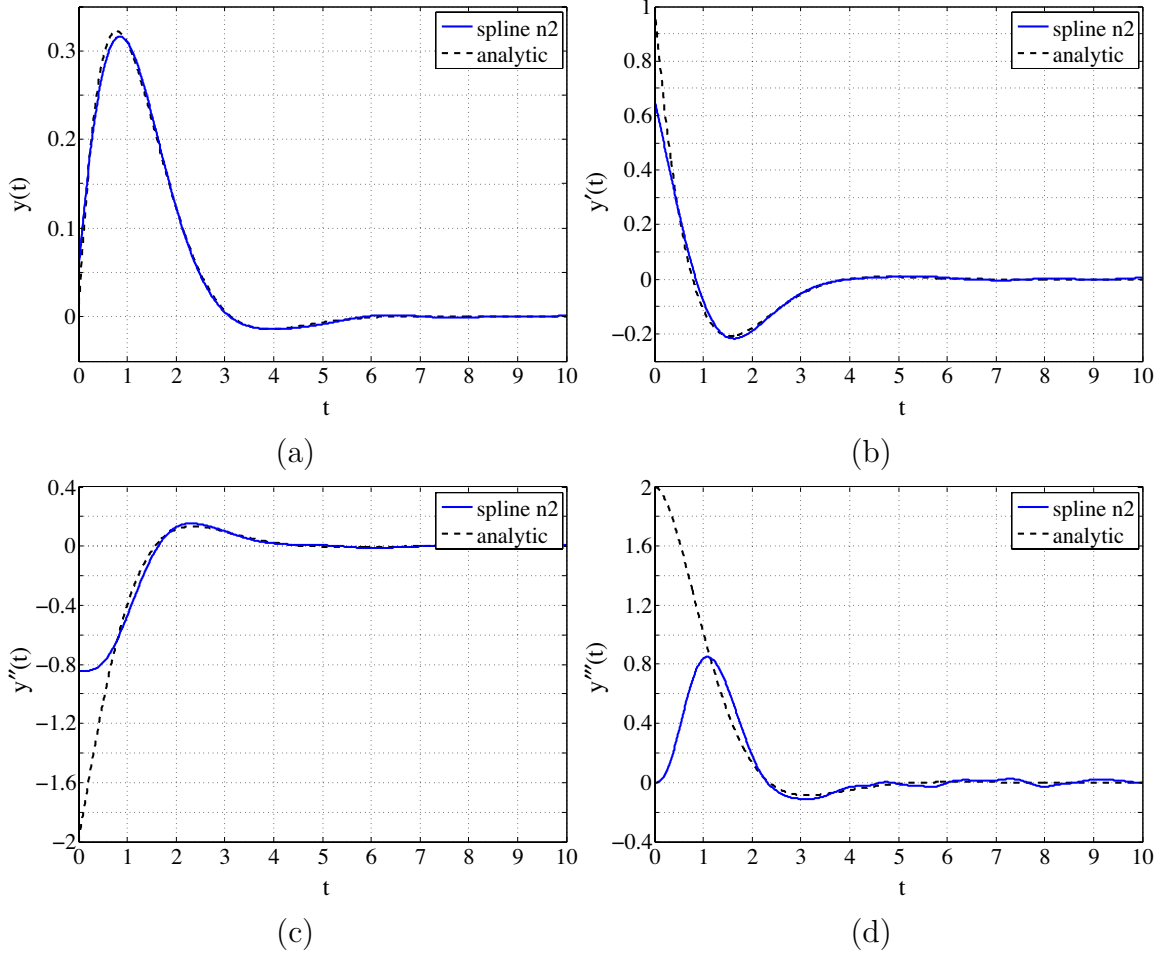


Figure 5-2: Comparison of the analytic function $y(t) = e^{-t} \cdot \sin(t)$ and spline fit n2 (see figure 5-1), as well as their first three derivatives with respect to time.

and one requirement of the quintic spline fitting procedure is that the third derivative is zero at the endpoints. If one desires to accurately represent the third derivative at the endpoints, a spline of higher degree than quintic must be used.

The results shown in figures 5-1 and 5-2 indicate that the ‘best’ smoothing spline corresponds to the one for which $E = E_{\text{cr}}$. This spline has the minimum error tolerance, without the introduction of much roughness due to measurement error. I define E_{cr} as the error tolerance for which the $R(E)$ frontier has its maximum positive curvature; this definition allows one to automate the process of determining E_{cr} , as will be discussed in Section 5.3.

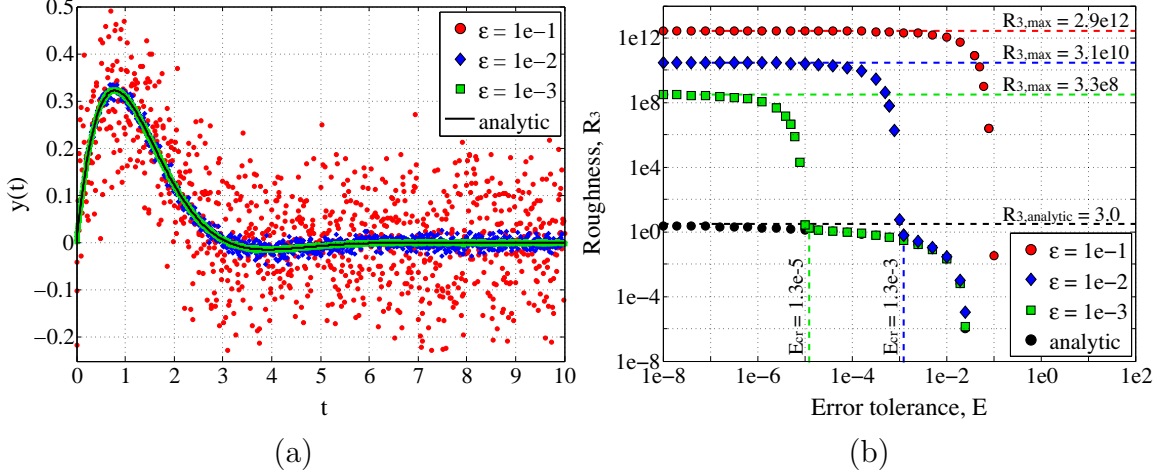


Figure 5-3: (a) Example analytic function $y(t) = e^{-t} \cdot \sin(t)$ and noisy ‘data’ $\tilde{y}(t) = y(t) + \mathcal{N}(0, \epsilon^2)$ with $\epsilon = \{10^{-1}, 10^{-2}, 10^{-3}\}$. (b) Roughness of quintic splines, R_3 , versus error tolerance, E .

5.2.1 Roughness and error scaling

Here I explore the effect of measurement error on the critical error tolerance and maximum roughness. I develop scaling arguments that can be used to estimate critical error tolerance, E_{cr} , and maximum roughness, R_{max} , given the measurement error, ϵ . These relations allow me to automate the spline fitting procedure, and since I can exactly compute R_{max} for a given experimental data set, these relations also allow me to estimate the measurement error.

Analytical example data with measurement error, $\epsilon = \{10^{-1}, 10^{-2}, 10^{-3}\}$, and their corresponding $R(E)$ frontiers are shown in figures 5-3a and 5-3b, respectively. The $\epsilon = 10^{-2}$ data are the same as figure 5-1. The $\epsilon = 10^{-3}$ data have a lower critical error tolerance than the $\epsilon = 10^{-2}$ data, as shown in figure 5-3b. The $\epsilon = 10^{-3}$ data more accurately represent the analytic function than the $\epsilon = 10^{-2}$ data, so the spline fit to the $\epsilon = 10^{-3}$ data at its critical error tolerance more accurately represents the analytic function than the spline fit to the $\epsilon = 10^{-2}$ data at its critical error tolerance. The $R(E)$ frontier corresponding to the $\epsilon = 10^{-1}$ data has no kink, because the noise level is so large that the analytic function cannot be resolved from these data.

To develop scaling arguments for the critical error tolerance and maximum roughness, consider a hypothetical data set, $\tilde{y}(t_i) = (-1)^i \cdot \epsilon$ with $t_i = i \cdot \Delta t$ and $i = 1 \dots N$, as if the true function were $y(t) = 0$ and this data set represents measurement noise in an average sense.

The critical error tolerance is the minimum error with which the spline still represents the true function (i.e. $s(t) \approx 0$). Thus, the critical error tolerance scales as

$$E_{\text{cr}} \sim \int_{t_1}^{t_N} |\tilde{y}(t_i) - 0|^2 dt \sim N\epsilon^2 \Delta t \quad (5.2.2)$$

In my analytical example, $N = 10^3$, $\epsilon = 10^{-2}$, and $\Delta t = 10^{-2}$, so by (5.2.2), $E_{\text{cr}} \sim 10^3 \cdot 10^{-4} \cdot 10^{-2} = 10^{-3}$, which agrees with the computed value of $E_{\text{cr}} = 1.3 \times 10^{-3}$ up to an $O(1)$ constant. Note that for the $\epsilon = 10^{-3}$ data, (5.2.2) predicts $E_{\text{cr}} \sim 10^{-5}$, which also agrees with the computed value of $E_{\text{cr}} = 1.3 \times 10^{-5}$ shown in figure 5-3.

The maximum roughness occurs when the spline passes through every data point. To scale the maximum roughness, we need to scale the second and third derivatives, which we can do for my hypothetical error data set using the ‘forward divided difference’ formulae

$$\frac{d^2 s(t_i)}{dt^2} = \frac{s_{i+2} - 2s_{i+1} + s_i}{\Delta t} \sim \frac{4\epsilon}{\Delta t^2} \quad (5.2.3)$$

$$\frac{d^3 s(t_i)}{dt^3} = \frac{s_{i+3} - 3s_{i+2} + 3s_{i+1} - s_i}{\Delta t} \sim \frac{8\epsilon}{\Delta t^3} \quad (5.2.4)$$

Thus, the maximum roughness scales by

$$R_{2,\text{max}} = \int_{t_1}^{t_N} \left| \frac{d^2 s}{dt^2} \right|^2 dt \sim N \left(\frac{4\epsilon}{\Delta t^2} \right)^2 \Delta t = 16N\Delta t^{-3}\epsilon^2 \quad (5.2.5)$$

$$R_{3,\text{max}} = \int_{t_1}^{t_N} \left| \frac{d^3 s}{dt^3} \right|^2 dt \sim N \left(\frac{8\epsilon}{\Delta t^3} \right)^2 \Delta t = 64N\Delta t^{-5}\epsilon^2 \quad (5.2.6)$$

For my example $\epsilon = 10^{-2}$ data, (5.2.6) predicts $R_{3,\text{max}} \sim 64 \cdot 10^3 \cdot 10^{10} \cdot 10^{-4} = 6.4 \times 10^{10}$, which agrees with the computed value of $R_{3,\text{max}} = 3.1 \times 10^{10}$ up to an $O(1)$ constant.

To improve upon the roughness scaling equations (5.2.5) and (5.2.6), consider the following Monte Carlo experiment. Create a data set of Gaussian noise, where $\tilde{y}(t_i) = \mathcal{N}(0, \epsilon^2)$, again $t_i = i \cdot \Delta t$ and $i = 1 \dots N$, and the true function is $y(t) = 0$, as with my scaling arguments. Now, fit a natural interpolating spline through that data ($E = 0$), and compute its roughness. By repeating this procedure several times, with several different N, ϵ , and Δt , I observe that on average

$$R_{2,\max} \approx 36N\Delta t^{-3}\epsilon^2 \quad (\text{cubic spline}) \quad (5.2.7)$$

$$R_{3,\max} \approx 31N\Delta t^{-5}\epsilon^2 \quad (\text{quintic spline}) \quad (5.2.8)$$

Surprisingly, the front-factors in formulae (5.2.7) and (5.2.8) appear to be insensitive to probability distribution. To show this, one may repeat the Monte Carlo experiment, this time drawing the random numbers from a uniform distribution on the range $\sqrt{3}\epsilon \cdot [-1, 1]$. (The front-factor, $\sqrt{3}\epsilon$, makes this probability distribution have a standard deviation of ϵ , which is equivalent to the above normal distribution.) Using the uniform distribution, one still finds that the roughness formulae (5.2.7) and (5.2.8) hold true. Practically speaking, the fact that the front-factors in (5.2.7) and (5.2.8) are insensitive to error probability distribution means that no matter how the measurement error actually is distributed, (5.2.7) and (5.2.8) still give a good estimate of the maximum roughness of the data. More importantly, since $R_{2,\max}$ and $R_{3,\max}$ can be computed for an experimental data set, equations (5.2.7) and (5.2.8) can be used to estimate the measurement error!

5.2.2 Comparison between `csaps` and the present method

Let us now compare my spline fitting method to the automated method in `csaps`. Since `csaps` can only fit cubic splines, I use cubic smoothing splines for the comparison herein.

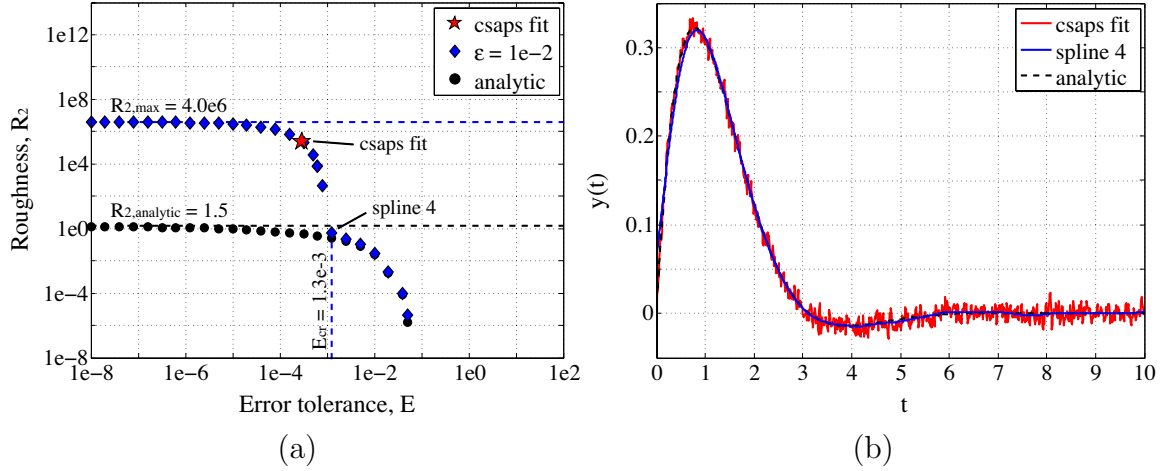


Figure 5-4: (a) Roughness, R_2 , versus error tolerance, E , of cubic splines fit to the example $\epsilon = 10^{-2}$ data. The spline fit by `csaps` has $E = 2.9 \times 10^{-4}$ and $R_2 = 2.5 \times 10^5$. (b) The spline fit by `csaps` is quite rough, whereas spline 4 smoothly approximates the analytic function.

An efficient frontier of minimum roughness cubic splines (fit to the $\epsilon = 10^{-2}$ data) versus error tolerance is shown in figure 5-4a. It exhibits a kink at, $E_{\text{cr}} = 1.3 \times 10^{-3}$, which is the same critical error tolerance as with the quintic smoothing splines (see figure 5-1b). This is to be expected, since the critical error tolerance scaling equation (5.2.2) does not depend on fit type. This kink allows one to select ‘spline 4’ as the best fit to the data using cubic smoothing splines, which yields a smooth curve in figure 5-4b.

Figure 5-4 illustrates that my method fits a smooth spline to the noisy data, whereas the present implementation of `csaps` does not. In this case, the smoothing parameter selected by `csaps` corresponds to an error tolerance lower than the critical value, which is why the `csaps` fit does not smooth the data adequately.

5.2.3 Predictive error

One final assessment of my spline fit I can make is to examine its *predictive error*, P , which is defined as the integral of the squared deviation between the smoothing

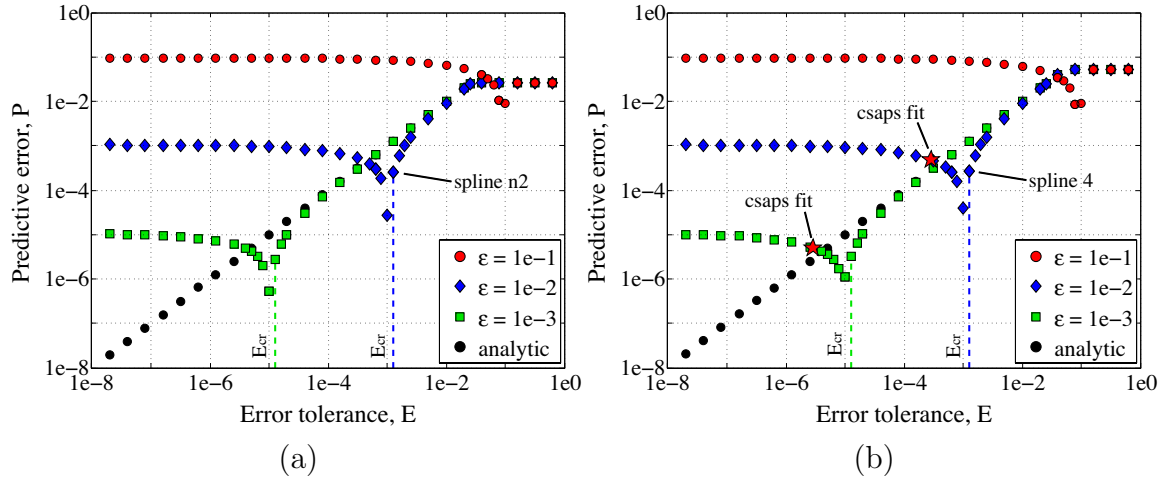


Figure 5-5: Predictive error, P , versus error tolerance, E , of splines fit to the example $\epsilon = \{10^{-1}, 10^{-2}, 10^{-3}\}$ data: (a) quintic splines, (b) cubic splines. The spline fit by `csaps` to the $\epsilon = 10^{-2}$ data has $E = 2.9 \times 10^{-4}$ and $P = 4.8 \times 10^{-4}$, and spline 4 has $E = 1.3 \times 10^{-3}$ and $P = 2.7 \times 10^{-4}$.

spline and the true function:

$$P(s) = \int_{t_1}^{t_N} |y(t) - s(t)|^2 dt \quad (5.2.9)$$

Since I know the true function in this analytical example, I can compute P for each spline on the $R(E)$ frontier. Plots of P versus E for the example analytic data are shown in figure 5-5. These plots show that, for both noise levels $\epsilon = \{10^{-2}, 10^{-3}\}$ and for both cubic and quintic splines, the spline with the critical error tolerance has nearly the minimum predictive error. The spline with the minimum P has slightly more roughness than the spline corresponding to E_{cr} . Thus, my definition of E_{cr} strikes a balance between minimizing predictive error and minimizing roughness.

These figures show that the ‘best’ spline fit, which is the one that balances both having the minimum predictive error and having the minimum roughness, is indeed the spline fit given by solving the Reinsch problem with an error tolerance of E_{cr} . In the next section, I describe a method for automating the process of determining E_{cr} and finding the best fit spline for a given data set.

5.3 Automated algorithm

In this section, I describe an algorithm for automatically selecting the best spline fit for a given set of experimental data. The ‘best’ smoothing spline is the one generated by solving the Reinsch problem with $E = E_{\text{cr}}$, which corresponds to the point on the $R(E)$ frontier that has the maximum positive curvature in log-log space. To find this point of maximum curvature, I employ a procedure inspired by the ‘bisection method’ of root finding (Recktenwald, 2000). The general idea is to create a stencil of trial E values, solve the Reinsch problem for each E in the stencil, compute the roughness of each resulting spline, use these roughness values to estimate the curvature of the $R(E)$ frontier, select the stencil point with the maximum positive curvature, refine the resolution of the stencil in the neighborhood of the selected point, and iterate until the stencil becomes acceptably fine.

In order to have three choices for the point on the $R(E)$ frontier that has maximum positive curvature, I employ a five-point stencil. The endpoints of this stencil must bound E_{cr} , and the central point should be at a good initial guess for E_{cr} . I can make such a guess by combining equation (5.2.2) with (5.2.7) or (5.2.8) to yield

$$E_{\text{cr,guess}} = \frac{R_{2,\text{max}}}{36\Delta t^{-4}} \quad (\text{cubic spline}) \quad (5.3.1)$$

$$E_{\text{cr,guess}} = \frac{R_{3,\text{max}}}{31\Delta t^{-6}} \quad (\text{quintic spline}) \quad (5.3.2)$$

where $R_{2,\text{max}}$ or $R_{3,\text{max}}$ is found by computing the roughness of the natural interpolating spline fit through the data.

In order to determine the endpoints of the initial E stencil, we must bound error tolerance. The lower bound for E is, of course, zero. However, it is more practical to implement a finite value, say 10^{-14} , which is two orders of magnitude larger than the typical machine zero and yields stable behavior. An upper bound for the error tolerance, E_{ub} , in the cubic/quintic case is the error tolerance that allows

`spaps` to fit the data using linear/quadratic piecewise polynomials, which have zero second/third derivative and hence zero roughness. Since it is possible to fit data with less error using piecewise linear/quadratic polynomials rather than using a single linear/quadratic polynomial fit to the entire data set, the single polynomial can be used to compute an upper bound for the error tolerance. Thus, E_{ub} is found by performing a linear/quadratic least squares fit to the entire data set and computing the error of that curve.

Using the upper and lower bounds as the endpoints of the initial E stencil, a five-point stencil is generated with

$$\begin{aligned} E_1^1 &= 10^{-14} \\ E_2^1 &= \sqrt{10^{-14} \cdot E_{\text{cr,guess}}} \\ E_3^1 &= E_{\text{cr,guess}} \\ E_4^1 &= \sqrt{E_{\text{cr,guess}} \cdot E_{\text{ub}}} \\ E_5^1 &= E_{\text{ub}} \end{aligned}$$

where the superscript indicates iteration number and the subscript indicates stencil point number. The value of E_2^1 is set such that $\log_{10} E_2^1 = \frac{1}{2}(\log_{10} E_1^1 + \log_{10} E_3^1)$ (i.e. $\log_{10} E_2^1$ bisects its neighbors). Since we are searching for a particular E value between a finite E_{ub} and zero, and since the roughness values of these splines span several orders of magnitude, it is appropriate to work in log-log space.

The roughness of each point in the stencil is computed as follows: for each E_j^1 ($j = 1, \dots, 5$), find the corresponding smoothing spline using `spaps(t, \tilde{y}, E_j^1)`, compute its derivatives, and compute the roughness, R_j^1 . The curvatures (in log-log space) at

points $j = 2, 3$, and 4 are estimated using divided differences

$$\left[\frac{d(\log_{10} R)}{d(\log_{10} E)} \right]_{E=E_j^1} = \frac{\frac{\log_{10}(R_{j+1}^1) - \log_{10}(R_j^1)}{\log_{10}(E_{j+1}^1) - \log_{10}(E_j^1)} - \frac{\log_{10}(R_j^1) - \log_{10}(R_{j-1}^1)}{\log_{10}(E_j^1) - \log_{10}(E_{j-1}^1)}}{\frac{1}{2}(\log_{10}(E_{j+1}^1) - \log_{10}(E_{j-1}^1))} \quad (5.3.3)$$

The stencil is then refined in the neighborhood of the point that has the maximum positive curvature. If the maximum curvature lay at point p in the k^{th} iteration, then the stencil for the $(k + 1)^{\text{th}}$ iteration would be:

$$\begin{aligned} E_1^{k+1} &= E_{p-1}^k \\ E_2^{k+1} &= \sqrt{E_{p-1}^k \cdot E_p^k} \\ E_3^{k+1} &= E_p^k \\ E_4^{k+1} &= \sqrt{E_p^k \cdot E_{p+1}^k} \\ E_5^{k+1} &= E_{p+1}^k \end{aligned}$$

such that point E_p^k becomes the center of the new stencil, and points E_2^{k+1} and E_4^{k+1} bisect points from the previous stencil in log space.

The double-bisection procedure iterates until the resolution of stencil is deemed precise enough. In the present implementation, when the criterion

$$\left| \frac{\log_{10} E_3^k - \log_{10} E_4^k}{\log_{10} E_4^k} \right| < 1\%$$

is satisfied, E_4^k is selected as the error tolerance corresponding to the ‘best’ fit smoothing spline. For $N \sim O(10^3)$ and $\epsilon \sim O(10^{-2})$, this typically requires less than ten double-bisection iterations, which corresponds to solving the **spaps** problem for less than 25 smoothing splines in total. Evaluating **spaps** is computationally-intensive and accounts for most of the computing time of the algorithm. In the double-bisection algorithm, three of the points from the previous stencil carry over, so only two new

smoothing splines need to be determined during each iteration. Using the present double bisection procedure automates curve fitting process. Of course, if a researcher were to fit a smoothing spline manually, it would be prudent to compute the entire $R(E)$ frontier and to manually choose the spline at the critical error tolerance.

5.4 Experimental example

To demonstrate the utility of the present spline fitting method, I use a physical example derived from the high speed video analysis of a sphere falling through water. In this laboratory experiment, a standard billiard ball is dropped into a quiescent pool of water, as shown in figure 5-6. The velocity and acceleration of the ball must be determined from the derivatives of the position data. Further details of the physics involved with this water entry problem can be found in references (Truscott and Techet, 2009; Truscott et al, 2010).

The goal of the experiment is to find the unsteady force coefficient (i.e. the net hydrodynamic force, normalized by the instantaneous dynamic pressure force (Kundu and Cohen, 2004))

$$C_F(t) = \frac{F(t)}{\frac{1}{2}\rho[V(t)]^2A} \quad (5.4.1)$$

where $F(t) = ma(t) + mg$ is the net force on the billiard ball, $m = 0.17$ kg is the ball mass, $a(t) = \frac{d^2\tilde{y}(t)}{dt^2}$ is the instantaneous acceleration of the ball, $g = 9.8$ m/s² is the acceleration due to gravity, $\rho = 1000$ kg/m³ is the density of water, $V(t) = \frac{d\tilde{y}(t)}{dt}$ is the instantaneous velocity of the ball, $A = \pi(\frac{d}{2})^2 = 0.0026$ m² is the cross-sectional area of the ball, and $d = 0.057$ m = 2.25 inches is the ball diameter. In order to compute the force coefficient accurately, we must accurately evaluate the first and second derivatives of the measured $\tilde{y}(t)$ position data.

In the present experiment, a high-speed digital camera acquired $N = 230$ still images at 1000 frame/s ($\Delta t = 0.001$ s) as the ball plunged into the basin. The

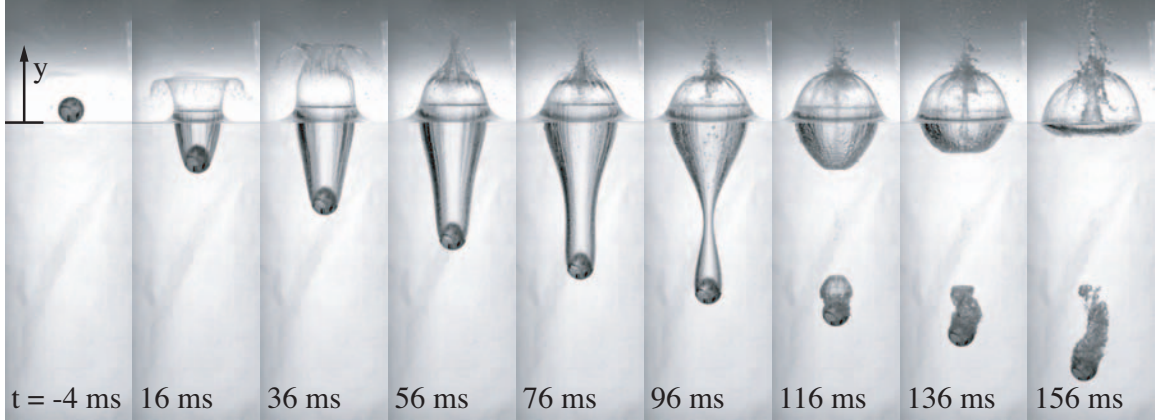


Figure 5-6: A billiard ball falls into a quiescent pool of water. Position, y , is measured in each timestep, t , by inspection of the images.

position of the center of the billiard ball, $\tilde{y}(t)$, is measured in meters above the quiescent free surface, and time, t , is measured in seconds after impact. (Note that the timing of the camera is accurate to within nanoseconds, so I assume the time of each measurement to be exact.) The image cross-correlation procedure used to acquire the $\tilde{y}(t)$ position data is explained in detail in (Truscott et al, 2010). Suffice it to say that the procedure yields position with sub-pixel accuracy, and since the optical zoom was 0.762 mm/px, I expect the measurement error to be on the order of $\epsilon \sim O(10^{-1})$ mm.

The experimental $\tilde{y}(t)$ position data are shown in figure 5-7a. (Note that the abscissa represents *time*, so this is the trajectory of the ball in time. The ball falls nearly straight down in space.) The data are very well resolved in time and evolve smoothly; every fifth data point is shown.

5.4.1 Application of the present spline fitting method

The present spline fitting method is now used to determine the velocity and acceleration from the position data. The minimum roughness versus error tolerance frontier is shown in figure 5-7b for quintic splines. Quintic splines must be used in

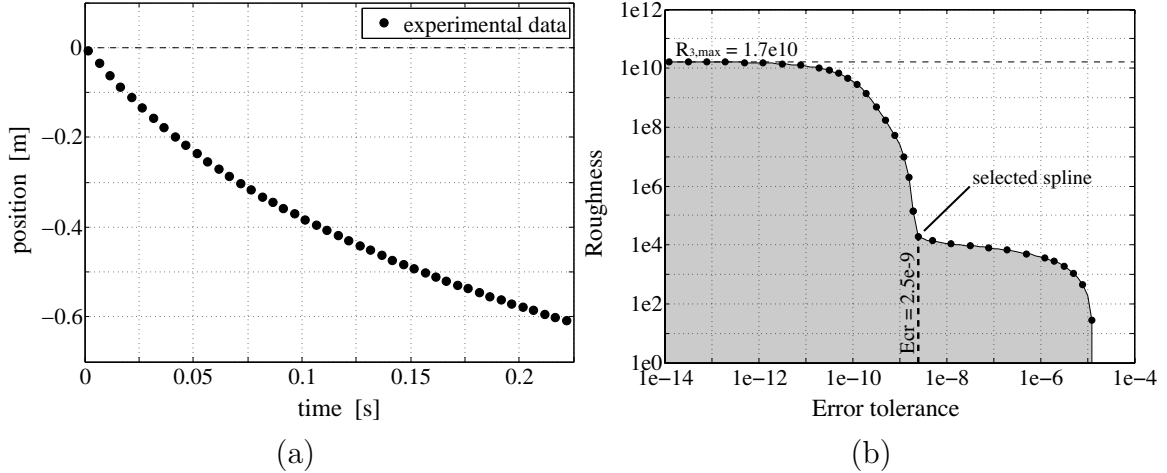


Figure 5-7: (a) Position of the billiard ball as a function of time, $\tilde{y}(t)$. Every fifth data point is shown. (b) Roughness of quintic smoothing splines, R_3 , versus error tolerance, E . The kink in this $R(E)$ frontier is at critical error tolerance, $E_{cr} = 2.5 \times 10^{-9}$.

order to obtain a smooth second derivative (i.e. acceleration). This chart shows a kink at critical error tolerance $E_{cr} = 2.5 \times 10^{-9}$. The roughness increases six orders of magnitude as E is decreased below E_{cr} . The maximum roughness, which corresponds to the interpolating spline ($E = 0$), is $R_{3,\max} = 1.7 \times 10^{10}$. It is expected that the smoothing spline corresponding to the critical error tolerance contains very little noise due to measurement error and best approximates the true $y(t)$ curve.

The maximum roughness equation (5.2.8) and critical error tolerance equation (5.2.2) can be used to derive estimates of the error in our experimental measurement of ball position:

$$\begin{aligned}\epsilon &\approx \sqrt{\frac{R_{3,\max}}{31N\Delta t^{-5}}} = 0.048 \text{ mm} \\ \epsilon &\approx \sqrt{\frac{E_{cr}}{N\Delta t}} = 0.11 \text{ mm}\end{aligned}$$

These estimates agree up to the $O(1)$ scaling factor in (5.2.2), and they are equivalent to about 0.1% of the ball diameter. Also note that $0.11 \text{ mm} = 0.14 \text{ px}$, so this estimate agrees with the assertion that our experimental procedure has sub-pixel accuracy.

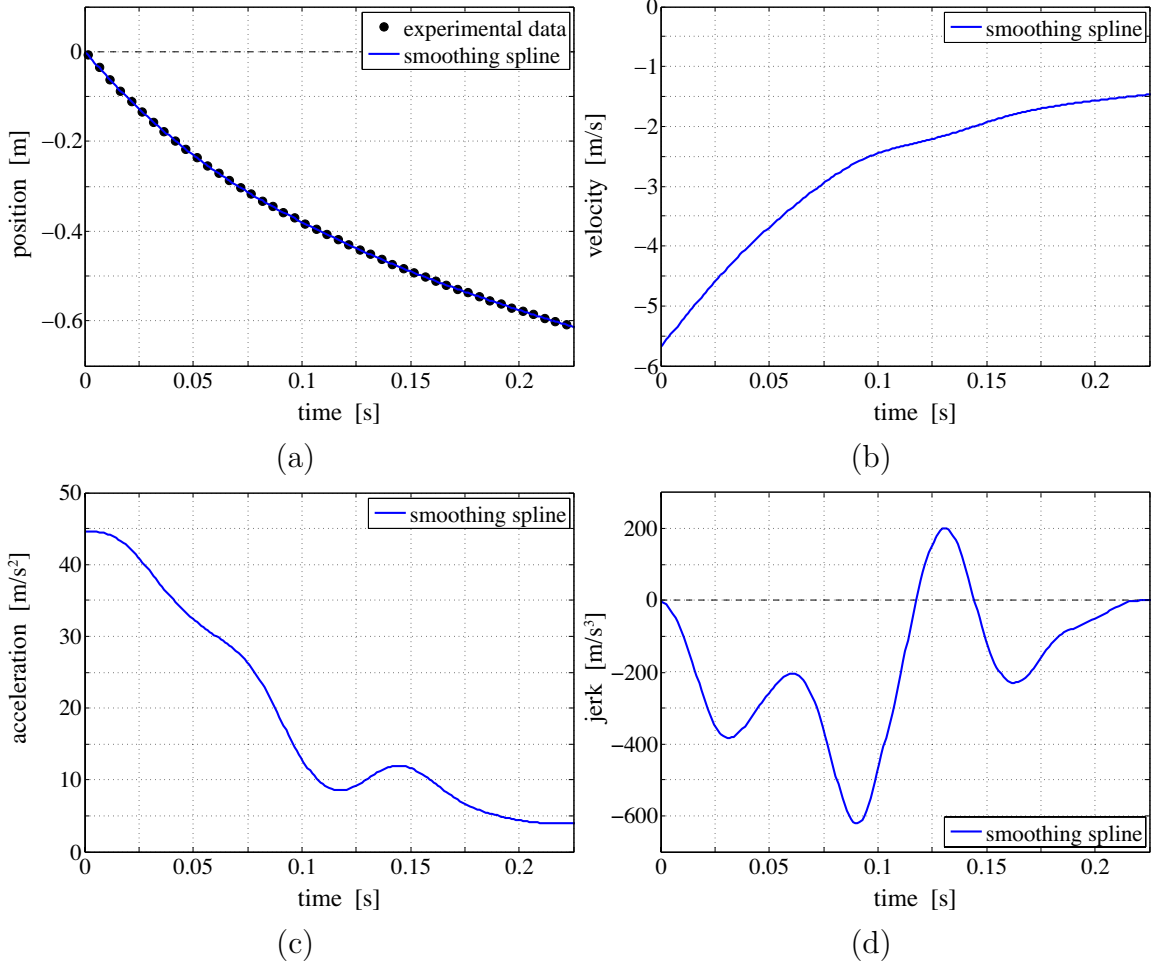


Figure 5-8: The selected smoothing spline fit, $s(t)$, and its derivatives $s'(t)$, $s''(t)$, and $s'''(t)$. Note that the ball experiences more than $4g = 39 \text{ m/s}^2$ acceleration at impact: An aggressive roller coaster may subject its passengers to $4g$ at the bottom of the first drop (Bibel, 2008).

The selected spline fit and its derivatives are shown in figure 5-8. Note that the y coordinate is defined positive *upwards*: The ball falls downwards, so its velocity is less than zero, and it accelerates upwards (i.e. its downward speed decreases over time), so its acceleration is greater than zero. The smoothing spline, as well as its three derivatives, all evolve smoothly in time, which is expected in a physical system which evolves smoothly. The only physically unrealistic feature of these curves is the slope of the acceleration at time $t = 0$ (and therefore, also the value of the jerk, $s'''(t = 0)$). This implies physically that the net force is unchanging at the moment of impact,

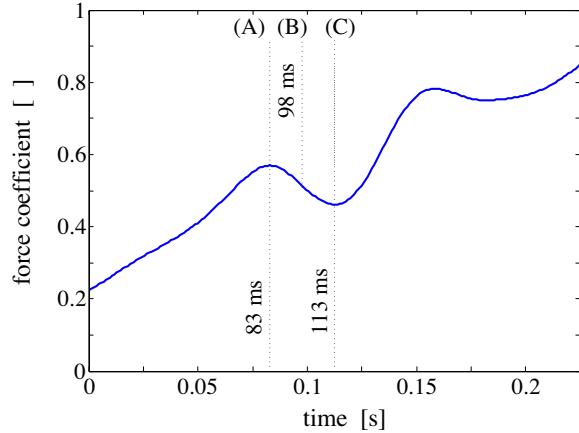


Figure 5-9: Force coefficient versus time for the billiard ball water entry experiment: (A) local maximum force coefficient; (B) pinch-off; and (C) local minimum force coefficient.

which is obviously not true. This result occurred because the quintic spline fitting procedure requires that $s'''(t) = 0$ at the endpoints. Therefore, these portions of the $s''(t)$ and $s'''(t)$ curves are simply ignored. The velocity and acceleration can now be used to compute the net hydrodynamic force on the billiard ball.

Figure 5-9 shows the force coefficient (5.4.1) during the water entry event². For reference, the force coefficient for a ball of the size and speed in this experiment, when immersed in a free stream of steadily-flowing water, is about 0.2 - 0.5 (Kundu and Cohen, 2004). The data in figure 5-9 show that the force coefficient increases from initial water impact until time $t = 83$ ms. Between 83 ms and 113 ms, the force coefficient drops dramatically during the cavity pinch-off process; cavity pinch-off occurs at $t = 98$ ms (just after the sixth image shown in figure 5-6). A local minimum of force coefficient occurs at $t = 113$ ms, as the lower cavity sheds from the sphere and begins to disintegrate into bubbles. Further discussion of the fluid dynamics can be found in Chapter 6.

²Since the ball slows down during the course of the experiment, the expected force decreases. Thus, examining the force (in physical units) is not as insightful as examining the non-dimensional force coefficient.

5.4.2 A check for the derivatives $s'(t)$, $s''(t)$, and $s'''(t)$

It is desirable to perform a check on the derivatives of the smoothing spline, which I can do by comparing them to estimates made from the noisy experimental data. For this, we need a regression technique which behaves like a non-parametric model -- one in which the fitting parameters are free to change along the length of the curve.

As a check of the first derivative, a line may be fit to a small window of data using least squares regression. The slope of this line represents the ‘slope’ of the data at the center of the window³. Mathematically, to find the first derivative of $\tilde{y}(t)$ data at time, t_i , fit a line $(a_1 t + a_2)$ to the data within the window $[t_{i-w}, t_{i+w}]$. The width of the window is $2w+1$ data points, where a larger w yields more smoothing of the data but a less localized estimate. The first derivative of this linear polynomial (namely a_1) is the estimate of the first derivative at time, t_i . This process would be repeated with the window centered at each $t_{w+1} \leq t_i \leq t_{N-w}$ to obtain the derivative estimate for each time. Since this procedure involves performing a least squares fit to a small window of data, I call this *windowed least squares* (WLS).

Higher order derivatives can also be estimated using windowed least squares. At each discrete time, a least squares linear polynomial fit gives an estimate of the first derivative at that time, a quadratic polynomial fit gives an estimate of the second derivative, a cubic polynomial fit gives an estimate of the third derivative at that time, and so on. The windowed least squares fit types and derivative estimates are summarized in table 5.1, and the estimates of the first and second derivatives are shown in figure 5-10. These data agree quite well with the derivatives of the smoothing spline, as expected.

The windowed least squares method provides a good estimate of the derivatives of the function, because the general trend of the data surrounding each point is captured by the least squares regression technique. However, this method does not ensure that

³This is equivalent to performing a Taylor series expansion about the center of the data window.

Table 5.1: Windowed least squares estimates of the first, second, and third derivatives of noisy $\tilde{y}(t)$ data.

windowed least squares fit	derivative estimate
linear: $a_1 t + a_2$	$y'_{\text{wls}}(t) \approx a_1$
quadratic: $a_1 t^2 + a_2 t + a_3$	$y''_{\text{wls}}(t) \approx 2 \cdot a_1$
cubic: $a_1 t^3 + a_2 t^2 + a_3 t + a_4$	$y'''_{\text{wls}}(t) \approx 3 \cdot 2 \cdot a_1$

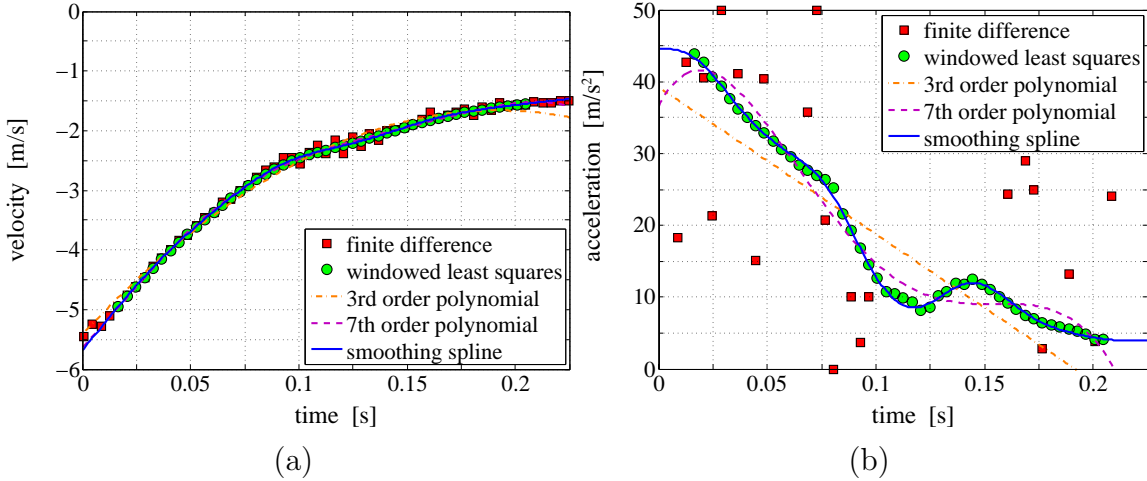


Figure 5-10: Velocity, $y'(t)$, and acceleration, $y''(t)$, computed by: finite difference, ‘■’; windowed least squares, ‘●’; third-order polynomial least squares fit to the entire data set, ‘---’; seventh-order polynomial least squares fit to the entire data set, ‘--’; and the selected smoothing spline, for which $E = E_{\text{cr}}$, ‘—’.

the derivative is a smooth function as the window is moved along the data set. It also fails to predict the derivative near the ends of the data interval ($t_i < t_{w+1}$ and $t_i > t_{N-w}$), since the window would then extend beyond the interval of available data.

Two less accurate methods for estimating the derivatives are also shown in figure 5-10: least squares regression to the entire data set, and finite differences. The derivatives of a least squares regression to all the data are inherently questionable, because the fitting parameters depend on the entire data set. Clearly, one cannot assume that the dynamics of our billiard ball during early times (e.g. during cavity formation) are the same as the dynamics during later times (e.g. after cavity collapse). Fitting a single polynomial to all of the data implicitly demands that the physics at

all times be the same, which is clearly not true in this experiment.

It would be appropriate to fit a polynomial to all of the data (using least squares) if the physics were the same throughout the experiment and the form of the true function is known (e.g. a quadratic polynomial fit to position data of a ball falling in a vacuum). However, if the form of the true function is unknown (which is usually the case in scientific research), then this method can give misleading results. For example, both 3rd-order and 7th-order polynomials fit well to all of the position data in the billiard ball example problem. However, their second derivatives are quite different, and neither agrees with the smoothing spline prediction or windowed least squares estimate (see figure 5-10b). From the present smoothing spline approach, it is clear that the acceleration of the sphere is not linear throughout its fall. The 7th order fit at least gives a closer approximation of the acceleration than the 3rd order fit, which (in spite of it implying a linear acceleration) is all too often used in these types of experiments.

Finite difference methods amplify measurement noise, yielding poor estimates of derivatives. For example, the central divided difference formula predicts

$$\begin{aligned} \frac{d\tilde{y}(t_i)}{dt} &= \frac{\tilde{y}_{i+1} - \tilde{y}_{i-1}}{2\Delta t} + O(\Delta t^2) \\ &= \frac{y(t_{i+1}) - y(t_{i-1})}{2\Delta t} + \frac{\tilde{\epsilon}_{i+1} - \tilde{\epsilon}_{i-1}}{2\Delta t} + O(\Delta t^2) \\ &= \frac{dy(t_i)}{dt} + O\left(\frac{\epsilon}{\Delta t}\right) + O(\Delta t^2) \end{aligned} \quad (5.4.2)$$

where $O(\)$ denotes the order of magnitude of the error in the prediction. For a small timestep, $\Delta t \ll 1$, the measurement error, ϵ , is amplified. The noise is amplified again upon taking each successive derivative, yielding derivatives with unsatisfactorily-large error on the order of

$$\frac{d\tilde{y}}{dt} \sim O\left(\frac{\epsilon}{\Delta t}\right), \quad \frac{d^2\tilde{y}}{dt^2} \sim O\left(\frac{\epsilon}{\Delta t^2}\right), \quad \frac{d^3\tilde{y}}{dt^3} \sim O\left(\frac{\epsilon}{\Delta t^3}\right), \dots$$

Similarly, all finite difference methods amplify measurement noise, even when a larger time step is used⁴. This error amplification is quite noticeable in the acceleration estimates in figure 5-10b.

5.5 Conclusions

I have shown that performing data regression using smoothing splines is the best method for predicting instantaneous derivatives of noisy experimental data. It agrees well with the windowed least squares method, which is a good means to approximate these derivatives. Other methods, such as finite differences or fitting polynomials to the entire data set yield poor estimates.

Finding the derivative of noisy data amounts to fitting an analytic curve that best approximates the true function that the data represents. The MATLAB function `spaps(t, \tilde{y} , E)` fits a smoothing spline to given $\tilde{y}(t)$ data, with minimum roughness and error at most equal to E . I have presented a novel and robust method for selecting the value of the error tolerance, E , that produces the ‘best’ spline fit, one which follows the roughness of the true function but does not introduce roughness due to measurement error.

My method is based on two critical insights. First, by systematically exploring the $R(E)$ relationship implicit in the ‘Reinsch problem’, I discovered that the $R(E)$ frontier has a kink at a *critical error tolerance*, E_{cr} . Second, I showed both graphically and with scaling arguments that E_{cr} corresponds to the spline with the minimum error to the data possible without introducing roughness due to the noise in the data. In my analytical example, I also showed that the spline corresponding to E_{cr} has nearly

⁴Even if n timesteps are skipped on either side of the data point, the central difference formula predicts

$$\frac{dy(\tilde{t}_i)}{dt} = \frac{y(t_{i+n}) - y(t_{i-n})}{2n\Delta t} + O\left(\frac{\epsilon}{n\Delta t}\right) + O(n^2\Delta t^2)$$

which may never have satisfactorily-small error.

the minimum possible predictive error, P , which supports my claim that choosing an error tolerance of E_{cr} produces the best possible spline fit.

The critical error tolerance, E_{cr} , corresponds to the point on the $R(E)$ frontier with the maximum positive curvature (in log space). I automate finding E_{cr} for a given data set by using the double-bisection procedure developed herein. For experimental measurements with high-precision (small ϵ) and high-resolution (large N), my method robustly fits the data and yields the desired derivatives.

One extension of this work is to apply my methodology to two-dimensional data (e.g. measurements made along two spatial dimensions or measurements made along one spatial dimension over several timesteps). My method can also be extended to more complicated types of smoothing splines (e.g. with non-uniform knot locations, or with non-uniform weighting on the roughness). Examining a roughness versus ‘fitting parameter’ frontier, however, will remain as the hallmark of my methodology.

With the advent of high-speed, high-resolution imaging and data acquisition systems, researchers are able to acquire data with high temporal and spatial resolution, at very high precision. My method can be used to very-accurately regress these data and compute their first few derivatives.

5.6 Appendix: non-dimensional equations

Readers who prefer to consider the arguments made herein using non-dimensional quantities may normalize the data as follows:

$$\hat{y} = \frac{y}{Y} \quad \tilde{\hat{y}} = \frac{\tilde{y}}{Y} \quad \hat{\epsilon} = \frac{\epsilon}{Y} \quad \hat{t} = \frac{t - t_1}{T}$$

where Y is a reference length scale (such as the total distance traveled by the billiard ball) and $T = t_N - t_1$ is the duration of the measurement times. In non-dimensional form, the experimental data are: $\hat{y}_i = \hat{y}(\hat{t}_i) + \hat{\epsilon}_i$ (eqn. 5.1.1). The non-dimensional

error tolerance and roughness are

$$\hat{E} = \frac{E}{Y^2 T} \geq \int_0^1 |\hat{y}_i - \hat{s}(\hat{t}_i)|^2 d\hat{t} \quad (\text{eqn. 5.1.2})$$

$$\hat{R}_2 = \frac{R_2 T^3}{Y^2} = \int_0^1 \left| \frac{d^2 \hat{s}}{d\hat{t}^2} \right|^2 d\hat{t} \quad (\text{eqn. 5.1.3})$$

$$\hat{R}_3 = \frac{R_3 T^5}{Y^2} = \int_0^1 \left| \frac{d^2 \hat{s}}{d\hat{t}^3} \right|^3 d\hat{t} \quad (\text{eqn. 5.1.4})$$

and the non-dimensional critical error tolerance and maximum roughness are

$$\hat{E}_{\text{cr}} = \frac{E_{\text{cr}}}{Y^2 T} \sim \hat{\epsilon}^2 \quad (\text{eqn. 5.2.2})$$

$$\hat{R}_{2,\text{max}} = \frac{R_{2,\text{max}} T^3}{Y^2} \approx 36 N^4 \hat{\epsilon}^2 \quad (\text{eqn. 5.2.7})$$

$$\hat{R}_{3,\text{max}} = \frac{R_{3,\text{max}} T^5}{Y^2} \approx 31 N^6 \hat{\epsilon}^2 \quad (\text{eqn. 5.2.8})$$

These roughness formulae indicate that the total time interval, T , does not affect the prominence of the kink in the $R(E)$ curve; rather, the number of data points, N , and the non-dimensional error, $\hat{\epsilon}$, affect the prominence of the maximum roughness due to measurement error, versus the roughness of the true function itself.

I can also show that, in non-dimensional terms, error is amplified when estimating derivatives by finite difference schemes. The measured data have error on the order of $O(\hat{\epsilon})$. The central difference formula predicts

$$\frac{d\hat{y}(\hat{t}_i)}{d\hat{t}} = \frac{\hat{y}(\hat{t}_{i+1}) - \hat{y}(\hat{t}_{i-1})}{2\Delta\hat{t}} + O\left(\frac{\hat{\epsilon}}{\Delta\hat{t}}\right) + O(\Delta\hat{t}^2)$$

Since the non-dimensional time step is small, $\Delta\hat{t} = \frac{\Delta t}{T} = \frac{1}{N} \ll 1$, measurement noise is amplified by the finite difference procedure, $O\left(\frac{\hat{\epsilon}}{\Delta\hat{t}}\right)$.

This non-dimensionalization shows that as the temporal resolution of the measurements increases (i.e. as N increases) and as the measurement precision increases (i.e. as $\hat{\epsilon}$ decreases), the smoothing spline fit becomes more accurate.

Bibliography

- Bibel G (2008) Beyond the Black Box: the Forensics of Airplane Crashes John Hopkins University Press, p340.
- de Boor C (1978) A Practical Guide to Splines Springer.
- de Boor C (2008) MATLAB Spline Toolbox 3: User's Guide The MathWorks.
- Chung WL (1980) “Automatic curve fitting using an adaptive local algorithm,” ACM Transactions on Mathematical Software **6**(1):45–57.
- Craven P, Wahba G (1979) “Smoothing noisy data with spline functions: Estimating the correct degree of smoothing by the method of generalized cross-validation,” Numerische Mathematik **31**:377–403.
- Hurvich CM, Simonoff JS (1998) “Smoothing parameter selection in nonparametric regression using an improved akaike information criterion,” J R Statist Soc B **60**(2):271–293.
- Kohn R, Ansley CF (1987) “A new algorithm for spline smoothing based on smoothing a stochastic process,” SIAM J Sci Stat Comput **8**(1):33–48.
- Kundu PK, Cohen IM (2004) Fluid Mechanics Elsevier Academic Press.
- Pope SB, Gadh R (1988) “Fitting noisy data using cross-validated cubic smoothing splines,” Communications in Statistics - Simulation and Computation **17**(2):349–376.
- Recktenwald GW (2000) Numerical Methods with MATLAB: Implementations and Applications Prentice-Hall.
- Reinsch CH (1967) “Smoothing by spline functions,” Numerische Mathematik **10**:177–183.
- Silverman BW (1985) “Some aspects of the spline smoothing approach to non-parametric regression curve fitting,” J R Statist Soc B **47**(1).

Teanby NA (2007) “Constrained smoothing of noisy data using splines in tension,” Mathematical Geology **39**:41–434.

Truscott T, Techet A (2009) “Water entry of spinning spheres,” Journal of Fluid Mechanics **625**:135–165.

Truscott TT, Epps BP, Techet AH (2010) “Unsteady forces on spheres during water entry,” in preparation.

Wahba G (1990) Spline Models for Observable Data SIAM.

Wahba G, Wold S (1975) “A completely automatic french curve: Fitting spline functions by cross validation,” Communications in Statistics - Simulation and Computation **4**(1):1–17.

Wecker W, Ansley C (1983) “The signal extraction approach to non-linear regression and spline smoothing,” Journal of the American Statistical Association **78**:81–89.

Wood SN (2000) “Modelling and smoothing parameter estimation with multiple quadratic penalties,” J R Statist Soc B **62**(2):413–428.

Chapter 6

Unsteady forces on spheres during water entry

In this chapter, I consider the hydrodynamic forces acting on a billiard ball as it falls into a basin of water. This free-surface flow problem is of general interest to the U.S. Navy in the deployment of mines, underwater launching of torpedos, and in the design of surface-piercing projectiles. Industrial applications include those in which structural interactions with the water surface are important, such as ship slamming, loading on oil platforms in extreme waves, and ink jet printing. The case presented herein is but one of many experiments performed by Truscott (2009). The purpose of this chapter is to present a potential flow model that explains the unsteady forces on a sphere during a cavity-forming free-surface impact event.

I begin this chapter by applying the impulse-force framework derived in Chapter 1 to the free-surface water entry problem. I continue by developing a potential flow model for the flow and sub-surface air cavity created by the sphere during water entry. This allows us to examine the unsteady hydrodynamic forces acting on the sphere, and I compare these results to the theoretical forces on a sphere in an infinite fluid (with no surface and no cavity).

The impulse-force framework of this thesis states that the total force on a body is the sum of the vortex impulse force and the pressure impulse force acting on the body surface, $\mathbf{F} = \mathbf{F}_v + \mathbf{F}_p$. In a series of particle image velocimetry experiments, Truscott (2009) found that little vorticity is shed into the fluid while an air cavity exists behind the sphere. Thus, I assume the vorticity is a constant zero, $\omega = 0$, and I model the flow as solely potential flow, $\mathbf{u} = \nabla\phi$. In this case, the vortex impulse force is zero, $\mathbf{F}_v = 0$, and the total force on the sphere is given by the pressure impulse force $\mathbf{F} = \mathbf{F}_p$, which is given by equation (1.2.16) and is reproduced here

$$\mathbf{F}_p = -\frac{d}{dt} \left[\int_{S_b} \rho\phi \hat{\mathbf{n}} dS \right] \quad (1.2.16)$$

I now show that for potential flow, the force given by equation (1.2.16) is equivalent to integrating the pressure over the body surface (i.e. evaluating (1.0.2) directly). Since the body surface S_b moves with velocity \mathbf{u}_b , the time derivative in equation (1.2.16) is evaluated as follows

$$\mathbf{F}_p = - \int_{S_b} \rho \frac{\partial \phi}{\partial t} \hat{\mathbf{n}} dS - \int_{S_b} \rho (\hat{\mathbf{n}} \cdot \mathbf{u}_b) \nabla \phi dS \quad (6.0.1)$$

The second term in (6.0.1) can be manipulated by first making use of the no-through-flow boundary condition for the potential function ($\hat{\mathbf{n}} \cdot \mathbf{u}_b = \hat{\mathbf{n}} \cdot \nabla\phi$ on S_b), and then by employing the divergence theorem

$$\begin{aligned} \mathbf{F}_p &= -\rho \int_{S_b} \frac{\partial \phi}{\partial t} \hat{\mathbf{n}} dS - \rho \int_{S_b} (\hat{\mathbf{n}} \cdot \nabla\phi) \nabla\phi dS \\ &= \int_{S_b} \left(-\rho \frac{\partial \phi}{\partial t} - \frac{1}{2} \rho (\nabla\phi \cdot \nabla\phi) \right) \hat{\mathbf{n}} dS \\ &= \int_{S_b} (p_\infty - \rho \frac{\partial \phi}{\partial t} - \frac{1}{2} \rho |\nabla\phi|^2) \hat{\mathbf{n}} dS \end{aligned} \quad (6.0.2)$$

where p_∞ is the (constant) stagnation pressure (and the integral of a constant over the

body surface is zero). Note that (6.0.2) is simply the evaluation of (1.0.2), assuming inviscid flow, wherein viscous stresses are zero ($\mathbf{T} = 0$), and the pressure is given by unsteady Bernoulli's equation

$$p = p_\infty - \rho \frac{\partial \phi}{\partial t} - \frac{1}{2} \rho |\nabla \phi|^2 \quad (6.0.3)$$

In other words, the pressure impulse force is equivalent to integrating the pressure, as derived from potential flow, over the body surface.

In the sphere impact problem, gravitational effects must be considered as well, in which case the unsteady Bernoulli equation becomes

$$p = p_\infty - \rho \frac{\partial \phi}{\partial t} - \frac{1}{2} \rho |\nabla \phi|^2 - \rho g z \quad (6.0.4)$$

and the total force on the sphere is

$$\mathbf{F} = \int_{S_b} (p_\infty - \rho \frac{\partial \phi}{\partial t} - \frac{1}{2} \rho |\nabla \phi|^2 - \rho g z) \hat{\mathbf{n}} dS \quad (6.0.5)$$

Given the potential function that represents a fluid flow, $\phi(\mathbf{x}, t)$, one can use (6.0.4) and (6.0.5) to estimate the total force on the sphere. The problem now is to determine the potential function that describes the flow created by the water entry of the sphere.

It is important to reiterate here that the total instantaneous force on the sphere can be found from the position data measured during each sphere impact experiment by fitting a smoothing spline to the position data (using the method described in Chapter 5) and evaluating equation (5.4.1). This smoothing spline would yield the total force on the sphere (i.e. the answer) but does not afford any physical insight. In order to gain a deeper understanding of how the three components of pressure in (6.0.4) modulate the unsteady forces on the sphere, I created the potential flow model that is the subject of the remainder of this chapter.

6.1 Introduction

Free-surface impact of spheres has enamored the scientific community with its symmetry, beauty, and complexity for over a century. The first images of this phenomenon were recorded by Worthington (1908), while more recent studies include the parameters required for cavity formation (Duez et al, 2007) and a full characterization of the cavity dynamics (Aristoff and Bush, 2009) and (Duclaux et al, 2007). The hydrodynamic observations and measurements obtained from these studies can be applied to several problems in naval hydrodynamics. Early applied studies focused on the impact of float planes on the water surface (von Karman, 1929), torpedo water entry (May and Hoover, 1963), and general impact dynamics (Wagner, 1932), which was recently reviewed by (Korobkin and Pukhnachov, 1988). Typically, the studies that focus on the dynamics of water entry of spheres have chosen to keep all parameters constant while varying: impact speed (May and Hoover, 1963), atmospheric pressure (Gilbarg and Anderson, 1948), impact angle (Asfar and Moore, 1987), or surface treatment (Duez et al, 2007). Most studies have focused on the growth of the cavity and the pinch-off location (Birkhoff and Isaacs, 1951), (Glasheen and McMahon, 1996), (Lee et al, 1997) and (Bergmann et al, 2009) for both spheres and disks.

The impact of a sphere with the free surface may or may not create an air cavity, depending on the impact speed and surface treatment, and the unsteady forces acting on the sphere depend upon whether or not this cavity is formed (Truscott, 2009). Experimental measurement of these forces is difficult, because it requires finding the acceleration of the sphere. This could be done in one of two ways, each of which are challenging: (1) Imbedding an accelerometer in the sphere (and measuring acceleration directly) would require much effort to repair and reshape the surface to remove any parting line or scarring that may otherwise confound experimental results, or (2) Inferring acceleration from position is also non-trivial, as discussed

in Chapter 5, as it requires high-precision high-resolution position data. We choose option (2). Through the use of high-speed imaging, position measurement using an image processing technique with sub-pixel accuracy, and the novel smoothing-spline-fitting method presented in Chapter 5, we are now able to infer the unsteady forces acting on the sphere. Further, by developing a 3D axisymmetric potential flow model, we are also able to explain the origin of the forces acting on the sphere.

The billiard ball case discussed in Chapter 5 and again presented herein is one from a larger study conducted in collaboration with Truscott (2009). Results of this broad study demonstrate the effects of (1) surface treatment: hydrophobic treatments enhance cavity formation, whereas hydrophilic treatments inhibit cavity formation; and (2) mass ratio (sphere density / water density): heavy spheres experience little deceleration, whereas light spheres undergo large decelerations. The purpose of this chapter is to describe the physics of the hydrophobic (cavity forming) cases. A potential flow model is derived, and this model well describes the results of experiments within a wide range of mass ratios. The billiard ball has a moderate mass ratio ($m^* = 1.8$), and this case is representative of the results of the broad study. The billiard ball case is presented and discussed at length, and then other cases are presented to highlight the effect of mass ratio. This chapter also demonstrates the application of the theoretical framework of this thesis to a hydrodynamics problem dominated by potential flow effects.

6.2 Materials and methods

This experiment consists of dropping different types of spheres from varying heights into a large tank of water. An extensive experimental study was performed with spheres of varying materials, diameters, and impact speeds. The key experimental parameters for each of the trials presented herein are listed in table 6.1. Note that the

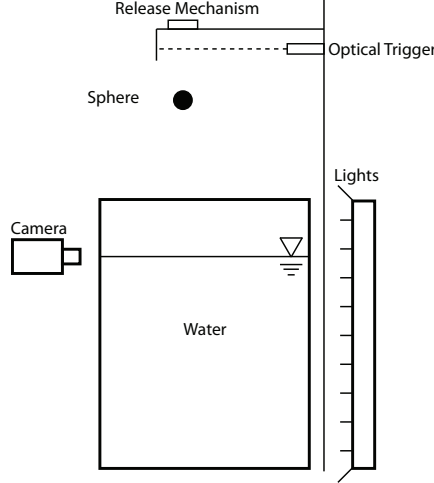


Figure 6-1: Experimental setup: The tank is made with a steel frame and 1-inch thick acrylic, measures $91 \times 152 \times 152$ cm, and holds 2200 L of water. The sphere falls freely into the tank, and a high-speed camera images the event.

Case	m^* $\frac{\rho_s}{\rho}$	D [m]	U_0 [m/s]	θ_s [deg]	Re $\frac{U_0 D}{\nu}$	Fr $\frac{U_0^2}{g D}$	We $\frac{\rho U_0^2 D}{\sigma}$	Bo $\frac{\rho g D^2}{\sigma}$
Acrylic (PIV)	1.2	0.02540	3.43	120	8.71e4	47.2	4.27e3	90.4
Acrylic	1.2	0.02540	3.43	120	8.71e4	47.2	4.27e3	90.4
Billiard	1.8	0.05715	5.67	120	3.24e5	57.3	2.63e4	458
Ceramic	3.9	0.02540	3.43	120	8.71e4	47.2	4.27e3	90.4
Steel	7.8	0.02540	3.43	120	8.71e4	47.2	4.27e3	90.4

Table 6.1: Table of experimental parameters: mass ratio m^* ; diameter D ; impact speed U_0 ; static wetting angle θ_s ; Reynolds number Re ; Froude number Fr ; Webber number We ; and Bond number Bo ; where the properties of water used are: density $\rho = 1000$ kg/m³, kinematic viscosity $\nu = 10^{-6}$ m²/s, and surface tension $\sigma = 0.07$ N/m, and the acceleration due to gravity is $g = 9.81$ m/s².

sphere diameter and impact speed (as derived from the drop height) are the same for all cases except the billiard ball case. The acrylic, ceramic, and steel cases represent a controlled study of the effects of mass ratio. The acrylic sphere was dropped once while imaging using flood lighting and again while imaging a 2D PIV laser sheet (see (Truscott, 2009) for details regarding the particle image velocimetry experimental setup); these two trials have the same experimental parameters, and the PIV trial demonstrates the lack of vorticity shed by the sphere during the event.

The data required for the potential flow model are three time-series: (1) sphere position, (2) sphere velocity, and (3) cavity shape. Smoothed position and velocity data were determined from the raw position data using a smoothing spline that was fit by the method presented in Chapter 5. The methods of image acquisition and processing used to find the sphere position and cavity shape are detailed in (Truscott, 2009) and are summarized as follows.

A high speed camera (IDT XS-3 CCD) was used to record each of the falling spheres at 1000 frames/sec (fps). The image resolution was 756×1260 pixels and the field of view was 57.61×96.01 cm yielding a 13.12 px/cm magnification. The position of the sphere was located in each image with sub-pixel accuracy using a cross-correlation procedure similar to that used in particle image velocimetry. First, we performed a cross-correlation between a template image of the sphere and the image of interest. The cross-correlation returns a matrix of values (-1 to 1) indicating the most likely position of the sphere in the image (to the nearest pixel). Next, the cross-correlation data surrounding the most likely location of the sphere are fit with Gaussian curves in both the vertical and horizontal directions, and the peaks of these fits locate the position of the sphere. This method is highly accurate; it was shown in Chapter 5 that the estimated error for the position data in the billiard ball case was on the order of 0.14 px.

The cavity shape was determined for each image using a Canny edge finding image processing technique, which detects the highly contrasted edges of the cavity, as viewed in figure 6-4. These position and cavity shape data were shifted such that the undisturbed free-surface is at zero height ($z = 0$), and time is zero when the center of the sphere crosses the undisturbed free surface. That is, when the sphere is centered about the undisturbed free-surface height, it is said to be at $(r, z, t) = (0, 0, 0)$. Further details of these procedures will be published in (Truscott et al, 2010).

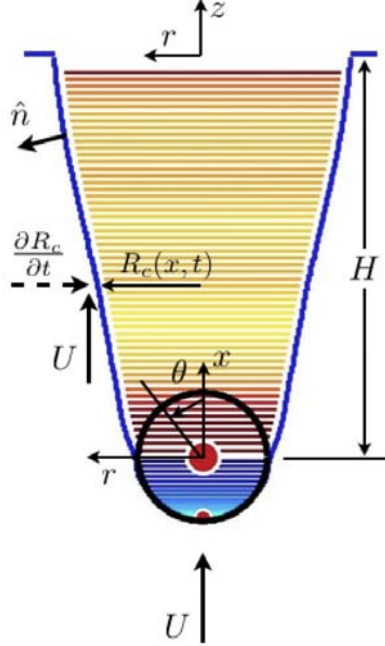


Figure 6-2: Illustration of the potential flow model, showing the sphere at depth H . In the sphere frame of reference, the free-stream velocity is U , and the cavity grows behind the sphere.

6.3 Potential flow model

The cavity model described herein requires the following experimental data as input: depth and velocity of the sphere, $H(t)$ and $U(t)$ (which are given from the selected smoothing spline); and cavity geometry, $R_c(x, t)$, which is given from inspecting the cavity shapes in the raw images acquired during the experiment.

The model assumes that viscous forces and surface tension forces are negligible, and that the flow can be modeled as ideal, axisymmetric flow. Also, it is assumed that the pressure in the cavity is atmospheric, since the dynamic pressure required to draw air into the cavity is negligible. It is important to note that the potential flow model is fully three-dimensional (3D), but since it is axisymmetric, we only concern ourselves with the meridional plane.

To facilitate the algebra, two reference frames are used: the sphere frame (x, r) with origin at the center of the sphere, and the lab frame (z, r) with origin fixed at

the undisturbed free surface. It is assumed that the sphere did not deviate laterally during the impact event, so the radial direction is synonymous for both coordinate systems. Figure 6-2 shows that the axial directions are coincident $\hat{e}_x = \hat{e}_z$ and that the mapping between the coordinate systems is $x = z + H$. For clarity, the cavity model is presented using dimensional units of the images (length measured in pixels and time measured in frames elapsed), but the final force coefficients are properly non-dimensionalized.

The velocity potential is modeled using 3D axisymmetric singularities located in the cavity (i.e. out of the fluid). As such, the total velocity potential is the sum of that from a *doublet*, *point source*, and N *ring sources*:

$$\phi = \phi_d + \phi_p + \sum_{i=1}^N \phi_{s_i} \quad (6.3.1)$$

as illustrated in figure 6-2. The total fluid velocity in the meridional plane is

$$\vec{u} = u \hat{e}_x + v \hat{e}_r = \nabla \phi \quad (6.3.2)$$

which has contributions from the *doublet*, *point source*, and N *ring sources*.

The potential function and fluid velocity at field point (x, r) induced by a 3D *doublet* located at $(x = 0, r = 0)$ are

$$\phi_d(x, r) = Q_d \cdot \frac{x}{(x^2 + r^2)^{3/2}} \quad (6.3.3)$$

$$u_d(x, r) = Q_d \cdot \frac{r^2 - 2x^2}{(x^2 + r^2)^{5/2}} \quad (6.3.4)$$

$$v_d(x, r) = Q_d \cdot \frac{-3xr}{(x^2 + r^2)^{5/2}} \quad (6.3.5)$$

where $Q_d = \frac{UR^3}{2}$ is the strength of the doublet, as prescribed by the potential flow around a sphere in infinite fluid.

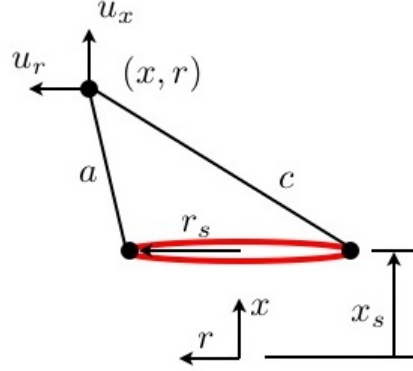


Figure 6-3: Illustration of a 3D ring source.

The *point source* and N *ring sources* effectively form a *source sheet* that corrects for the presence of the sub-surface air cavity.

The potential function and fluid velocity at field point (x, r) induced by a *3D point source* located at $(x = -x_p, r = 0)$ are

$$\phi_p(x, r) = Q_p \cdot \frac{-1}{4\pi((x + x_p)^2 + r^2)^{1/2}} \quad (6.3.6)$$

$$u_p(x, r) = Q_p \cdot \frac{x + x_p}{4\pi((x + x_p)^2 + r^2)^{3/2}} \quad (6.3.7)$$

$$v_p(x, r) = Q_p \cdot \frac{r}{4\pi((x + x_p)^2 + r^2)^{3/2}} \quad (6.3.8)$$

where Q_p is the volume flow rate out of the point source. Herein, $x_p = R - R_{\text{inset}}$, where $R = 37.5\text{px}$ is the sphere radius, and we choose $R_{\text{inset}} = 2\text{px}$.

Consider the potential function and fluid velocity at field point (x, r) induced by a *3D ring source* of strength Q_s , radius r_s , and axial position $x = x_s$. The volume flow rate out of the ring source is, by construction, Q_s . The potential function is found by integrating that of 3D point sources of strength $Q_s/(2\pi r_s)$ distributed about the circumference of the ring

$$\phi_s(x, r) = \int_0^{2\pi} \frac{-[Q_s/(2\pi r_s)]}{4\pi((x - x_s)^2 + (r - r_s \cos \beta)^2 + (r_s \sin \beta)^2)^{1/2}} \cdot r_s d\beta$$

After much algebra, one obtains

$$\phi_s(x, r) = Q_s \cdot \frac{-K}{2\pi^2 a} \quad (6.3.9)$$

$$u_s(x, r) = Q_s \cdot \frac{(x - x_s)E}{2\pi^2 c^2 a} \quad (6.3.10)$$

$$v_s(x, r) = Q_s \cdot \frac{(r^2 - r_s^2 - (x - x_s)^2)E + c^2 K}{4\pi^2 r c^2 a} \quad (6.3.11)$$

where Q_s is the volume flow rate out of the ring source,

$$a = \sqrt{(x - x_s)^2 + (r - r_s)^2}$$

$$c = \sqrt{(x - x_s)^2 + (r + r_s)^2}$$

$$m = \frac{c^2 - a^2}{a^2}$$

$$K = \bar{K}(-m) = \sqrt{m+1} \bar{K}\left(\frac{m}{m+1}\right)$$

$$E = \bar{E}(-m) = \sqrt{m+1} \bar{E}\left(\frac{m}{m+1}\right)$$

and \bar{K} and \bar{E} are complete elliptic integrals of the first and second kinds, respectively Abramowitz and Stegun (1972).

The layout of the ring sources is as follows. For ring sources in the sphere,

$$r_s = (R - R_{\text{inset}}) \sin \theta \quad (6.3.12)$$

$$x_s = (R - R_{\text{inset}}) \cos \theta \quad (6.3.13)$$

where $\theta = [91^\circ, 96^\circ, \dots, 179^\circ]$ and $R_{\text{inset}} = 2\text{px}$. For ring sources in the cavity,

$$r_s = R_c(x_s, t) - R_{\text{inset}} \sqrt{1 + \left(\frac{\partial R_c(x_s, t)}{\partial x}\right)^2} \quad (6.3.14)$$

$$x_s = [1, 2, \dots, N_c] \cdot \delta x \quad (6.3.15)$$

where $\delta x = 1\text{px}$, and N_c is the number of sources in the cavity.

The $R_c(x, t)$ data were prepared as follows. The raw cavity shape data, $\tilde{R}_c(x, t)$, were obtained from the high-speed image sequence using a Canny edge-detection algorithm. The raw $\tilde{R}_c(x, t)$ data for each time step were then fit with a cubic smoothing spline to yield spatially-smoothed cavity radius data, $\tilde{\tilde{R}}_c(x, t)$. Finally, an offset $R_c(x, t) = \tilde{\tilde{R}}_c(x, t) + R - \tilde{\tilde{R}}_c(x = 0, t)$ was added to the smoothed cavity radius data as a small correction that ensures that the cavity radius intersects the sphere equator. This procedure yields smoothed cavity shape data and ensures that the slope $\frac{\partial R_c}{\partial x}$ was smooth. However, the cavity radius data was not smoothed in time, so the temporal derivative $\frac{\partial R_c}{\partial t}$ still contains some noise. One point of ongoing work is to apply my smoothing-spline fitting procedure to the multi-dimensional case. With a 2D spline surface fitting method, two-dimensional data such as $\tilde{R}_c(x, t)$ could be smoothed simultaneously in space and time using best-fit splines, yielding smooth spatial and temporal derivatives, $(\frac{\partial R_c}{\partial x}, \frac{\partial R_c}{\partial t})$.

The strengths of the N ring sources are found by solving the ‘no flow through the cavity surface’ boundary condition, which is most easily computed in the *sphere frame of reference*, since the cavity radius data is tabulated as a function of distance behind the sphere, $R_c(x, t)$. Selecting N control points (x_i, r_i) , $i = 1, \dots, N$, distributed over the sphere surface ($x = R \cos \theta, r = R \sin \theta$) and cavity surface ($x, r = R_c(x, t)$), the appropriate boundary condition is

$$\vec{u}(x, r) \cdot \hat{n}(x, r) = \begin{cases} U \cos(\pi - \theta) & \text{on sphere} \\ \frac{\frac{\partial R_c}{\partial t} + U \frac{\partial R_c}{\partial x}}{\sqrt{1 + (\frac{\partial R_c}{\partial x})^2}} & \text{on cavity} \end{cases} \quad (6.3.16)$$

where the unit normal vector pointing out of the sphere/cavity is

$$\hat{n}(x, r) = \begin{cases} \cos \theta \hat{e}_x + \sin \theta \hat{e}_r & \text{on sphere} \\ \frac{-\frac{\partial R_c}{\partial x} \hat{e}_x + \hat{e}_r}{\sqrt{1 + (\frac{\partial R_c}{\partial x})^2}} & \text{on cavity} \end{cases} \quad (6.3.17)$$

The contributions to the total velocity at the N control points due to the doublet, point source, and ring sources can be written in matrix form as

$$\mathbf{B}_0 = \begin{cases} U \cos(\pi - \theta) & \text{on sphere} \\ \frac{\partial R_c}{\partial t} + U \frac{\partial R_c}{\partial x} \\ \sqrt{1 + \left(\frac{\partial R_c}{\partial x} \right)^2} & \text{on cavity} \end{cases} \quad (6.3.18)$$

$$\mathbf{B}_d = \vec{u}_d(x, r) \cdot \hat{n}(x, r) \quad (6.3.19)$$

$$\mathbf{B}_p = \vec{u}_p(x, r) \cdot \hat{n}(x, r) = \mathbf{b}_p \cdot Q_p \quad (6.3.20)$$

$$\mathbf{B}_s = \vec{u}_s(x, r) \cdot \hat{n}(x, r) = \mathbf{A}_s \cdot \mathbf{Q}_s \quad (6.3.21)$$

where the through-flow velocity matrices \mathbf{B} are all size $[N, 1]$, the point source influence matrix \mathbf{b}_p is size $[N, 1]$, the point source strength Q_p is a scalar, the ring source influence matrix \mathbf{A}_s is size $[N, N]$, and the ring source strength matrix is $\mathbf{Q}_s = [Q_{s_1}, \dots, Q_{s_N}]^\top$. Thus (6.3.16) is written in matrix form as

$$\mathbf{A}_s \cdot \mathbf{Q}_s = \mathbf{B}_0 - \mathbf{B}_d - \mathbf{b}_p \cdot Q_p \quad (6.3.22)$$

In theory, equation (6.3.22) is a linear system of equations that can be solved for the source strengths, \mathbf{Q}_s . In practice, solving (6.3.22) by matrix inversion results in a non-physical set of source strengths that do not vary smoothly over the length of the cavity¹. Physically, the cavity shape varies smoothly in x , so source strengths should also vary smoothly in x as well. In order to solve for the source strengths, the following method is used.

The numerical method is predicated on the fact that the total volume flow rate into the cavity in the absence of sources must be balanced by the total volume flow

¹I suspect this is due to the noise in computing $\frac{\partial R_c}{\partial t}$ from the experimentally-measured cavity shape data, $R_c(x, t)$. Although I smoothed $R_c(x, t)$ spatially (for each timestep), I was not able to simultaneously smooth $R_c(x, t)$ temporally as well; therefore the $\frac{\partial R_c}{\partial t}$ term in \mathbf{B}_0 contained measurement error, and I suspect this noise corrupts the direct matrix inversion method for finding \mathbf{Q}_s . In hindsight, I suppose I could have tried smoothing the noise out of \mathbf{B}_0 directly, which may have resolved this issue.

rate out of the source sheet. Since each ring source dominates the flow in its vicinity (by construction), the volume flow rate into each slice of the cavity is approximately balanced by the volume flow rate of the source at that station. Note that at this point, we do not know the point source strength. We proceed with an iterative procedure, whereby Q_p is estimated, \mathbf{Q}_s is determined to satisfy (6.3.22), Q_p is updated, and so on until both Q_p and \mathbf{Q}_s have converged.

The volume flow rate into an infinitesimal slice of the cavity is the through-flow velocity times the surface area of the slice. The surface area of each infinitesimal slice of the cavity between control points is

$$\mathbf{S} = \begin{cases} 2\pi R^2 \sin \theta \cdot d\theta & \text{on sphere} \\ 2\pi R_c \sqrt{1 + \left(\frac{\partial R_c}{\partial x}\right)^2} \cdot dx & \text{on cavity} \end{cases} \quad (6.3.23)$$

For a given guess of Q_p and \mathbf{Q}_s , the net inflow velocity and volume flow rate are

$$\mathbf{B}_{\text{net}} = \mathbf{B}_0 - \mathbf{B}_d - \mathbf{b}_p \cdot Q_p - \mathbf{A}_s \cdot \mathbf{Q}_s \quad (6.3.24)$$

$$\mathbf{Q}_{\text{net}} = \mathbf{B}_{\text{net}} * \mathbf{S} \quad (6.3.25)$$

where the $*$ operator indicates element-wise vector multiplication. In order to obtain the next guess for the source strengths, these net volume inflow rates are added to the ring source strengths

$$\mathbf{Q}_s^{\text{next}} = \mathbf{Q}_s^{\text{current}} + \mathbf{Q}_{\text{net}} \quad (6.3.26)$$

Since each ring source strength dominates the velocity in its vicinity, iteratively updating \mathbf{Q}_s via (6.3.24), (6.3.25), and (6.3.26) converges to a set of smoothly-varying \mathbf{Q}_s that satisfy the no throughflow condition (6.3.22), given the current guess for the point source strength Q_p .

The point source strength is then updated as follows: Q_p is set to cancel the velocity induced by the ring sources at the stagnation point ($x = -R, r = 0$). This satisfies (6.3.16) at the stagnation point, because the doublet strength was already chosen to balance the free-stream velocity. Evaluating (6.3.10) at ($x = -R, r = 0$), noting that $\bar{E}(0) = \frac{\pi}{2}$, yields the velocity in the positive x direction

$$u_s(-R, 0) \hat{e}_x = \sum_{i=1}^N Q_{s_i} \cdot \frac{-(x_{s_i} + R)}{4\pi((x_{s_i} + R)^2 + r_{s_i}^2)^{3/2}} \hat{e}_x \quad (6.3.27)$$

Thus, the next guess for the point source strength is

$$Q_p^{\text{next}} = u_s(-R, 0) \cdot 4\pi R_{\text{inset}}^2 \quad (6.3.28)$$

The iterative scheme continues for each guess of Q_p by evaluating (6.3.24), (6.3.25), and (6.3.26) until \mathbf{Q}_s converges. Then Q_p is updated by (6.3.27) and (6.3.28), and an updated set of \mathbf{Q}_s are found. This procedure continues until Q_p and \mathbf{Q}_s converge, which ensures that the no through-flow boundary condition (6.3.22) is satisfied at all the control points and at the stagnation point.

The forces on the sphere are found by integrating the gauge pressure over the sphere surface. The gauge pressure at the sphere surface is computed by evaluating unsteady Bernoulli's equation in the *lab frame of reference*

$$p - p_a = -\rho \frac{\partial \phi}{\partial t} - \frac{1}{2} \rho |\vec{u}|^2 - \rho g z \quad (6.3.29)$$

where the three terms are the *unsteady*, *dynamic*, and *hydrostatic* pressure.

The instantaneous force coefficient is found by integrating the gauge pressure (6.3.29) over the lower hemisphere and normalizing by the instantaneous dynamic

pressure force $\frac{1}{2}\rho[U(t)]^2\pi R^2$ in the usual way

$$C_F = \frac{\int_0^{\frac{\pi}{2}} (p - p_a) \cos(\pi - \theta) 2\pi R^2 \sin(\pi - \theta) d(\pi - \theta)}{\frac{1}{2}\rho[U(t)]^2\pi R^2} \quad (6.3.30)$$

This yields force components

$$C_F = C_{F_{\text{unsteady}}} + C_{F_{\text{dynamic}}} + C_{F_{\text{hydrostatic}}} \quad (6.3.31)$$

which are defined positive when the force on the sphere is directed upwards (in the positive z direction), causing a deceleration of the sphere.

The partial derivative $\frac{\partial\phi}{\partial t}$ is computed in the *lab frame of reference* as follows. First note that points on the lower hemisphere of the sphere at time t are located at $(r = R\sin\theta, z = R\cos\theta - H(t))$, where we define $\theta = [91^\circ, 92^\circ, \dots, 179^\circ]$ (i.e. $\delta\theta = 1^\circ$). The potential function at time t is $\phi(R\cos\theta, R\sin\theta, t)$. Since the sphere center was at $H(t - \delta t)$ at time $t - \delta t$, the potential function at time $t - \delta t$ was $\phi(R\cos\theta - H(t) + H(t - \delta t), R\sin\theta, t - \delta t)$. Thus,

$$\frac{\partial\phi}{\partial t} = \frac{\phi(R\cos\theta, R\sin\theta, t) - \phi(R\cos\theta - H(t) + H(t - \delta t), R\sin\theta, t - \delta t)}{\delta t} \quad (6.3.32)$$

The pressure in the air cavity is assumed to be atmospheric, so there should be zero gauge pressure on the upper hemisphere of the sphere and at the sphere equator. However, since this model requires computing finite differences for $\frac{\partial R_c}{\partial t}$ and $\frac{\partial\phi}{\partial t}$, the resulting pressure at the sphere equator is not necessarily atmospheric, and the resulting unsteady force is incorrect. As a correction to the unsteady force, the average gauge pressure within five degrees of the equator is assumed to be the pressure in the cavity, and this pressure coefficient is added to $C_{F_{\text{unsteady}}}$ as a correction.

The force due to surface tension is ignored in the cavity model, since it is small in the cases considered herein

$$C_{F_{\text{surface tension}}} \sim \frac{2\pi R\sigma}{\frac{1}{2}\rho[U(t)]^2\pi R^2} \sim \frac{\sigma}{\rho U_0^2 R} \ll 1 \quad (6.3.33)$$

In the next section, I present detailed results of this potential flow model for the billiard ball water entry case discussed in Chapter 5. Then in the following section, mass ratio effects are discussed.

6.4 Results and discussion

Figures 6-4 and 6-5 show the time-series of images for the billiard ball impact event discussed in Chapter 5 (same data as figure 5-6). The images in figures 6-4 and 6-5 begin after impact and show an air cavity has already formed above the sphere. As the sphere descends through the water, the air cavity forms as the flow separates from the sphere near the equator. Initially, the cavity surface (and the fluid) moves outward radially, but hydrostatic pressure continually acts on the fluid, eventually causing the cavity to stop growing. By the time the cavity begins to close, the sphere has descended some distance downward. During cavity closure, the inward radial velocity of the surface continually increases until the moment of cavity *pinch-off*, when two cavities are formed. Post pinch-off images are shown in figure 5-6, and these depict a violent cavity collapse. In particular, the lower cavity disintegrates into small bubbles as water rapidly fills in behind the sphere.

This cavity closure event is quite rapid, and it is anticipated that it causes a dramatic drop in the net force acting on the sphere just after the moment of pinch-off. As a thought experiment, consider the effects of hydrostatic pressure. In particular, net the hydrostatic pressure force (acting upwards) is unabated while the cavity exists. However, in the moments after pinch-off, water rushes in behind the sphere, and

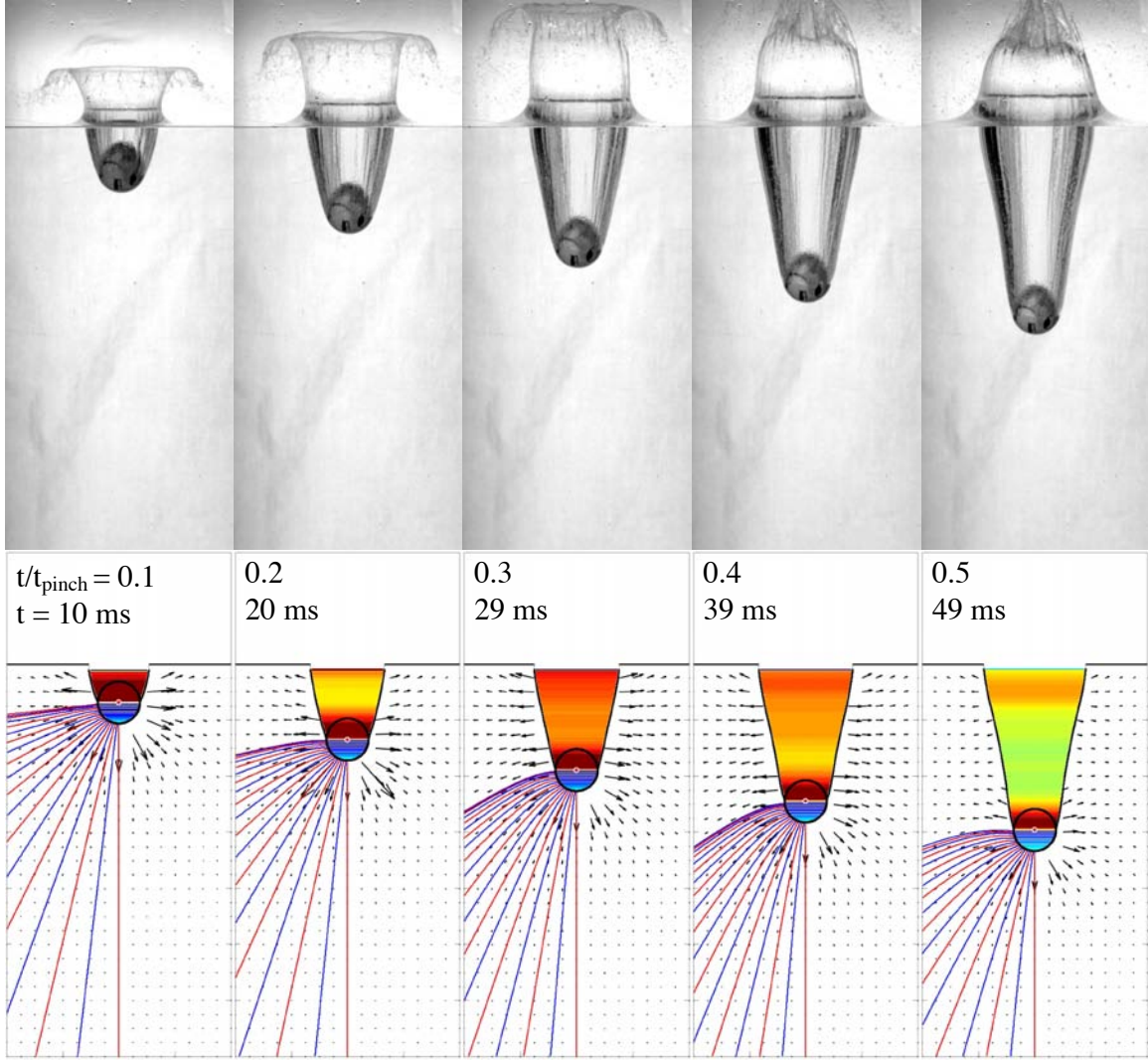


Figure 6-4: Filmstrip depicting water entry for the billiard ball case: (top) raw images, (bottom) potential flow simulation. Images are synched in time.

hydrostatic pressure builds behind (i.e. above) the sphere. This rapid pressure rise above the sphere reduces the net upwards hydrostatic pressure force quite rapidly after pinch-off. Thus, I anticipate that the total force on the sphere should fall dramatically in the moments after pinch-off. In particular, I expect that the actual instantaneous force coefficient is much more singular than the spline fit in figure 5-9 might suggest.

Figure 6-6 shows the effect that choosing alternate spline fits to the sphere position data has on the total instantaneous force coefficient (5.4.1). Three spline fits are

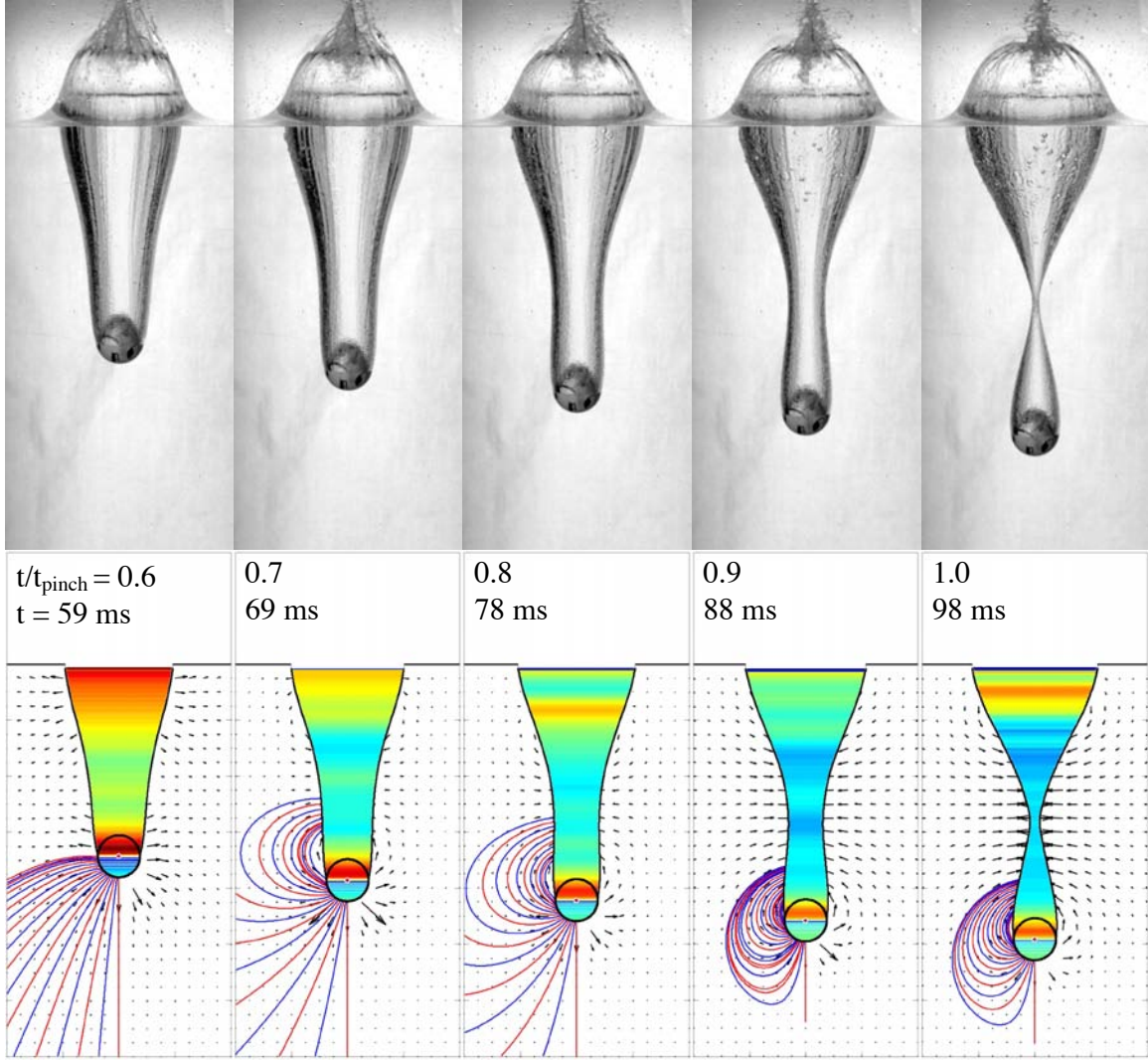


Figure 6-5: Filmstrip depicting water entry for the billiard ball case: (top) raw images, (bottom) potential flow simulation. Images are synched in time.

highlighted in figure 6-6a, and their corresponding force coefficients are shown in figure 6-6b. The black spline is that given in Chapter 5. Comparing the orange and black splines, it is evident that as error tolerance is reduced, the force coefficient rises and falls more dramatically during pinch-off. Error tolerance cannot be made arbitrarily small due to the noise in the data, and the red spline illustrates a noisy force coefficient predicted by a spline with an error tolerance less than the critical error tolerance (which was shown in Chapter 5 to be the best fit spline).

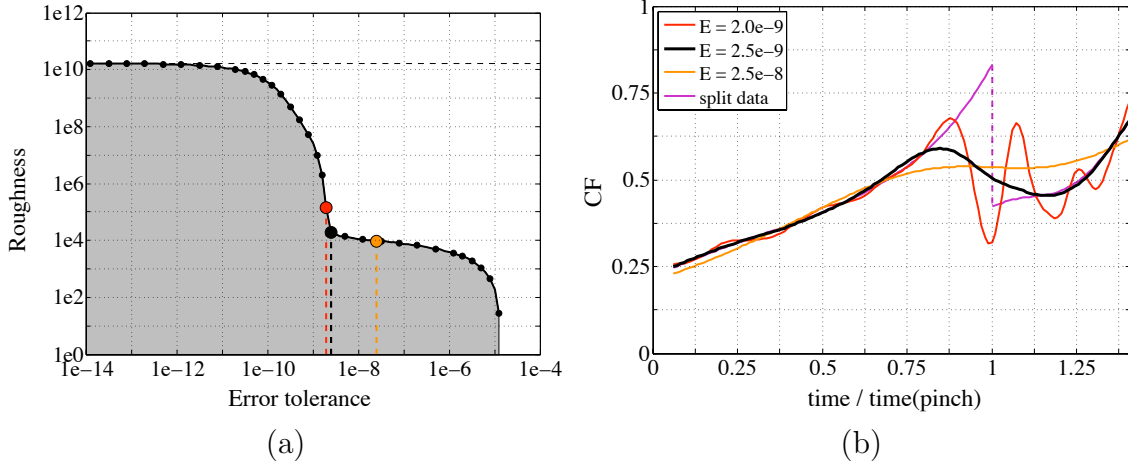


Figure 6-6: (a) *Roughness* (5.1.4) versus *error tolerance* (5.1.2) efficient frontier for quintic smoothing splines fit to position data for the billiard ball case (same data as figure 5-7). (b) Force coefficients derived from selected splines via equation (5.4.1).

To derive an ‘upper limit’ for how singular the change in total force may be during pinch-off, I created a *composite force coefficient* that is discontinuous at the time of pinch-off, shown as the purple lines (connected by a vertical dashed line) in figure 6-6b. This composite force coefficient was formed by fitting two splines -- one to the position data before pinch-off and the other to the position data after pinch-off -- and finding the force coefficients from each of these splines using equation (5.4.1). Since each spline terminates at the pinch-off time, this composite spline is not required to be continuous at pinch-off. The *composite force coefficient* (purple line) agrees well with the *single force coefficient* (black line) for times away from pinch-off, as expected from the nature of the spline fitting procedure. However, the composite force coefficient continues to rise until the time of pinch-off and then falls singularly, whereas the single force coefficient smoothes the forces during pinch-off (since the single spline fit is required to be continuous through pinch-off). It is anticipated that the forces are not truly singular, so the actual force coefficient may resemble something between these predictions, or it may rise until pinch-off and then fall in a smooth manner in the few moments after pinch-off.

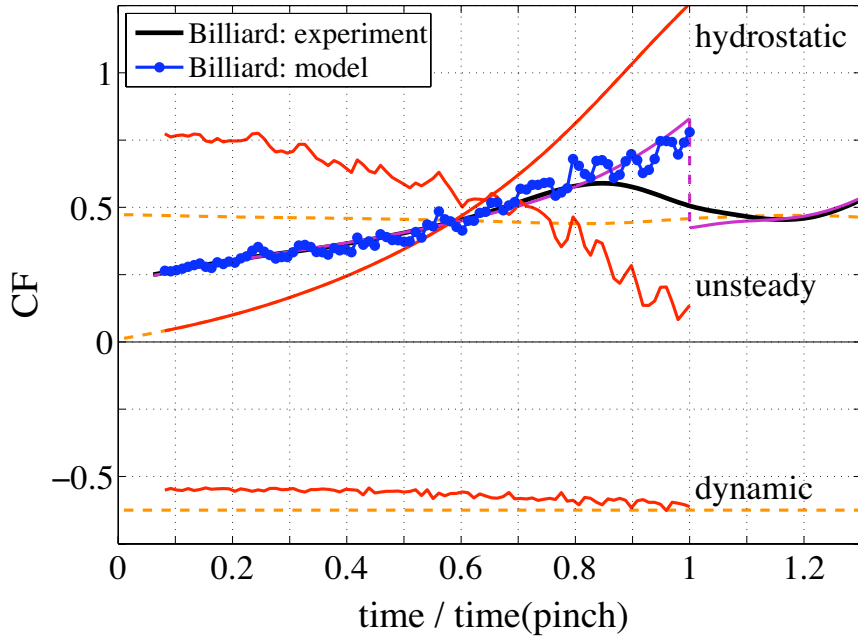


Figure 6-7: Instantaneous force coefficient versus time normalized by pinch-off time: [black line] force coefficient (5.4.1), derived from one spline fit to all the position data (same as figure 6-6b); [discontinuous purple line] composite force coefficient (5.4.1), derived from one spline fit to the position data before pinch-off and another spline fit to the data after pinch-off (same as figure 6-6b); [dotted blue line] total force coefficient predicted by the potential flow model (6.3.31); [red lines] unsteady, dynamic, and hydrostatic pressure forces predicted by the model (see eqns. 6.3.29 and 6.3.30); [orange dashed lines] theoretical unsteady, dynamic, and hydrostatic pressure forces (eqns. 6.4.1, 6.4.2, and 6.4.3).

The force coefficient derived from the best-fit single spline (black line) and composite spline (purple discontinuous line) shown in figure 6-6b are reproduced in figure 6-7. Figure 6-7 also presents the results of the potential flow model. In particular, this figure shows that the total force predicted by the model (blue dotted line) agrees well with the composite force coefficient. This agreement indicates that the potential flow model accurately predicts the forces on the sphere.

Figure 6-7 also shows the *unsteady*, *dynamic*, and *hydrostatic* pressure forces on the sphere (solid red lines), as computed by my potential flow model. For comparison, consider the canonical theoretical problem of flow around a sphere in an infinite fluid (dashed orange lines). Upon integrating the gauge pressure on the leading half of the

sphere, one finds theoretical force coefficients (Milne-Thomson, 1968)

$$C_{F_{\text{unsteady}}^{\text{theoretical}}} = \frac{1}{2} - \frac{\frac{1}{2}(\rho_3^2 \pi R^3 a(t))}{\frac{1}{2}\rho[U(t)]^2 \pi R^2} \quad (6.4.1)$$

$$C_{F_{\text{dynamic}}^{\text{theoretical}}} = -\frac{5}{8} \quad (6.4.2)$$

$$C_{F_{\text{hydrostatic}}^{\text{theoretical}}} = \frac{\rho g H(t) \pi R^2}{\frac{1}{2}\rho[U(t)]^2 \pi R^2} + \frac{\frac{1}{2}(\rho_3^4 \pi R^3 g)}{\frac{1}{2}\rho[U(t)]^2 \pi R^2} \quad (6.4.3)$$

The first term in the unsteady force accounts for the lab-fixed reference frame (which was used in the model), and the second term is the added mass of half a sphere (where a positive (i.e. upwards) sphere acceleration $a(t)$ causes a negative (i.e. downwards) force). The dynamic pressure force coefficient is a constant, since it only depends on geometry; for reference, the dynamic pressure force for a complete sphere is zero. The hydrostatic force is that given by the hydrostatic pressure acting at the equator and the buoyancy acting on a half-submerged sphere.

Let us compare the model results (solid red lines) and theoretical forces (dashed orange lines) shown in figure 6-7. The *hydrostatic pressure force* computed by the model matches almost exactly with the theoretical value (6.4.3), as expected by Archimedes' principle. This indicates that sufficient resolution was used in numerically integrating the forces in (6.3.30). There also is close agreement between the *dynamic pressure force* computed by the model and that predicted by the theory (6.4.2). This indicates that the presence of the cavity does not dramatically alter the overall dynamic pressure force on the sphere. However, the *unsteady pressure force* on the sphere computed by the model is substantially different than the theoretical prediction (6.4.1). This indicates that the dominant effect that the presence of the cavity has is to alter the *unsteady pressure force* on the sphere. Since I prescribed the doublet strength based on the sphere velocity, which is consistent with the theoretical argument leading to (6.4.1), the unsteady pressure force due to the doublet alone should agree with this theoretical result. I have verified that these results agree

within 1% for all time steps, but these data are not shown in figure 6-7 since they would simply overlay on the theoretical unsteady pressure force prediction. The effect of the single point source is negligible, so the cause of the difference between the total model unsteady pressure force and that predicted by the model is due to the ring sources representing the effect of the cavity.

To better understand the nature of the forces on the sphere computed by the potential flow model, consider again figures 6-4 and 6-5. The lower panel shows a simulation of the potential flow model. The sphere position and cavity shape shown were interrogated from the raw images, as discussed in Section 6.2. These figures show the velocity field, as computed by the potential flow model, and instantaneous streamlines are plotted in alternating colors for clarity. The cavity shading represents the strength of the ring source at each depth. Dark red rings represent strong positive sources (which expel fluid), and dark blue rings represent negative sources (i.e. sinks, which absorb fluid), while green represents zero strength. The timesteps shown correspond to the raw images shown in the upper panel of figures 6-4 and 6-5.

Figures 6-4, 6-5, and 6-7 show that the unsteady force is larger than the theoretical value for $t/t_{\text{pinch-off}} \lesssim 0.75$, when a large portion of the rings in the cavity are positive-strength sources. This can be seen in the first seven frames of figures 6-4 and 6-5, where most of the rings in the cavity are shaded green to red. For later times, $0.75 \lesssim t/t_{\text{pinch-off}} \leq 1$, the cavity collapses, many rings are negative-strength sources (i.e. sinks that draw fluid in) shaded green to blue in figure 6-5, and the unsteady force predicted by the model is less than that predicted theoretically.

What sets the ring source strength? To answer this, let us ignore the interaction between the rings for a moment. Then for a slice of the cavity with radius $R_c(x, t)$ and axial length δx , the volume flow rate out of the cavity required by (6.3.16) and (6.3.23) reduces to $Q_s = \left(\frac{\partial R_c}{\partial t} + U \frac{\partial R_c}{\partial x} \right) \cdot 2\pi R_c \delta x$. Thus, the strength of a ring will be positive (i.e. it will be a source) if the growth rate of the cavity $\frac{\partial R_c}{\partial t}$ and wall slope $\frac{\partial R_c}{\partial x}$

are positive. In these experiments, the rings behind the sphere equator all start out as (positive) sources, pushing fluid outwards as the cavity grows. After some time, the cavity starts collapsing for some period of time before the wall slope reaches vertical (i.e. $\frac{\partial R_c}{\partial t} < 0$ while $\frac{\partial R_c}{\partial x} > 0$ still). Eventually, the wall slope is sufficiently small for the ring to become a sink. As the cavity collapses further and the wall slope turns negative, the ring becomes an even stronger sink, drawing fluid into the cavity.

It is important to note here that it is critical to formulate the potential flowfield using 3D potential flow constructs in order to accurately predict the unsteady forces on the sphere. The results in figure 6-7 show that the unsteady pressure force on the sphere is modulated by the presence of the ring sources in the cavity, at some axial distance behind the sphere. It is critical to formulate the potential flow model using 3D potential flow constructs that enable ‘crosstalk’ between each axial position along the cavity and the sphere surface. If the cavity model were constructed strip-wise, say using 2D point sources at each axial position along the cavity, these 2D sources would have no effect on the potential function at other stations along the cavity or at the sphere surface. Thus, a locally 2D potential flow model would be unable to accurately represent the potential function on the sphere surface and would be unable to accurately compute the unsteady pressure force on the sphere.

6.4.1 PIV results

The potential flow model assumes that viscous friction and vortex shedding are negligible. At this point I will demonstrate that this assumption is valid and that no significant vortical structures are created by the sphere during water entry.

To experimentally quantify the vorticity shed by the sphere during water entry, 2D particle image velocimetry data were collected for a series of trials. Figure 6-8a shows the PIV data for one such trial with the acrylic sphere. The experimental parameters are listed in table 6.1. In this experiment, the fluid was imaged with a vertical light

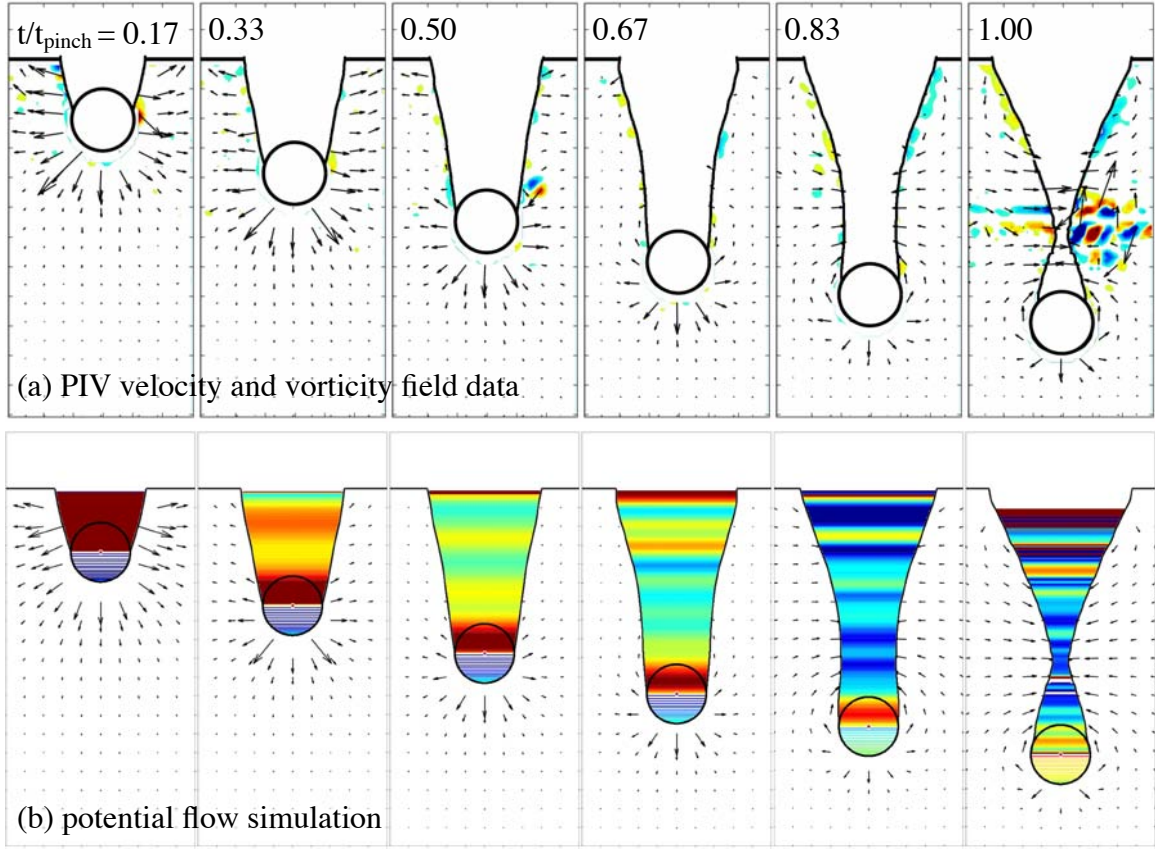


Figure 6-8: Filmstrip of the cavity impact event: (a) PIV velocity and vorticity field data, (b) potential flow simulation. The velocity vectors are not drawn to scale.

sheet emitted from a laser on the left side of the page; no shadow appears to the right of the sphere, because a mirror on the right side of the tank reflected the laser sheet back towards the sphere. This time-series of PIV velocity and vorticity fields shows very little vorticity in the flowfield for most timesteps. The intense ‘vorticity’ at the pinch-off depth (at the pinch-off time) actually is an artifact of reflections of the laser sheet off the cavity surface as it collapses through the sheet, as shown in figure 6-9.

The maximum vorticity level observed in vortical patches that appear for times before pinch-off was approximately $\bar{\omega} \approx 150 \text{ 1/s}$. Assuming the small vortical patches in figure 6-8a are cross-sections of toroidal vortex rings, then the circulation of such a vortex ring would be approximately $\Gamma = \bar{\omega} A_v$, where A_v is the area of the vortical

patch. For the circulation of such a vortex ring to be significant, it would have to induce a vertical velocity on the order of the sphere impact speed $U_0 = 3.43$ m/s. The centerline velocity induced by the vortex ring is Γ/D_v , where the data in figure 6-8a show that it is safe to assume that $D_v \approx D = 0.0254$ m (i.e. the sphere diameter). Setting $\Gamma/D \sim U_0$ and noting that the cross-sectional area of the sphere is $A = \pi D^2/4$, the area of a vortical patch required to make it significant is $A_v/A = 4U_0/\pi D\bar{\omega} = 1.1$. Clearly, the area of the vortical patches observed in figure 6-8a are much smaller than $1.1A$, indicating that their effect is insignificant.

Sphere position and cavity shape data were acquired for this case as in the other cases, and they were used to create a potential flow model of this case. The cavity shape data for this trial was *very noisy* though, because the laser lighting required for PIV did not well illuminate the cavity edges, causing poor performance of the Canny edge finding algorithm. As such, the unsteady forces computed in the potential flow simulation were quite noisy, although they still did show the general trends observed in the billiard ball case. The simulation is shown in figure 6-8b; this figure shows very good qualitative agreement between the *measured* PIV velocity fields and the *simulated* potential flow model velocity fields, giving further evidence that the potential flow model accurately represents the physics of this water entry problem.

In the mass ratio study that follows, the acrylic sphere was again dropped from the same height, but this time imaged using the house flood lighting. Figure 6-9 shows good agreement between the total force coefficient (obtained by spline fits to the measured position data via (5.4.1)) for the ‘house lights’ and ‘PIV’ trials. This provides validation for the experimental methods for preparing and dropping the spheres and the numerical methods for interrogating the sphere position and fitting these data with a smoothing spline to derive the force coefficient. Figure 6-9 shows that the experimental methods used to obtain the ‘experimental’, smoothing-spline-derived force coefficient are highly accurate and repeatable.

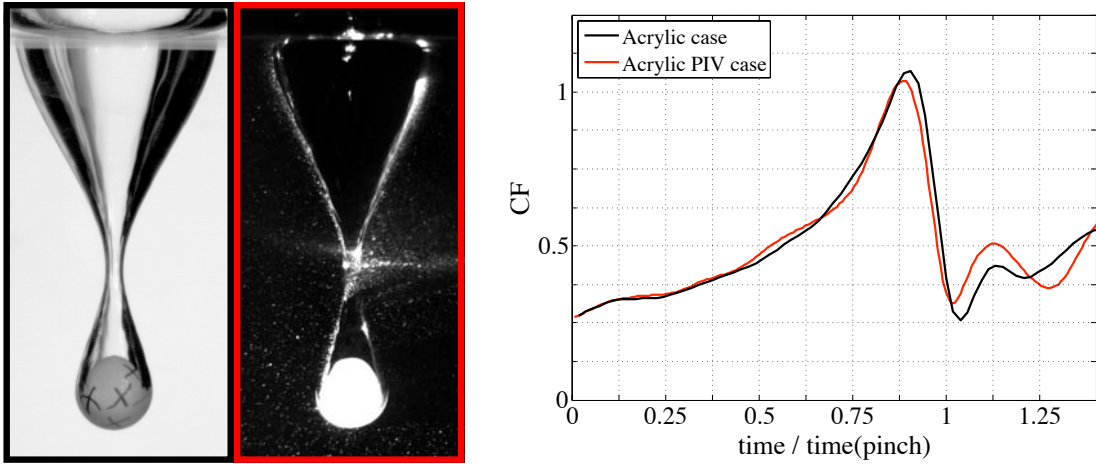


Figure 6-9: The smoothing-spline-derived force coefficients C_F (5.4.1) show good agreement between the ‘house lights’ and ‘PIV’ trials, demonstrating good repeatability of the experimental methods.

6.5 Effect of mass ratio

One of the dominant physical parameters of this problem is the *mass ratio*

$$m^* = \frac{\rho_s}{\rho} \quad (6.5.1)$$

where ρ_s is the density of the sphere and ρ is the fluid density. A series of experiments were performed by Truscott (2009) in a controlled study of the effect of mass ratio, and the parameters of these experiments are given in table 6.1.

Figure 6-10 shows a time-series of images for each trial. These images show that the time to cavity pinch-off is nearly the same, regardless of mass ratio. However, the depth of the sphere at the time of cavity pinch-off, and the depth of the pinch-off itself both increase with increasing mass ratio.

Figure 6-11 shows the position data acquired from these high-speed images, as well as the velocity, acceleration, and force coefficient derived from spline fits to these position data. For reference, the billiard ball case is also shown ($m^* = 1.8$). The position data in figure 6-11a show a distinct mass ratio effect. For smaller mass ratios



Figure 6-10: Three spheres of the same diameter ($D = 0.0254$ m) dropped from the same height ($h = 60$ cm), coated with the same surface treatment (static advancing contact angle $\theta_s = 120^\circ$), but all have different mass ratios $m^* = \rho_s/\rho$ as indicated. The impact speed is $U_0 = \sqrt{2gh} = 3.43$ m/s, and the time step between images is 0.0071 sec for all cases.

(e.g. the acrylic case, $m^* = 1.2$), the depth versus time trajectory has a visible amount of curvature, indicating non-zero accelerations and time-varying instantaneous force on the sphere. For larger mass ratios (e.g. the steel case, $m^* = 7.8$), the depth versus time trajectory has little curvature, indicating small accelerations and a nearly-constant instantaneous force on the sphere. It should be noted that in the limit of infinite mass ratio, the total hydrodynamic force on the sphere would be negligible, and the sphere would fall under the action of gravity alone $a(t) = -g$; in this limit, the position data would have negative (downwards) curvature in time, and the acceleration would be constant. The acceleration and force coefficient plots in

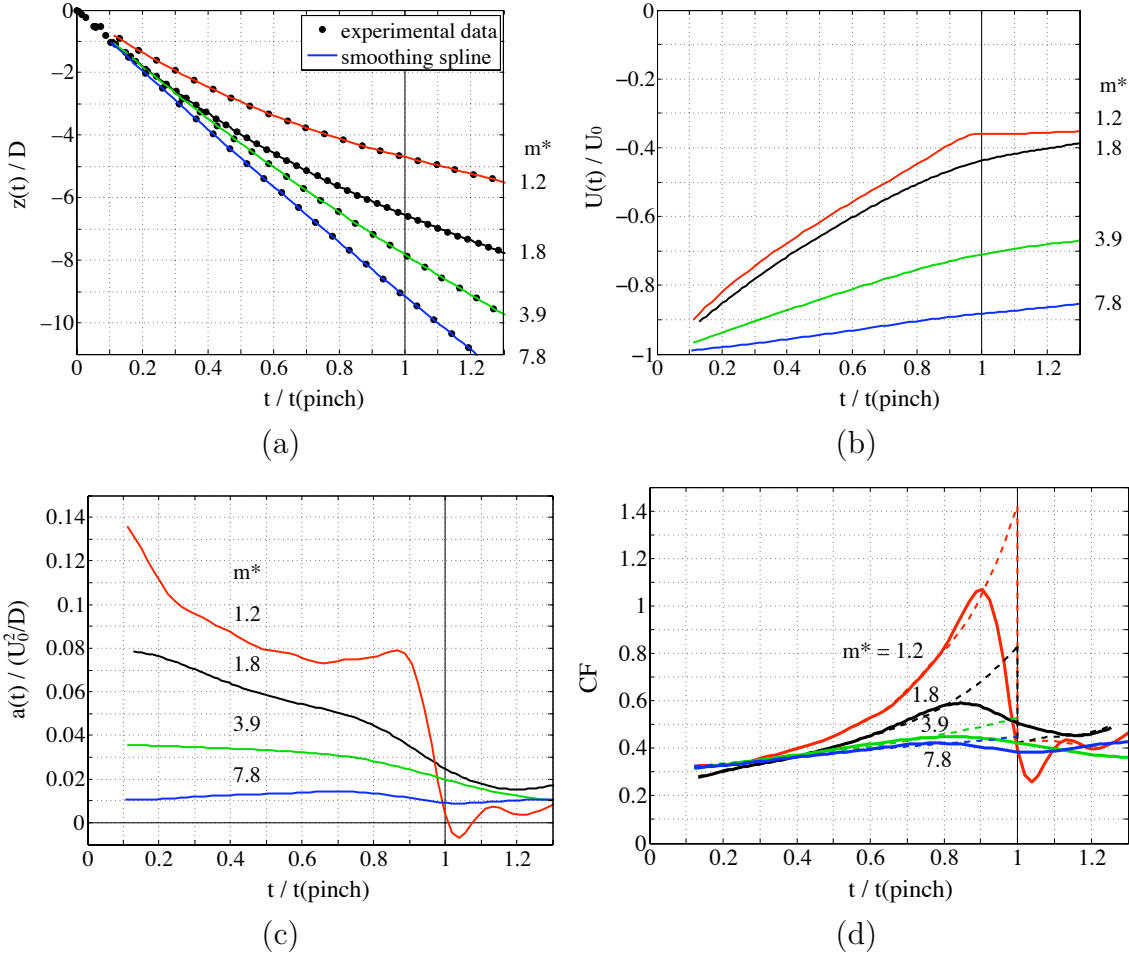
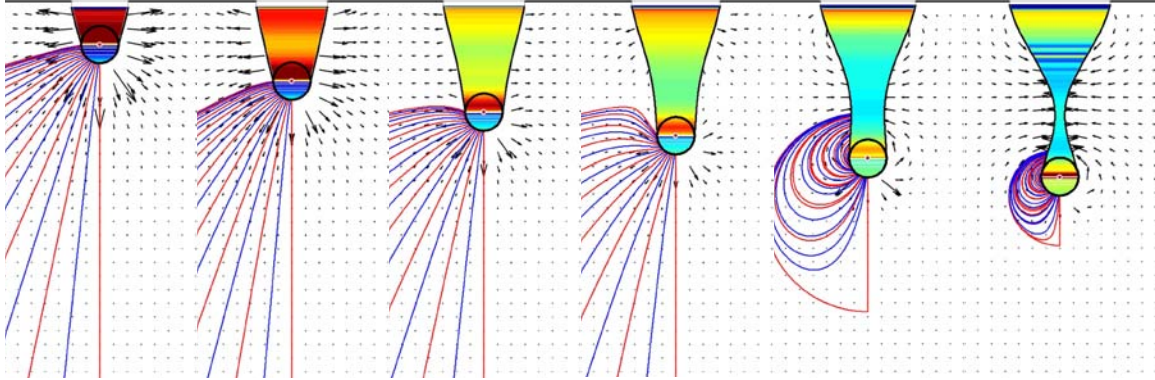


Figure 6-11: ‘Experimental’ data showing the effects of mass ratio $m^* = \rho_s/\rho$: (a) measured position versus time data and best-fit quintic smoothing splines; (b) velocity; (c) acceleration; and (d) total force coefficient predicted by the smoothing spline. Also shown in (d), composite force coefficient curves predicted by quintic smoothing splines fit to the data split before and after pinch-off (dashed lines).

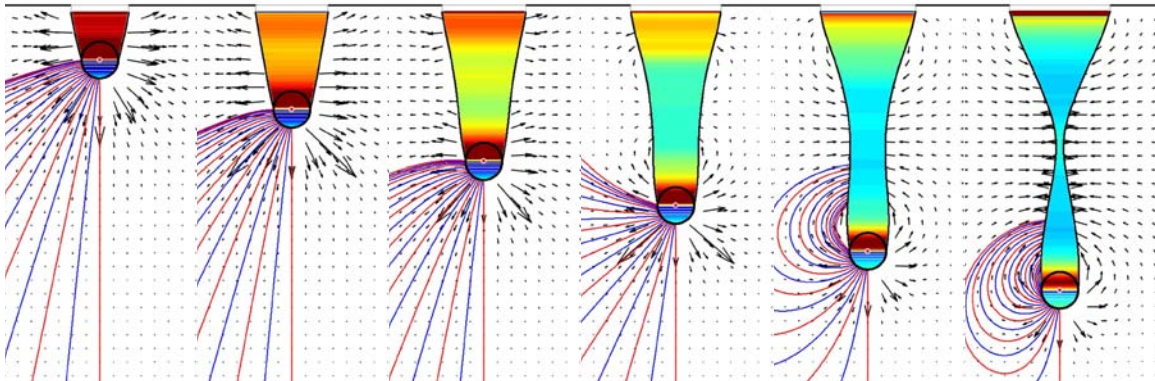
figures 6-11c and 6-11d, also show these trends. In figure 6-11d, force coefficients derived from a single spline fit to all of the position data are shown as solid lines, and composite force coefficients derived from splines fit to the data before and after pinch-off are shown as dashed lines. These experimental data show that for low mass ratio spheres, the instantaneous force coefficient is quite unsteady in time.

Figure 6-12 shows a time-series of images of the potential flow model simulation for each trial. The colormap used to plot the source strengths in the cavity is the same

(a) acrylic: $m^* = 1.2$



(b) ceramic: $m^* = 3.9$



(c) steel: $m^* = 7.8$

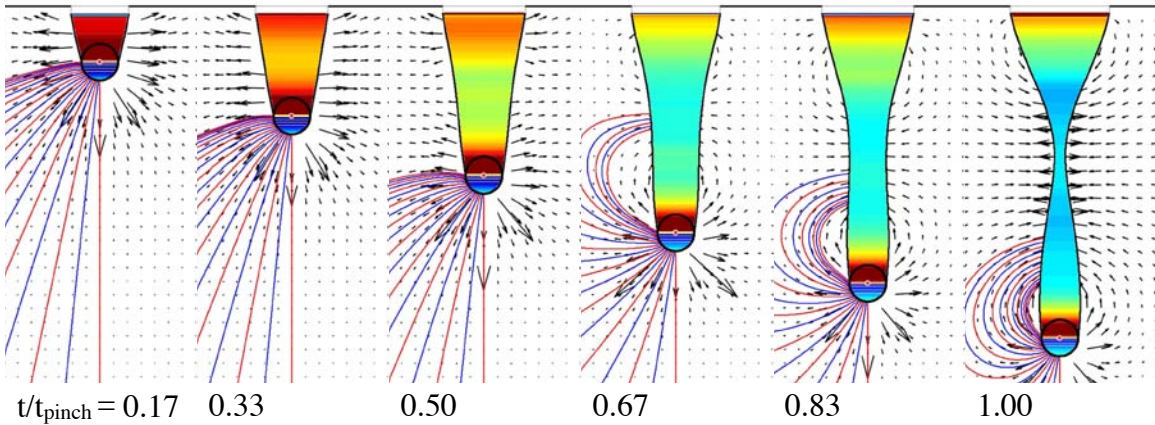


Figure 6-12: Potential flow model simulation for the acrylic, ceramic, and steel cases.

as the billiard ball case (figures 6-4 and 6-5). Figure 6-12 shows that the magnitude of the source strengths for the acrylic sphere case are generally less than the steel case. In particular, consider the strengths of the ring sources on the lower hemisphere of the sphere at the time of cavity pinch-off: These strengths are near zero for the acrylic

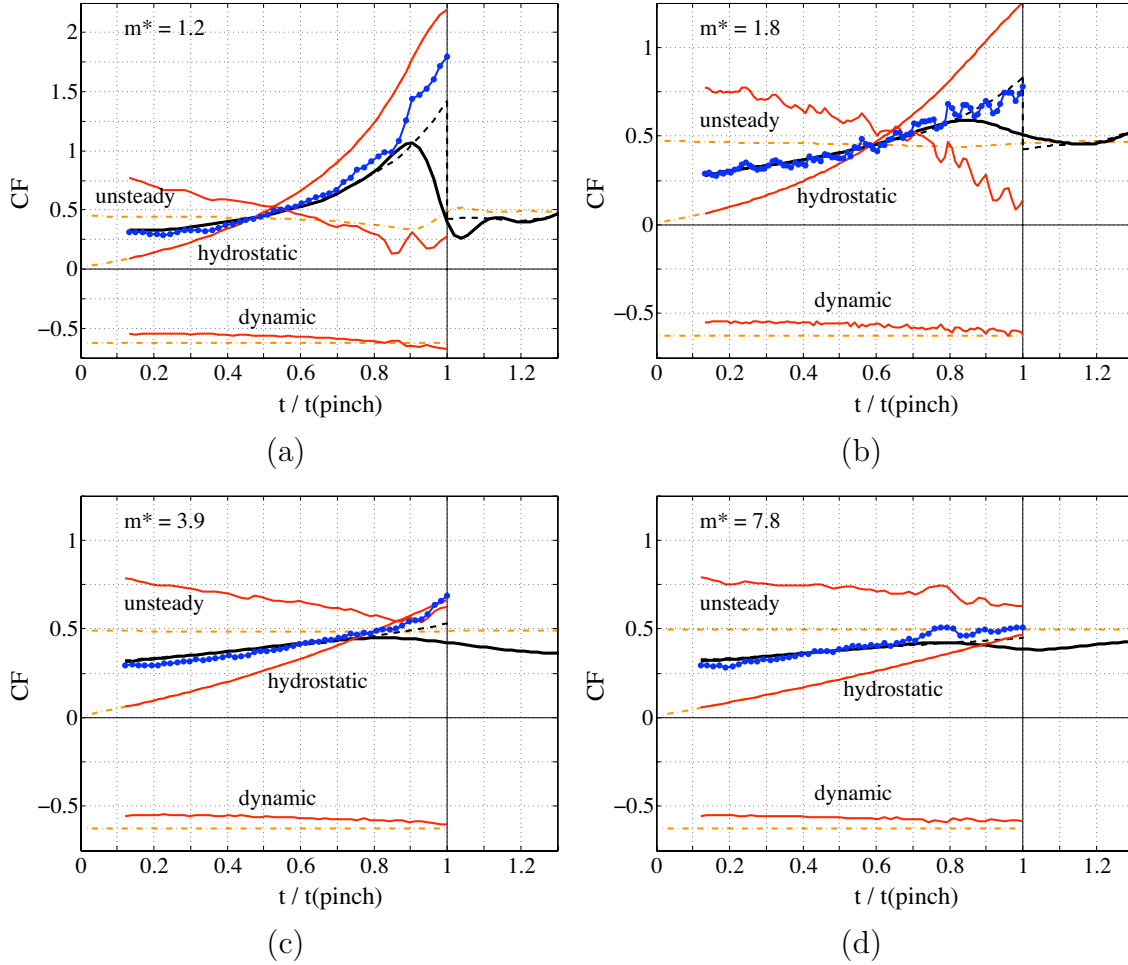


Figure 6-13: *Instantaneous force coefficient versus time normalized by pinch-off time:* [black line] force coefficient (5.4.1), derived from one spline fit to all the position data; [dashed black line] composite force coefficient (5.4.1), derived from one spline fit to the position data before pinch-off and another spline fit to the data after pinch-off; [dotted blue line] total force coefficient predicted by the potential flow model (6.3.31); [red lines] unsteady, dynamic, and hydrostatic pressure forces predicted by the model (see eqns. 6.3.29 and 6.3.30); [orange dashed lines] theoretical (eqns. 6.4.1, 6.4.2, and 6.4.3). Four cases are shown: (a) acrylic $m^* = 1.2$; (b) billiard $m^* = 1.8$ (same data as figure 6-7); (c) ceramic $m^* = 3.9$; (d) steel $m^* = 7.8$.

sphere but are quite strong negative sources for the steel sphere. Similarly, the source rings representing the near cavity (i.e. less than one sphere radius above its equator) for the acrylic case are much weaker than those for the steel case at pinch-off. This shows graphically how the unsteady pressure force changes much more dramatically for the low-mass-ratio acrylic sphere than it does for the high-mass-ratio steel sphere.

Figure 6-13 shows the force coefficient results predicted by the model for each case, as compared to the experimental (smoothing-spline-derived) C_F curves. The potential flow model correctly predicts the overall force coefficient for all cases, validating its applicability over a wide range of mass ratios. For all four cases, the *hydrostatic* and *dynamic* pressure forces agree with the theoretical forces on the leading hemisphere of a sphere in an infinite fluid with no cavity, and the *unsteady* pressure force is much different than theory predicts; these results indicate that the dominant effect of the cavity is to alter the *unsteady* pressure force on the sphere. Interestingly, the unsteady pressure force for the ceramic ($m^* = 3.9$) and steel ($m^* = 7.8$) cases never dips below the theoretical prediction. This is due to the strong positive-strength sources in the near cavity that create the cavity as these spheres descend through the water.

6.6 Summary

I began this chapter by showing that the *pressure impulse force* on a body is the net pressure force on the body, with the pressure computed using unsteady Bernoulli's equation (consistent with potential flow theory). The experimental and potential flow results of this chapter show that for the water entry problem, in which there is no viscous wake, this potential flow force well represents the total force on the body.

In this chapter, I considered the physics problem of a sphere falling into a basin of water. I created a potential flow model to represent the sphere and cavity, and I used this model to determine the instantaneous forces on the sphere during water entry. The total force computed by my model agreed well with the force determined ‘experimentally’ using a smoothing spline fit to the measured position data. In my model, I accounted separately for the *unsteady* ($-\rho\frac{\partial\phi}{\partial t}$), *dynamic* ($-\frac{1}{2}\rho|\vec{u}|^2$), and *hydrostatic* ($-\rho gz$) pressure components acting on the sphere, so I could compare the values computed by the model with the theoretical forces on the leading hemisphere of

a sphere in infinite flow. I found good agreement between both the model hydrostatic and dynamic pressure forces and their theoretical counterparts. This suggests that the total force on the sphere is modulated by the unsteady pressure force, which I found to depend strongly on the growth and collapse of the sub-surface air cavity.

This chapter demonstrates the versatility of the theoretical framework of this thesis. In the absence of vorticity, the impulse-force framework distills to potential flow theory. With the inclusion of a viscous wake, the vortex impulse force acts as a correction to the force predicted by potential flow theory.

Bibliography

- Abramowitz M, Stegun IA (1972) Handbook of Mathematical Functions Dover.
- Aristoff JM, Bush JWM (2009) “Water entry of small hydrophobic spheres,” Journal of Fluid Mechanics **619**:45–78.
- Asfar K, Moore S (1987) “Rigid-body water impact at shallow angles of incidence,” In: Proceedings of the Sixth International Offshore Mechanics and Arctic Engineering Symposium, ASME, vol 2, pp 105–112.
- Bergmann R, van der Meer D, Gekle S, van der Bos A, Lohse D (2009) “Controlled impact of a disk on a water surface: cavity dynamics,” Journal of Fluid Mechanics in press.
- Birkhoff G, Isaacs R (1951) “Transient cavities in air-water entry,” Tech. Rep. 1490, Navord Report.
- Duclaux V, Caillé F, Duez C, Ybert C, Bocquet L, Clanet C (2007) “Dynamics of transient cavities,” Journal of Fluid Mechanics **591**:1–19.
- Duez C, Ybert C, Clanet C, Bocquet L (2007) “Making a splash with water repellency,” Nature Physics **3**:180–183.

Gilbarg D, Anderson RA (1948) “Influence of atmospheric pressure on the phenomena accompanying the entry of spheres into water,” J Applied Physics **19**(2):127–139.

Glasheen JW, McMahon TA (1996) “Vertical water entry of disks at low Froude numbers,” Physics of Fluids **8**(8):2078–2083.

von Karman T (1929) “The impact on seaplane floats during landing,” Technical Notes 321, National Advisory Committee for Aeronautics, Aerodynamic Institute of the Technical High School, Aachen.

Korobkin AA, Pukhnachov VV (1988) “Initial stage of water impact,” Annual Review of Fluid Mechanics **20**:159–185.

Lee M, Longoria RG, Wilson DE (1997) “Cavity dynamics in high-speed water entry,” Physics of Fluids **9**:540–550.

May A, Hoover WR (1963) “A study of the water-entry cavity,” Unclassified NOLTR 63-264, United States Naval Ordnance Laboratory, White Oak, Maryland.

Milne-Thomson L (1968) Theoretical Hydrodynamics 5th edn. Dover.

Truscott TT (2009) Cavity dynamics of water entry for spheres and ballistic projectiles PhD thesis, MIT.

Truscott TT, Epps BP, Techet AH (2010) “Unsteady forces on spheres during water entry,” in preparation.

Wagner H (1932) “Phenomena associated with impacts and sliding on liquid surfaces,” ZAMM **12**:193–235.

Worthington AM (1908) A Study of Splashes Longmans Green and Co., Plymouth. Printed by William Brendon and Son, Ltd., 1908; reprinted, The Macmillian Co., New York, 1963

Part III

Marine propulsion and energy harvesting

[THIS PAGE INTENTIONALLY LEFT BLANK]

Chapter 7

Off-design performance analysis of marine propellers and turbines using lifting line theory

This chapter presents a method for off-design performance analysis of marine propellers and hydrokinetic turbines (the undersea analog to wind turbines). The method is rooted in *lifting line theory*, in which the lifting surface (i.e. wing, propeller blade, etc.) and its wake are modeled as a rectangular vortex ring. The force on the wing is given by the Kutta-Joukowsky theorem

$$\mathbf{F}/\text{span} = \rho V \Gamma \mathbf{e}_z + \rho w \Gamma \mathbf{e}_x \quad (7.0.1)$$

where the two components are the lift and drag per unit span (Anderson, 2007). I now show how this result is derived using the theoretical framework of this thesis.

Consider a rectangular vortex ring of circulation Γ and breadth b , extending into the wake a length ℓ , as illustrated in figure 7-1. The free-stream speed is $\mathbf{V} = V \mathbf{e}_x$, and the vortex ring induces a downwash at the wing of $\mathbf{w} = -w \mathbf{e}_z$, so the total inflow speed at the wing is $V^* = \sqrt{V^2 + w^2}$.

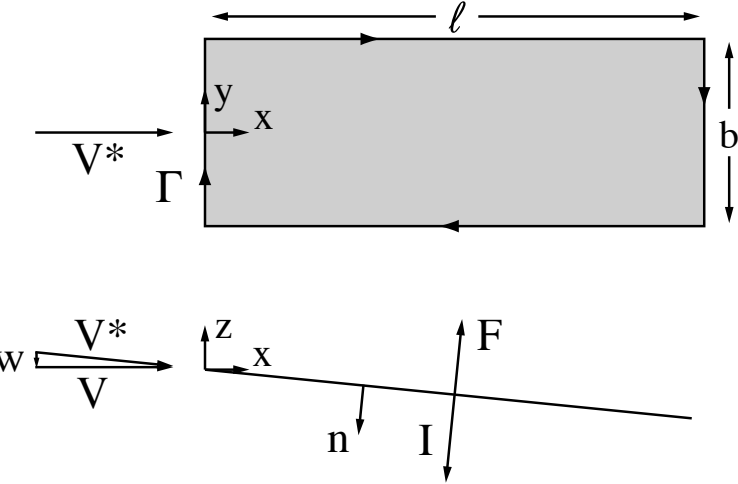


Figure 7-1: Illustration of a steady wake.

The impulse of the vortex ring (which represents the wing and its wake) is

$$\mathbf{I} = \frac{1}{2}\rho \int \mathbf{x} \times \boldsymbol{\omega} d\mathbf{x} = \rho \Gamma b \ell \mathbf{n} \quad (7.0.2)$$

where the unit normal vector is $\mathbf{n} = -\frac{w}{V^*} \mathbf{e}_x - \frac{V}{V^*} \mathbf{e}_z$. Although the motion is steady-state (so $\mathbf{F}_p = 0$) and the circulation is constant, the impulse of the vortex ring continually grows, since $\frac{d\ell}{dt} = V^*$. Therefore, the force on the wing is

$$\mathbf{F} = \mathbf{F}_v + \mathbf{F}_p = -\frac{d\mathbf{I}}{dt} = \rho V \Gamma b \mathbf{e}_z + \rho w \Gamma b \mathbf{e}_x \quad (7.0.3)$$

Taking $b = 1$ recovers the force per unit span (7.0.1).

In the case of a lifting surface with a non-uniform circulation distribution $\Gamma(y)$, we can consider the wake to be composed of infinitesimal-width rings (i.e. $b = dy$) and integrate along the span to find the total force

$$\mathbf{F} = \int \rho V(y) \Gamma(y) dy \mathbf{e}_z + \int \rho w(y) \Gamma(y) dy \mathbf{e}_x \quad (7.0.4)$$

as illustrated in figure 7-2.

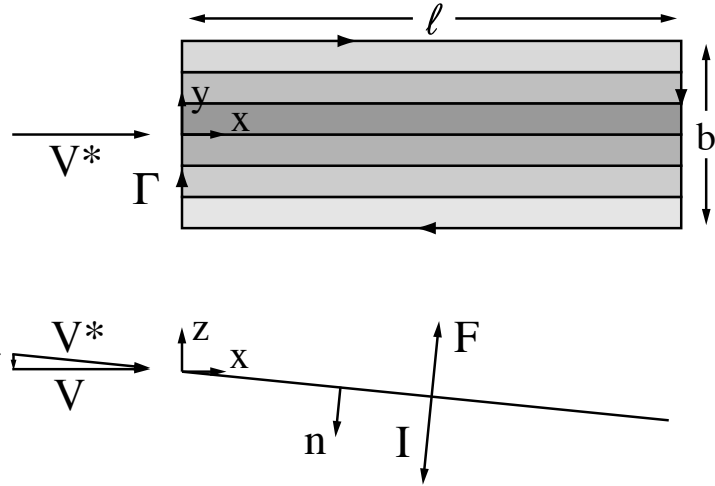


Figure 7-2: Illustration of a non-uniform steady wake.

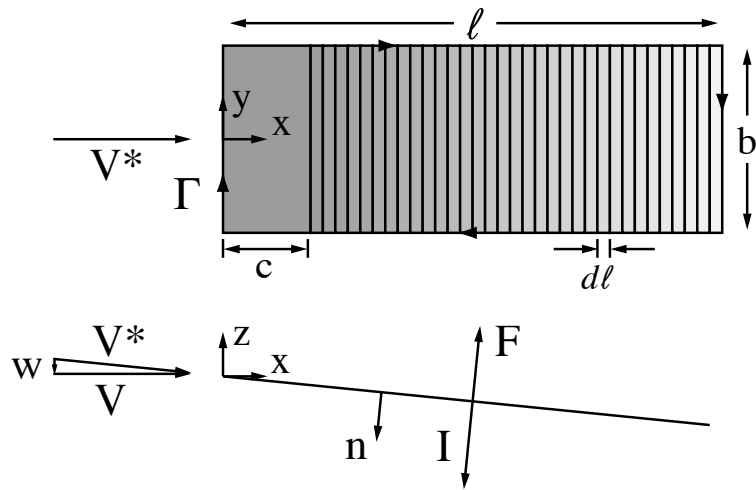


Figure 7-3: Illustration of an unsteady wake.

Figure 7-3 illustrates the unsteady case. Here, we assume that the wing is a rectangle of span b and chord c with circulation $\Gamma(t)$, and the wake is composed of rectangular rings of span b and length $d\ell$. Since the circulation of each wake vortex remains constant by Kelvin's theorem (Saffman, 1995), the rate of change of the impulse of the vortex system is

$$\frac{d\mathbf{I}}{dt} = \left(\rho \Gamma \frac{d\ell}{dt} b + \rho \frac{d\Gamma}{dt} cb \right) \mathbf{n} \quad (7.0.5)$$

where the first term is the rate of generation of impulse in the wake (as in the steady case), and the second term is the rate of increase of impulse of the vortex ring that represents the wing. As before, $\frac{d\ell}{dt} = V^*$, so the impulsive vortex force on the wing is

$$\mathbf{F}_v = -\frac{d\mathbf{I}}{dt} = \rho V \left(\Gamma + \frac{\partial \Gamma}{\partial t} \frac{c}{V^*} \right) b \mathbf{e}_z + \rho w \left(\Gamma + \frac{\partial \Gamma}{\partial t} \frac{c}{V^*} \right) b \mathbf{e}_x \quad (7.0.6)$$

which is in agreement with unsteady lifting line theory (Theodorsen, 1935). The impulsive pressure force on the wing is given by added mass theory

$$\mathbf{F}_p = -\frac{d}{dt} \left[\int_{S_b} \rho \phi \hat{\mathbf{n}} dS \right] = -\rho \frac{\pi}{4} b c^2 (\mathbf{a} \cdot \mathbf{n}) \mathbf{n} \quad (7.0.7)$$

where \mathbf{a} is the acceleration of the wing (Newman, 1977). The total unsteady force on the wing is $\mathbf{F} = \mathbf{F}_v + \mathbf{F}_p$, as discussed in Chapter 1. As in the steady case, a non-uniform circulation distribution can be treated by setting $b = dy$ and integrating the unsteady force over the wing span.

Propeller lifting line theory is a general extension of the above wing theory. In the propeller case, the blade travels in a helical path, and the the wake is modeled as a helical vortex sheet. The propeller wake downwash has both axial and tangential velocity components, and the force on the propeller blade can be decomposed into axial and tangential components that produce thrust and torque.

The following text draws from:

B.P. Epps, M.J. Stanway, and R.W. Kimball, “OpenProp: An Open-source Design Tool for Propellers and Turbines,” SNAME Propellers and Shafting, Williamsburg, VA. Sep. 16, 2009.

B.P. Epps, J. Chalfant, K. Flood, A.H. Techet, R.W. Kimball, & C. Chryssostomidis, “OpenProp: An Open-Sourced Parametric Design and Analysis Tool for Propellers,” Grand Challenges in Modeling and Simulation, Istanbul, Turkey. July 14, 2009.

7.1 Introduction

I have implemented my method for off-design performance analysis of propellers and turbines in a computational tool called **OPENPROP**. **OPENPROP** is an open-source code suite that can be used for the design, analysis, and fabrication of optimized propellers and horizontal-axis turbines (Kimball and Epps, 2007). The numerical model is based on propeller lifting line theory, which is used in parametric design codes employed by the U.S. Navy as well as commercial designers. **OPENPROP** is written in MATLAB M-code, which is widely used in academia and industry. **OPENPROP** is designed to be a user-friendly tool that can be used by both propeller design professionals as well as novices to propeller design.

A team of researchers at MIT and Maine Maritime Academy have contributed to the current **OPENPROP** code. **OPENPROP** began in 2001 with the propeller code PVL developed by Kerwin (2007) as part of his MIT propeller design course notes. The first MATLAB version of this code, MPVL, incorporated graphical user interfaces for parametric design and preliminary bladerow design (Chung, 2007). Geometry routines were later added which interfaced with the CAD program Rhino to generate a 3D printable propeller (D'Epagnier et al, 2007). These early codes were capable of designing propellers using a simple Lerbs's criteria optimizer routine (Lerbs, 1952). Epps et al (2009b) implemented Coney's generalized propeller optimizer (Coney, 1989) and also created a turbine optimization routine. Epps et al (2009a) created an off-design analysis routine to predict the performance curve for a given propeller or turbine design. On- and off-design cavitation analysis capabilities were implemented by Flood (2009). Stubblefield (2008) extended the numerical model to handle the design of ducted propellers. My unique contributions to **OPENPROP** are:

1. Created an off-design performance analyzer, which can be used with either propellers or horizontal-axis turbines,
2. Created a horizontal-axis turbine design optimizer (presented in Chapter 9),

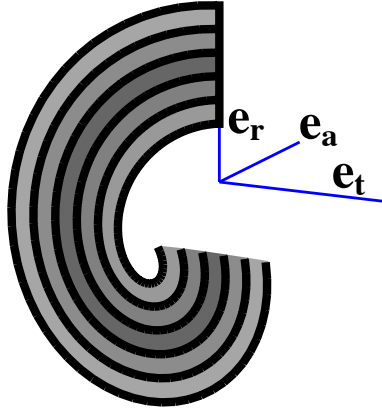


Figure 7-4: Propeller lifting line model: The key propeller blade is modeled as a lifting line, and the wake from each blade is modeled as a helical vortex sheet that extends indefinitely downstream. The axial direction, \mathbf{e}_a , points upstream.

3. Implemented the generalized propeller optimizer created by Coney (1989) using a novel wake-alignment procedure,
4. Created tools to find the influence functions for a user-defined wake geometry,
5. Created blade thickness- and chord-distribution design tools,
6. Developed tools for geometry export to SOLIDWORKS,
7. Modularized the code using data structures and stand-alone function calls,

What follows is the theoretical foundation and numerical implementation of the OPENPROP propeller/turbine design code suite. It draws from the theory presented in (Coney, 1989), (Kerwin, 2007), (Kerwin and Hadler, 2010), (Abbott and von Doenhoff, 1959), and (Carlton, 1994). In this chapter, all equations are given in dimensional terms, and their non-dimensionalized forms are given in table 7.1.

7.2 Propeller lifting-line formulation

OPENPROP is based on *moderately-loaded lifting line theory*, in which a propeller blade is represented by a lifting line, with trailing vorticity aligned to the local flow velocity (i.e. the vector sum of free-stream plus induced velocity). The induced

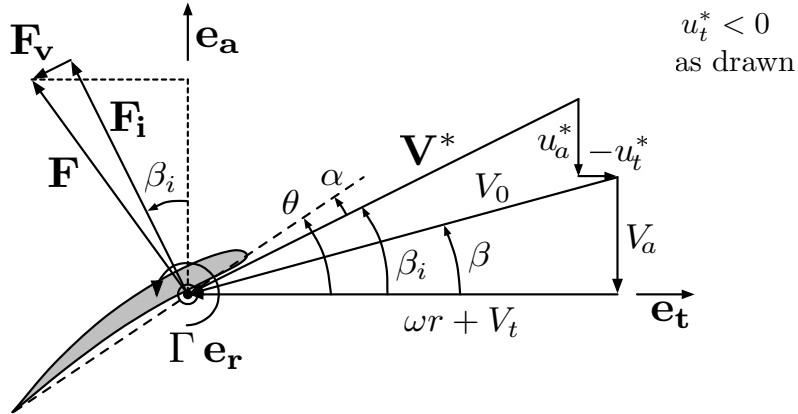


Figure 7-5: Propeller velocity/force diagram, as viewed from the tip towards the root of the blade. All velocities are relative to a stationary blade section at radius r .

velocities are computed using a vortex lattice, with helical trailing vortex filaments shed at discrete stations along the blade, as illustrated in figure 7-4. The blade itself is modeled as discrete sections, having 2D section properties at each radius. Loads are computed by integrating the 2D section loads over the span of the blade.

The velocity/force diagram shown in figure 7-5 illustrates the velocities and forces (per unit span) on a 2D blade section in the axial \mathbf{e}_a and tangential \mathbf{e}_t directions. The propeller shaft rotates with angular velocity $\omega \mathbf{e}_a$, such that the apparent tangential (swirl) inflow at radius r is $-\omega r \mathbf{e}_t$. Also shown in figure 7-5 are the axial and tangential inflow velocities, $\mathbf{V}_a = -V_a \mathbf{e}_a$ and $\mathbf{V}_t = -V_t \mathbf{e}_t$; induced axial and tangential velocities, $\mathbf{u}_a^* = -u_a^* \mathbf{e}_a$ and $\mathbf{u}_t^* = -u_t^* \mathbf{e}_t$ (note that $u_t^* < 0$ during normal propeller operation, so \mathbf{u}_t^* actually points in the \mathbf{e}_t direction, as drawn); and the total resultant inflow velocity, \mathbf{V}^* , which has magnitude

$$V^* = \sqrt{(V_a + u_a^*)^2 + (\omega r + V_t + u_t^*)^2} \quad (7.2.1)$$

and is oriented at pitch angle,

$$\beta_i = \arctan \left(\frac{V_a + u_a^*}{\omega r + V_t + u_t^*} \right) \quad (7.2.2)$$

to the \mathbf{e}_t axis. Also shown on figure 7-5 are the angle of attack, α ; blade pitch angle $\theta = \alpha + \beta_i$; circulation, $\Gamma \mathbf{e}_r$; (inviscid) Kutta-Joukowski lift force, $\mathbf{F}_i = \rho \mathbf{V}^* \times (\Gamma \mathbf{e}_r)$; and viscous drag force, \mathbf{F}_v , aligned with \mathbf{V}^* . Assuming the Z blades are identical, the total thrust and torque *on the propeller* are

$$\mathbf{T} = Z \int_{r_h}^R [F_i \cos \beta_i - F_v \sin \beta_i] dr \quad (\hat{e}_a) \quad (7.2.3)$$

$$\mathbf{Q} = Z \int_{r_h}^R [F_i \sin \beta_i + F_v \cos \beta_i] r dr \quad (-\hat{e}_a) \quad (7.2.4)$$

where $F_i = \rho V^* \Gamma$ and $F_v = \frac{1}{2} \rho (V^*)^2 C_D c$ are the magnitudes of the inviscid and viscous force per unit radius, ρ is the fluid density, C_D is the section drag coefficient, c is the section chord, and r_h and R are the radius of the hub and blade tip, respectively.

The fluid dynamic power of the propeller acting *on the fluid* is the product of torque and angular velocity

$$P = Q\omega \quad (7.2.5)$$

where $P > 0$ indicates that power is being put into the fluid by the propeller (i.e. the torque resists the motion). The useful power produced by the propeller is TV_s where V_s is the ship speed (i.e. free-stream speed), so the efficiency of the propeller is

$$\eta = \frac{TV_s}{Q\omega} \quad (7.2.6)$$

Following Kerwin (2007), OPENPROP employs a standard propeller vortex lattice model to compute the axial and tangential induced velocities, $\{u_a^*, u_t^*\}$. In the vortex lattice formulation, a Z -bladed propeller is modeled as a single representative radial lifting line, partitioned into M panels. A horseshoe vortex filament with circulation $\Gamma_{(i)}$ surrounds the i^{th} panel, consisting of helical trailing vortex filaments shed from the panel endpoints ($r_{v(i)}$ and $r_{v(i+1)}$) and the segment of the lifting line that spans the panel. The induced velocities are computed at *control points* on the lifting line

at radial locations $r_{c(m)}$, $m = 1 \dots M$, by summing the velocity induced by each horseshoe vortex

$$u_a^*(m) = \sum_{i=1}^M \Gamma(i) \bar{u}_a^{*(m,i)} \quad (7.2.7)$$

$$u_t^*(m) = \sum_{i=1}^M \Gamma(i) \bar{u}_t^{*(m,i)} \quad (7.2.8)$$

where $\bar{u}_a^{*(m,i)}$ and $\bar{u}_t^{*(m,i)}$ are the axial and tangential velocity induced at $r_{c(m)}$ by a unit-strength horseshoe vortex surrounding panel i . Since the lifting line itself does not contribute to the induced velocity,

$$\bar{u}_a^{*(m,i)} = \bar{u}_{a(m,i+1)} - \bar{u}_{a(m,i)} \quad (7.2.9)$$

$$\bar{u}_t^{*(m,i)} = \bar{u}_{t(m,i+1)} - \bar{u}_{t(m,i)} \quad (7.2.10)$$

where $\bar{u}_{a(m,i)}$ and $\bar{u}_{t(m,i)}$ are the axial and tangential velocities induced at $r_{c(m)}$ by a unit-strength constant-pitch constant-radius helical vortex filament shed from $r_{v(i)}$, with the circulation vector directed *downstream* (i.e. away from the lifting line) by right-hand rule. These are computed using the approximations by Wrench (1957):

for $r_{c(m)} < r_{v(i)}$:

$$\begin{aligned} \bar{u}_{a(m,i)} &= \frac{Z}{4\pi r_c} (y - 2Zyy_0F_1) \\ \bar{u}_{t(m,i)} &= \frac{Z^2}{2\pi r_c} (y_0F_1) \end{aligned} \quad (7.2.11)$$

for $r_{c(m)} > r_{v(i)}$:

$$\begin{aligned} \bar{u}_{a(m,i)} &= -\frac{Z^2}{2\pi r_c} (yy_0F_2) \\ \bar{u}_{t(m,i)} &= \frac{Z}{4\pi r_c} (1 + 2Zy_0F_2) \end{aligned} \quad (7.2.12)$$

where

$$\begin{aligned}
F_1 &\approx \frac{-1}{2Zy_0} \left(\frac{1+y_0^2}{1+y^2} \right)^{\frac{1}{4}} \left\{ \frac{U}{1-U} + \frac{1}{24Z} \left[\frac{9y_0^2+2}{(1+y_0^2)^{1.5}} + \frac{3y^2-2}{(1+y^2)^{1.5}} \right] \ln \left| 1 + \frac{U}{1-U} \right| \right\} \\
F_2 &\approx \frac{1}{2Zy_0} \left(\frac{1+y_0^2}{1+y^2} \right)^{\frac{1}{4}} \left\{ \frac{1}{U-1} - \frac{1}{24Z} \left[\frac{9y_0^2+2}{(1+y_0^2)^{1.5}} + \frac{3y^2-2}{(1+y^2)^{1.5}} \right] \ln \left| 1 + \frac{1}{U-1} \right| \right\} \\
U &= \left(\frac{y_0 (\sqrt{1+y^2} - 1)}{y (\sqrt{1+y_0^2} - 1)} \exp \left(\sqrt{1+y^2} - \sqrt{1+y_0^2} \right) \right)^Z \\
y &= \frac{r_c}{r_v \tan \beta_w} \\
y_0 &= \frac{1}{\tan \beta_w}
\end{aligned}$$

and β_w is the pitch angle of the helical vortices in the wake. Consistent with *moderately-loaded lifting line theory*, I set $\beta_w = \beta_i$ in order to ‘align’ the wake with the local flow at the blade (Kerwin, 2007).

Following Kerwin (2007), a propeller hub is modeled as an image vortex lattice, with the image trailing vortex filaments having equal and opposite strength as the real vortex filaments, radii $r_{im(i)} = \frac{r_h^2}{r_v(i)}$, and pitch angle $\tan[\beta_i^{im}] = \frac{r_v(1) \cdot \tan[\beta_i^v(1)]}{r_{im}}$. The image vorticity is shed through the trailing surface of the hub and rolls up into a *hub vortex* of radius, r_o , and the drag due to the hub vortex is $\mathbf{D}_h = \frac{\rho Z^2}{16\pi} \left[\ln \left(\frac{r_h}{r_o} \right) + 3 \right] [\Gamma(1)]^2 (-\mathbf{e}_a)$. In OPENPROP the default hub radius is $\frac{r_h}{r_o} = 0.5$.

7.3 Propeller design optimization

The performance of a propeller can be computed given the circulation distribution, Γ , and flow parameters $\{V^*, \beta_i, u_a^*, u_t^*, \bar{u}_a^*, \bar{u}_t^*\}$. These all must be self-consistent for the state to be physically realistic. That is, equations $\{(7.2.1), (7.2.2), (7.2.7), (7.2.8), (7.2.9), (7.2.10)\}$ must all hold, given Γ . Thus, propeller design optimization reduces to finding the optimum circulation distribution.

Following Coney (1989), the propeller optimization problem is to find the set of M circulations of the vortex lattice panels that produce the least torque

$$Q = \rho Z \sum_{m=1}^M \{ [V_a + u_a^*] \Gamma + \frac{1}{2} V^* C_D c [\omega r_c + V_t + u_t^*] \} r_c \Delta r_v \quad (7.3.1)$$

for a specified thrust, T_s ,

$$\begin{aligned} T = \rho Z \sum_{m=1}^M & \{ [\omega r_c + V_t + u_t^*] \Gamma - \frac{1}{2} V^* C_D c [V_a + u_a^*] \} \Delta r_v \\ & - \text{Hflag} \cdot \frac{\rho Z^2}{16\pi} \left[\ln \left(\frac{r_h}{r_o} \right) + 3 \right] [\Gamma_{(1)}]^2 = T_s \end{aligned} \quad (7.3.2)$$

where Hflag is set to 1 to model a hub or 0 for no hub. Here, $\{\rho, Z, \omega\}$ are constants and $\{\Gamma, u_a^*, u_t^*, V^*, c, V_a, V_t, C_D, r_c, \Delta r_v\}$ are evaluated at $r_{c(m)}$ in the summation.

Coney (1989) employs the method of the Lagrange multiplier from variational calculus. He forms an auxiliary function, $H = Q + \lambda_1(T - T_s)$, where λ_1 is the unknown Lagrange multiplier that introduces the thrust constraint (7.3.2). Clearly, if $T = T_s$, then a minimum H coincides with a minimum Q . To find this minimum, the derivatives with respect to the unknowns are set to zero

$$\frac{\partial H}{\partial \Gamma_{(i)}} = 0 \quad \text{for } i = 1 \dots M \quad (7.3.3)$$

$$\frac{\partial H}{\partial \lambda_1} = 0 \quad (7.3.4)$$

which is a system of $M + 1$ equations for as many unknowns $\{\Gamma_{(i=1\dots M)}, \lambda_1\}$. This non-linear system of equations is solved iteratively until convergence of the optimized circulation distribution, Γ , and flow parameters $\{V^*, \beta_i, u_a^*, u_t^*, \bar{u}_a^*, \bar{u}_t^*\}$.

The section chord length, c , can also be optimized . Equation (7.3.1) shows that minimizing c minimizes the parasitic torque due to viscous drag. However, since c is related to the loading by $C_L = \frac{\Gamma}{\frac{1}{2}(V^*)c}$, where C_L is the section lift coefficient, the

chord cannot be made arbitrarily small. If a maximum allowable lift coefficient is chosen, (typically, $0.1 < C_{L_{\max}} < 0.5$), then the “optimum” chord is

$$c = \frac{|\Gamma|}{\frac{1}{2}(V^*)C_{L_{\max}}} \quad (7.3.5)$$

Turning our attention back to equations (7.3.3) and (7.3.4), we can now evaluate the required partial derivatives of Γ , λ_1 , u_a^* , u_t^* , V^* , and c with respect to $\Gamma(i)$ and λ_1 :

$$\frac{\partial \Gamma(m)}{\partial \Gamma(i)} = \begin{cases} 0 & (m \neq i) \\ 1 & (m = i) \end{cases}, \quad \frac{\partial \lambda_1}{\partial \lambda_1} = 1 \quad (7.3.6)$$

$$\frac{\partial u_a^*(m)}{\partial \Gamma(i)} = \bar{u}_a^*(m,i) \quad , \quad \frac{\partial u_t^*(m)}{\partial \Gamma(i)} = \bar{u}_t^*(m,i) \quad (7.3.7)$$

$$\begin{aligned} \frac{\partial V^*(m)}{\partial \Gamma(i)} &= \frac{1}{2}(V^*)^{-1} \left(\begin{array}{l} 2(V_a + u_a^*) \frac{\partial u_a^*(m)}{\partial \Gamma(i)} + \\ 2(\omega r_c + V_t + u_t^*) \frac{\partial u_t^*(m)}{\partial \Gamma(i)} \end{array} \right) \\ &= \sin(\beta_i(m)) \bar{u}_a^*(m,i) + \cos(\beta_i(m)) \bar{u}_t^*(m,i) \end{aligned} \quad (7.3.8)$$

$$\frac{\partial c(m)}{\partial \Gamma(i)} = \frac{2}{V^*(m)C_{L_{\max}}} \frac{\partial \Gamma(m)}{\partial \Gamma(i)} \cdot \frac{\Gamma(m)}{|\Gamma(m)|} - \frac{c(m)}{V^*(m)} \frac{\partial V^*(m)}{\partial \Gamma(i)} \quad (7.3.9)$$

All other partial derivatives are zero or are ignored.

The system of equations $\{(7.3.3), (7.3.4)\}$ is non-linear, so the following iterative approach is used to solve them. During each solution iteration, flow parameters $\{u_a^*, u_t^*, \bar{u}_a^*, \bar{u}_t^*, V^*, \frac{\partial V^*}{\partial \Gamma}, c, \frac{\partial c}{\partial \Gamma}, \lambda_1\}$ are frozen in order to linearize $\{(7.3.3), (7.3.4)\}$. The linear system of equations, with the linearized unknowns marked as $\{\check{\Gamma}, \check{\lambda}_1\}$, is

$$\begin{aligned}
\frac{\partial H}{\partial \Gamma(i)} = & \rho Z \sum_{m=1}^M \check{\Gamma}(m) \cdot [\bar{u}_a^*(m,i) r_c(m) \Delta r_v(m) + \bar{u}_a^*(i,m) r_c(i) \Delta r_v(i)] \\
& + \rho Z V_a(i) r_c(i) \Delta r_v(i) \\
& + \rho Z \sum_{m=1}^M \frac{1}{2} C_D \left[\frac{\partial V^*(m)}{\partial \Gamma(i)} c(m) + V^*(m) \frac{\partial c(m)}{\partial \Gamma(i)} \right] [\omega r_c(m) + V_t(m) + u_t^*(m)] r_c(m) \Delta r_v(m) \\
& + \rho Z \sum_{m=1}^M \frac{1}{2} C_D V^*(m) c(m) [\bar{u}_t^*(m,i)] r_c(m) \Delta r_v(m) \\
& + \rho Z \lambda_1 \sum_{m=1}^M \check{\Gamma}(m) \cdot [\bar{u}_t^*(m,i) \Delta r_v(m) + \bar{u}_t^*(i,m) \Delta r_v(i)] \\
& + \rho Z \check{\lambda}_1 [\omega r_c(i) + V_t(i)] \Delta r_v(i) \\
& - \rho Z \check{\lambda}_1 \sum_{m=1}^M \frac{1}{2} C_D \left[\frac{\partial V^*(m)}{\partial \Gamma(i)} c(m) + V^*(m) \frac{\partial c(m)}{\partial \Gamma(i)} \right] [V_a(m) + u_a^*(m)] \Delta r_v \\
& - \rho Z \check{\lambda}_1 \sum_{m=1}^M \frac{1}{2} C_D V^*(m) c(m) [\bar{u}_a^*(m,i)] \Delta r_v \\
& - \text{Hflag} \cdot \frac{\partial \Gamma(1)}{\partial \Gamma(i)} \cdot \lambda_1 \frac{\rho Z^2}{8\pi} \left[\ln \left(\frac{r_h}{r_o} \right) + 3 \right] \check{\Gamma}(1) \\
= 0 \quad & \text{for } i = 1 \dots M \tag{7.3.10}
\end{aligned}$$

$$\begin{aligned}
\frac{\partial H}{\partial \lambda_1} = & \rho Z \sum_{m=1}^M \check{\Gamma}(m) \cdot [\omega r_c(m) + V_t(m) + u_t^*(m)] \Delta r_v(m) \\
& - \rho Z \sum_{m=1}^M \frac{1}{2} C_D V^*(m) c(m) [V_a(m) + u_a^*(m)] \Delta r_v(m) \\
& - \text{Hflag} \cdot \frac{\rho Z^2}{16\pi} \left[\ln \left(\frac{r_h}{r_o} \right) + 3 \right] \Gamma(1) \cdot \check{\Gamma}(1) \\
& - T_s \\
= 0 \quad & \tag{7.3.11}
\end{aligned}$$

The system $\{(7.3.10), (7.3.11)\}$ is solved for the now linear $\{\check{\Gamma}, \check{\lambda}_1\}$, the circulation and Lagrange multiplier are updated ($\Gamma = \check{\Gamma}, \lambda_1 = \check{\lambda}_1$), and the new Γ is used to update the flow parameters. Coney (1989) describes a ‘wake alignment procedure’ for updating the flow parameters, whereby he iteratively updates: (1) the induced velocities $\{u_a^*, u_t^*\}$ via $\{(7.2.7), (7.2.8)\}$; (2) the inflow angle β_i via (7.2.2); and (3) the horseshoe influence functions $\{\bar{u}_a^*, \bar{u}_t^*\}$ via $\{(7.2.9), (7.2.10)\}$, and iteration continues until convergence of these flow parameters. Given the now-aligned wake, he then updates the remaining flow parameters $\{V^*, \frac{\partial V^*}{\partial \Gamma}, c, \frac{\partial c}{\partial \Gamma}\}$ and continues the main iterative loop, finding the next guess for Γ . This wake alignment procedure is time-consuming and tenuous, because it is prone to crash if the induced velocities do not vary smoothly over the span.

I have implemented a slightly different optimization procedure in **OPENPROP**. In my implementation, I still solve $\{(7.3.10), (7.3.11)\}$ for a guess for $\{\check{\Gamma}, \check{\lambda}_1\}$, update the circulation and Lagrange multiplier ($\Gamma = \check{\Gamma}, \lambda_1 = \check{\lambda}_1$), and use the new Γ to update the flow parameters. However, in my procedure, I do not iteratively “align the wake”; instead, I make one new guess for the wake flow parameters and continue with the main iterative loop to find the next guess for Γ . Therefore, each iteration of the main loop involves updating Γ via $\{(7.3.10), (7.3.11)\}$. The critical step in the procedure is that $\{u_a^*, u_t^*\}$ are updated via $\{(7.2.7), (7.2.8)\}$ and then “repaired” by smoothing the velocities at the blade root and tip. This minor smoothing is critical to enable the entire system of equations to converge, because the alignment of the wake and the horseshoe influence functions which are fed into the next solution iteration are very sensitive to irregularities in the induced velocities. This smoothing is reasonable in the vortex-lattice model, since it introduces no more error than ignoring hub or tip vortex roll-up, or other flow features. Using these smooth induced velocities, the remaining flow parameters $\{\beta_i, \bar{u}_a^*, \bar{u}_t^*, V^*, \frac{\partial V^*}{\partial \Gamma}, c, \frac{\partial c}{\partial \Gamma}\}$ are updated via $\{(7.2.2), (7.2.9), (7.2.10), (7.2.1), (7.3.8), (7.3.5), (7.3.9)\}$. This process is repeated until convergence of all of

the flow parameters, yielding an optimized circulation distribution and a physically-realistic design operating state. Initial values of $\{\beta_i, V^*, \frac{\partial V^*}{\partial \Gamma}, \frac{\partial c}{\partial \Gamma}\}$ are computed with $\{u_a^*, u_t^*\} = 0$. The Lagrange multiplier is initialized at $\lambda_1 = -R$, and the section chord lengths at $c \approx 0$. If chord-length optimization is not desired, then $\frac{\partial c(m)}{\partial \Gamma(i)}$ is set to zero and the chord is set to the input value during the optimization process.

7.3.1 A modified design optimization method

It is of considerable interest to the propeller designer to adjust the circulation at the hub to prevent hub vortex shedding and cavitation. Coney (1989) gives a procedure for reducing the hub circulation using a *hub unloading factor*, which will not be discussed here. I developed an alternate design procedure that can be used to optimize the circulation distribution given the constraint of a prescribed hub circulation.

In Coney's optimization method (solving (7.3.10) and (7.3.11) for the optimum circulation distribution, Γ , and the associated Lagrange multiplier, λ_1), he ignores the derivatives of the induced velocities with respect to changes in wake influence. That is, equation (7.3.7) should be

$$\frac{\partial u_a^{*(m)}}{\partial \Gamma(i)} = \bar{u}_a^{*(m,i)} + \sum_{j=1}^M \Gamma(j) \frac{\partial \bar{u}_a^{*(m,j)}}{\partial \Gamma(i)} \quad (7.3.12)$$

and likewise for u_t^* . If equations (7.3.10) and (7.3.11) are modified to include this additional term, this results in an “optimum” circulation distribution being heavily loaded at the tip and unloaded at the root. This is physically unrealistic, because it would result in a strong tip vortex and a wake vortex sheet which is inconsistent with the model of the constant pitch helical wake (Kerwin, personal communication). Ignoring part of equation (7.3.12) is somewhat arbitrary.

Another somewhat arbitrary, yet quite useful change to the design optimization procedure is to fix the value of the Lagrange multiplier, λ_1 . In this new scheme, the

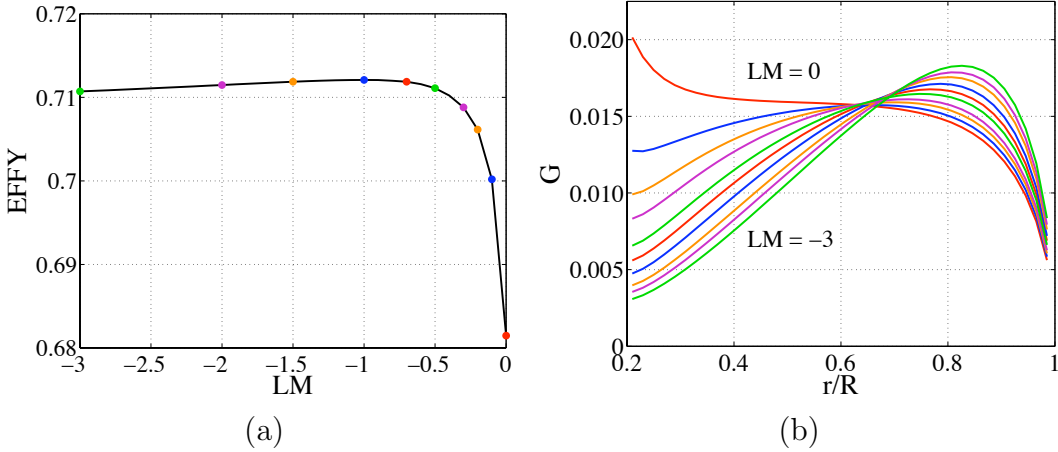


Figure 7-6: (a) Efficiency versus fixed Lagrange multiplier value ($LM = \frac{\lambda_1}{R}$), and (b) the corresponding optimized circulation distributions ($G = \frac{\Gamma}{2\pi RV_s}$), for the example propeller from Section 7.3.2. As the fixed LM becomes more negative, hub loading decreases, but efficiency is hardly affected.

optimum circulation distribution would still be found by iteratively solving (7.3.10) and (7.3.11), but one would *not* update λ_1 to the new value determined during each solution iteration. Using this procedure, each unique value of λ_1 results in a unique “optimum” circulation distribution. Of course, if one happened to fix λ_1 to the value that Coney’s method would result in, then the resulting circulation distributions would be the same in either case.

Interestingly, by fixing λ_1 , one can tune the circulation at the hub, as shown in figure 7-6. This figure shows the efficiency and circulation distribution for a range of fixed Lagrange multipliers for the example propeller described in Section 7.3.2. Figure 7-6 shows that as the fixed Lagrange multiplier value increases, the hub loading decreases, but the efficiency is hardly affected. Thus, by fixing λ_1 , an “optimum” circulation distribution can be found for the desired hub circulation.

The overall optimum circulation distribution can, of course, be found manually by trying several values of λ_1 . In this example, a fixed $\lambda_1 = -R$ actually results in a propeller with an ever-so-slightly higher efficiency than the propeller designed by Coney’s optimization scheme (with variable λ_1).

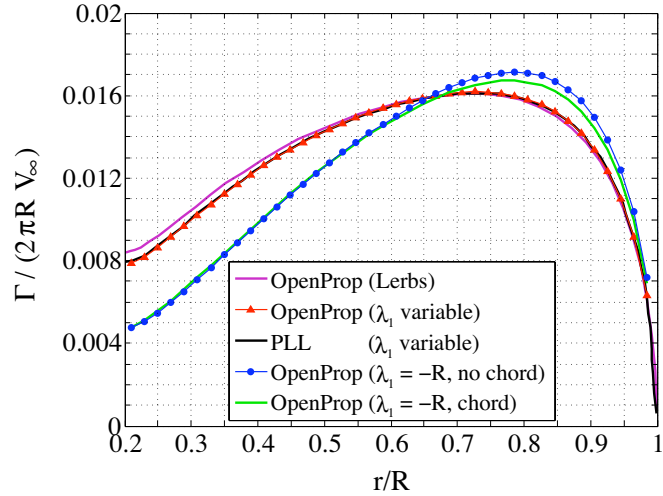


Figure 7-7: Example propeller circulation optimization. The OPENPROP variable- λ_1 circulation distribution ($\eta = 0.7096$) is almost identical to the PLL result, and both are similar to the OPENPROP Lerbs result ($\eta = 0.7088$). The OPENPROP fixed- λ scheme yields a quite different circulation distribution, with efficiency $\eta = 0.7121$ if chord is not optimized and $\eta = 0.7950$ if both chord and circulation are optimized.

7.3.2 Example propeller design

An example propeller optimization was performed for a 6-bladed propeller, with the following specs: $D = 3$ m, $D_h = 0.6$ m, $V_s = 4.5$ m/s, $n = 2$ rev/s, $T_s = 45,000$ N, such that $J = \frac{V_s}{nD} = 0.75$ and $K_{T_s} = \frac{T_s}{\rho n^2 D^4} = 0.1355$. Viscous forces are considered, with $C_D = 0.008$. Additional input parameters can be found in (Chung 2007, p. 50).

In this example, I compare the circulation distributions “optimized” using: Coney’s implementation of his method (Coney, 1989) in the U.S. Navy code PLL (with variable λ_1 and no chord-length optimization); my implementation of Coney’s method in OPENPROP (with variable λ_1 and no chord-length optimization); my fixed- λ_1 method (with and without chord optimization); and an optimizer implemented in OPENPROP that uses the Lerbs criterion (Lerbs, 1952). The optimized propellers are characterized by their circulation distribution, thrust coefficient, $K_T = \frac{T}{\rho n^2 D^4}$, torque coefficient, $K_Q = \frac{Q}{\rho n^2 D^5}$, and efficiency, $\eta = \frac{J}{2\pi} \frac{K_T}{K_Q}$. For reference, the efficiency of an actuator disc with $C_{T_s} = \frac{T_s}{\frac{1}{2}\rho V_s^2 \frac{\pi D^2}{4}} = 0.6134$ is $\eta = \frac{2}{1+\sqrt{1+C_{T_s}}} = 0.8810$.

The “optimized” circulation distributions are shown in figure 7-7. The the OPENPROP Lerbs optimizer result provides a good baseline for comparison: It has performance $K_T = 0.1355$, $K_Q = 0.0228$, and $\eta = 0.7088$. The circulation distribution computed using the OPENPROP optimizer with variable λ_1 is nearly identical to the PLL optimizer result, and both are quite similar to the OPENPROP Lerbs optimizer result. OPENPROP computes $K_T = 0.1355$, $K_Q = 0.0228$, and $\eta = 0.7096$ for its circulation distribution, which converged with $\lambda_1 = -0.3387R$.

If the Lagrange multiplier is fixed at $\lambda_1 = -R$, my OPENPROP code computes a circulation distribution that is quite different than the variable- λ_1 OPENPROP and PLL results. The performance metrics for the propeller optimized with fixed $\lambda_1 = -R$ are $K_T = 0.1355$, $K_Q = 0.0227$, and $\eta = 0.7121$, which is a slightly higher efficiency than that given by the variable- λ_1 optimization scheme, but with much less hub loading. Not surprisingly, an even-higher-efficiency propeller is found by fixing $\lambda_1 = -R$ and optimizing both circulation and chord length, which yields $K_T = 0.1355$, $K_Q = 0.0203$, and $\eta = 0.7950$.

This example validates the OPENPROP design optimizer with the U.S. Navy code PLL, showing good agreement between the optimum circulation distributions determined by each code. This example also illustrates that by fixing the Lagrange multiplier, one can alter the circulation distribution (thus changing the hub circulation) with little effect on the predicted efficiency.

7.4 Propeller geometry

Once the design operating state of the propeller/turbine is known, the geometry can be determined to give such performance. The 3D geometry is built from given 2D section profiles that are scaled and rotated according to the design lift coefficient, chord length, and inflow angle $\{C_{L_0}, c, \beta_{i_0}\}$.

A given 2D section profile includes camber and thickness normalized by the chord, $\{\tilde{f}/c, \tilde{t}/c\}$, ideal angle of attack, $\tilde{\alpha}_I$, and ideal lift coefficient, \tilde{C}_{L_I} . Note that $\{\tilde{f}, \tilde{\alpha}_I, \tilde{C}_{L_I}\}$ scale linearly with the maximum camber, \tilde{f}_0 (Abbott and von Doenhoff, 1959). The section lift coefficient is given in terms of the geometry by $C_L = 2\pi(\alpha - \alpha_I) + C_{L_I}$ for $|\alpha - \alpha_I| \ll |\alpha - \alpha_I|_{\text{stall}}$, and the stall model is described in Section 7.5. In the geometry module, the angle of attack of each blade section is set to the ideal angle of attack ($\alpha = \alpha_I$) to prevent leading edge flow separation and/or cavitation. The lift coefficient then becomes the ideal lift coefficient ($C_L = C_{L_I}$). In order to achieve the desired lift coefficient, C_{L_0} , the given \tilde{C}_{L_I} is scaled by scaling the section camber. Thus, the desired lift coefficient and section geometry is

$$\{C_L, f_0, f, \alpha_I\} = \frac{C_{L_0}}{\tilde{C}_{L_I}} \cdot \{\tilde{C}_{L_I}, \tilde{f}_0, \tilde{f}, \tilde{\alpha}_I\} \quad (7.4.1)$$

The pitch angle of the blade section is then fixed at

$$\theta = \alpha_I + \beta_{i_0} \quad (7.4.2)$$

With this computed blade 2D section geometry, OPENPROP can then form the full 3D propeller geometry and export files for rapid prototyping of physical parts.

7.5 Off-design performance analysis

This section details the analysis of a propeller operating at an off-design (*OD*) *advance coefficient*

$$J_{s,OD} = \frac{V_s}{n_{OD} D} = \frac{\pi V_s}{\omega_{OD} R} \quad (7.5.1)$$

An off-design operating state is defined by the rotation rate, ω_{OD} , and unknown flow parameters $\{V^*, \alpha, C_L, \Gamma, u_a^*, u_t^*, \beta_i, \bar{u}_a^*, \bar{u}_t^*\}$, which all must be self-consistent for the state to be physically realistic.

To proceed, we need equations for the angle of attack, α , lift coefficient, C_L , and circulation, Γ . In the analyzer, the pitch angle, θ , of each blade section is fixed, so the net angle of attack is

$$\alpha - \alpha_I = \beta_{i_0} - \beta_i \quad (7.5.2)$$

The circulation can be computed from the 2D section lift coefficient, which is given in terms of the loading by

$$C_L = \frac{2\Gamma}{V^* c} \quad (7.5.3)$$

The 2D section lift and drag coefficients are shown in figure 7-8 and given in closed form by equations

$$\begin{aligned} C_L &= C_{L,0} + \frac{dC_L}{d\alpha} \Delta\alpha \\ &\quad - \frac{dC_L}{d\alpha} (\Delta\alpha - \Delta\alpha_{\text{stall}}) \cdot F(\Delta\alpha - \Delta\alpha_{\text{stall}}) \\ &\quad + \frac{dC_L}{d\alpha} (-\Delta\alpha - \Delta\alpha_{\text{stall}}) \cdot F(-\Delta\alpha - \Delta\alpha_{\text{stall}}) \end{aligned} \quad (7.5.4)$$

$$\begin{aligned} C_D &= C_{D,0} \\ &\quad + A \cdot (\Delta\alpha - \Delta\alpha_{\text{stall}}) \cdot F(\Delta\alpha - \Delta\alpha_{\text{stall}}) \\ &\quad + A \cdot (-\Delta\alpha - \Delta\alpha_{\text{stall}}) \cdot F(-\Delta\alpha - \Delta\alpha_{\text{stall}}) \\ &\quad - 2A \cdot (-\Delta\alpha_{\text{stall}}) \cdot F(-\Delta\alpha_{\text{stall}}) \end{aligned} \quad (7.5.5)$$

where the auxiliary function $F(x) = \frac{\arctan(Bx)}{\pi} + \frac{1}{2}$ has limits $F(x \rightarrow -\infty) \rightarrow 0$ and $F(x \rightarrow \infty) \rightarrow 1$. Here: $\Delta\alpha = \alpha - \alpha_I$ [rad]; $\Delta\alpha_{\text{stall}} = 8\frac{\pi}{180}$ [rad] is the default OPENPROP stall angle; $B = 20$ is the default OPENPROP stall sharpness parameter; $A = \frac{2-C_{D,0}}{\frac{\pi}{2}-\Delta\alpha_{\text{stall}}}$ is drag coefficient post-stall slope; and $\frac{dC_L}{d\alpha} = 2\pi$ is default OPENPROP lift curve slope, which is consistent with linear foil theory. These values are used in all calculations unless specifically noted otherwise. Thus $C_L \approx C_{L,0} + 2\pi(\alpha - \alpha_I)$ before stall and approximately constant post stall. The drag coefficient is approximately constant until stall and then rises to the canonical value of 2 when the inflow is normal

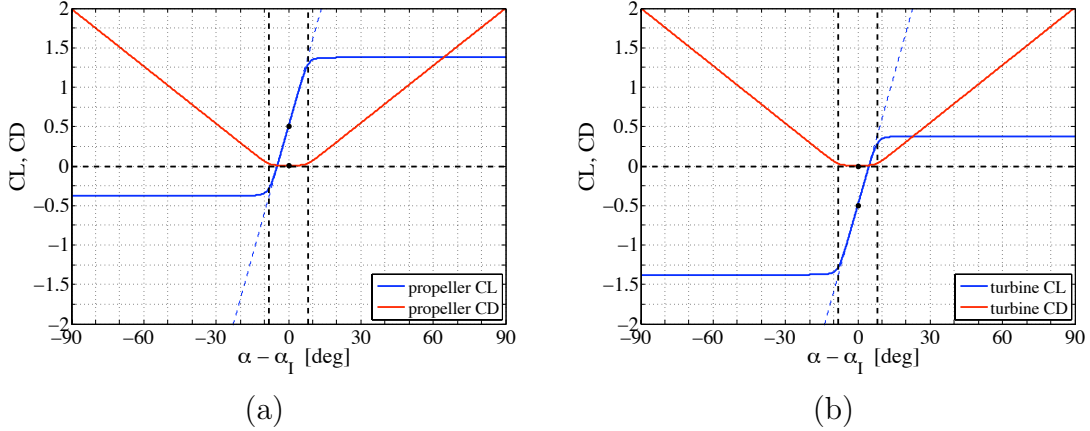


Figure 7-8: Lift coefficient, C_L , and drag coefficient, C_D , versus net angle of attack, $\alpha - \alpha_I$, for the (a) propeller and (b) turbine cases, with $\frac{dC_L}{d\alpha} = 2\pi$ and on-design specifications $C_{L_0} = 0.5$ and $C_{D_0} = 0.05$. The vertical dashed lines at $|\alpha - \alpha_I|_{\text{stall}} = \pm 8$ deg indicate the stall angle of attack.

to the blade. This type of model is used in ASWING (Drela, 1999). Equations (7.5.4) and (7.5.5) offer the flexibility to change the stall angle, lift curve slope, and drag coefficient to more accurately model foil sections of moderate thickness to chord ratios.

The operating states of a propeller or turbine for each given ω_{OD} are computed as follows. An operating state is defined by ω_{OD} and unknown flow parameters $\{V^*, \alpha, C_L, \Gamma, u_a^*, u_t^*, \beta_i, \bar{u}_a^*, \bar{u}_t^*\}$, which all must be self-consistent for the state to be physically-realistic. That is, equations $\{(7.2.1), (7.5.2), (7.5.4), (7.5.3), (7.2.7), (7.2.8), (7.2.2), (7.2.9), (7.2.10)\}$ must all hold, given ω_{OD} . Since there are M vortex panels, there are $7M + 2M^2$ unknowns and a system of $7M + 2M^2$ non-linear equations that govern the state of the system. This system is solved in OPENPROP using an approach similar to a Newton solver.

Since the $7M + 2M^2$ equations are coupled through the parameters $\{\beta_i, \bar{u}_a^*, \bar{u}_t^*\}$, I decouple them by considering two state vectors: $\mathbf{X} = \{V^*, \alpha, C_L, \Gamma, u_a^*, u_t^*\}^\top$ and $\mathbf{Y} = \{\beta_i, \bar{u}_a^*, \bar{u}_t^*\}$. During each solution iteration, state vector \mathbf{X} is updated, and then \mathbf{Y} is updated; this process repeats until convergence of the entire system.

Consider state vector \mathbf{X} : It consists of M sets of 6 state variables, one set per vortex panel. The 6 variables for each vortex panel are coupled to one another, but not to the other variables in \mathbf{X} . Thus, \mathbf{X} can be partitioned into M state vectors, $\mathbf{X} = \{\mathbf{x}_1, \dots, \mathbf{x}_M\}^\top$, where $\mathbf{x}_m = \{V^*, \alpha, C_L, \Gamma, u_a^*, u_t^*\}^\top$ with each variable evaluated at $r_c(m)$. Each of these state vectors can be updated independently.

Each vortex panel state vector, \mathbf{x}_m , is updated using a Newton solver. Define the residual vector for the m^{th} panel as

$$\mathbf{R}_m = \begin{bmatrix} V^* - \sqrt{(V_a + u_a^*)^2 + (\omega_{OD}r_c + V_t + u_t^*)^2} \\ \alpha - (\alpha_I + \beta_{i_0} - \beta_i) \\ C_L - C_L(\alpha) \\ \Gamma - \left(\frac{1}{2}C_L V^* c\right) \\ u_a^* - [\bar{u}_a^*] \cdot [\Gamma] \\ u_t^* - [\bar{u}_t^*] \cdot [\Gamma] \end{bmatrix} \quad (7.5.6)$$

where each variable is evaluated at $r_c(m)$. In order to drive the residuals to zero, the desired change in the state vector, $\mathbf{d}\mathbf{x}_m$, is found by solving the matrix equation

$$0 = \mathbf{R}_m + \mathbf{J}_m \cdot \mathbf{d}\mathbf{x}_m$$

where non-zero the elements of the Jacobian matrix, $\mathbf{J}_{m(i,j)} = \frac{\partial \mathbf{R}_m(i)}{\partial \mathbf{x}_m(j)}$, are

$$\begin{aligned}
\mathbf{J}_{m(i,i)} &= \frac{\partial R_{V^*}}{\partial V^*} = \frac{\partial R_\alpha}{\partial \alpha} = \frac{\partial R_{C_L}}{\partial C_L} = \frac{\partial R_\Gamma}{\partial \Gamma} = \frac{\partial R_{u_a^*}}{\partial u_a^*} = \frac{\partial R_{u_t^*}}{\partial u_t^*} = 1 \quad (i = 1 \dots 6) \\
\mathbf{J}_{m(1,5)} &= \frac{\partial R_{V^*}}{\partial u_a^*} = -\frac{V_a + u_a^*}{\sqrt{(V_a + u_a^*)^2 + (\omega_{OD}r_c + V_t + u_t^*)^2}} \\
\mathbf{J}_{m(1,6)} &= \frac{\partial R_{V^*}}{\partial u_t^*} = -\frac{\omega_{OD}r + V_t + u_t^*}{\sqrt{(V_a + u_a^*)^2 + (\omega_{OD}r_c + V_t + u_t^*)^2}} \\
\mathbf{J}_{m(2,5)} &= \frac{\partial R_\alpha}{\partial u_a^*} = \frac{\partial R_\alpha}{\partial \beta_i} \cdot \frac{\partial \beta_i}{\partial \tan(\beta_i)} \cdot \frac{\partial \tan(\beta_i)}{\partial u_a^*} = \frac{1}{1 + \tan^2(\beta_i)} \cdot \frac{1}{\omega_{OD}r_c + V_t + u_t^*} \\
\mathbf{J}_{m(2,6)} &= \frac{\partial R_\alpha}{\partial u_t^*} = \frac{\partial R_\alpha}{\partial \beta_i} \cdot \frac{\partial \beta_i}{\partial \tan(\beta_i)} \cdot \frac{\partial \tan(\beta_i)}{\partial u_t^*} = \frac{1}{1 + \tan^2(\beta_i)} \cdot \frac{-\tan(\beta_i)}{\omega_{OD}r_c + V_t + u_t^*} \\
\mathbf{J}_{m(3,2)} &= \frac{\partial R_{C_L}}{\partial \alpha} = -\frac{dC_L(\alpha)}{d\alpha} \\
\mathbf{J}_{m(4,1)} &= \frac{\partial R_\Gamma}{\partial V^*} = -\frac{1}{2} C_L c \\
\mathbf{J}_{m(4,3)} &= \frac{\partial R_\Gamma}{\partial C_L} = -\frac{1}{2} V^* c \\
\mathbf{J}_{m(5,4)} &= \frac{\partial R_{u_a^*}}{\partial \Gamma} = -\bar{u}_a^*(m,m) \\
\mathbf{J}_{m(6,4)} &= \frac{\partial R_{u_t^*}}{\partial \Gamma} = -\bar{u}_t^*(m,m) \\
\mathbf{J}_{m(5,2)} &= \frac{\partial R_{u_a^*}}{\partial \alpha} = \frac{\partial R_{u_a^*}}{\partial \beta_i} \cdot \frac{\partial \beta_i}{\partial \alpha} = \sum_{j=1}^M \Gamma_{(j)} \frac{\partial \bar{u}_a^*(m,j)}{\partial \beta_i(m)} \\
\mathbf{J}_{m(6,2)} &= \frac{\partial R_{u_t^*}}{\partial \alpha} = \frac{\partial R_{u_t^*}}{\partial \beta_i} \cdot \frac{\partial \beta_i}{\partial \alpha} = \sum_{j=1}^M \Gamma_{(j)} \frac{\partial \bar{u}_t^*(m,j)}{\partial \beta_i(m)}
\end{aligned}$$

where the flow parameters are evaluated at $r_{c(m)}$ unless explicitly stated. All other terms are zero or are ignored.

The state vector for the next iteration, then, is $\mathbf{x}_m^{\text{next}} = \mathbf{x}_m^{\text{current}} + \mathbf{d}\mathbf{x}_m$. By solving one Newton iteration for each of the $m = 1, \dots, M$ vortex panels, state vector $\mathbf{X} = \{\mathbf{x}_1, \dots, \mathbf{x}_M\}^\top$ is updated.

Given the new \mathbf{X} values, \mathbf{Y} is updated: β_i is updated via (7.2.2), and then $\{\bar{u}_a^*, \bar{u}_t^*\}$ are updated via $\{(7.2.9), (7.2.10)\}$. In the next solution iteration, these new values of \mathbf{Y} are used to update \mathbf{X} , and so on. Since the solution scheme updates both \mathbf{X} and

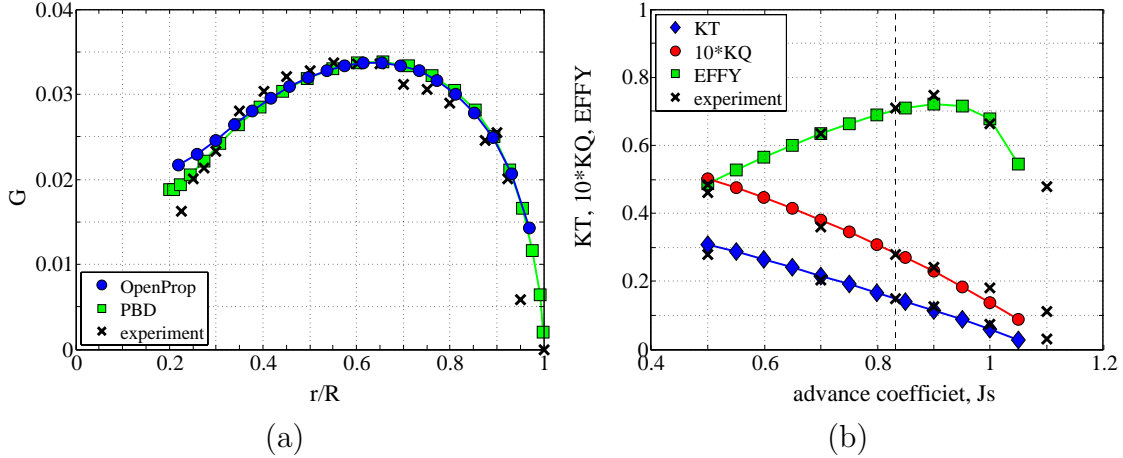


Figure 7-9: (a) Design circulation distribution for U.S. Navy propeller 4119, and (b) off-design performance curves for propeller 4119. OPENPROP results agree with PBD code solution and experimental data from (Black, 1997).

\mathbf{Y} in each iteration, it accounts for the coupled interaction between all $7M + 2M^2$ unknown flow parameters and converges on a physically-realistic operating state of the system.

The system is said to converge when all $6M$ elements of \mathbf{X} have converged. Since β_i is directly related to α and \bar{u}_a^* and \bar{u}_t^* are functions of β_i , once α converges, this implies that \mathbf{Y} has converged as well. For each operating state, the analyzer computes the propeller/turbine thrust, torque, and power coefficients and efficiency.

The OPENPROP analyzer was validated with *U.S. Navy propeller 4119*. Figure 7-9a shows the circulation distribution of an OPENPROP-designed version of 4119, showing good agreement with U.S. Navy code PBD and experimental data from (Black, 1997). Figure 7-9b also shows good agreement between the off-design performance curve predicted by OPENPROP and experimental data from (Black, 1997), thus validating the performance analysis method presented herein.

The performance analyzer also enables cavitation analysis, which requires the blade surface pressure distribution. The pressure distribution is computed in OPENPROP using either of two 2D foil solvers that require the lift coefficient

distribution. The lift coefficient distribution is found in the analyzer for each off-design operating state. Peterson (2008) developed a cavitation analysis module using the open-source code XFOIL (Drela, 1989). Chung (2007) implemented a simpler 2D vortex lattice code that can also be used as the 2D foil solver engine. The pressure distribution results are incorporated in a module that generates Brockett diagrams for a given blade design and off-design operating state. Using the Brockett diagram, the thickness ratio can be chosen to give adequate on-design cavitation margin and off-design angle of attack margin. The 2D solvers can also be used to analyze the blade pressure coefficient distributions for determining cavitation margin and location by comparing the pressure coefficient to the local cavitation number of the section.

7.5.1 Example propeller off-design analysis

As an illustrative example of off-design performance analysis, I now replicate the propellers designed in Coney (1989, p. 28-31). In this exercise, several propellers are designed to give the same thrust coefficient, $C_T = 0.512$, for a range of design advance coefficients

$$J_s = \frac{V_s}{nD} = \frac{\pi V_s}{\omega R}$$

Each is a hubless, five-bladed propeller with a diameter $D = 1$ m, hub diameter $D_{\text{hub}} = 0.2$ m, and ship speed $V_s = 1$ m/s. The chord lengths are optimized for each propeller, with $C_{L,\max} = 0.2$, and viscous effects are ignored.

Each of the circulation distributions in figure 7-10a were optimized to give the same thrust, for the prescribed advance coefficient. The distributions I computed using OPENPROP agree well with those computed by Coney; minor disagreement is expected, since Coney did not align the wake to the local flow (i.e. he computed the wake influence functions with the wake aligned to the undisturbed flow, which is acceptable for lightly-loaded propellers such as these). The on-design efficiencies

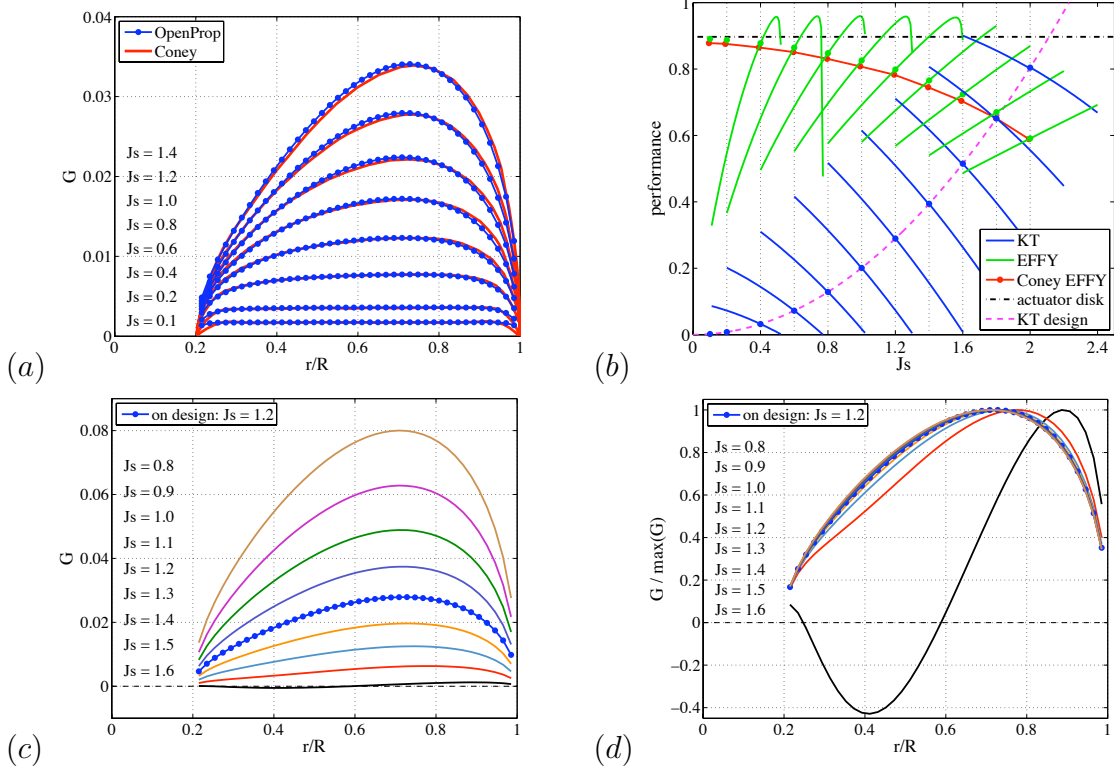


Figure 7-10: Example 5-bladed propellers from Coney (1989): (a) on-design circulation distributions for propellers designed for selected advance coefficients, (b) off-design performance of these propellers, (c) off-design circulation distributions for the propeller with on-design advance coefficient $J_s = 1.2$: (d) off-design circulation distributions each normalized by its maximum value.

computed by Coney also agree well with those I calculate, as shown in figure 7-10b.

Using my off-design performance analyzer, I computed the performance of each of these propellers for a range of advance coefficients. I show in figure 7-10b the off-design efficiency, EFFY, and thrust coefficient, KT, of all these propellers; the torque coefficient is omitted for clarity. The black dash-dotted line represents the efficiency of an *actuator disc* producing a thrust coefficient of $C_T = 0.512$, which is

$$EFFY = \frac{2}{1 + \sqrt{1 + C_T}} = 0.8970 \quad (7.5.7)$$

Propellers designed for advance coefficients approaching zero approach the actuator disk efficiency, since the rotation rate approaches infinity in this limit, and the blades

lose their identity and ‘become’ the actuator disk. The magenta dashed line represents the required thrust coefficient, for a given advance ratio, since

$$K_T = \frac{\pi}{8} C_T \cdot J_s^2 \quad (7.5.8)$$

by definition. Each of the propellers meets this thrust requirement on-design, and they produce larger K_T for smaller off-design J_s , and visa versa. This change in loading is due to the change in net angle of attack: Referring to the propeller velocity/force diagram, figure 7-5, recall the raw inflow angle is defined as

$$\tan \beta = \frac{V_s}{\omega r} = \frac{J_s}{\pi} \cdot \frac{R}{r} \quad (7.5.9)$$

For small off-design J_s , the apparent tangential inflow due to propeller rotation is larger, and the inflow angle is smaller. This corresponds to an increased angle of attack (since the blade pitch is fixed) and, therefore, increased loading. Figure 7-10c shows the load distribution for several off-design advance coefficients for the propeller designed for $J_s = 1.2$; loading increases as J_s decreases, and visa versa. For larger off-design J_s , this corresponds to larger inflow angles, reduced angle of attack, and reduced loading.

Consideration of equation (7.5.9) reveals that a change in advance coefficient should affect the innermost blade sections more than the outermost sections, since $\frac{R}{r}$ increases with decreasing radial position r . Thus, the off-design circulation distribution should shift inwards for lower advance coefficients (i.e. higher rotation rates) and shift outwards for higher advance coefficients. This is demonstrated in figure 7-10, which shows the off-design circulation distributions, each normalized by its maximum value. This effect is minimal for low advance coefficients but is quite dramatic for higher advance coefficients, which tend to unload the root more than the tip, shifting the circulation distribution outboard.

7.6 Non-dimensional parameters

Table 7.1 summarizes the non-dimensional form of the flow- and performance parameters discussed herein.

OPENPROP	Herein	Description
Vs	V_s	ship speed (free-stream speed) [m/s]
R	R	propeller radius [m]
D	D	propeller diameter [m]
n	n	rotation rate [rev/s] ($\omega = 2\pi n$)
Rhub_oR	r_h/R	normalized hub radius
RC	r_c/R	normalized control point radius
DR	$\Delta r_v/R$	normalized difference in vortex radii
CoD	c/D	normalized section chord
VAC	V_a/V_s	normalized axial inflow velocity
VTC	V_t/V_s	normalized tangential inflow velocity
UASTAR	u_a^*/V_s	normalized induced axial velocity
UTSTAR	u_t^*/V_s	normalized induced tangential velocity
UAHIF	$2\pi R \cdot \bar{u}_a^*$	normalized axial horseshoe influence function
UTHIF	$2\pi R \cdot \bar{u}_t^*$	normalized tangential horseshoe influence function
G	$\Gamma/(2\pi RV_s)$	normalized circulation
VSTAR	V^*/V_s	normalized total inflow speed
dVdG	$2\pi R \cdot \frac{\partial V^*}{\partial \Gamma}$	normalized $\frac{\partial V^*}{\partial \Gamma}$
dcdG	$\pi V_s \cdot \frac{\partial c}{\partial \Gamma}$	normalized $\frac{\partial c}{\partial \Gamma}$
dVdW	$\frac{\partial V^*}{\partial \omega}/R$	normalized $\frac{\partial V^*}{\partial \omega}$
LM	λ_1/R	normalized Lagrange multiplier
CT	$C_T = \frac{T}{\frac{1}{2}\rho V_s^2 \pi R^2}$	thrust coefficient based on ship speed
CQ	$C_Q = \frac{Q}{\frac{1}{2}\rho V_s^2 \pi R^3}$	torque coefficient based on ship speed
CP	$C_P = \frac{Q\omega}{\frac{1}{2}\rho V_s^3 (\pi R^2)}$	power coefficient ($C_P = \frac{\omega R}{V_s} C_Q = \lambda C_Q = \frac{C_Q \pi}{J_s}$)
KT	$K_T = \frac{T}{\rho n^2 D^4}$	thrust coefficient based on blade tip speed
KQ	$K_Q = \frac{Q}{\rho n^2 D^5}$	torque coefficient based on blade tip speed
Js	$J_s = \frac{V_s}{nD} = \frac{\pi V_s}{\omega R}$	advance coefficient
L	$\lambda = \frac{\omega R}{V_s} = \frac{\pi}{J_s}$	tip-speed ratio

Table 7.1: Table of non-dimensional flow parameters in OPENPROP.

7.7 Summary

We began this chapter by developing lifting line theory using the impulse-force framework presented in Chapter 1 of this thesis: We showed that both steady and unsteady forces given by lifting line theory can also be computed using a vortex lattice, with the net force on the body being equal to the sum of the impulsive pressure force and the force due to the rate of increase of impulse in the fluid. We then applied lifting line theory to the design optimization and off-design analysis of marine propellers.

Two main contributions were made in this chapter: (1) a propeller optimization method for prescribed hub loading, and (2) a lifting-line-based off-design performance analysis method for propellers. A propeller optimization method was presented in Section 7.3.1, whereby the designer can optimize the circulation distribution while prescribing the hub loading, and figure 7-6 shows that this can be done with little if any penalty in efficiency for a range of hub loadings. This is a valuable method to prevent hub cavitation and noise, while still designing a nearly-optimum propeller.

This chapter features a method for off-design analysis of marine propellers using lifting line theory. In Section 7.5, I described the system of equations which must be satisfied for an off-design state to be physically realistic, and I described an approach similar to a Newton solver that can be used to determine this state, given an off-design advance coefficient. I validated my method with experimental data for U.S. Navy propeller 4119, as shown in figure 7-9. My off-design analysis method makes **OPENPROP** a valuable tool for the preliminary design of ocean-going vehicles. The designer can now obtain a preliminary propeller design *and* its performance curve, which can be used in ship-level design studies, such as determining powering requirements and fuel consumption of the vehicle. My performance analysis also enables cavitation analysis or structural analysis for off-design conditions, which are valuable tools for the propeller designer.

Bibliography

- Abbott IH, von Doenhoff AE (1959) Theory of Wing Sections Dover.
- Anderson JD (2007) Fundamentals of Aerodynamics 4th edn. McGraw Hill.
- Black SD (1997) Integrated lifting surface / Navier-Stokes design and analysis methods for marine propulsors PhD thesis, MIT.
- Carlton JS (1994) Marine Propellers and Propulsion Butterworth-Heinemann.
- Chung HL (2007) An enhanced propeller design program based on propeller vortex lattice lifting line theory Master's thesis, MIT.
- Coney WB (1989) A Method for the Design of a Class of Optimum Marine Propulsors PhD thesis, MIT.
- D'Epagnier KP, Chung HL, Stanway MJ, Kimball RW (2007) "An open source parametric propeller design tool," In: Oceans.
- Drela M (1989) "XFOIL: An analysis and design system for low Reynolds number airfoils," In: Low Reynolds Number Aerodynamics: Proceedings for the Conference Notre Dame, Springer-Verlag.
- Drela M (1999) "Integrated simulation model for preliminary aerodynamic, structural, and control-law design of aircraft," In: AIAA SDM Conference 99-1394.
- Epps BP, Chalfant JS, Kimball RW, Techet AH, Flood K, Chryssostomidis C (2009a) "OPENPROP: An open-source parametric design and analysis tool for propellers," In: Grand Challenges in Modeling and Simulation (GCMS09) Istanbul, Turkey.
- Epps BP, Stanway MJ, Kimball RW (2009b) "OPENPROP: An open-source design tool for propellers and turbines," In: SNAME Propellers and Shafting.
- Flood K (2009) Propeller performance analysis using lifting line theory Master's thesis, MIT.

Kerwin JE (2007) Hydrofoils and propellers MIT course 2.23 notes.

Kerwin JE and Hadler JB (2010) Principles of Naval Architecture: Propulsion SNAME, to appear.

Kimball RW, Epps BP (2007) OPENPROP MATLAB code, open-source at <http://web.mit.edu/OpenProp/www>

Lerbs H (1952) “Moderately loaded propellers with a finite number of blades and an arbitrary distribution of circulation,” In: SNAME Transactions vol 60.

Newman J (1977) Marine Hydrodynamics MIT Press.

Peterson CJ (2008) Minimum pressure envelope cavitation analysis using two-dimensional panel method Master’s thesis, MIT.

Saffman P (1995) Vortex Dynamics Cambridge University Press.

Stubblefield JM (2008) Numerically based ducted propeller design using vortex lattice lifting line theory Master’s thesis, MIT.

Theodorsen T (1935) “General theory of aerodynamic instability and the mechanism of flutter,” Technical Report TR490, NACA.

Wrench JW (1957) “The calculation of propeller induction factors,” Technical Report 1116, David Taylor Model Basin.

[THIS PAGE INTENTIONALLY LEFT BLANK]

Chapter 8

Propeller off-design performance experiments

In this chapter, I present the results of steady propeller performance and unsteady startup experiments. We will find that the thrust, torque, and efficiency measured during steady tests match that predicted by my off-design performance analysis method, providing important validation data for my OPENPROP code suite. We will find that the propeller generates a vortex ring during unsteady start-up, which is similar to the vortex rings formed by a swimming fish during unsteady maneuvering.

8.1 Experimental setup

Steady and unsteady propeller performance tests were performed in the MIT Water Tunnel using an experimental setup similar to that used by Stettler (2004), as shown in figure 8-1. The propeller was mounted on a trolling motor (Minn Kota motor assembly, part number 2069060), which is a brushed DC motor that has maximum voltage and current ratings of 12V and 30A, respectively. This motor has torque constant $k_m = 0.06454 \text{ Nm/A}$ and speed constant $k_\omega = 15.494 \text{ (rad/s)/V}$ (as will be shown in the next section), which means that the maximum voltage and amperage

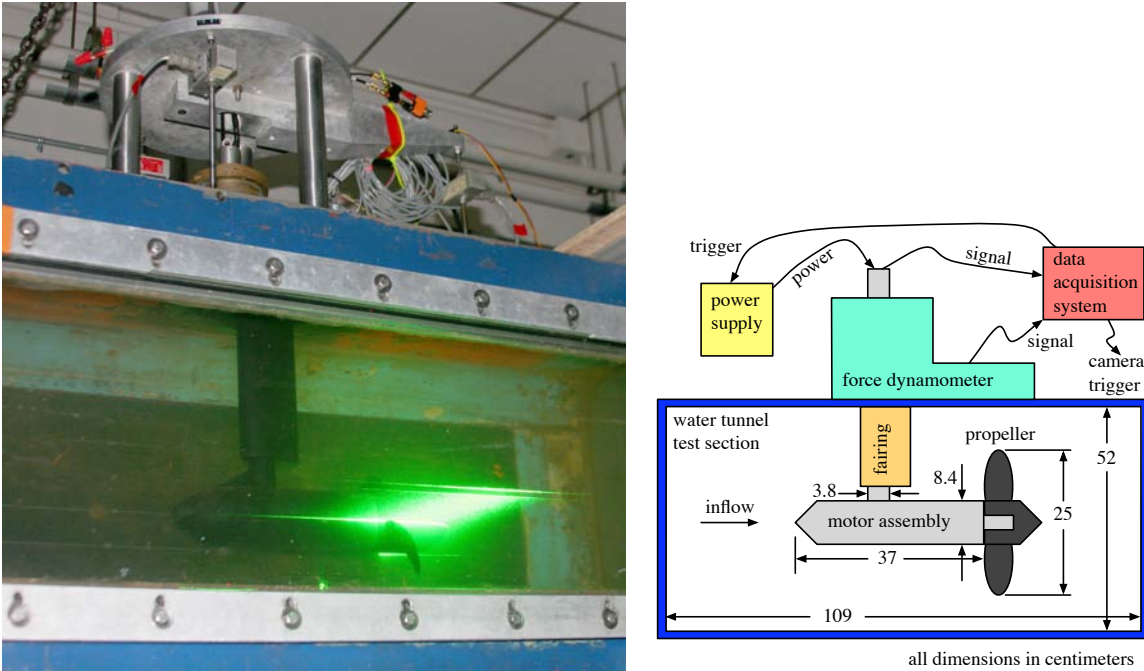


Figure 8-1: Propeller test setup: power is delivered to and Hall-effect signal is acquired from the motor assembly by umbilical. The data acquisition system triggers the power supply and PIV camera to start the unsteady start-up tests.

equate to a maximum speed and torque of 29.6 rev/s and 1.94 Nm, respectively. The motor assembly was held in the collet of the force dynamometer, which sits atop the tunnel test section. The force dynamometer has linear strain gauges, which were used to directly measure the net force on the motor assembly (i.e. the propeller thrust less the drag on the motor housing). The hydrodynamic torque was found by measuring the motor current.

The desired quantities are the net hydrodynamic thrust and torque on the propeller versus flow speed and rotation rate. Using the force dynamometer in the water tunnel, we can measure total force on the motor assembly, which is the net thrust produced by the propeller less the drag on the motor housing. We cannot directly measure torque, but we can infer it from the current flowing through the DC motor. We also do not directly measure the propeller rotation rate, but we can infer it from the angular position of the propeller. The angular position of the propeller

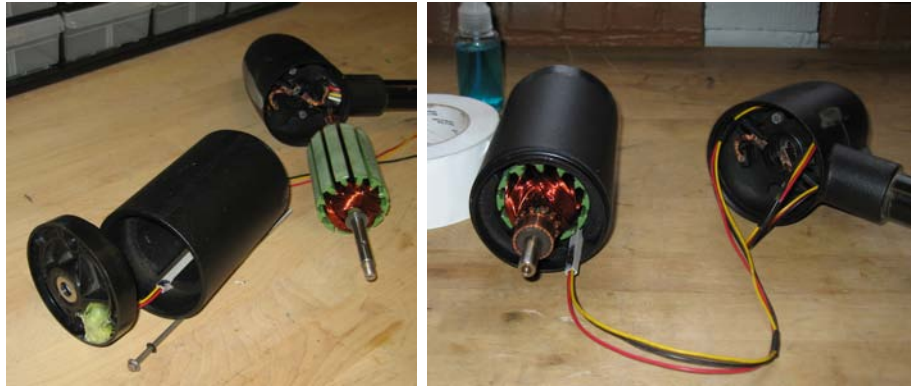


Figure 8-2: Hall-effect sensor installation.

is measured using a Hall-effect sensor (Allegro Microsystems A1211LUA-T (3-pin SIP) with $10k\Omega$ pull-up resistor connecting the power terminal and output-signal terminal, to improve signal quality) mounted to the aft surface of the motor (see figure 8-2) -- the output of this sensor is a 0 to 5 volt square wave, which flips when a magnet passes the sensor. For this, 32 magnets (Hamlin Electronics, 175 Gauss, 4mm-diameter, 20mm length cylinder) of alternating pole were imbedded into the propeller hub. Each passing magnet energizes or de-energizes the Hall-effect sensor. The flow speed is measured using the laser Doppler velocimetry (LDV) laser system at the water tunnel. Thus, we measure flow speed, total thrust, motor current, and propeller angular position, and we infer the net hydrodynamic thrust, torque, and propeller rotation rate.

8.1.1 Calibration tests

In this section, I outline the calibration tests required in order to compute the propeller thrust and torque from the data collected during the propeller experiments.

I performed a series of calibration tests to characterize the propeller thrust. The net force on the motor assembly, $f_{\text{net force}}$ [Volts], was measured using linear strain gauges in the force dynamometer; multiplying this voltage by a calibration constant,

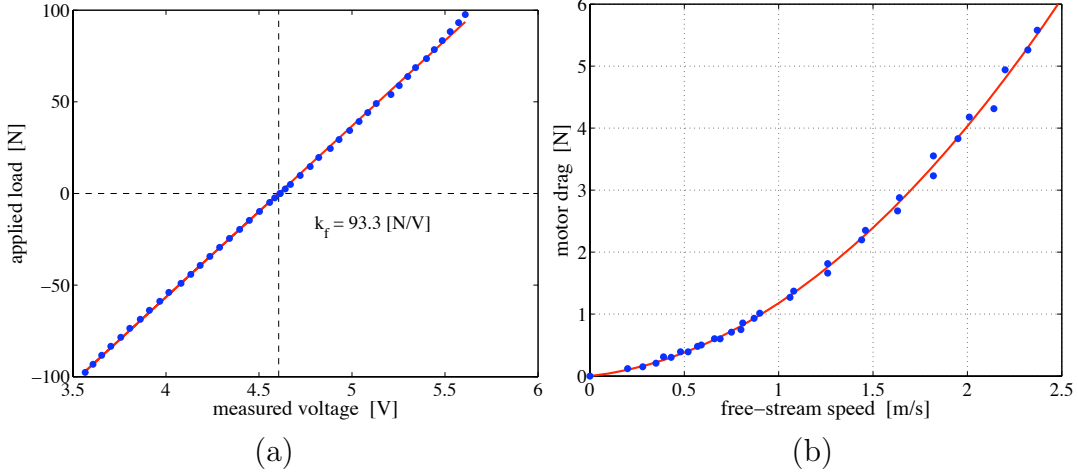


Figure 8-3: Thrust calibration data: (a) applied calibration load [N] versus measured “force” [V], where the slope of a linear fit to these data is the calibration constant, $k_f = 93.3 \text{ [N/V]}$; (b) drag on motor housing [N] versus flow speed [m/s]

k_f [N/V], yields the net force in Newtons. The propeller thrust, T [N] (positive upstream), is this net force plus the drag on the motor housing, $F_{\text{motor drag}}$ [N] (positive downstream), which is a function of the axial flow speed, V_a [m/s]:

$$T = k_f f_{\text{net force}} + F_{\text{motor drag}}(V_a) \quad (8.1.1)$$

where these forces may be steady or unsteady in time.

The force calibration constant, k_f , was determined in the usual way: The motor assembly was mounted in the force dynamometer, and a rope was fixed to the end of the motor shaft (where the propeller attaches) and routed over a pulley. A series of calibration weights (of known weight *in Newtons*) were hung on the end of a rope, and the resulting “force” was measured *in Volts* using the LabView data acquisition system. The data are shown in figure 8-3a, where the slope of a linear fit to the data is the calibration constant, $k_f = 93.3 \text{ [N/V]}$.

The drag on the motor housing was determined for a series of flow speeds. In these calibration tests, a bare hub was placed on the aft end of the motor assembly in

place of a propeller, and the motor assembly was mounted to the force dynamometer and situated in the water tunnel test section. The flow speed was measured ahead of the motor housing using the in-house laser Doppler velocimetry (LDV) system. The motor housing drag force was measured for a series of free-stream flow speeds; these data are plotted in figure 8-3b and are fit well with the polynomial

$$F_{\text{motor drag}} = f_1 V_a + f_2 V_a^2 \quad (8.1.2)$$

with $f_1 = 0.33604 \text{ N}/(\text{m/s})$ and $f_2 = 0.83952 \text{ N}/(\text{m/s})^2$. Equation (8.1.2) is used to infer the hub drag in the steady and unsteady propeller experiments.

I performed another series of calibration tests to characterize the motor torque. The hydrodynamic torque on the propeller, Q , can be inferred from accurate measurement of motor current and rotation rate. In the general, unsteady case, the net hydrodynamic torque is

$$Q(t) = k_m i_m(t) - B(\omega(t)) - I_a \dot{\omega}(t) \quad (8.1.3)$$

where k_m is the motor torque constant [Nm/A], i_m is the current [A], B is the parasitic torque loss due to friction [Nm], ω is the rotation rate [rad/s], $\dot{\omega}$ is the rotational acceleration [rad/s^2], and I_a is the total moment of inertia of the propeller and motor armature about the drive shaft axis [$\text{kg}\cdot\text{m}^2$]. The quantities k_m , B , and I_a were determined experimentally as follows.

First, the motor torque constant, k_m , was found in the usual way: The motor torque constant, $k_m = \frac{\text{torque}}{\text{current}}$ [Nm/A], is, by SI unit equivalence, equal to the reciprocal of the motor voltage constant $k_\omega = \frac{\text{rotation rate}}{\text{back EMF}}$ [$(\text{rad}/\text{s})/\text{V}$]:

$$k_m = \frac{1}{k_\omega} \quad (8.1.4)$$

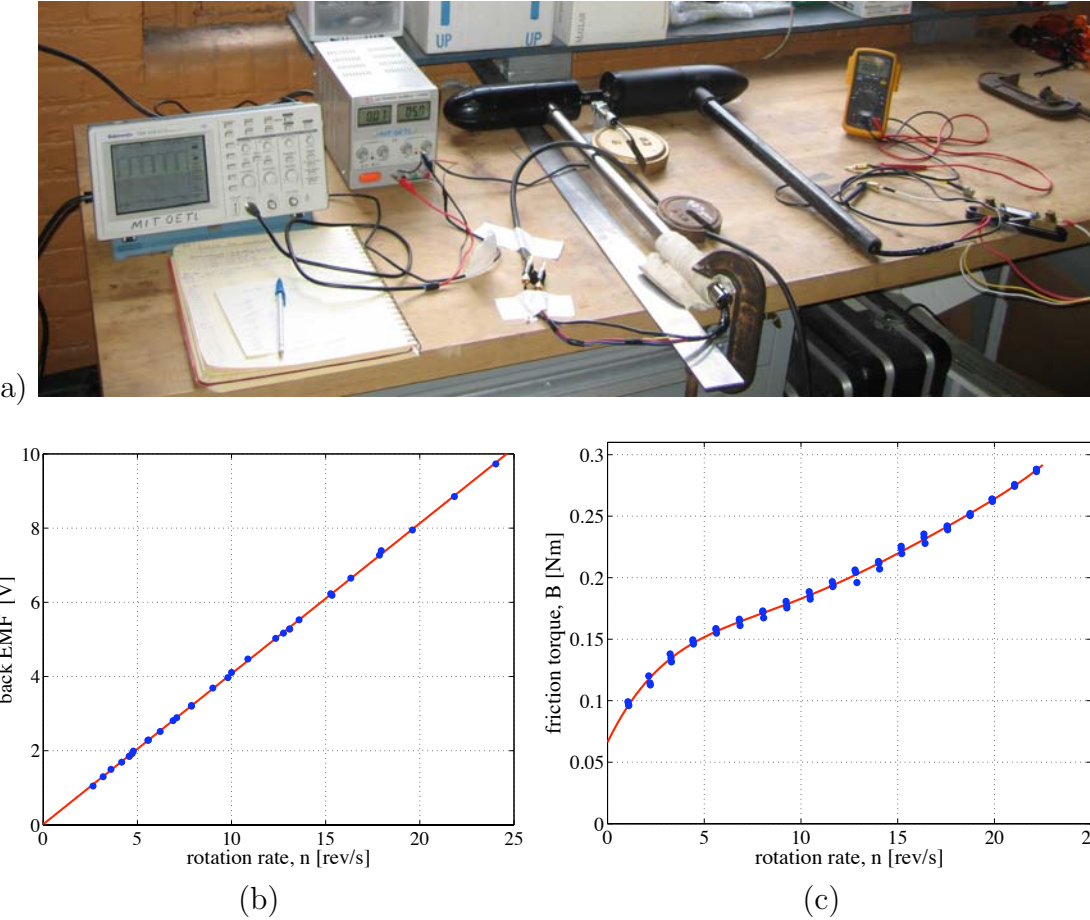


Figure 8-4: (a) Experimental setup for the motor speed constant calibration test; (b) measured back EMF [Volts] of the motor versus rotation rate [rev/s], where the reciprocal of the slope of a linear fit to the data is 2.47 (rev/s)/V, which equates to a motor speed constant of $k_\omega = 15.49$ (rad/s)/V and torque constant of $k_m = 0.06454$ Nm/A; (c) measured parasitic friction torque versus rotation rate, $B(n)$.

To find k_ω , the trolling motor was driven by an auxiliary motor at several rotation speeds, ω [rad/s] (measured using a Monarch Instrument - Remote Optical Sensor optical tachometer), and the (open-circuit) back EMF voltage across the motor terminals, V_{EMF} [V], was measured using a multimeter. The data are shown in figure 8-4, where the reciprocal of the slope of a linear fit to the data is 2.47 (rev/s)/V, which equates to a motor speed constant of $k_\omega = 15.49$ (rad/s)/V and torque constant of $k_m = 0.06454$ Nm/A.

b_0	6.6190×10^{-2}	Nm
b_1	5.1259×10^{-3}	Nm/(rad/s)
b_2	-1.1441×10^{-4}	Nm/(rad/s) ²
b_3	1.4539×10^{-6}	Nm/(rad/s) ³
\tilde{b}_0	6.6190×10^{-2}	Nm
\tilde{b}_1	3.2207×10^{-2}	Nm/(rev/s)
\tilde{b}_2	-4.5167×10^{-3}	Nm/(rev/s) ²
\tilde{b}_3	3.6064×10^{-4}	Nm/(rev/s) ³

Table 8.1: Motor friction torque: calibration fitting parameters.

Second, the parasitic friction curve, $B(\omega)$, was determined as follows: A bare hub was mounted on the motor, and the assembly was submerged in the water tunnel. The motor was operated at several rotation speeds, ω [rad/s] (as determined from Hall-effect sensor data acquired during each trial), and the current flowing through the motor, $i_m = V_S/R_S$, was determined for each trial by measuring the voltage, V_S , across a (Shunt) resistor of known resistance, $R_S = 50\text{mV}/15\text{A}$. In these experiments, $\dot{\omega} = 0$ (since steady) and $Q = 0$ (since no propeller), so equation (8.1.3) becomes $B(\omega) = k_m i_m = k_m \frac{V_S}{R_S}$. Several trials were performed, and the B vs. ω data are shown in figure 8-4. These data are fit well by a cubic polynomial,

$$B(\omega) = b_0 + b_1\omega + b_2\omega^2 + b_3\omega^3 \quad (8.1.5)$$

which is equivalent to

$$B(n) = \tilde{b}_0 + \tilde{b}_1 n + \tilde{b}_2 n^2 + \tilde{b}_3 n^3 \quad (8.1.6)$$

where the fitting parameters are given in table 8.1.

Third, the total moment of inertia of the propeller and motor armature, I_a , was determined by performing current step-input tests in air with the propeller attached to the motor. Here, we record time-series of Hall-effect sensor and motor current data for a series of trials. We assume the aerodynamic torque is negligible ($Q = 0$), since this

torque is much less than that which will be produced during underwater trials. During early times of these trials, $0 \leq t \leq \delta t$, the propeller accelerates rapidly from rest, and we assume that the friction torque is constant and therefore taken to be the mean value of the friction over the range of rotation speeds attained, $\bar{B} = \frac{1}{\omega(\delta t)} \int_0^{\omega(\delta t)} B(\omega) d\omega$. Also, the current is nearly constant and therefore taken to be the mean value during these early times $\bar{i_m} = \frac{1}{\delta t} \int_0^{\delta t} i_m(t) dt$. Thus, equation (8.1.3) becomes

$$I_a = \frac{k_m \bar{i_m} - \bar{B}}{\dot{\omega}} \quad (8.1.7)$$

where $\dot{\omega}$ is the constant acceleration, which is found by fitting a quadratic polynomial to the position data for the early times of each trial. For each trial, this procedure yielded an estimate for the moment of inertia: The mean and standard deviation are $I_a = 1.02\text{e-}3 \pm 5.74\text{e-}5 [\text{kg}\cdot\text{m}^2]$.

8.1.2 PIV test setup

Flow field measurements were made using high-speed particle image velocimetry (PIV) in the MIT Water Tunnel, with a horizontal light sheet illuminating the wake, as shown in figure 8-1. The water was seeded with $50 \mu\text{m}$ neutrally-buoyant particles (Dantec polyamid seeding particles), and a horizontal laser sheet (LaVision 3.3W, 10kHz, 532 nm laser, fitted with optics to produce a 10° fan of light) was positioned such that it was at the motor housing mid-plane. A high-speed camera (IDT XS-3 CCD camera, 85 mm Nikkon lens) imaged from below at 1000 fps. Image resolution was 1152×1024 pixels, and the field of view was $14.3 \text{ cm} \times 12.7 \text{ cm}$, giving a 80.5 px/cm zoom.

Each time-series of PIV images was processed using the LaVision DaVis 7.2 software package. In this experiment, we performed the first pass with 64×64 px interrogation windows and the second pass with 32×32 px windows, with 50%

overlap in adjacent windows for higher resolution velocity fields. The output were velocity fields of 72×64 vectors, with approximately 40 vectors along the propeller span. The data were post-processed in Matlab to determine vorticity, circulation, and wake geometry using the procedures outlined in previous chapters of this thesis. The circulation, Γ , of each vortex was computed by evaluating Stokes theorem numerically

$$\Gamma = \sum_{i,j} \omega_{(i,j)} \delta A \quad (8.1.8)$$

where $\omega_{(i,j)}$, is the vorticity at field point (i,j) , and $\delta A = (16 \text{ px})^2 = 0.0340 \text{ cm}^2$ was the area of each interrogation window. The summation is performed over the field points with vorticity greater than 10 1/s , which represents an iso-vorticity contour of about 5% of the maximum vorticity for many frames.

8.2 Propeller design

I designed a two-bladed propeller for use in steady off-design performance tests and unsteady start-up tests. The propeller was specifically designed to operate in the test setup described above. The inflow velocity profile was not measured prior to propeller design and assumed uniform ($V_a/V_s = 1$ for all blade sections). The swirl inflow velocity was zero ($V_t = 0$), and the propeller had zero rake or skew. The section drag coefficient was assumed to be $C_D = 0.010$ for all blade sections. Other relevant design parameters are listed in table 8.2, and their justification is given below.

The hub diameter ($D_{\text{hub}} = 3.3 \text{ in}$) was chosen to match the diameter of the trolling motor used in the experiments. The propeller diameter ($D = 0.25 \text{ m} \approx 10 \text{ in}$) was chosen to be as large as possible while still leaving sufficient clearance at the edge of the viewing windows in the water tunnel, so the PIV experiments could be performed with a suitable field of view. The choice of two blades ($Z = 2$) was driven by the size of the Dimension Elite 3D printer used to fabricate the propeller, which has an

Parameter	Value	Description
Z	2	number of blades
N	480 [RPM]	rotation rate
n	8 [rev/s]	rotation rate
D	0.25 [m]	propeller diameter (approx 10 in)
T	30 [N]	required thrust (approx 11.24 lb)
V_s	1.5 [m/s]	ship speed (free-stream speed)
D_{hub}	0.08382 [m]	hub diameter (3.3 in)
M	20	number of vortex panels
R_{hv}	0.5	hub vortex radius / hub radius
HUF	0	Hub Unloading Factor (no unloading)
TUF	0	Tip Unloading Factor (no unloading)
SCF	1	Swirl Cancellation Factor (no cancellation)
ρ	1000[kg/m ³]	water density

Table 8.2: Propeller design input parameters.

8-inch by 12-inch planform area for printing. Thus, a two-bladed propeller could be printed with a 10-inch diameter, whereas a propeller with three or more blades would be restricted to maximum a diameter of 8 inches. The free-stream speed and thrust were chosen to give a thrust coefficient typical of a marine propeller (see table 8.3) while having low enough torque that the trolling motor could drive the propeller.

A parametric design study was performed to select the rotation rate for the propeller. The results of this study are shown in figure 8-5. Figure 8-5 shows the efficiency of propellers with $Z = \{2, 3, 4, 5\}$ blades designed for a range of rotation rates, $300 \text{ [RPM]} < N < 1200 \text{ [RPM]}$. The selected rotation rate, $N = 480 \text{ [RPM]}$ has nearly the best efficiency for these propellers and yields an advance coefficient, $J_s = 0.75$, which is typical of a marine propeller.

8.2.1 Optimized performance

The propeller circulation distribution was optimized using the (Coney, 1989) method, with variable λ_1 , no chord optimization, and the input parameters given in Section 8.2. The non-dimensional design performance of this optimized propeller is shown in

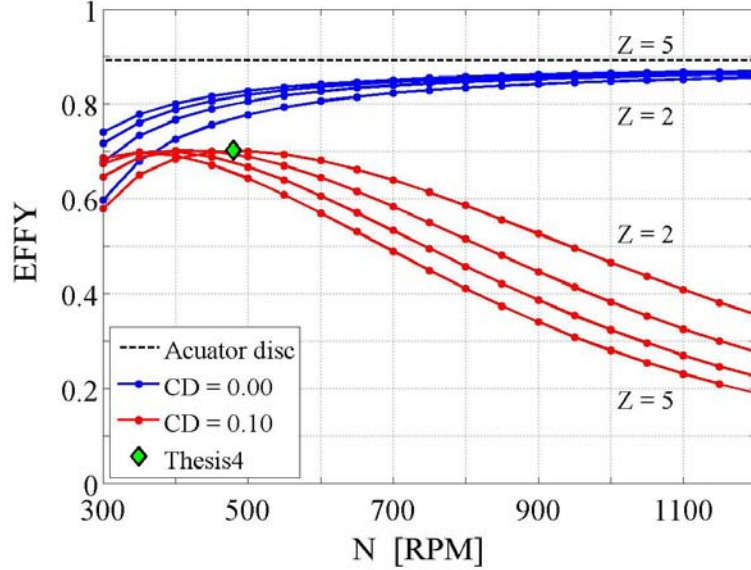


Figure 8-5: Parametric design study results: efficiency versus rotation rate and number of blades, as computed using the OPENPROP Lerbs optimization routine.

$J_s = \frac{V_s}{nD}$	0.75	advance ratio
$KT = \frac{T}{\rho n^2 D^4}$	0.1200	thrust coefficient
$KQ = \frac{Q}{\rho n^2 D^5}$	0.0204	torque coefficient
$EFFY = \frac{TV_s}{Q\omega}$	0.7019	efficiency

Table 8.3: Design performance parameters.

table 8.3. The values for KT and J_s meet those prescribed by the input parameters, and the torque coefficient and efficiency are typical for this loading. Tabulated flow parameters for blade sections at the control points are given in table 8.4.

The optimized circulation distribution is shown in figure 8-6a. Unfortunately, the LDV laser was not operable at the time of publication of this thesis, so measurements of the swirl velocity could not be made to verify this circulation distribution. In lieu of swirl velocity measurements, PIV data was taken for the horizontal mid-plane of the motor housing during on-design propeller operation ($V_s = 1.5$ m/s, $n = 7.9$ rev/s in the trial shown in figure 8-6b). In theory, the trailing streamwise vorticity has strength $\gamma = \frac{d\Gamma}{dr}$, so if all of the same-signed trailing vorticity rolled up into a

r/R	G	C_L	β_I	α	θ	$\frac{c}{D}$	$\frac{f_0}{c}$	$\frac{t_0}{c}$
0.3517	0.0464	0.6809	40.6497	0.9532	41.6029	0.2411	0.0453	0.1449
0.3845	0.0467	0.6226	38.0342	0.8717	38.9058	0.2494	0.0414	0.1351
0.4173	0.0473	0.5759	35.7163	0.8063	36.5226	0.2571	0.0383	0.1261
0.4502	0.0479	0.5351	33.6542	0.7491	34.4033	0.2646	0.0356	0.1179
0.4830	0.0484	0.4989	31.8116	0.6985	32.5101	0.2713	0.0332	0.1103
0.5158	0.0487	0.4668	30.1572	0.6536	30.8108	0.2769	0.0310	0.1035
0.5486	0.0489	0.4368	28.6644	0.6115	29.2759	0.2822	0.0291	0.0972
0.5815	0.0489	0.4095	27.3108	0.5733	27.8841	0.2864	0.0272	0.0914
0.6143	0.0486	0.3854	26.0779	0.5395	26.6175	0.2886	0.0256	0.0862
0.6471	0.0481	0.3623	24.9503	0.5073	25.4575	0.2901	0.0241	0.0813
0.6799	0.0473	0.3399	23.9149	0.4759	24.3908	0.2911	0.0226	0.0768
0.7128	0.0463	0.3184	22.9611	0.4457	23.4068	0.2911	0.0212	0.0726
0.7456	0.0449	0.2985	22.0800	0.4180	22.4980	0.2889	0.0199	0.0686
0.7784	0.0431	0.2794	21.2641	0.3912	21.6553	0.2849	0.0186	0.0650
0.8113	0.0409	0.2600	20.5070	0.3640	20.8710	0.2795	0.0173	0.0619
0.8441	0.0381	0.2429	19.8032	0.3401	20.1432	0.2692	0.0162	0.0592
0.8769	0.0348	0.2266	19.1479	0.3172	19.4651	0.2539	0.0151	0.0567
0.9097	0.0305	0.2078	18.5368	0.2909	18.8277	0.2348	0.0138	0.0543
0.9426	0.0250	0.1883	17.9660	0.2636	18.2297	0.2052	0.0125	0.0519
0.9754	0.0171	0.1736	17.4318	0.2430	17.6748	0.1470	0.0115	0.0541

Table 8.4: Optimized blade performance: radius/propeller radius, r/R ; non-dimensional circulation, $G = \frac{\Gamma}{2\pi RV_s}$; lift coefficient, C_L ; total inflow angle, β_I [deg]; angle of attack, α [deg]; blade pitch angle, θ [deg]; chord/diameter, $\frac{c}{D}$; camber ratio, $\frac{f_0}{c}$; and thickness ratio, $\frac{t_0}{c}$. The chord lengths were not optimized during the design.

single tip vortex, then (by the fundamental theorem of calculus) the strength of this tip vortex would equal the maximum circulation in the distribution. The circulation about the tip vortex was estimated by integrating the measured PIV vorticity over the vortex area $\Gamma = \int \omega dA = 0.0455 \text{ m}^2/\text{s}$, as shown in a representative PIV frame in figure 8-6b. The non-dimensional tip vortex circulation is $G = \frac{\Gamma}{2\pi RV_s} = 0.0388$, which agrees qualitatively with the peak circulation in the distribution shown.

Figure 8-6c shows the thrust and torque loading per unit span. These graphs are intended to show what part of the blade is carrying the most load, and it is evident that the majority of the load is produced at about the 80% span section.

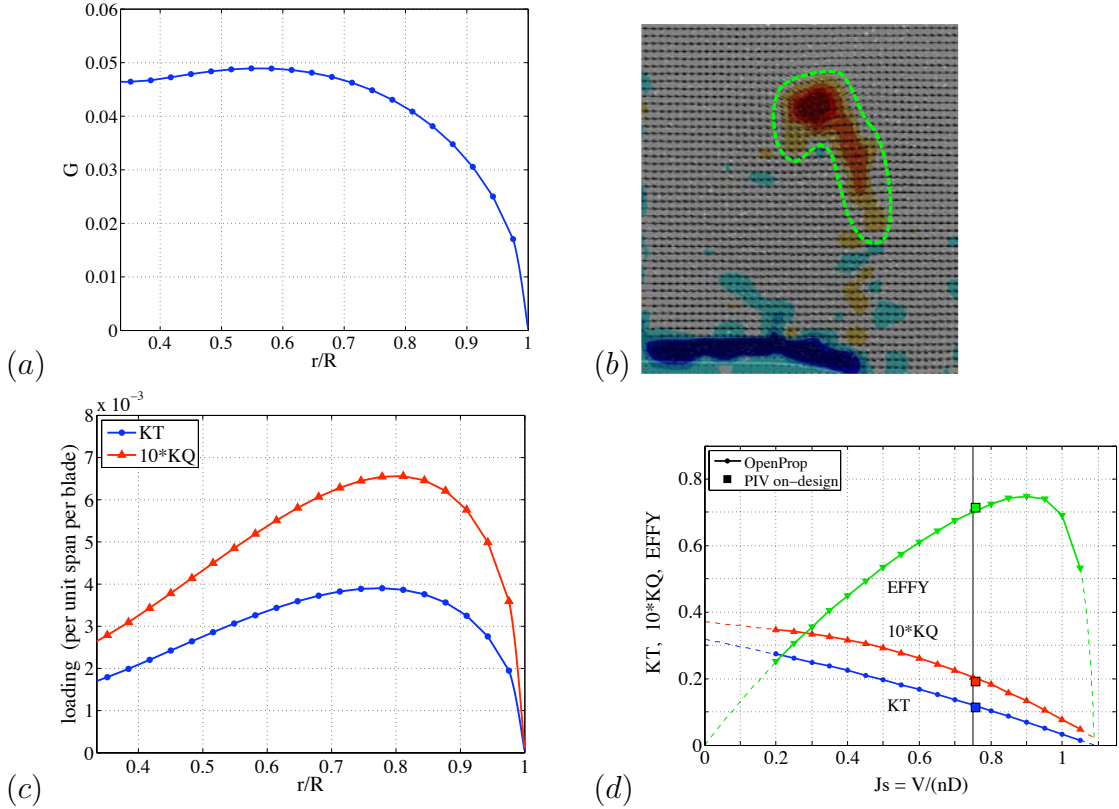


Figure 8-6: On-design performance: (a) design circulation distribution $G = \frac{\Gamma}{2\pi RV_s}$; (b) a representative PIV velocity and vorticity field shows a tip vortex of strength $G = 0.0388$; (c) load distribution; (d) off-design performance curve, showing good agreement with loads measured during the on-design PIV experiment, ‘■’.

As part of the design process, I wanted to check that my trolling motor apparatus could operate the propeller over a range of off-design speeds. To perform this check, I used my off-design performance analysis method (implemented in OPENPROP) to create performance curves for the propeller, as shown in figure 8-6d. This graph shows that the curves for KT , KQ , and $EFFY$ versus J_s are typical of a marine propeller, and these data allowed me to verify that this propeller would in fact work with my experimental setup. The thrust, torque, and efficiency data measured during the steady on-design PIV experiment are also shown in figure 8-6d; these data agree with the on-design performance predictions by OPENPROP.

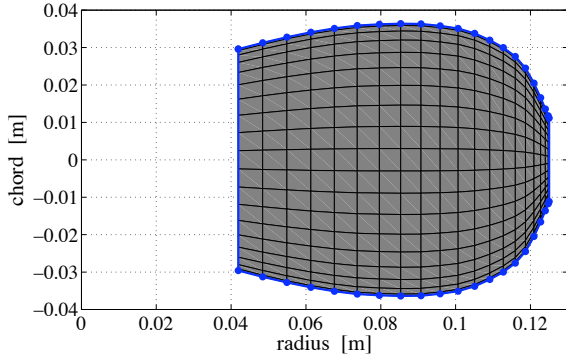


Figure 8-7: Expanded blade shape: chord-length versus radius.

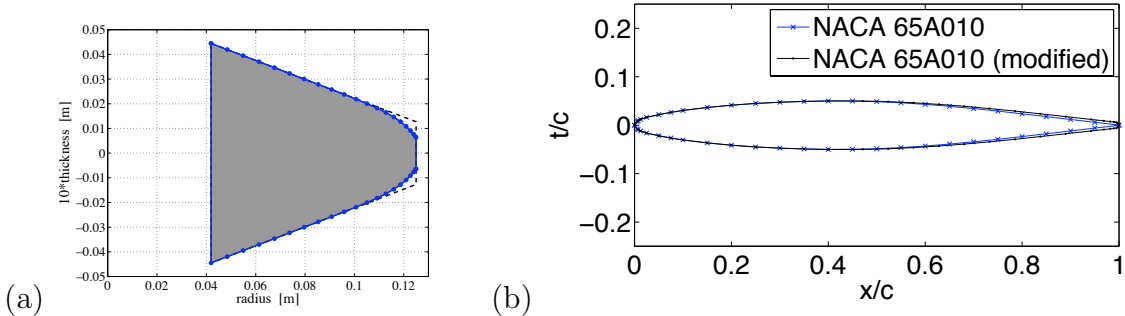


Figure 8-8: Blade thickness: (a) thickness distribution (ten times the maximum section thickness versus radius); (b) NACA65A010 and NACA65A010 (modified) thickness forms.

8.2.2 Blade shape

The expanded blade shape is shown in figure 8-7, and the chord-length data are given in table 8.4. This shape was chosen to give a reasonably large chords for most of the span, while also maintaining a rounded blade tip. Large chord lengths enable large blade thickness while still having small thickness to chord ratio. OPENPROP is based on linear foil theory, which requires a small thickness to chord ratio. The blade thickness was required to be large enough such that the blade would not flex during testing and such that the propeller could be fabricated on campus via 3D printing.

Providing sufficient blade thickness is paramount with fabricating propellers using 3D printing, because (1) the ABSplus plastic material used by the 3D printer is rather

flexible, and (2) the wire diameter of the printer I used was 0.007 inch, both of which limit the minimum allowable thickness of any portion of the blade. To facilitate blade thickness design, I created the quasi-linear thickness profile shown in figure 8-8a. The thickness distribution is given by

$$t_0(r) = \left(t_{0,\text{hub}} + (t_{0,\text{tip}} - t_{0,\text{hub}}) \frac{r - R_{\text{hub}}}{R - R_{\text{hub}}} \right) \cdot \left(1 - \left(1 - \frac{t_{0,\text{tip}}^{\text{mod}}}{t_{0,\text{tip}}} \right) \cdot e^{(-4.6 \frac{R-r}{R-r_{\text{mod}}})} \right) \quad (8.2.1)$$

where I chose a tip-thickness reduction factor of $\frac{t_{0,\text{tip}}^{\text{mod}}}{t_{0,\text{tip}}} = 0.50$, and the values 4.6 and $r_{\text{mod}} = 0.8 \cdot R$ were chosen such that the otherwise-linear thickness profile is essentially only modified from the 80% span to the tip ($r_{\text{mod}} < r < R$). In this way, the blade is made thick for much of the span yet has reduced thickness at the tip. The nominal maximum thickness at the tip section was chosen to be $t_{0,\text{tip}} = 0.00254 \text{ m} = 0.1 \text{ inch}$. The final, modified tip thickness is $t_0(r = R) = t_{0,\text{tip}}^{\text{mod}} = 0.05 \text{ inch}$, which was still large enough that the tip geometry could be resolved by the 3D printer. The hub section thickness, $t_{0,\text{hub}} = 0.35 \text{ inch}$, was chosen to mitigate blade bending; this yields a blade thickness fraction of: $BTF = \frac{t_{0,\text{axis}}}{D} = \frac{t_{0,\text{tip}} + \frac{t_{0,\text{hub}} - t_{0,\text{tip}}}{1 - D_{\text{hub}}/D}}{D} = 0.0484$, which is typical of a marine propeller (Carlton, 1994).

The thickness form used was a version of the ‘NACA 65A010’ thickness form (Abbott and von Doenhoff, 1959, p. 369), which I modified slightly to be amenable to 3D printing. The ‘NACA 65A010’ and ‘NACA 65A010 (modified)’ forms are shown in figure 8-8, and their geometry is tabulated in table 8.5. For the modified shape, I truncated and rounded the trailing edge and then stretched the aft half of the blade section to be the original length. This yielded a blade section with a finite thickness trailing edge that a 3D printer can resolve. In the fabrication of the propeller, I sanded the trailing edge to be sharp again, so that the final shape of the blade resembled the original ‘NACA 65A010’ form.

'NACA65A010'		'NACA65A010 (modified)'	
x/c	t/c	x/c	t/c
0.0000	0.00000	0.00000000	0.00000000
0.0050	0.00765	0.00500000	0.00765000
0.0075	0.00928	0.00750000	0.00928000
0.0125	0.01183	0.01250000	0.01183000
0.0250	0.01623	0.02500000	0.01623000
0.0500	0.02182	0.05000000	0.02182000
0.0750	0.02650	0.07500000	0.02650000
0.1000	0.03040	0.10000000	0.03040000
0.1500	0.03658	0.15000000	0.03658000
0.2000	0.04127	0.20000000	0.04127000
0.2500	0.04483	0.25000000	0.04483000
0.3000	0.04742	0.30000000	0.04742000
0.3500	0.04912	0.35000000	0.04912000
0.4000	0.04995	0.40000000	0.04995000
0.4500	0.04983	0.47120419	0.04983000
0.5000	0.04863	0.52356021	0.04863000
0.5500	0.04632	0.57591623	0.04632000
0.6000	0.04304	0.62827225	0.04304000
0.6500	0.03899	0.68062827	0.03899000
0.7000	0.03432	0.73298429	0.03432000
0.7500	0.02912	0.78534031	0.02912000
0.8000	0.02352	0.83769634	0.02352000
0.8500	0.01771	0.89005236	0.01771000
0.9000	0.01188	0.94240838	0.01188000
0.9500	0.00604	0.96858639	0.00896000
1.0000	0.00021	0.98167539	0.00749953
		0.98952880	0.00662364
		0.99476440	0.00604000
		0.99738220	0.00404902
		1.00000000	0.00021000

Table 8.5: Thickness to chord ratio versus chordwise position for the 'NACA65A010' (Abbott and von Doenhoff, 1959, p. 369) and 'NACA65A010 (modified)' forms.

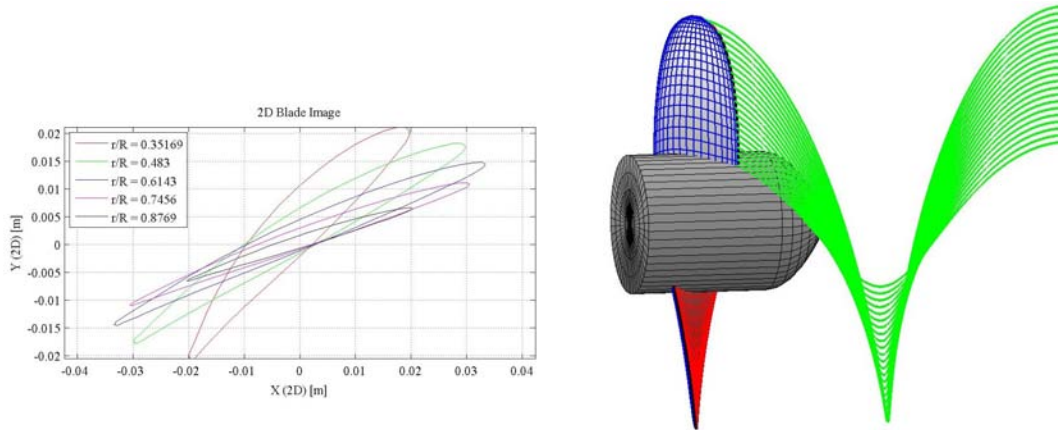


Figure 8-9: OPENPROP rendering of the propeller blades.

The 3D blade geometry was built from 2D sections, as described in Section 7.4. The geometry of each 2D section is defined by the meanline camber profile and thickness forms. The meanline selected was the ‘*NACA a=0.8 (modified)*’ meanline type (Abbott and von Doenhoff, 1959, p. 403) . This meanline type has an ideal lift coefficient of $\tilde{C}_{L_I} = 1.0$ and an ideal angle of attack of $\tilde{\alpha}_I = 1.40$ with a maximum camber ratio of $\tilde{f}_0/c = 0.06651$. The actual camber and ideal angle of attack of the sections was scaled by the desired section lift coefficient, per equation (7.4.1).

8.2.3 Fabrication

The resulting 2D and 3D blade geometry is shown in figure 8-9. Outputs from OPENPROP were used to build a model of the propeller in SOLIDWORKS, as shown in figure 8-10. The blades were lofted and attached to a hub, which was designed to mate to the motor housing. The hub diameter is 3.3 inches, and a recess is made to mate with the motor shaft pin and nut retention system. The process of creating a final propeller in SOLIDWORKS is non-trivial, and the steps are outlined here:

1. Create the hub in SOLIDWORKS (and save a backup copy of the part file). Build the blades directly onto the hub.

2. Create the key blade:
 - Run the OPENPROP Geometry command to create the geometry data file: ‘filenameSolidWorks.txt’. Make sure that the first and last points of each SectionCurve are the same (i.e. each section is a closed contour).
 - Run the OPENPROP SOLIDWORKS macro. This should result in several blade section curves and guide curves drawn over surface points.
 - Create a Surface Loft of SectionCurves 1-21 using GuideCurves 1-6.
 - Create a Surface-Fill at the blade tip using TipSectionCurve21 and all of the TipCurves.
 - Create a Surface-Fill at the blade root using RootSectionCurve1 and all of the RootCurves.
 - Knit the three surfaces into a solid.
3. Create Z blades using a Circular Pattern of Solid Bodies about the hub axis (sketch an axis if you haven’t already).
4. Combine the blades and hub using the Add operation.
5. Add a Fillet/Round radius to the seam between the hub and each blade. I used a radius of 0.1 inch for the propeller presented herein.

With a completed propeller and hub drawn in SOLIDWORKS, you can export an STL file, which is the required file format for 3D printing.

I 3D printed my propeller on a Dimension Elite printer, in ABSplus plastic, with a wire diameter of 0.007 inch, at the MIT Edgerton Center Student Shop. The following steps were used to prepare the propeller for the tests. During the milling process, the prototype propeller was held by a 7/8” tapered mandrel, which was press-fit into the aft hole of the hub. The propeller was first machined on a lathe, to flatten the hub face and true the propeller shaft hole. The propeller shaft hole was made true using a 3/8” end mill to center the hole and 3/8” reamer to ream the hole. The propeller was then held (by the mandrel) in a milling machine V-block for preparation of the

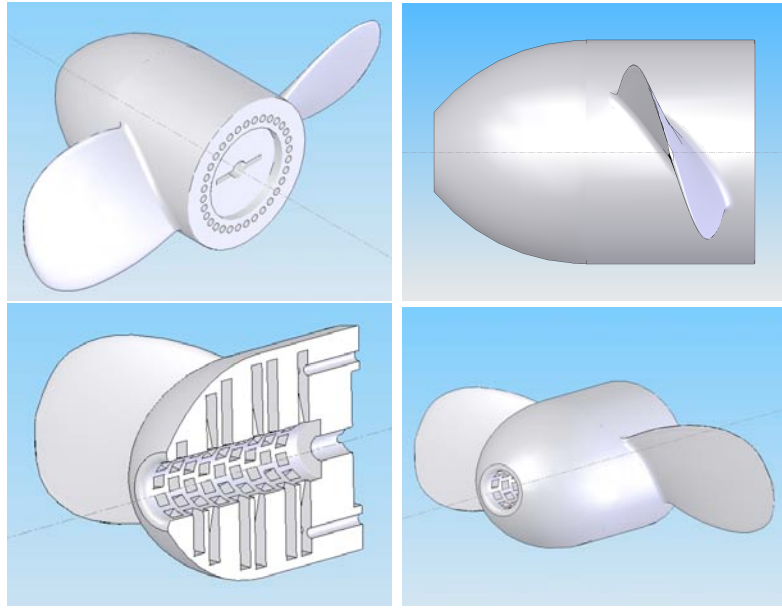


Figure 8-10: SolidWorks rendering of the propeller and hub.

shaft pin slot and magnet holes. The slot for the shaft pin was finished using a 1/8" ball end-mill, and the holes for the magnets were cleared using a #21 drill bit. The magnets were then pressed into each hole with alternating signed poles facing out. After this machining, the mandrel was pressed out of the propeller, which was now ready for sanding and painting. The blade surfaces were sanded and then coated with a thin layer of epoxy to make them smooth and increase their stiffness. Finally, the blades and hub were spray-painted black such that they did not reflect the intense laser light during PIV experiments, as shown in figure 8-11.

8.3 Steady propeller performance experiments

Thrust and torque measurements were made in the water tunnel for a range of steady flow speeds ($V_s = 0.1$ to 1.9 m/s) and steady rotation rates ($n = 1.4$ to 9.5 rev/s), spanning the advance ratios ($J_s = 0.3$ to 1.1). In these experiments, the flow speed was determined using the in-house LDV system, and the drag on the motor housing



Figure 8-11: Finished hub and propeller.

was inferred from the calibration data (8.1.2). The net force on the motor assembly was measured using the force dynamometer, so the thrust produced by the propeller was computed by (8.1.1), which is reproduced here

$$T = k_f f_{\text{net force}} + F_{\text{motor drag}}(V_s) \quad (8.1.1)$$

The torque on the propeller was inferred from measurements of the current supplied to the motor. In these steady tests, the torque (8.1.3) is

$$Q = k_m i_m - B(\omega) \quad (8.3.1)$$

where the steady rotation rate, ω , is the slope of a linear fit to the angular position data acquired from the Hall-effect sensor, and the friction torque, $B(\omega)$, is inferred from the calibration (8.1.5). No tunnel corrections were made (e.g. for blockage effects) during these measurements.

These data are normalized in the usual way to form thrust and torque coefficients

$$K_T = \frac{T}{\rho n^2 D_p^4} \quad (8.3.2)$$

$$K_Q = \frac{Q}{\rho n^2 D_p^5} \quad (8.3.3)$$

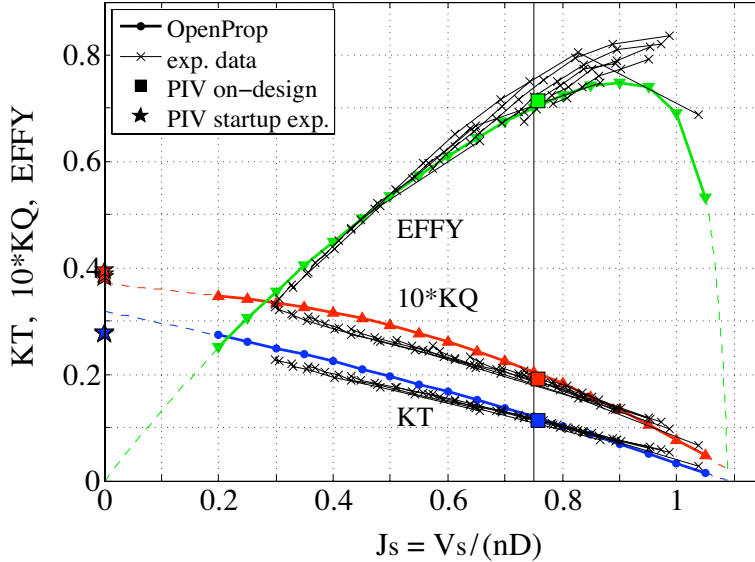


Figure 8-12: Off-design propeller performance curves, with experimental data.

where $D_p = 0.2487\text{m}$ is the actual diameter of the printed propeller. The efficiency of the propeller is by definition

$$EFFY = \frac{TV_s}{Q\omega} = \frac{K_T J_s}{2\pi K_Q} \quad (8.3.4)$$

In figure 8-12, these data are plotted versus advance coefficient

$$J_s = \frac{V_s}{nD_p} \quad (8.3.5)$$

Figure 8-12 shows good agreement between the OPENPROP off-design performance predictions and the experimental results. The measured data match within 10% of the predicted performance for most advance ratios. These data provide valuable validation for my off-design performance analysis method.

The off-design performance analysis method described in Chapter 7 accounts for changes in blade section loading due to changes in angle of attack (both due to changes in advance coefficient and induced velocities). The lift coefficient is computed from the

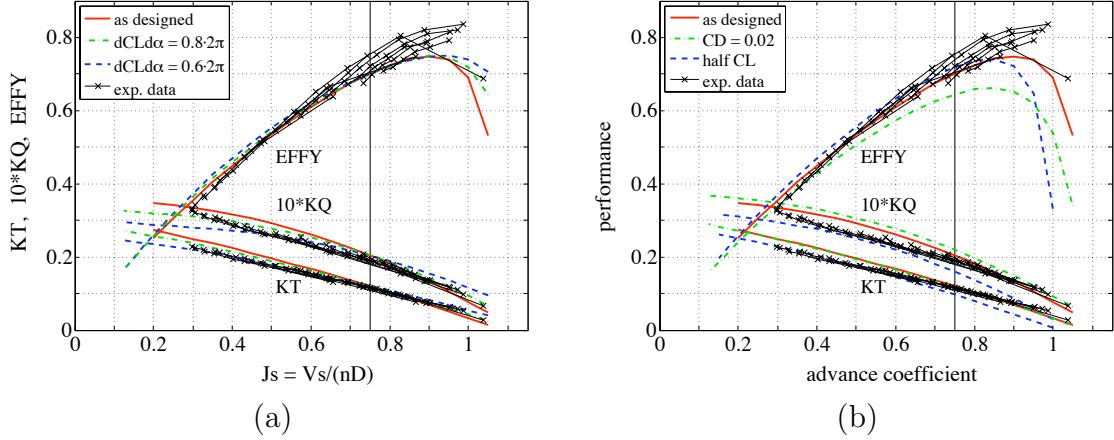


Figure 8-13: Effect of parameters on the off-design analysis: (a) lift-curve slope, $\frac{dC_L}{d\alpha}$; (b) drag coefficient, $C_D = 0.02$, and as-built lift coefficient, $C_{L,0} = \frac{1}{2} C_{L,\text{design}}$.

angle of attack by equation (7.5.4), which is approximately $C_L \approx C_{L,0} + \frac{dC_L}{d\alpha}(\alpha - \alpha_I)$ prior to stall. The default lift curve slope is $\frac{dC_L}{d\alpha} = 2\pi$, but it is of interest to see how this value affects the lifting line analysis predictions. Figure 8-13a shows that as $\frac{dC_L}{d\alpha}$ is reduced, the overall thrust and torque curves flatten. This is to be expected, since the advance coefficient is a proximal measure of the angle of attack. Therefore, reducing $\frac{dC_L}{d\alpha}$ in effect reduces the sensitivity to changes in advance coefficient.

Figure 8-13b shows two other hypothetical scenarios: (1) suppose the section drag coefficient $C_{D,0}$ was 0.02 as opposed to the design assumption of 0.01; and (2) suppose the blade was incorrectly manufactured, such that it produced an on-design lift coefficient distribution of half the design intent $C_{L,0}$. Clearly, the data does not correlate with scenario (1), since $C_{D,0} = 0.02$ results in higher torque loads and lower efficiencies than were measured. The data also do not correlate with scenario (2), as this results in much lower loading (particularly on design) than were measured. These data suggests that the propeller was built and performs close to the design intent.

8.4 Unsteady start-up experiments

A series of unsteady start-up experiments were performed, in which PIV velocity fields were obtained in conjunction with measuring the unsteady thrust and torque on the propeller. In these experiments, the propeller started at rest with the blades in the PIV laser plane (i.e. the blades were parallel to the floor). When triggered, the LabView system first began acquiring thrust and torque data and then simultaneously (1) triggered the PIV camera system to begin recording and (2) triggered the power supply to deliver power to the propeller. Figure 8-14 shows the unsteady forces for one such trial, which had a final rotation rate of $n_f = 5.04 \text{ rev/s}$.

The propeller thrust (figure 8-14a) was inferred as follows. Since the flow speed of the water tunnel was zero, the drag on the motor housing was assumed to be zero, and the propeller thrust was assumed to be the total force measured by the dynamometer. Although axial flow was induced by the propeller, the PIV velocity data (figure 8-17) show that it was on the order of 1 m/s, which corresponds to a motor housing drag of about 1 N. This is less than 5% of the typical measured forces, so it is acceptable to assume that hub drag is negligible in these experiments. Thus, the raw thrust data (blue dots in figure 8-14a) are the load measured by the force dynamometer scaled by the calibration constant

$$T = k_f f_{\text{net force}} \quad (8.4.1)$$

These data were sampled at 5000 Hz. Since no analog signal conditioning was used prior to data acquisition, the raw data contain significant noise content, especially at 60 and 120 Hz due to electrical noise. These raw data were filtered in MATLAB using a low-pass Butterworth filter with a 10 Hz cutoff frequency, and the filtered thrust data are shown as a red line in figure 8-14a. The filtered thrust data were then

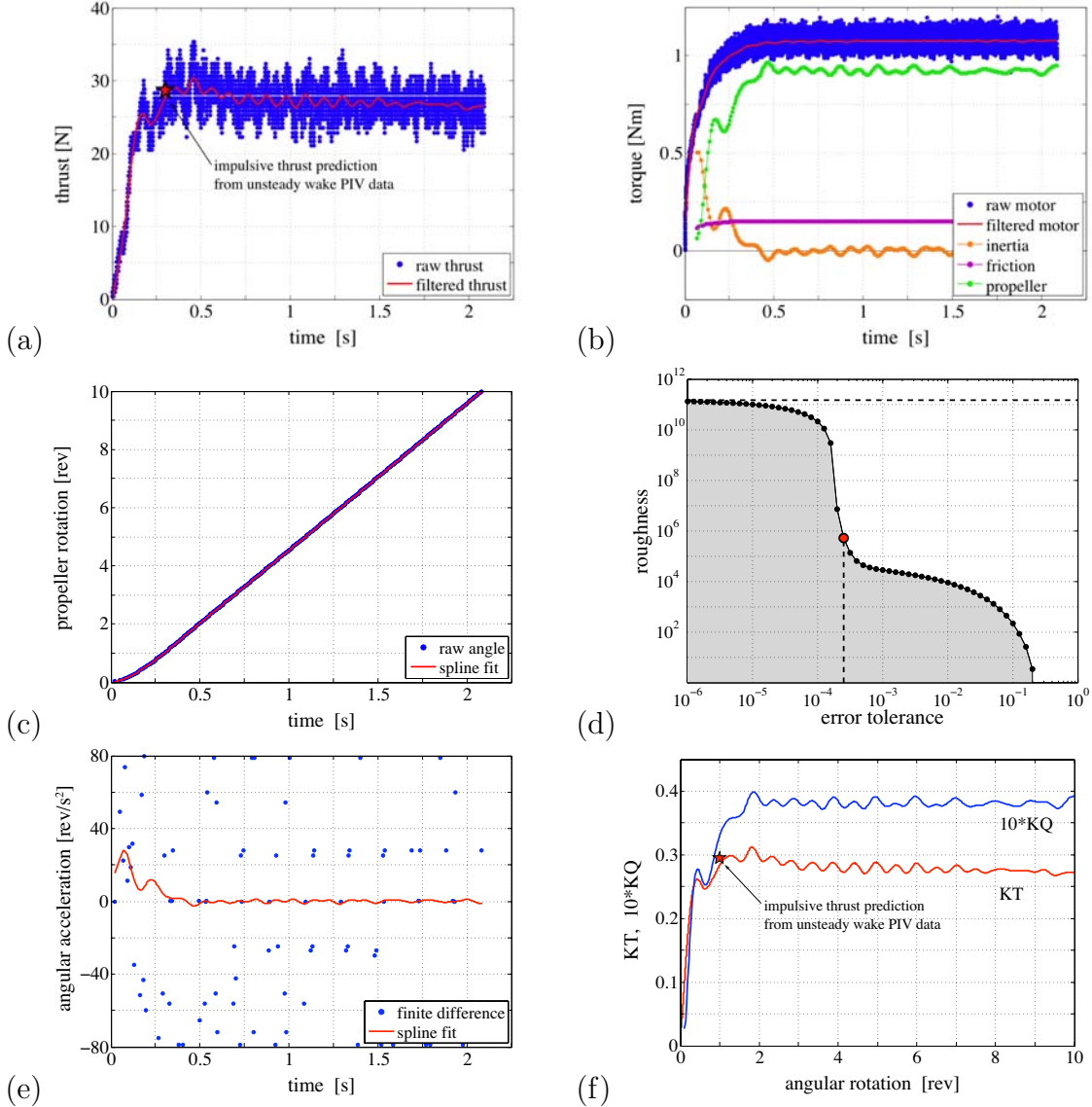


Figure 8-14: Measured forces during one unsteady start-up trial that had a final rotation rate of $n_f = 5.04$ rev/s: (a) thrust versus time; (b) torque versus time; (c) angular position versus time; (d) roughness versus error tolerance for smoothing splines fit to the angular position data; (e) angular acceleration versus time; and (f) thrust and torque coefficients versus angular position.

normalized to give the thrust coefficient (see figure 8-14f),

$$K_T = \frac{T}{\rho n_f^2 D_p^4} \quad (8.4.2)$$

where $D_p = 0.2487$ m is the actual diameter of the printed propeller, and n_f was the final rotation rate of the propeller once it reached steady-state.

The unsteady torque on the propeller was inferred from measurement of the motor current, $i_m(t)$ via equation (8.1.3), which is reproduced here

$$Q(t) = k_m i_m(t) - B(\omega(t)) - I_a \dot{\omega}(t) \quad (\text{eqn. 8.1.3})$$

where the friction torque, $B(\omega(t))$, was computed from the calibration (8.1.5).

The raw current measurements (blue dots in figure 8-14b) were acquired at 5000 Hz (in sync with the thrust measurements), and these data were also filtered with a 10 Hz low-pass Butterworth filter (red line in figure 8-14b). In these experiments, the power supply was commanded to deliver a constant current to the motor, so the current was supposed to be a step input. The data in figure 8-14b show that the actual current delivered to the motor was a rounded step but was constant once it reached the required value.

In these unsteady experiments, the instantaneous angular velocity and acceleration $\{\omega(t), \dot{\omega}(t)\}$ were derived from a smoothing spline fit to the angular position data (blue dots in figure 8-14c) acquired from the Hall-effect sensor (using the method presented in Chapter 5). The Hall-effect sensor outputs a square wave that rises or falls when each magnet passes the sensor. Since the 32 magnets are equispaced about the propeller hub, the angular position is known when each rise and fall happens, but the time of each rise and fall may have measurement error. Thus, the Hall-effect sensor data is of the form $\theta(\tilde{t})$, where $\tilde{t} = t + \epsilon$ (i.e. the measured time equals the true time plus some small error). This is equivalent to having data in which the times are exact but the angles are slightly wrong, since by a Taylor series expansion $\theta(\tilde{t}) = \theta(t + \epsilon) = \theta(t) + \theta'(t) \epsilon = \theta(t) + O(\epsilon) = \tilde{\theta}(t)$. Thus, my method could be used to fit a smoothing spline to the measured angular position data. Derivatives of this smoothing spline were computed exactly with remarkable accuracy, since the smoothing spline is both analytic and follows the local trends in the data.

Figure 8-14d shows the roughness versus error tolerance frontier for smoothing splines fit to the angular position data. Each point on this curve represents the minimum roughness possible for a smoothing spline fit to the data for the specified error tolerance. Splines exist with more roughness than those on this frontier, but they are undesirable, since they are inefficient (i.e. they have more roughness than the splines on the frontier). The best fit spline is the one marked by a red bullet, which has the minimum error tolerance possible without also having a lot of roughness due to the noise in the data. Splines with less error tolerance than the selected spline are quite noisy and do not represent the smooth continuous motion of the propeller. The selected spline fit to the angular position data is shown as a red line in figure 8-14c. This spline was used to compute the angular velocity (not shown) and the angular acceleration (figure 8-14e) of the propeller. For comparison, the angular acceleration derived by finite differences of the angular position data appears as random noise in figure 8-14e.

The net propeller torque was then normalized to give the torque coefficient

$$K_Q = \frac{Q}{\rho n_f^2 D_p^5} \quad (8.4.3)$$

which is shown in figure 8-14f.

The results from three selected trials are shown in figure 8-15. These trials had final rotation rates of $n_f = [5.04, 5.72, \text{ and } 6.29]$ rev/s (where the $n_f = 5.04$ rev/s case is the one shown in figure 8-14). In these trials, the propeller accelerates rapidly from rest, reaching its final speed in less than one half of a second. Although the rotation speeds, thrusts, and torques are different for each trial, they all resemble the same form, so it is expected that they would collapse onto single curves with the proper scaling. From the vortex impulse perspective, we expect that the forces on the propeller scale by the size and strength of the wake, not by time. “Size” of the

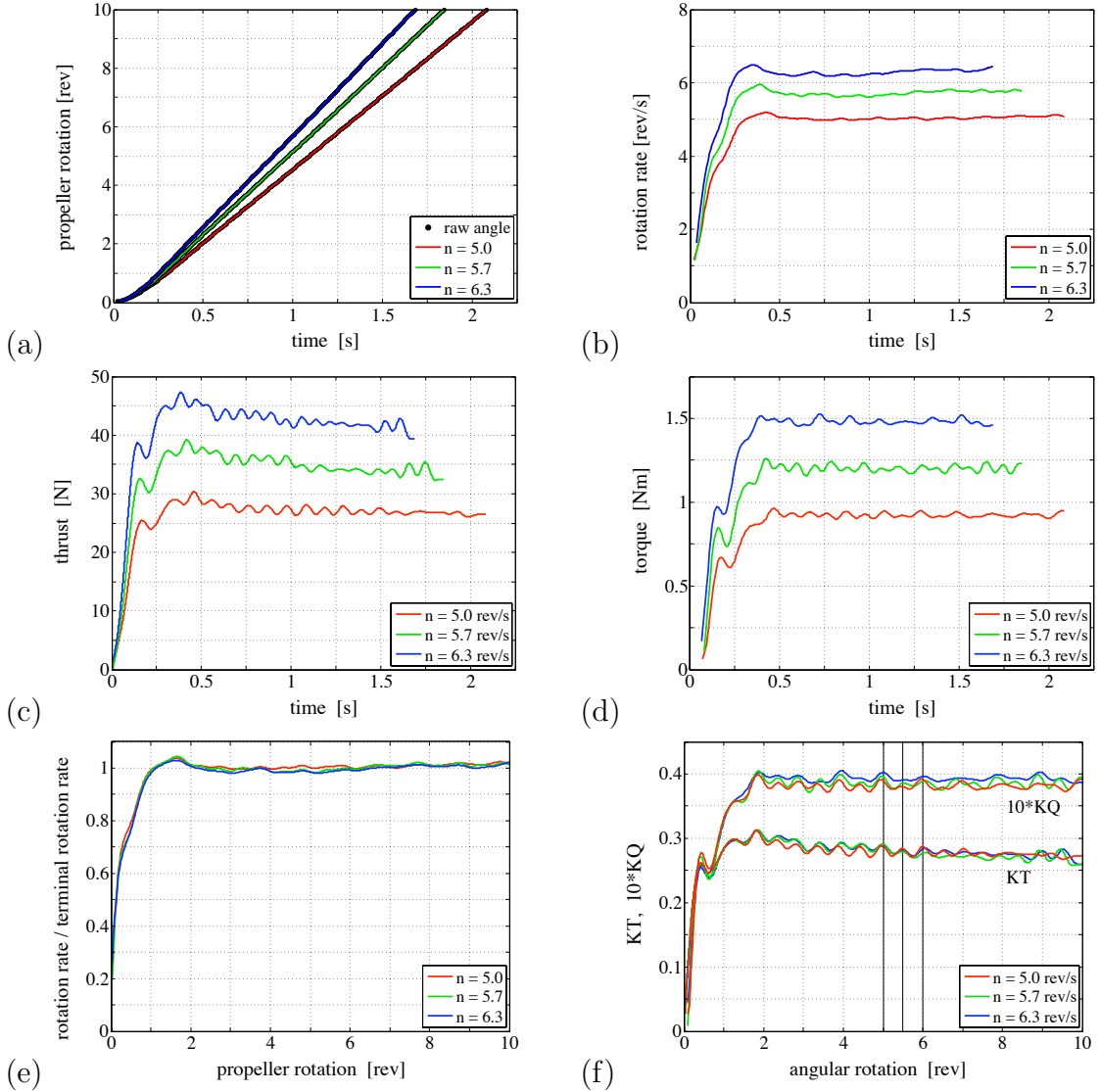


Figure 8-15: Measured forces during three selected unsteady start-up experiments for trials with final rotation rates $n_f = [5.04, 5.72, \text{ and } 6.29]$ rev/s: (a) angular position versus time; (b) angular velocity versus time; (c) thrust versus time; (d) torque versus time; (e) normalized rotation rate versus angular position; and (f) thrust and torque constants versus angular position.

wake in this experiment corresponds to the distance traveled by the propeller blade. Therefore, the appropriate non-dimensionalization of time is to instead consider the angular displacement of the propeller, which can be given in radians or in propeller revolutions, as shown in figure 8-15. The rotation rate curves collapse onto a single curve if each is normalized by the steady-state rotation rate and plotted against

angular displacement, given in figure 8-15 as propeller revolutions. Similarly, the thrust and torque curves collapse if normalized in the usual way to be thrust and torque coefficients and plotted against angular displacement, in revolutions.

The unsteady thrust and torque coefficients shown in figure 8-15 oscillate with a regular pattern, and this is simply due to the experimental setup. In this experiment, the propeller blades start parallel to the floor (in the PIV laser plane). Loads are highest for multiples of half-revolutions, when the two blades are again horizontal. Loads are lowest for multiples of quarter-revolutions, when the blades are vertical and one blade is in the wake of the fairing that supports the motor assembly (see figure 8-1). The oscillations in this data simply show that loads are reduced as each blade passes the support fairing, as expected.

The oscillations in the thrust and torque coefficients (figure 8-15f) also highlight the power of the smoothing spline method of Chapter 5. By fitting a smoothing spline to the angular position data using my method, we were able to deduce the oscillations in the angular acceleration of the propeller and thus, the inertial torque (figure 8-14b). Since the current supplied to the motor was constant after say two revolutions, the oscillations in the torque coefficient appear due to the unsteady inertial torque, which was derived from the smoothing spline. The oscillations in the thrust coefficient data (figure 8-15f) also appear in the raw thrust data (figure 8-14a). Since the oscillations in the thrust and torque coefficients were derived by different measurements and different data processing techniques, they must be real. Without a proper smoothing spline fit, one would not be able to deduce these minute oscillations in the torque from the given angular position data.

The steady state operation of the propeller, say between 6 and 10 revolutions, represents the *bollard pull* condition, where $J_s = \frac{V_s}{nD} = 0$. Bollard pull thrust and torque coefficients were computed for these trials by averaging the data for each trial between 6 and 10 revolutions, and these results are shown as stars in

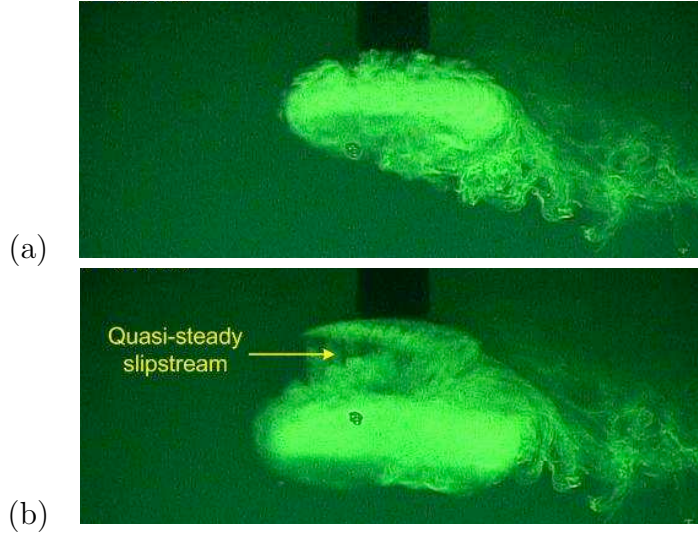


Figure 8-16: Dye visualization of a 3-bladed propeller during impulsive start from rest showing (a) the formation of an initial vortex ring and then (b) the development of a slipstream and helical wake. This figure is reprinted from (Stettler, 2004, p. 84).

figure 8-12. The torque coefficients are slightly higher than those that would be predicted by extrapolating the OPENPROP predictions to zero advance coefficient. Similarly, the thrust coefficients are slightly lower than that which would be predicted by extrapolating the OPENPROP predictions to zero advance coefficient. Since $Q \sim \sin(\beta_i)$ and $T \sim \cos(\beta_i)$, these data suggest that the inflow angle, β_i , is larger at bollard pull than the OPENPROP prediction might assert. However, the OPENPROP bollard pull performance predictions are within 10% of the measured performance, which is acceptable.

8.4.1 Unsteady wake flow visualization

A qualitative illustration of the vortical structures formed by a propeller during unsteady startup is shown in figure 8-16, as reprinted from (Stettler, 2004, p. 84). Stettler (2004) showed using fluorescent dye that a propeller initially makes a three-dimensional ring-like vortex structure during unsteady startup. As this ring convects downstream, a slipstream forms, and the wake takes on the usual helical shape.

In figure 8-17, I characterize one plane of the wake created by my propeller during unsteady startup, in an effort to quantitatively describe the structure of the wake. PIV velocity and vorticity fields are plotted over raw images, where red represents counter-clockwise vorticity and blue represents clockwise vorticity. A solid propeller blade is shown every half-revolution (when each blade passes through the PIV plane), and a dashed outline is shown for the frames when no blade is in the PIV plane. The vortices shed from the blade tips are labeled 1 through 9; it is important to remember that these are cross-sections of the three-dimensional vortex structures that are shed from the propeller blades and they do not necessarily represent discrete vortices.

At the start of the experiment, the propeller blades are in the PIV plane. As the propeller starts from rest, a starting vortex is shed; this vortex is a closed loop, and both positive (1A) and negative (1B) cross-sections of this loop are visible in the 0.25 rev frame of figure 8-17. This vortex structure does not move out of the way of the oncoming blade and is absorbed into vortex 2 in the 0.50 rev frame. As the propeller completes its first full revolution, vortex 2 represents a complete vortex ring. Vortex 3 is shed and precesses first through vortex ring 2 and then around it; by the end of the second full revolution, these vortices have coalesced into one vortex ring that slowly moves downstream out of the field of view. After the second full revolution, a slipstream becomes visible as the axial induced velocity grows; the slipstream is sketched as a dashed line in figure 8-17. After the propeller has reached steady state, one continuous helical vortex is shed from the tip of each blade (i.e. two helices in the wake, out of phase with one another). Thus, the vortices numbered 6 and 8 represent cross-sections of a single helical vortex shed from one blade tip, and vortices numbered 5, 7, and 9 represent cross-sections of the helical vortex shed from the other blade tip.

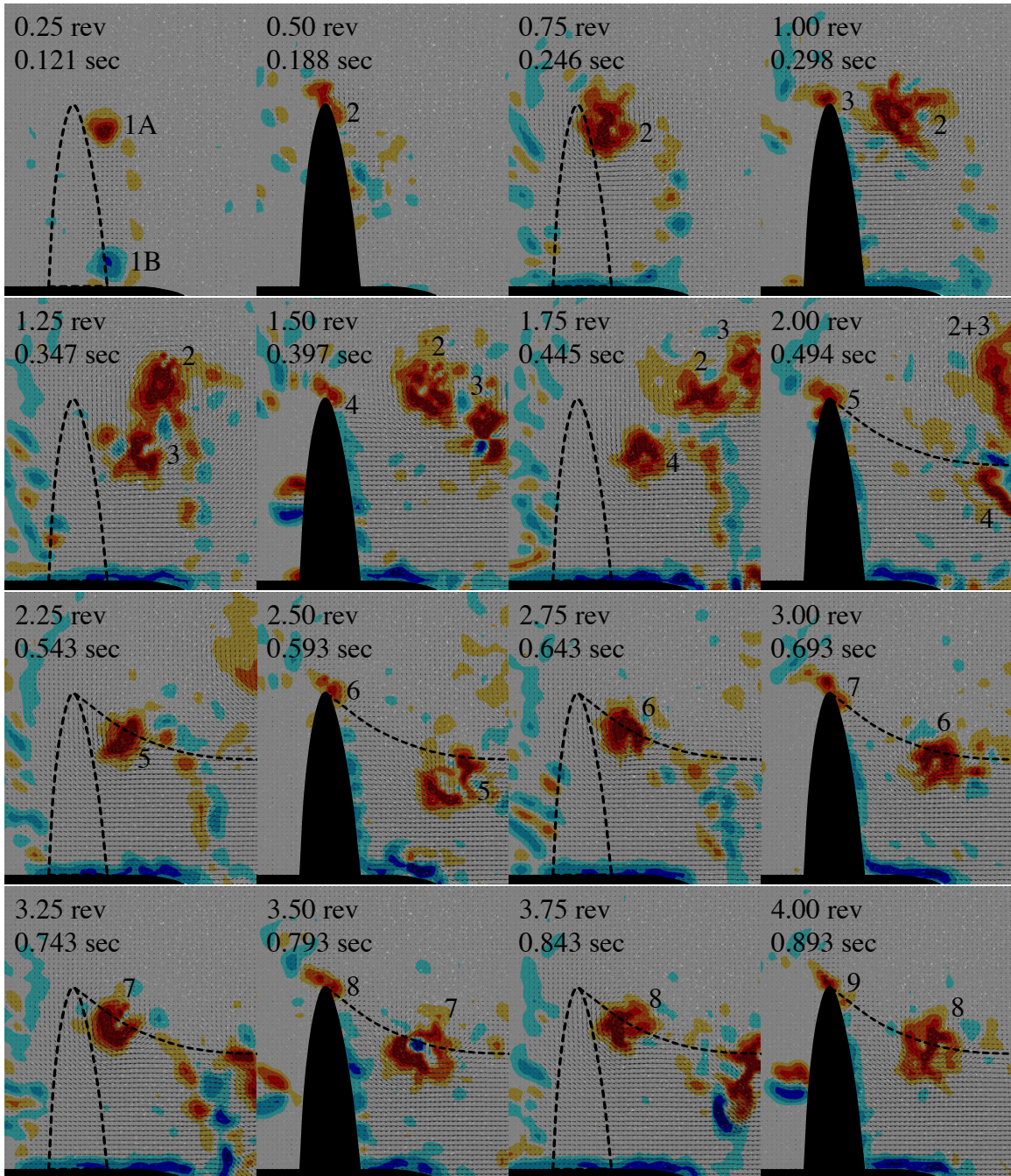


Figure 8-17: Time-series of PIV velocity and vorticity fields showing the unsteady wake development behind the propeller during startup. Anti-clockwise vorticity is red, and clockwise vorticity is blue. The hub and propeller blade are masked in black, and a dashed outline is drawn when no blade is in the PIV plane. The vortices shed from the blade tips are labeled 1-9, and the slipstream is sketched by a dashed line.

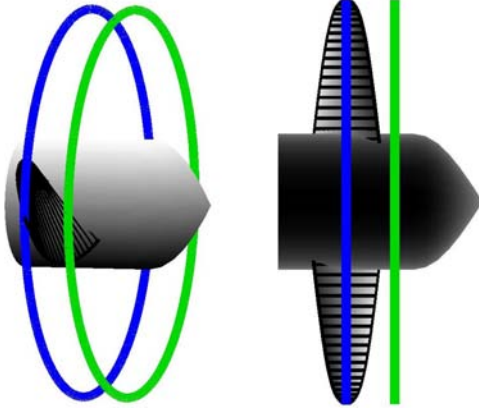


Figure 8-18: Vortex ring model of the unsteady wake produced by the propeller during an impulsive start from rest. After the first full revolution, two vortex rings are formed with strength Γ_2 (green) and Γ_3 (blue).

8.4.2 Impulsive force model

I now show how to apply the impulse framework of this thesis to derive an estimate of the thrust produced by the propeller during the unsteady start-up experiment. Specifically, I will estimate the thrust after one complete revolution of the propeller. The thrust is the axial component of the total force on the propeller blades

$$T = \mathbf{F} \cdot \mathbf{e}_a = (\mathbf{F}_v + \mathbf{F}_p) \cdot \mathbf{e}_a \quad (8.4.4)$$

In the spirit of figures 7-2 and 7-3, I model each propeller blade as being composed of vortex panels with length equal to the local chord $c(r)$ and span dr , as shown in figure 8-18. The normal vector \mathbf{n} points outwards from the (downstream) pressure side of the blade (which is consistent with the impulse model of a wing shown in figure 7-3). Referring to the propeller velocity/force diagram, figure 7-5, the normal vector is

$$\mathbf{n} = -\cos \theta \mathbf{e}_a + \sin \theta \mathbf{e}_t \quad (8.4.5)$$

where $\theta(r)$ is the pitch angle of the blade section.

Figure 8-17 shows that as the propeller traces out its first revolution, it sheds trailing vortices 2 and 3, and using this PIV data, I will quantify their circulations Γ_2 and Γ_3 . I model this (probably quite complex) vortical structure as two axisymmetric vortex rings (of diameter equal to the propeller diameter), as illustrated in figure 8-18. The impulse of this model wake is the sum of the impulse of the two vortex rings: $\mathbf{I}_w = (I_2 + I_3)(-\mathbf{e}_a)$, where $I_i = \rho\Gamma_i \frac{\pi D^2}{4}$ for $i = 2, 3$. and the thrust due to the creation of this wake in time t_3 is

$$-\frac{d\mathbf{I}_w}{dt} \cdot \mathbf{e}_a = \frac{I_2 + I_3}{t_3} \quad (8.4.6)$$

The total thrust due to the vortex impulse force is this component (which accounts for the creation of the vortical wake), plus a contribution due to the rate of change of impulse of the bound vortex panels representing the blade sections (analogous to equation (7.0.6)), as illustrated in figure 8-19a

$$\mathbf{F}_v \cdot \mathbf{e}_a = -\frac{d\mathbf{I}_w}{dt} \cdot \mathbf{e}_a + Z \int_{r_{\text{hub}}}^R \rho \frac{\partial \Gamma}{\partial t} c (-\mathbf{n} \cdot \mathbf{e}_a) dr \quad (8.4.7)$$

Since the circulation distribution is not uniform, the force must be integrated over the span. However, figure 7-10d shows that the circulation distribution is nearly the same shape for low advance coefficients (the advance coefficient is zero during startup). Therefore, the bound vortex force is approximately

$$Z \int_{r_{\text{hub}}}^R \rho \frac{\partial \Gamma}{\partial t} c (\cos \theta) dr \approx \left[Z \int_{r_{\text{hub}}}^R \rho \frac{\Gamma_d(r)}{\Gamma_{d,\text{max}}} c \cos \theta dr \right] \frac{\partial \Gamma_w}{\partial t} = \left[8.423 \text{ kg/m} \right] \frac{\partial \Gamma_w}{\partial t}$$

where Γ_w is the measured circulation of the tip vortex shed into the wake, $\frac{\Gamma_d(r)}{\Gamma_{d,\text{max}}}$ is the design circulation distribution normalized by its maximum value, and the integral within the brackets was evaluated using the known design parameters of the propeller. The average rate of increase of circulation during the first revolution

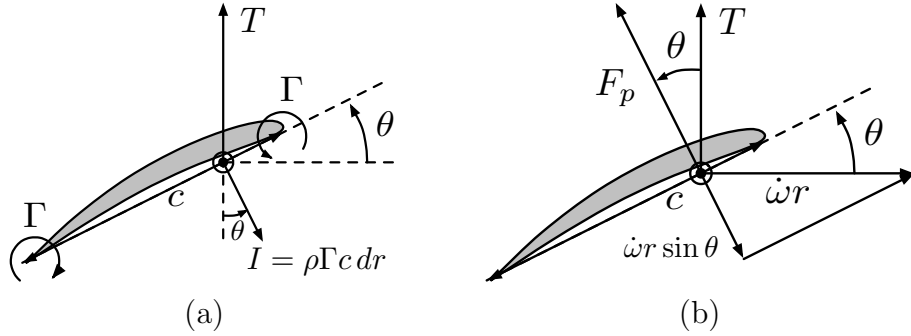


Figure 8-19: Illustration of the impulsive vortex and pressure forces on a vortex panel at radius r of chord c and span dr : (a) The vortex impulse is $\mathbf{I}_v = \rho\Gamma c dr \mathbf{n}$, and the thrust is the axial component of the reaction to the rate of change of this impulse, $dT = \rho\frac{\partial\Gamma}{\partial t} c dr (-\mathbf{n} \cdot \mathbf{e}_a)$; (b) the 2D added mass coefficient of the panel is $\rho\frac{\pi}{4}c^2$, and the acceleration of the panel normal to itself is $\dot{\omega}r \sin \theta \mathbf{n}$. Thus, the added mass force contributes thrust $dT = (\rho\frac{\pi}{4}c^2)(\dot{\omega}r \sin \theta)(-\mathbf{n} \cdot \mathbf{e}_a) dr$.

is $\frac{\partial\Gamma_w}{\partial t} = \frac{\Gamma_3}{t_3}$, where Γ_3 is the circulation of the tip vortex shed at the completion of the first revolution (which was interrogated a few timesteps later, when the propeller blade no longer obscured the PIV laser plane) and t_3 is the time to complete one revolution. In summary, the total vortex thrust is

$$\mathbf{F}_v \cdot \mathbf{e}_a = \frac{I_2 + I_3}{t_3} + \left[8.423 \text{ kg/m} \right] \frac{\Gamma_3}{t_3} \quad (8.4.8)$$

The impulsive pressure force on the propeller blade is given by equation (7.0.7), which is integrated over the span in this non-uniform case

$$\mathbf{F}_p \cdot \mathbf{e}_a = Z \int_{r_{\text{hub}}}^R \rho\frac{\pi}{4}c^2(\mathbf{a} \cdot \mathbf{n})(-\mathbf{n} \cdot \mathbf{e}_a) dr \quad (8.4.9)$$

The formulation of this equation is illustrated in figure 8-19b. Since the propeller rotates as a rigid-body, the acceleration of the blade section at radius r is $\mathbf{a} = \dot{\omega}r \mathbf{e}_t$, where $\dot{\omega}$ is the angular acceleration of the propeller. This ignores the relative acceleration of the blade to the fluid due to changes in induced velocity, which is acceptable in the early start-up times, when the induced velocities are small. Thus,

$\mathbf{a} \cdot \mathbf{n} = \dot{\omega}r \sin \theta$. The impulsive pressure thrust can also be evaluated using the known design parameters (as I did with the impulsive vortex thrust)

$$\mathbf{F}_p \cdot \mathbf{e}_a = \left[Z \int_{r_{\text{hub}}}^R \rho \frac{\pi}{4} c^2 (r \sin \theta) (\cos \theta) dr \right] \dot{\omega} = \left[0.0172 \text{ N}/(\text{rad}/\text{s}^2) \right] \dot{\omega} \quad (8.4.10)$$

Since the propeller reaches steady rotation at approximately the time it took to turn one revolution, the mean angular acceleration is $\dot{\omega} \approx \frac{\omega_s}{t_3}$, where ω_s is the rotation rate once the propeller reached steady state.

In summary, the thrust is

$$T = \mathbf{F} \cdot \mathbf{e}_a = \frac{dI_w}{dt} + Z \int_{r_{\text{hub}}}^R \rho \frac{\partial \Gamma}{\partial t} c \cos \theta dr + Z \int_{r_{\text{hub}}}^R \rho \frac{\pi}{4} c^2 (\dot{\omega} r \sin \theta) \cos \theta dr \quad (8.4.11)$$

which I approximated for this propeller as

$$T = \frac{I_2 + I_3}{t_3} + \left[8.423 \text{ kg/m} \right] \frac{\Gamma_3}{t_3} + \left[0.0172 \text{ N}/(\text{rad}/\text{s}^2) \right] \frac{\omega_s}{t_3} \quad (8.4.12)$$

The data for this trial are as follows. The circulation of vortices 2 and 3 shown in figure 8-17 are $\Gamma_2 = 0.0823 \text{ m}^2/\text{s}$ and $\Gamma_3 = 0.0697 \text{ m}^2/\text{s}$. Assuming the model vortex rings have diameters equal to the propeller diameter, $D = 0.2487 \text{ m}$, the impulse of these vortex rings are $I_2 = 3.998 \text{ kg-m/s}$ and $I_3 = 3.386 \text{ kg-m/s}$. The propeller completed one revolution at time $t_3 = 0.298 \text{ s}$, and the final rotation rate was $n_s = 5.04 \text{ rev/s}$, which corresponds to $\omega_s = 5.04 \text{ rev/s} \cdot 2\pi \text{ rad/rev} = 31.67 \text{ rad/s}$. Using these numbers, equation (8.4.12) predicts the thrust at time t_3 to be

$$T = 24.8 \text{ N} + 2.0 \text{ N} + 1.8 \text{ N} = 28.6 \text{ N} \quad (8.4.13)$$

This corresponds to a thrust coefficient of

$$KT = \frac{T}{\rho n_s^2 D^4} = 0.294 \quad (8.4.14)$$

at a rotation angle of 1 revolution. These data are plotted in figures 8-14a and 8-14f as a ‘*’. This thrust prediction agrees quite well with the measured thrust data. In this model, I ignored the actual geometry of the wake and modeled it as two axisymmetric vortex rings. The actual wake is probably quite a bit more complex than this model, but the thrust estimate is accurate nevertheless.

It is interesting to note that the first term in equation (8.4.13) dominates the thrust estimate. This is the reaction to the creation of impulse in the vortical wake. This term is over ten times as large as the other two terms. The form of the last two terms, as shown in equation (8.4.11), suggests that they scale by the *expanded area* of the blade (Carlton, 1994), $A_E = Z \int_{r_{\text{hub}}}^R c dr$. Since the impulse of the vortex rings is proportional to the disk area, $A = \frac{\pi D^2}{4}$, the relative importance of either of the last two terms in (8.4.11) scales by the *expanded area ratio*, $EAR = \frac{A_E}{A}$. For this propeller, $A = 0.0491 \text{ m}^2$ and $A_E = 0.0104 \text{ m}^2$, so the expanded area ratio is $EAR = 0.2118$, which is somewhat low for a marine propeller. It might be interesting to repeat this experiment with a propeller with a larger EAR to see if the wake creation term still dominates the total thrust estimate.

8.5 Summary

In this chapter, I discussed the design and construction of a two-bladed propeller, and I presented the results of performance curve characterization tests as well as unsteady start-up. Two important contributions were made in Section 8.2.3 regarding propeller fabrication by 3D printing. First, since a 3D printer requires finite thickness at the blade trailing edge, I created a ‘*NACA 65A010 (modified)*’ section thickness profile, which has the same leading half shape as the standard ‘*NACA 65A010*’ profile but has finite thickness at the trailing edge. Second, I created a modified linear thickness profile (eqn. 8.2.1), which can be used to generate blades that are nominally thick

enough to prevent blade flexure during testing but also have reduced thickness at the tip to maintain low thickness to chord ratios at the blade tip. These modified thickness distribution and section thickness profile are valuable tools for those who wish to rapid prototype their propeller using 3D printing.

My performance curve data (figure 8-12) provide an important validation for my off-design analysis methodology of Chapter 7. My analysis method captures the effect of changes in angle of attack due to changes in inflow speed and induced velocities. The data in figure 8-12 agree with this model, suggesting that other effects such as viscous de-cambering and 3D blade interaction effects are less important than correctly modeling the induced velocities and inflow angle. PIV tests at the design point show that the circulation of the tip vortex agrees with the circulation distribution predicted by my OPENPROP design optimizer. Taken together, these results validate the design and off-design performance predictions of my codes.

Unsteady start-up tests reveal the formation of a complex vortical structure in the wake of a propeller during a start-up event. The trailing vorticity is nominally shed in the form of a helix, but during startup, the pitch of this helix is so small that the first two loops coalesce into one leading vortex ring. This vortex ring precesses into the wake, as a slipstream forms and helical tip vortices are shed by each propeller blade. Using the impulse framework of this thesis, I developed an estimate for the thrust produced by the propeller after the first revolution. I modeled the wake at that instant as two axisymmetric vortex rings, and I used the unsteady wake PIV data to quantify the circulation of these vortices. The thrust estimate was dominated by the force required to create these rings, as the unsteady forces on the vortex panels representing the blades were quite small in comparison. This vortex ring model is analogous to the vortex ring model of the fish maneuvers presented in Chapter 2, which shows the versatility and flexibility of the impulsive framework for analyzing several types of propulsion problems.

Bibliography

- Abbott IH, von Doenhoff AE (1959) Theory of Wing Sections Dover.
- Carlton JS (1994) Marine Propellers and Propulsion Butterworth-Heinemann.
- Coney WB (1989) A Method for the Design of a Class of Optimum Marine Propulsors PhD thesis, MIT.
- Stettler J (2004) Steady and Unsteady Dynamics of an Azimuthing Podded Propulsor Related to Vehicle Maneuvering PhD thesis, MIT.

Chapter 9

Hydrokinetic turbine design and analysis

In this chapter, we consider the design and analysis of hydrokinetic turbines, the marine analog of wind turbines. We apply lifting line theory to the turbine problem and find that the same mathematical formulation given in Section 7.2 for propellers also applies to the turbine case. As such, the off-design performance method from Section 7.5 also applies to the turbine case. However, we will find that the propeller optimization method from Section 7.3 does not apply to turbines, as it results in designs that under-perform actuator disk theory. To achieve actuator disk performance, a novel turbine optimization method is presented. As a validation case, a turbine is designed, and performance experiments are presented.

9.1 Turbine lifting-line representation

In this section, I demonstrate that a turbine can be represented in the propeller lifting line formulation of Section 7.2 simply by allowing a negative circulation, $\Gamma < 0$, and other associated sign changes. If $\Gamma < 0$, then $\{F_i = \rho V^* \Gamma, C_L, u_a^*, u_t^*, f_0, \alpha\} < 0$ as well, via equations $\{(7.5.3), (7.2.7), (7.2.8), (7.4.1)\}$.

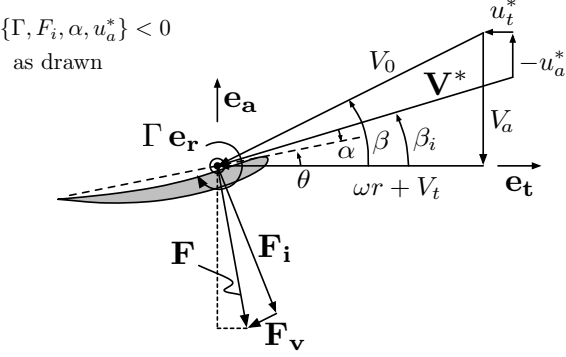


Figure 9-1: Turbine velocity/force diagram, as viewed from the tip towards the root of the blade. All velocities are relative to a stationary blade section at radius r .

Figure 9-1 shows the turbine velocity/force diagram, with $\{\Gamma, F_i, f_0, \alpha, u_a^*\} < 0$ and $u_t^* > 0$ as drawn. Since $u_a^* < 0$, \mathbf{u}_a^* points in the \mathbf{e}_a direction (as drawn). In this case, the turbine still rotates with angular velocity $\omega \mathbf{e}_a$, but the direction of the circulation is reversed (as drawn). This amounts to $|\Gamma|(-\mathbf{e}_r) = \Gamma \mathbf{e}_r$ with $\Gamma < 0$.

With, $\{\Gamma, F_i\} < 0$ but F_v always positive, the thrust and torque acting *on the turbine* are

$$\mathbf{T} = Z \int_{r_h}^R [|F_i| \cos \beta_i + F_v \sin \beta_i] dr \quad (-\mathbf{e}_a) \quad (\text{as drawn})$$

$$= Z \int_{r_h}^R [F_i \cos \beta_i - F_v \sin \beta_i] dr \quad (\mathbf{e}_a) \quad (\text{eqn. 7.2.3})$$

$$\mathbf{Q} = Z \int_{r_h}^R [|F_i| \sin \beta_i - F_v \cos \beta_i] r dr \quad (\mathbf{e}_a) \quad (\text{as drawn})$$

$$= Z \int_{r_h}^R [F_i \sin \beta_i + F_v \cos \beta_i] r dr \quad (-\mathbf{e}_a) \quad (\text{eqn. 7.2.4})$$

The fluid dynamic power of the turbine acting *on the fluid* is still

$$P = Q\omega \quad (\text{eqn. 7.2.5})$$

but since $Q < 0$ for the turbine case, $P < 0$, indicating that power is being extracted from the fluid by the turbine.

The geometry of a turbine is also correctly handled when $\Gamma < 0$. In this case, the 2D section lift coefficient

$$C_L = \frac{F_i}{\frac{1}{2}\rho(V^*)^2 c} = \frac{2\Gamma}{(V^*)c} \quad (7.5.3)$$

is also negative, and this carries through to negative values of the camber and angle of attack via

$$\{C_L, f_0, f, \alpha_I\} = \frac{C_{L_0}}{\tilde{C}_{L_I}} \cdot \{\tilde{C}_{L_I}, \tilde{f}_0, \tilde{f}, \tilde{\alpha}_I\} \quad (7.4.1)$$

where C_{L_0} is the on-design lift coefficient, which is negative.

In summary, the thrust, torque, and power are correctly predicted by equations (7.2.3), (7.2.4), and (7.2.5) when $\Gamma < 0$ for the turbine. Furthermore, since $\{u_a^*, u_t^*, C_L, f_0, \alpha\}$ depend linearly on the circulation, these parameters are also correctly handled when $\Gamma < 0$. Therefore, the same lifting line code can be used for both the propeller and turbine cases!

9.2 Turbine design optimization

9.2.1 Simple turbine optimization scheme

One might formulate the turbine optimization problem as follows: Find the set of M circulations of the vortex lattice panels that produce the least torque (i.e. the most negative torque, giving the largest power extraction at the specified rotation rate). In other words, solve the propeller optimization problem, $\{(7.3.3), (7.3.4)\}$, with no thrust constraint. For simplicity, consider the inviscid flow case, $C_D = 0$. In this formulation, the system of equations for minimizing torque (7.3.10) becomes:

$$0 = \frac{\partial Q}{\partial \Gamma_{(i)}} = \rho Z \sum_{m=1}^M \Gamma_{(m)} \cdot \begin{pmatrix} \bar{u}_a^*(m,i) r_c(m) \Delta r_{v(m)} + \\ \bar{u}_a^*(i,m) r_c(i) \Delta r_{v(i)} \end{pmatrix} + \rho Z V_{a(i)} r_c(i) \Delta r_{v(i)} \quad (\text{for } i = 1 \dots M) \quad (9.2.1)$$

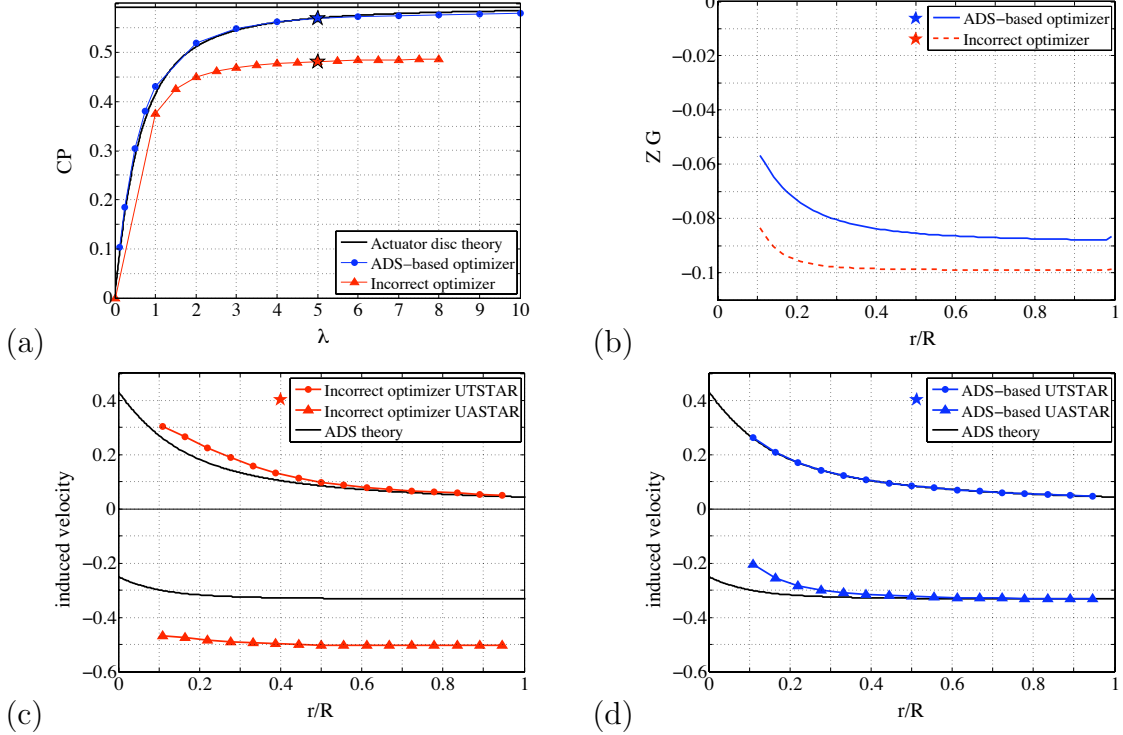


Figure 9-2: (a) Power coefficient, C_P , versus tip speed ratio, $\lambda = \frac{\omega R}{V_s}$, for turbines “optimized” by solving the system of equations (9.2.1). Optimization by solving equations (9.2.1) does not reproduce actuator-disc-with-swirl theory (black line), whereas using the actuator-disk-with-swirl-based optimizer (9.2.2) does. Here, $C_D = 0$ and $Z = 80$. (b) Circulation $G = \frac{\Gamma}{2\pi RV_s}$ versus radius for the turbines optimized for $\lambda = 5$. (c) Induced velocities $\{\frac{u_a^*}{V_s}, \frac{u_t^*}{V_s}\}$ for the simple optimizer (9.2.1). (d) Induced velocities $\{\frac{u_a^*}{V_s}, \frac{u_t^*}{V_s}\}$ for the actuator-disk-based optimizer (9.2.2).

Figure 9-2a shows that this scheme does **not** yield the largest power extraction possible (i.e. this scheme does not reproduce actuator disc theory). In this figure, a series of turbines were “optimized” by solving (9.2.1), and the power coefficients of these turbines are plotted against their tip-speed ratios. The theoretical maximum power extraction at these tip-speed ratios is given by actuator-disc-with-swirl-and-viscous-losses (*ADS*) theory (Stewart, 1976), which is shown as a solid black line in figure 9-2a. Clearly, “optimization” by solving equations (9.2.1) does not reproduce actuator-disc-with-swirl theory. However, turbines may be designed to replicate *ADS* theory using an ADS-based optimizer, as discussed in the following section. In this example, $C_D = 0$, $Z = 80$, and the axial inflow is $\frac{V_a}{V_s} = 1$ for all blade sections.

The question is: why does the system of equations (9.2.1) under-perform actuator disk theory? Figures 9-2b, 9-2c, and 9-2d show the reason for the under-performance of the (9.2.1) scheme. Optimizer (9.2.1) produces turbines that induce axial velocity $\frac{u_a^*}{V_s} = \frac{u_a^*}{V_a} \approx -\frac{1}{2}$ (as shown in figure 9-2c), whereas actuator disk theory prescribes $\frac{u_a^*}{V_a} = -\frac{1}{3}$ for maximum power extraction. Equations (9.2.1) do not yield turbines that extract as much power from the flow as *ADS* theory predicts, because solving (9.2.1) yields a circulation distribution which induces too much axial induced velocity, thereby reducing the flow rate through the turbine more than it should, resulting in less power available for extraction. For comparison, my ADS-based optimizer (9.2.2) produces turbines that induce axial velocity $\frac{u_a^*}{V_s} \approx -\frac{1}{3}$ (as shown in figure 9-2d), which is why the power produced by these turbines replicates that of *ADS* theory.

To deduce the under-performance of (9.2.1) mathematically, note that the horseshoe influence matrices $\{\bar{u}_a^*, \bar{u}_t^*\}$ are dominated by their diagonal terms. To the leading order, the influence functions and induced velocities behave like

$$\bar{u}_a^{*(m,i)} \approx \begin{cases} 0 & (m \neq i) \\ \bar{u}_a^{*(i,i)} & (m = i) \end{cases}$$

$$u_a^{*(i)} \approx \Gamma_{(i)} \bar{u}_a^{*(i,i)}$$

With these approximations, it is evident that the system of equations (9.2.1) behaves like M independent equations ($i = 1 \dots M$)

$$0 = \rho Z \cdot \Gamma_{(i)} \cdot [2 \bar{u}_a^{*(i,i)} r_{c(i)} \Delta r_{v(i)}] + \rho Z V_{a(i)} r_{c(i)} \Delta r_{v(i)}$$

which are each satisfied when

$$u_a^{*(i)} = -\frac{1}{2} V_{a(i)}$$

This result is consistent with the example induced velocity distribution shown in figure 9-2c, as discussed above. In short, the simple turbine optimization scheme (9.2.1) under-performs actuator disk theory, because solving (9.2.1) yields a circulation distribution which induces too much axial velocity. Physically, this results in a smaller flow rate through the turbine than actuator disk theory suggests and too little power available for extraction.

9.2.2 Improved, actuator-disk-based optimization scheme

I have created an actuator-disk-based turbine optimization procedure, which is formulated as follows. My procedure is a vortex-lattice adaptation of actuator-disc-with-swirl-and-viscous-losses (*ADS*) theory (Stewart, 1976). During the design optimization, flow parameters $\{\Gamma, u_a^*, u_t^*, \bar{u}_a^*, \bar{u}_t^*, \beta_i\}$ must be self consistent to define a physically-realistic operating state of the turbine. That is, equations $\{(7.2.7), (7.2.8), (7.2.9), (7.2.10), (7.2.2)\}$ must hold, given Γ .

In the present optimization scheme, I set the tangential induced velocity to the actuator disc with swirl (*ADS*) value

$$u_t^* \equiv u_{t,ADS}^* \quad (9.2.2)$$

The remaining flow parameters $\{\Gamma, u_a^*, \bar{u}_a^*, \bar{u}_t^*, \beta_i\}$ are determined iteratively. Initially setting $u_a^* = u_{a,ADS}^*$ allows one to start a loop that computes β_i via (7.2.2), then $\{\bar{u}_a^*, \bar{u}_t^*\}$ via $\{(7.2.9), (7.2.10)\}$. Then, the circulation distribution can then be determined by solving the matrix equation

$$[\bar{u}_t^*] \cdot [\Gamma] = [u_{t,ADS}^*]$$

for Γ . Finally, u_a^* is computed via (7.2.7), and the loop restarts. Iteration continues until every state variable has converged.

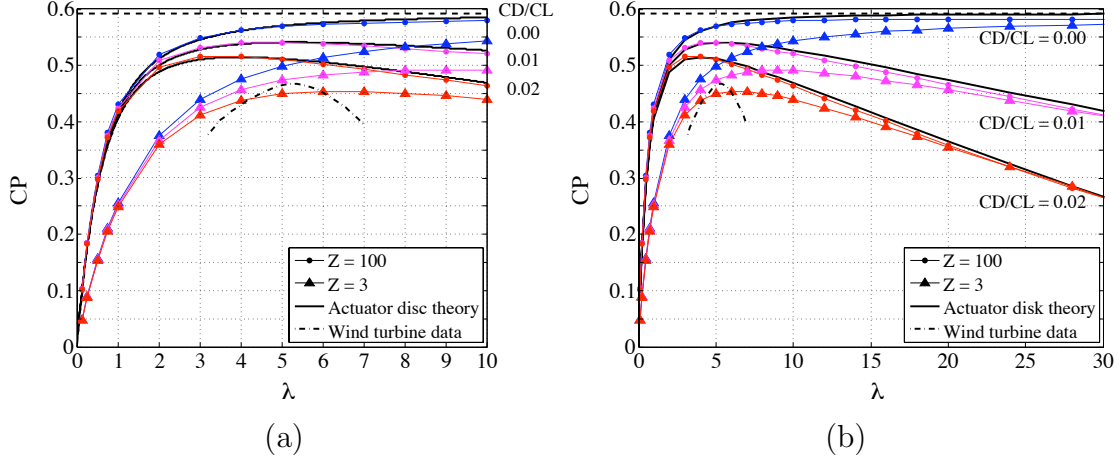


Figure 9-3: (a) Power coefficient, $C_P = P/\frac{1}{2}\rho V_\infty^3 \pi R^2$, versus tip speed ratio, $\lambda = \frac{\omega R}{V_\infty}$, for optimized turbines. The C_P of turbines designed with 100 blades agrees quite well with actuator-disc-with-swirl-and-viscous-losses theory (Stewart, 1976), as shown for three C_D/C_L ratios. Performance data of 3-bladed wind turbines in service, digitized from (Kahn 2006), is also shown for reference. (b) Power coefficients of 3-bladed and 100-bladed turbines converge for high tip speed ratios ($\lambda > 25$), as expected.

The performance of several turbines optimized using this scheme is shown in figure 9-3. Using this scheme (9.2.2), one can reproduce the C_P vs. λ performance curves from *ADS* theory (Stewart, 1976), as shown by the (essentially infinite-bladed) $Z = 100$ curves in figure 9-3a. An additional check that this scheme works correctly, which is shown in figure 9-3b, is that for very high tip speed ratios ($\lambda > 25$), each of the $Z = 3$ curves asymptotes to its corresponding $Z = 100$ curve, as expected.

Clearly, the scheme presented here could be augmented to set $u_a^* \equiv u_{a,ADS}^*$ and solve for whatever u_t^* , etc. is self-consistent with that. I find marginally-worse agreement with actuator disc theory using this approach. One point of ongoing work is to reformulate the turbine optimization problem in such a way that it does not require actuator disc theory as an input.

9.2.3 Chord length optimization

During the circulation optimization procedure, the chord, c , can be chosen in order to restrict the lift coefficient to a given maximum allowable absolute value, $C_{L_{\max}}$, such that

$$C_L = C_{L_{\max}} \cdot \frac{\Gamma}{|\Gamma|} \quad (9.2.3)$$

$$c = \frac{2|\Gamma|}{(V^*)C_{L_{\max}}} \quad (9.2.4)$$

It is important to restrict the maximum lift coefficient in order to prevent flow separation and cavitation at the leading edge of the propeller/turbine blade. The absolute values in (9.2.3) and (9.2.4) are necessary for the turbine case, in which $\Gamma < 0$ and $C_L = -C_{L_{\max}}$, but $c > 0$.

9.3 Off-design performance analysis

The same off-design performance analysis method presented in Chapter 7 can be used for propellers as well as turbines. The Newton solver implemented in **OPENPROP** was in fact written for the turbine case, where the operating state is characterized by an off-design (*OD*) *tip-speed ratio*,

$$\lambda_{OD} = \frac{\omega_{OD}R}{V_s} = \frac{\pi}{J_{s,OD}} \quad (9.3.1)$$

and unknown flow parameters $\{V^*, \alpha, C_L, \Gamma, u_a^*, u_t^*, \beta_i, \bar{u}_a^*, \bar{u}_t^*\}$. Since the same governing equations apply to the propeller and turbine cases, the same code can be used for either.

An example off-design analysis is presented in figure 9-4. For reference, the *ADS* performance frontier, industry wind turbine data, and the performance of *ADS*-based

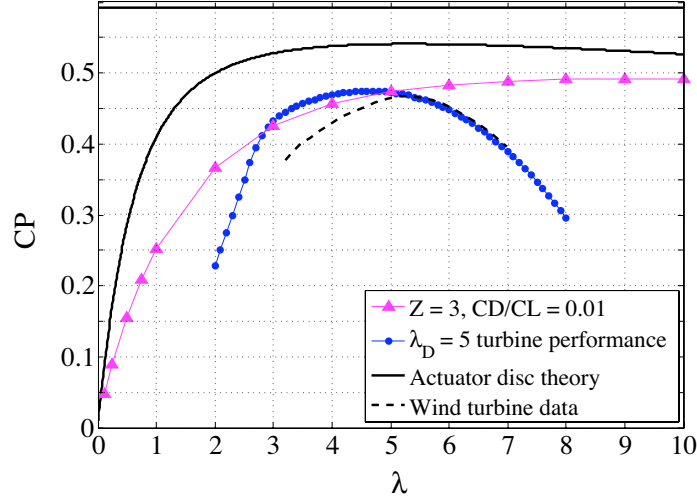


Figure 9-4: Power coefficient, C_P , versus off-design tip speed ratio, λ , for a turbine designed to operate at $\lambda_D = 5$, with specifications $C_D = 0.01$ and $Z = 3$.

optimized turbines with $C_D/C_L = 0.01$ and $Z = 3$ are reproduced from figure 9-3. The off-design performance is shown for the turbine designed to operate at $\lambda_D = 5$. The performance predicted by the analyzer ('•') agrees with the performance predicted by the optimizer ('▲') at $\lambda = 5$, and the performance for higher tip speed ratios compares quite favorably with wind turbine industry performance data from (Kahn 2006). For $\lambda < 3$, the power coefficient drops precipitously, as the net angle of attack drops below the specified stall angle (-8°) at many blade sections and the blade stalls. For $3 < \lambda < 5$, the turbine optimized for $\lambda_D = 5$ outperforms the *ADS*-based performance frontier. That is, the $\lambda_D = 5$ turbine ('•') outperforms the 'optimized' turbines at $\lambda = 4$ and 3 ('▲'), indicating that the *ADS*-based optimization method does not truly find the best configurations possible. Reformulating the turbine optimization method is one focus of ongoing work.

Parameter	Value	Description
Z	2	number of blades
n	19.1 rev/s	rotation rate (120 rad/s)
D	0.25 m	propeller diameter (approx 10 in)
V_s	3 m/s	ship speed (free-stream speed)
D_{hub}	0.08382 m	hub diameter (3.3 in)
M	20	number of vortex panels
ρ	1000 kg/m ³	water density
$\lambda = \frac{\omega R}{V_s}$	5	tip-speed ratio
$C_{L,\max}$	0.5	maximum allowable lift coefficient

Table 9.1: Turbine design input parameters.

9.4 Turbine off-design performance experiments

9.4.1 Turbine design

The author designed a two-bladed horizontal-axis turbine for use in off-design performance validation tests. The turbine was specifically designed to operate using the same experimental test setup used for propeller tests. As with the propeller designed in Chapter 8: the inflow velocity profile was assumed uniform ($V_a/V_s = 1$); the swirl inflow velocity was zero ($V_t = 0$); the turbine had zero rake or skew; and the section drag coefficient was assumed to be $C_D = 0.010$ for all blade sections. The choice of diameter, hub size, and blade number was also carry-over from the propeller design. Other relevant parameters appear in table 9.1, and their justification follows.

A parametric design study was performed to select the free-stream speed and rotation rate for the turbine. The results of this study are shown in figure 9-5. Figure 9-5 shows the power coefficient of turbines with $Z = \{2, 3, 4, 100\}$ blades designed for a range of tip speed ratios, $0.25 < \lambda = \frac{\omega R}{V_s} < 10$. The selected tip speed ratio, $\lambda = 5$, has nearly the best power coefficient for the two-bladed turbines and is typical of a marine current turbine. The free-stream speed and rotation rate were then chosen to give this tip speed ratio (see table 9.1) and to produce torque in the range that the trolling motor could be used in the experiments.

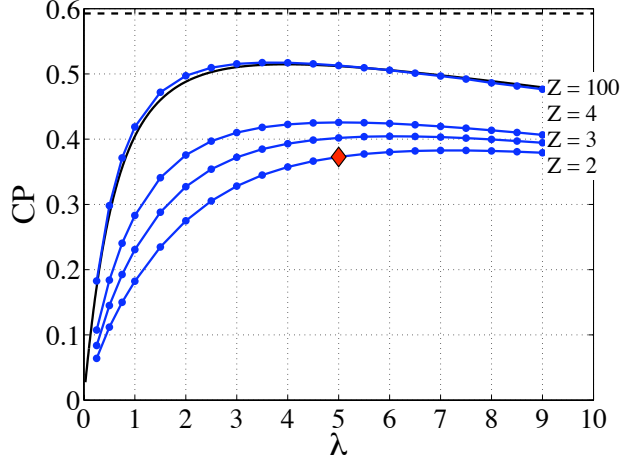


Figure 9-5: Parametric design study: power coefficient, C_P , versus tip-speed ratio, λ , and number of blades, $Z = \{2, 3, 4, 100\}$, as computed using the *ADS*-based turbine optimization method with $C_D/C_L = 0.02$. The design point is marked by the ‘♦’.

r/R	G	C_L	β_I	α	θ	$\frac{c}{D}$	$\frac{f_0}{c}$	$\frac{t_0}{c}$
0.3517	-0.0409	-0.5000	20.4575	-0.7000	19.7575	0.2567	-0.0333	0.0975
0.3845	-0.0410	-0.5000	18.9267	-0.7000	18.2267	0.2400	-0.0333	0.1011
0.4173	-0.0411	-0.5000	17.5991	-0.7000	16.8991	0.2250	-0.0333	0.1045
0.4502	-0.0411	-0.5000	16.4386	-0.7000	15.7386	0.2115	-0.0333	0.1076
0.4830	-0.0411	-0.5000	15.4169	-0.7000	14.7169	0.1992	-0.0333	0.1105
0.5158	-0.0411	-0.5000	14.5114	-0.7000	13.8114	0.1879	-0.0333	0.1132
0.5486	-0.0410	-0.5000	13.7039	-0.7000	13.0039	0.1773	-0.0333	0.1156
0.5815	-0.0408	-0.5000	12.9799	-0.7000	12.2799	0.1675	-0.0333	0.1179
0.6143	-0.0405	-0.5000	12.3273	-0.7000	11.6273	0.1582	-0.0333	0.1201
0.6471	-0.0401	-0.5000	11.7365	-0.7000	11.0365	0.1493	-0.0333	0.1223
0.6799	-0.0395	-0.5000	11.1992	-0.7000	10.4992	0.1406	-0.0333	0.1244
0.7128	-0.0388	-0.5000	10.7086	-0.7000	10.0086	0.1321	-0.0333	0.1267
0.7456	-0.0378	-0.5000	10.2592	-0.7000	9.5592	0.1236	-0.0333	0.1293
0.7784	-0.0366	-0.5000	9.8459	-0.7000	9.1459	0.1149	-0.0333	0.1324
0.8113	-0.0351	-0.5000	9.4649	-0.7000	8.7649	0.1059	-0.0333	0.1363
0.8441	-0.0331	-0.5000	9.1124	-0.7000	8.4124	0.0963	-0.0333	0.1416
0.8769	-0.0306	-0.5000	8.7856	-0.7000	8.0856	0.0857	-0.0333	0.1492
0.9097	-0.0272	-0.5000	8.4819	-0.7000	7.7819	0.0737	-0.0333	0.1608
0.9426	-0.0226	-0.5000	8.1990	-0.7000	7.4990	0.0591	-0.0333	0.1812
0.9754	-0.0157	-0.5000	7.9353	-0.7000	7.2353	0.0396	-0.0333	0.2325

Table 9.2: Optimized turbine blade load distribution and associated section geometry. All angles are given in degrees.

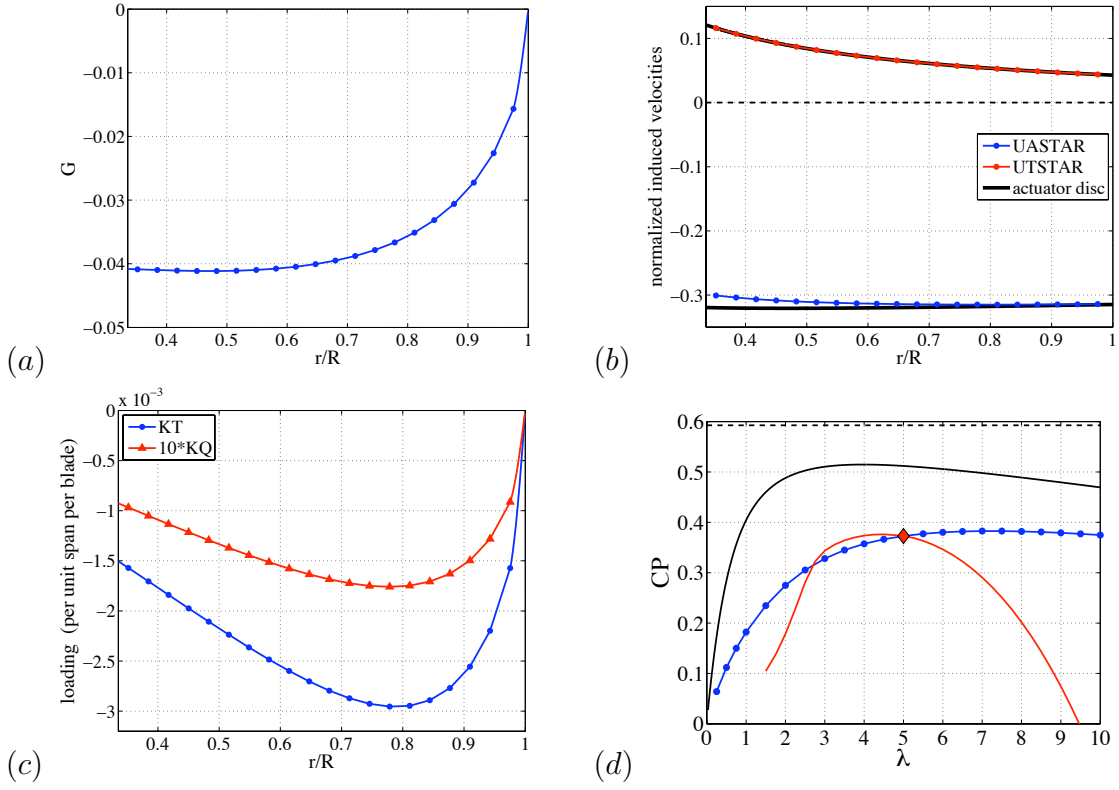


Figure 9-6: Optimized turbine loading and off-design performance: (a) non-dimensional circulation, $G = \frac{\Gamma}{2\pi RV_s}$, versus radius, $\frac{r}{R}$; (b) non-dimensional induced velocities, $\{\frac{u_a^*}{V_s}, \frac{u_t^*}{V_s}\}$, versus radius; (c) loading per unit span per blade versus radius; (d) predicted off-design power coefficient versus tip-speed ratio.

The optimized load distribution and the associated blade geometry is given in tabular form in table 9.2 and is also shown in figure 9-6. The off-design performance of the turbine is also shown in figure 9-6. The power coefficient falls for increasing tip speed ratios, since increasing the rotation rate decreases the angle of attack of each blade section, which decreases the loading produced by the blade. Conversely, decreasing the tip speed ratio increases the section angle of attack, increasing power production. However, the power coefficient drops precipitously for low tip-speed ratios, $\lambda < 3$, as sections of the blade exceed the stall angle of attack.

The blade geometry is shown in figures 9-7 and 9-8. Figure 9-7a shows the optimized chord distribution for this turbine. In order to minimize viscous drag,

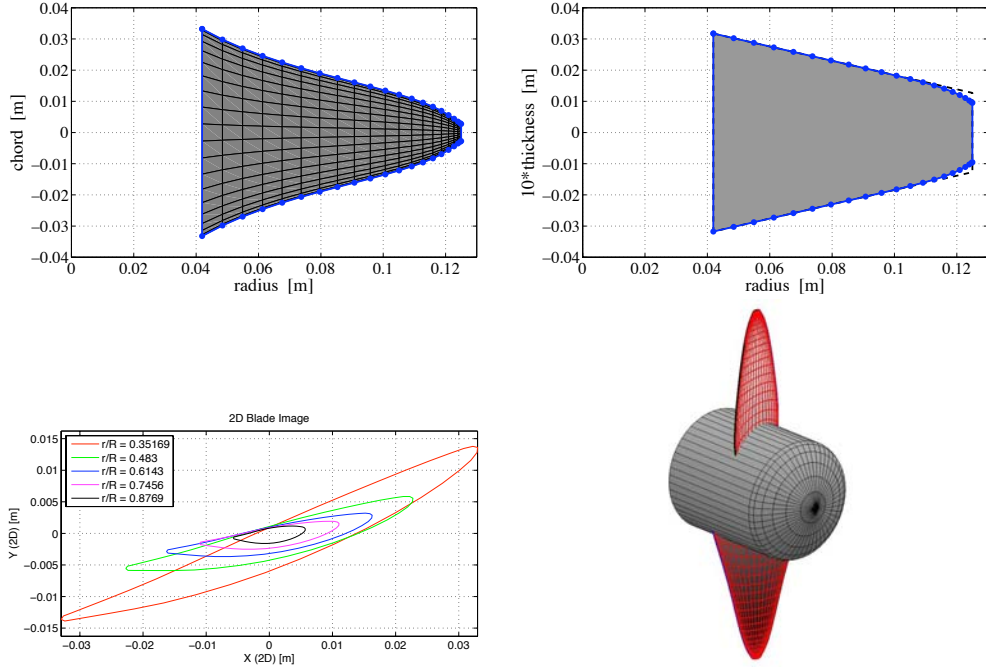


Figure 9-7: OPENPROP rendering of the turbine blades.

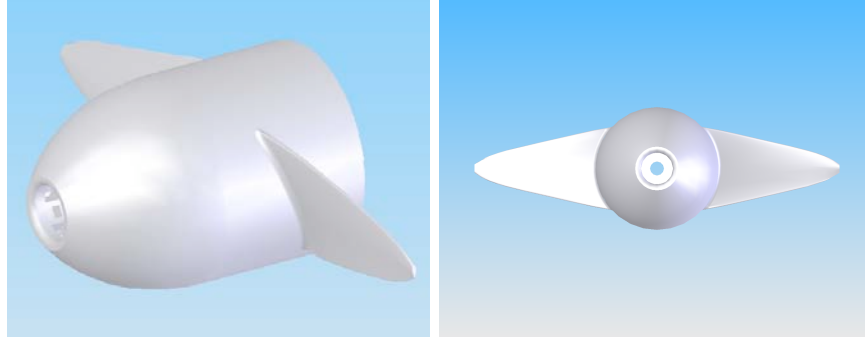


Figure 9-8: SOLIDWORKS model of the turbine and hub.

the chord lengths were minimized via equation (7.3.5), with a maximal allowable lift coefficient of $C_{L,\max} = 0.5$ for this turbine. The blade thickness distribution shown in figure 9-7b was given by equation (8.2.1), with hub and tip section thicknesses of $t_{0,\text{hub}} = 0.25$ inch and $t_{0,\text{tip}} = 0.10$ inch, a tip-modification radius of $r_{\text{mod}} = 0.8R$, and a tip-thickness reduction factor of $\frac{t_{0,\text{mod}}}{t_{0,\text{tip}}} = 0.75$. This thickness distribution is approximately linear for $r < r_{\text{mod}}$ and is modified by the exponential term for larger radii. The final, modified tip thickness is $t_0(r = R) = t_{0,\text{tip}}^{\text{mod}} = 0.075$ inch.



Figure 9-9: Finished turbine in the water tunnel. The flow is still left to right as in the propeller experiments, but the motor housing has been turned around such that the load on the propeller shaft is still compressive.

Figures 9-7c and 9-7d show the 2D and 3D blade geometries. Each 2D section uses a ‘*NACA 65A010 (modified)*’ thickness form and a ‘*NACA a=0.8 (modified)*’ camber profile, which has an ideal lift coefficient, ideal angle of attack, and camber ratio of $\tilde{C}_{L_I} = 1.0$, $\tilde{\alpha}_I = 1.40$, and $\tilde{f}_0/c = 0.06651$ respectively. These angle of attack and camber ratio are scaled by the desired lift coefficient ($C_L = C_{L,\max}$) to give the desired section geometry.

Figure 9-8 shows a SOLIDWORKS rendering of the turbine blades built on the same hub that was used for the propeller in Chapter 8. The turbine was 3D printed and machined as discussed in Chapter 8. The finished turbine is shown in figure 9-9.

In the turbine performance tests, the trolling motor apparatus was turned around (see figure 9-9), such that the forward end of the turbine is opposite that of the propeller presented in Chapter 8. The reason for this is because the trolling motor used in the performance tests only has a thrust bearing that can bear compressive load. In other words, if there were to be a (drag) force on a propeller or turbine that

would tend to pull the propeller/turbine away from the motor housing (i.e. put tension on the propeller shaft), there would be inordinate friction in the motor housing, because the thrust bearing would no longer be the bearing surface. In order to maintain compression on the thrust bearing, the trolling motor was turned around for the turbine tests, so the tip of the hub now is the nose of the motor assembly. A nose cone was 3D printed and fit snugly in the turbine hub, as shown in figure 9-9.

9.4.2 Steady performance experiments

A series of steady-state off-design performance tests were performed to characterize the turbine. In each test, the free-stream speed, V_s , was measured, and a time-series of turbine angular position data was acquired from the Hall-effect sensor, as described in Chapter 8. The steady rotation rate, ω , was determined for each trial by the slope of a linear fit to the Hall-effect sensor data. In these tests, the electrical leads to the trolling motor were left open-circuit, so the current flowing through the motor was zero ($i_m = 0$), and the net torque on the turbine was

$$|Q| = B(\omega) \quad (9.4.1)$$

where the friction torque, $B(\omega)$, is given by calibration equation (8.1.5), and the absolute value is used for convenience in plotting the data. The hydrodynamic power (acting on the turbine) and power coefficient are

$$P = |Q| \cdot \omega \quad (9.4.2)$$

$$C_P = \frac{|Q| \cdot \omega}{\frac{1}{2} \rho V_s^2 \pi R^2} \quad (9.4.3)$$

where V_s was measured for each trial, $\rho = 1000 \text{ kg/m}^3$ is the water density, and $R = 0.125 \text{ m}$ is the measured radius of the turbine. Power coefficient data are plotted against tip-speed ratio $\lambda = \frac{\omega R}{V_s}$ in figure 9-10.

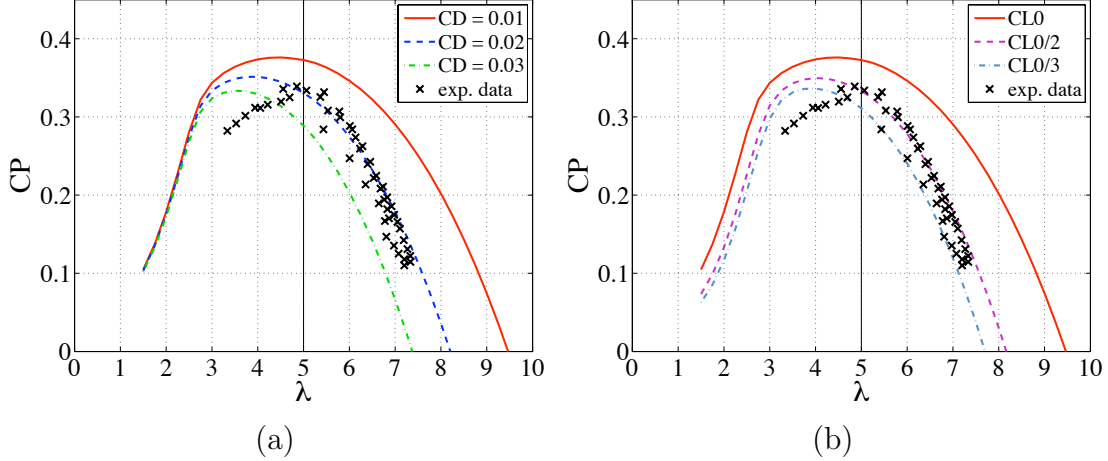


Figure 9-10: Off-design performance data for the turbine (same data in both figures) with performance curves illustrating hypothetical scenarios: (a) increased drag coefficient ($C_D = 0.01$ as designed), and (b) reduced on-design lift coefficient (the on-design lift coefficient is $C_L = C_{L,0}$ as designed).

The measured power coefficient data do not agree well with the predicted performance curve shown in figure 9-10 (the as-designed performance curve is shown as the solid red lines). However, the data in figure 9-10 suggest two possible explanations: (a) the section drag coefficient may be higher than 0.01, or (b) the effective camber of the turbine may be less than as designed, which would reduce the on-design lift coefficient. Both explanations are plausible, as performance curves created for either of these hypothetical scenarios agree with the experimental data in figures 9-10a and 9-10b over a large range of tip-speed ratios. (Note that it is purely coincidence that the C_D -doubled and $C_{L,0}$ -halved performance curves resemble one another. The performance curves for C_D tripled and $C_{L,0}$ divided by three do not overlay, as expected.)

The $C_D = 0.02$ performance curve shown in figure 9-10a fits the data well. If the drag coefficient is truly 0.02 for the NACA blade section forms (which were used for both the turbine and propeller), then the propeller experimental data should also agree with a hypothetical performance curve where we set $C_D = 0.02$ for the propeller. However, the measured propeller torque data were less than the ‘as designed’ torque

prediction, whereas increasing the drag coefficient raises the torque prediction. While thickness to chord ratio and Reynolds number differences between the propeller and turbine experiments might afford some wiggle room for C_D , this hypothesis is unlikely to be true.

The measured data also support the hypothesis that the as-built section lift coefficients are less than the design intent. This hypothesis is illustrated in figure 9-10b, where theoretical performance curves were created for the turbine by simply dividing the as-designed lift coefficient by 1/2 or 1/3 and finding the off-design states. This is not quite correct physically, because simply adjusting the on-design lift coefficient without also changing the other flow parameters (such as circulation) results in a design state which is not physically realizable. However, this rough procedure still illustrates the point that if the as-built lift coefficient were half of the design-intent values, then the turbine would perform roughly as how the data show.

This scenario is quite plausible, since it is known that 3D effects cause an effective de-cambering of about half. That is, due to 3D effects, the lift coefficient achieved for a given camber, f_0 , would be half of what (7.4.1) would dictate

$$C_{L_0} \approx \frac{1}{2} \cdot \frac{f_0}{\tilde{f}_0} \tilde{C}_{L_I} \quad (9.4.4)$$

Thus, since we built the propeller and turbine according to equation (7.4.1), we hypothesize that the on-design lift coefficient may be about half of the predicted value. It should be noted that the turbine blades were observed to flex slightly during the performance tests, which would certainly change the camber of the blades regardless of any 3D effects which may or may not have also occurred.

The experimental method used to obtain the power estimates should also be called into question, since we did not directly measure the torque generated by the turbine. Ideally, one would directly measure torque on the propeller shaft, with possibly the

friction in just one seal to account for. At the time of publication of this thesis, a graduate student was building a turbine test fixture, and further turbine performance tests are one point of ongoing work.

9.5 Summary

In this chapter, we applied lifting line theory to the design and analysis of hydrokinetic turbines. We showed that the same mathematical framework given in Chapter 7 for propellers also applies to the turbine case, where the circulation and a number of other flow parameters take on negative values. We also showed, however, that the propeller optimization scheme does not apply in the turbine case, as it results in turbines that under-perform actuator disk with swirl (*ADS*) theory. Actuator disk performance can be achieved by designing a turbine such that its tangential induced velocity matches that prescribed by *ADS* theory.

We used the *ADS*-based turbine optimization method to design a two-bladed turbine for use in off-design performance tests. In a series of performance tests, however, we found that the power coefficient did not match well with the predicted values. We hypothesize that this is due to effective de-cambering of the turbine blades, either due to 3D effects which change the on-design lift coefficient, or due to blade flexure during the tests. The experimental method used to obtain the power extraction can also be called into question, since we did not directly measure the torque generated by the turbine. Further performance tests are ongoing work.

Bibliography

- Stewart HJ (1976) “Dual optimum aerodynamic design for a conventional windmill,” *AIAA Journal* **14**(11):1524–1527.

Chapter 10

Summary and outlook

This thesis presents an impulse framework for estimating the fluid-dynamic force on a body in flow. Applications for this framework are drawn from hydrodynamics problems of interest: fish swimming and maneuvering, free-surface impact of spheres, and marine propeller and turbine design.

The impulse-force framework postulates that the total force on a body is the sum of the *vortex impulse force* and *pressure impulse force*

$$\mathbf{F} = \mathbf{F}_v + \mathbf{F}_p \quad (1.2.14)$$

where \mathbf{F}_v is the reaction to the rate of change of *vortex impulse* of the *additional vorticity* created by the body (including both the bound vorticity and the free vorticity shed into the wake), and \mathbf{F}_p is the reaction to the rate of change of *pressure impulse* required to generate the potential flow about the body

$$\mathbf{F}_v = -\frac{d\mathbf{I}_v}{dt} = -\frac{d}{dt} \left[\frac{1}{2} \rho \int_V \mathbf{x} \times \boldsymbol{\omega}_a dV \right] \quad (1.2.15)$$

$$\mathbf{F}_p = -\frac{d\mathbf{I}_p}{dt} = -\frac{d}{dt} \left[\int_{S_b} \rho \phi \hat{\mathbf{n}} dS \right] \quad (1.2.16)$$

I applied this impulse-force framework in a series of problems in this thesis.

In Chapter 2, I showed that the total momentum change of a fish making a rapid C-turn maneuver is accurately predicted by integrating these impulsive forces over the short duration of the maneuver: $m_{\text{fish}} \Delta \mathbf{V}_{\text{fish}} = \int_{t_{\text{start}}}^{t_{\text{end}}} (\mathbf{F}_v + \mathbf{F}_p) dt$. In this study, I modeled the wake created by the maneuvering fish as two vortex rings, which have a simple algebraic formula for their impulse, $I = \rho \Gamma A \left(1 + \frac{3}{4} \frac{a}{A}\right)$.

In Chapter 3, I considered steady swimming, for which we know the time-averaged force must be zero, $\langle \mathbf{F} \rangle = 0$. I modeled the time-averaged vortex impulse force, $\langle \mathbf{F}_v \rangle$, using the classical theory of von Kármán and Burgers, and I found good agreement between the swimming performance of a robotic fish and the scaling laws prescribed by this model.

In Chapters 5 and 6, I considered the free-surface impact of a falling sphere. In this problem, the air cavity formed behind a hydrophobic sphere during water entry prevents the formation of a vortical wake, so $\mathbf{F}_v = 0$. In this chapter, I applied potential flow theory to model the unsteady pressure impulse force on the sphere, since $\mathbf{F} = \mathbf{F}_p$. I found good agreement between the forces predicted by my potential flow model and the overall force deduced by fitting a smoothing spline to digitized sphere position data, using the method developed in Chapter 5.

The performance of a marine propeller, considered in Chapter 7, afforded the opposite scenario, in which $\mathbf{F}_p = 0$ and $\mathbf{F} = \mathbf{F}_v$ for steady-state operation. Applying the general impulse framework, I derived propeller lifting line theory, which I then used that to create an off-design performance analysis method for marine propellers and hydrokinetic turbines. The experimental performance data I collected in Chapter 8 agreed with predictions, thus validating the method.

Finally, I brought the thesis full circle by examining the unsteady start-up of a marine propeller, in which case both the vortex and pressure impulse forces contributed to the total load on the propeller, $\mathbf{F} = \mathbf{F}_v + \mathbf{F}_p$. This wide breadth of experiments showcases the versatility and utility of my impulse-force framework.

What are the nature of \mathbf{F}_v and \mathbf{F}_p ? In Chapter 6, I proved that the pressure impulse force is equivalent to computing the net pressure force on the body,

$$\begin{aligned}\mathbf{F}_p &\equiv -\frac{d}{dt} \left[\int_{S_b} \rho \phi \hat{\mathbf{n}} dS \right] & (??) \\ &= \int_{S_b} (p_\infty - \rho \frac{\partial \phi}{\partial t} - \frac{1}{2} \rho |\nabla \phi|^2) \hat{\mathbf{n}} dS & (6.0.2)\end{aligned}$$

with the pressure computed using Bernoulli's equation $p = p_\infty - \rho \frac{\partial \phi}{\partial t} - \frac{1}{2} \rho |\nabla \phi|^2$. Now $\mathbf{F} = \mathbf{F}_p$ only for ideal flows, in which viscous effects are ignored and the velocity field is modeled as that given solely by a potential function, $\mathbf{u} = \nabla \phi$. However, in Chapter 1, I noted that any incompressible fluid flow can be decomposed into a potential flow and the remaining component, $\mathbf{u} = \nabla \phi + \mathbf{u}_0$. Thus, for a real fluid flow, it is possible to determine its potential function, compute a “pressure” from Bernoulli's equation, and compute the resulting “net pressure force” from (6.0.2). These “pressure” and “net pressure force” will not be correct for any flow with non-zero \mathbf{u}_0 . That is, they will not be correct for any flow with non-zero vorticity, since $\boldsymbol{\omega} \equiv \nabla \times \mathbf{u} = \nabla \times \mathbf{u}_0$ (because of the well-known vector identity $\nabla \times \nabla \phi = 0$). The total force for a real flow is given by integrating the true pressure and tractive forces over the body surface

$$\mathbf{F} = \int_{S_b} \hat{\mathbf{n}} \cdot [p \mathbf{E} - \mathbf{T}] dS \quad (1.0.2)$$

Therefore, the vortex impulse force can be written as

$$\begin{aligned}\mathbf{F}_v &= \mathbf{F} - \mathbf{F}_p \\ &= \int_{S_b} \hat{\mathbf{n}} \cdot [p \mathbf{E} - \mathbf{T}] dS - \int_{S_b} (p_\infty - \rho \frac{\partial \phi}{\partial t} - \frac{1}{2} \rho |\nabla \phi|^2) \hat{\mathbf{n}} dS & (10.0.1)\end{aligned}$$

This result shows that the vortex impulse force can be thought of as a correction to the potential flow “net pressure force”, due to the presence of vorticity in the wake of the body.

To reiterate, for any flow, one can compute the velocity potential and use it to compute the pressure impulse force. The pressure impulse force is the net pressure force on the body, with the pressure computed using unsteady Bernoulli's equation. Since unsteady Bernoulli's is invalid for (real) viscous flows, it will not yield the correct pressure, and the total force on the body will be different than the pressure impulse force. The presence of viscosity enables vortex shedding from the body, which augments the pressure and tractive forces on the surface of the body. Equation (10.0.1) states that the vortex impulse force is a correction to the pressure impulse force, and if computed exactly would rectify the difference between (a) the force computed by integrating the true pressure and viscous stress over the body surface, and (b) the force computed by integrating the potential flow "pressure" (as derived from unsteady Bernoulli's equaiton) over the body surface.

The impulse-force equations (1.2.14), (1.2.15), and (1.2.16) provide a useful framework for analyzing the hydrodynamic forces on bodies in fluid flows. The studies presented herein demonstrated practical application of this framework, making use of simple potential flow constructs to model the motions of a body and the vortical structures in its wake. This framework affords one the ability for efficient numerical simulation for design or for analysis and interpretation of experimental findings.

This thesis also presents novel numerical methods for experimental data analysis. In Chapter 4, I considered the effects of performing a *singular value decomposition* (SVD) on experimental data, which inherently contains measurement error. I derived a 'threshold criterion' (4.2.1) that determines the validity of an experimentally-derived SVD mode. Experimental error also makes computing instantaneous derivatives of measured data challenging. In Chapter 5, I presented a novel method for fitting a *smoothing spline* (which can be used to compute these derivatives) based on the concept of a 'roughness to error tolerance efficient frontier'. These mathematical tools are quite general and extremely useful for analyzing measured data.

10.1 Contributions of this thesis

In this thesis, I derived an impulse-force framework useful for analysis of experimental results and efficient numerical simulation of forces on bodies in flow. I applied this framework to a number of hydrodynamics problems of interest: fish swimming and maneuvering, free-surface impact of spheres, and marine propeller and turbine design. Several contributions were made in this thesis, and some are highlighted below:

Part I: Fish propulsion

- Applied impulse-force framework to fish maneuvering and showed that the total change in momentum of the fish during a rapid maneuver balances the total impulse imparted to the fluid during the maneuver (Ch. 2).
- Demonstrated that the unsteady vortical wake generated by a maneuvering fish can be modeled as discrete axisymmetric vortex rings (Ch. 2).
- Confirmed experimentally that for high-Strouhal-number swimming, the vortices shed at the caudal fin eventually split and form a V-shaped double wake, whereas for low-Strouhal-number swimming, the vortices shed at the caudal fin form a single wake and do not split (Ch.3-4).
- Created a vortex impulse **thrust model for fish swimming**, based on the concept of a *composite wake*. Demonstrated that this model adequately predicts the thrust generated by a fish during steady swimming (Ch. 3).
- Demonstrated experimentally that **fish swimming speed scales by the strength and geometry of the composite wake** and *not* by tail flapping amplitude, for both a fish robot and a live fish (Ch. 3).
- Demonstrated that a fish wake, which resembles a reverse Kármán street, is adequately represented by just four biorthogonal decomposition modes (Ch. 4).

Part II: Methods for experimental data analysis and modeling

- Provided a unifying discussion of how the singular value decomposition relates to its special cases: the biorthogonal decomposition and the proper orthogonal decomposition (Ch. 4).
- Created a **threshold criterion** to determine if a singular value decomposition mode is corrupted by measurement error (Ch. 4).
- Demonstrated why, for high-precision high-resolution experimental data, a smoothing spline should be used to compute derivatives of the data, as opposed to data regression to an assumed functional form or finite differences (Ch. 5).
- Created a novel and robust **method for fitting a smoothing spline** to experimental data, based on the concept of a *roughness versus error tolerance efficient frontier* (Ch. 5).
- Developed an automated numerical method for finding the critical error tolerance corresponding to the best fit smoothing spline (Ch. 5).
- Determined the unsteady deceleration and **total force on a sphere during water entry** using a smoothing spline fit to measured position data (Ch. 5).
- Applied my impulse-force framework to the sphere impact problem and demonstrated that the total force on the sphere is accurately explained using a potential flow model (Ch. 6).
- Created an axisymmetric **3D potential flow model** of a sphere and its sub-surface air cavity during water entry, and validated this model using experimental data. With this model, **explained the nature of the unsteady forces on the sphere during water entry** due to the ‘unsteady’, ‘Bernoulli’, and ‘hydrostatic’ pressure components. Demonstrated how cavity growth and collapse modulates the ‘unsteady’ pressure force on the sphere (Ch. 6).

Part III: Marine propulsion and energy harvesting

- Demonstrated how propeller lifting line theory is represented in my impulse-force framework (Ch. 7).
- Presented the theoretical foundation and numerical implementation of my OPENPROP code suite, which can be used for the design optimization, rapid prototyping, and off-design analysis of marine propellers and hydrokinetic turbines (Ch. 7).
- Developed a propeller design method that determines the optimum load distribution, with the constraint of a prescribed hub loading (Ch. 7).
- Created and implemented a numerical **method for off-design performance analysis** of propellers or turbines using lifting line theory (Ch. 7).
- Validated my off-design performance analysis method by designing, building, and testing the performance of a two-bladed marine propeller (Ch. 8).
- Created a modified ‘NACA 65A010’ thickness form for use in designing propellers for rapid prototyping by 3D printing (Ch. 8).
- Characterized the unsteady vortical wake generated by a propeller during unsteady start-up experiments (Ch. 8).
- Explained why turbines are not successfully optimized if propeller vortex lattice theory is implemented without consideration of actuator disc theory (Ch. 9).
- Created and implemented a **turbine design optimization method** that unites propeller vortex lattice theory with actuator disc theory (Ch. 9).
- Validated my off-design performance analysis method by designing, building, and testing the performance of a two-bladed hydrokinetic turbine (Ch. 9).

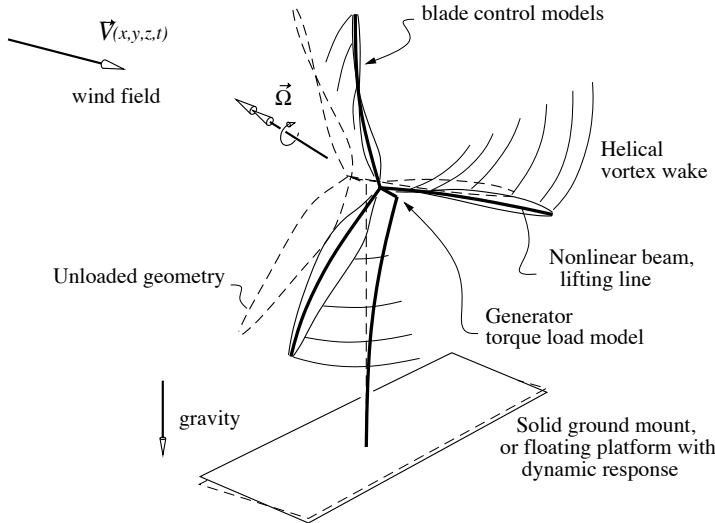


Figure 10-1: Model of a large flexible wind turbine on an offshore floating platform.

10.2 Extensions of this work

Building upon the theoretical framework of my thesis and drawing on my expertise with particle imaging velocimetry and my understanding of numerical methods, I am focused on developing accurate models and numerical tools with which to analyze a wide array of fluid dynamics problems. Looking forward, I plan to continue my research in these target areas: (a) offshore wind and marine hydrokinetic turbines; (b) biologically-inspired propulsion; and (c) numerical tools for experimentalists.

A major concern in the design and operation of large wind turbines is unsteady blade loads, since they can lead to fatigue failure of the blades themselves, or other turbine components. Peak unsteady loads can be reduced via active control of individual turbine blades, but prediction and mitigation of peak blade loads is challenging, because the aerodynamic, structural, and controls problems are coupled, often nonlinearly. The issue is complicated further in the offshore wind turbine case, where hydrodynamic loads (including wave forcing) are also part of the coupled dynamics problem. Thus, there is a pressing need for an efficient computational tool to analyze these types of problems early in the design cycle, before structural

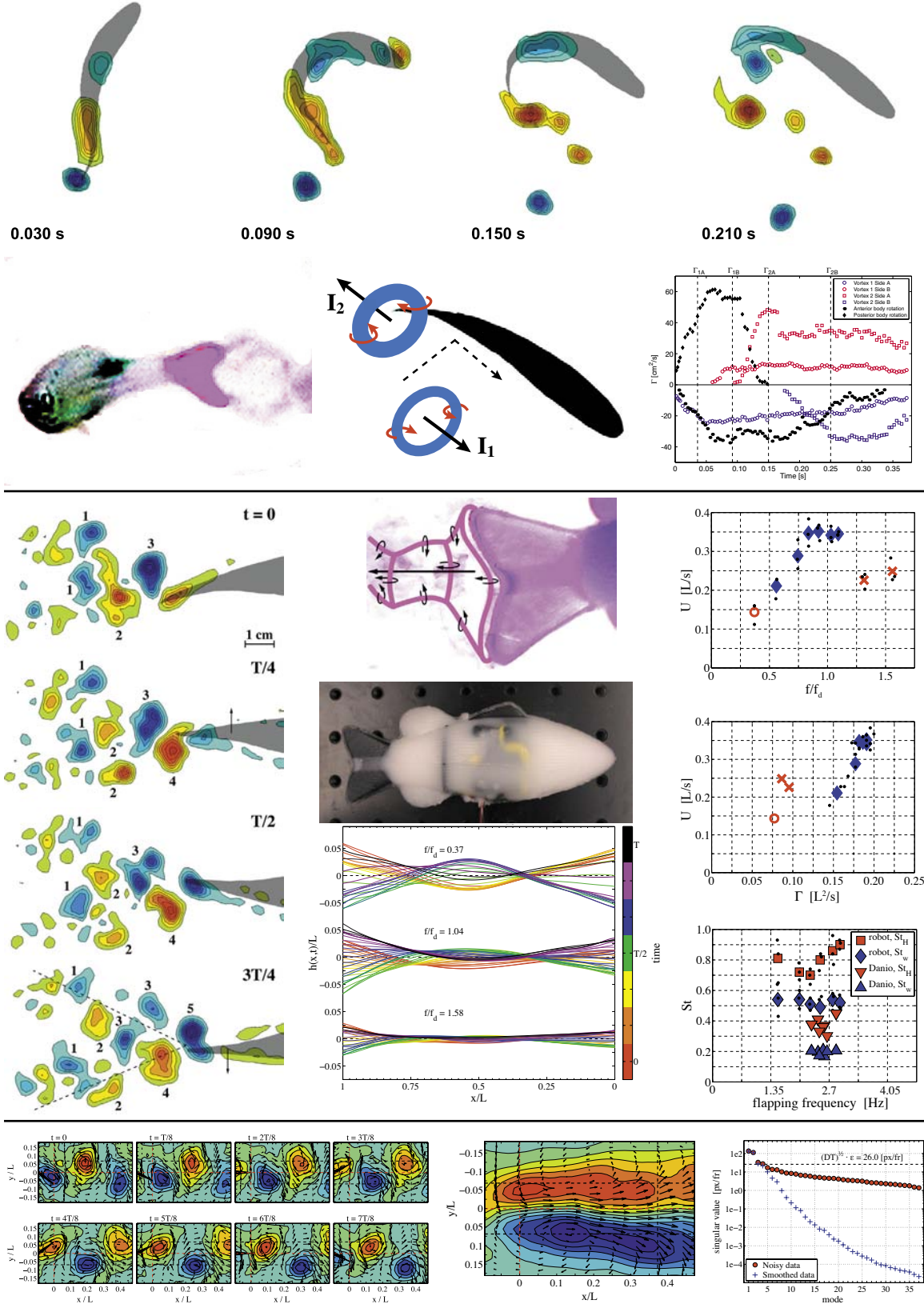
designs are frozen and full-blown CFD and FEA are performed. A concept of this tool is sketched in figure 10-1, showing a flexible wind turbine floating on an offshore platform. This work will be a natural outgrowth of my OPENPROP code suite, which currently can be used to design and analyze ‘rigid’ wind turbines.

Extending my early work with live maneuvering fish, further experimental work needs to be done to investigate how to achieve optimal vortex ring formation using flapping fins. Several key issues have yet to be addressed for fast starting and rapid maneuvering, namely the effects of parameters such as fin shape, aspect ratio, and flexibility. With this understanding, one could develop design guidelines for the control surfaces and kinematics of biologically-inspired underwater vehicles. This knowhow could also be applied to aggregates of jet-propelled devices, whose dynamic system model could be formed using the hydrodynamic impulses of the vortices created for maneuvering.

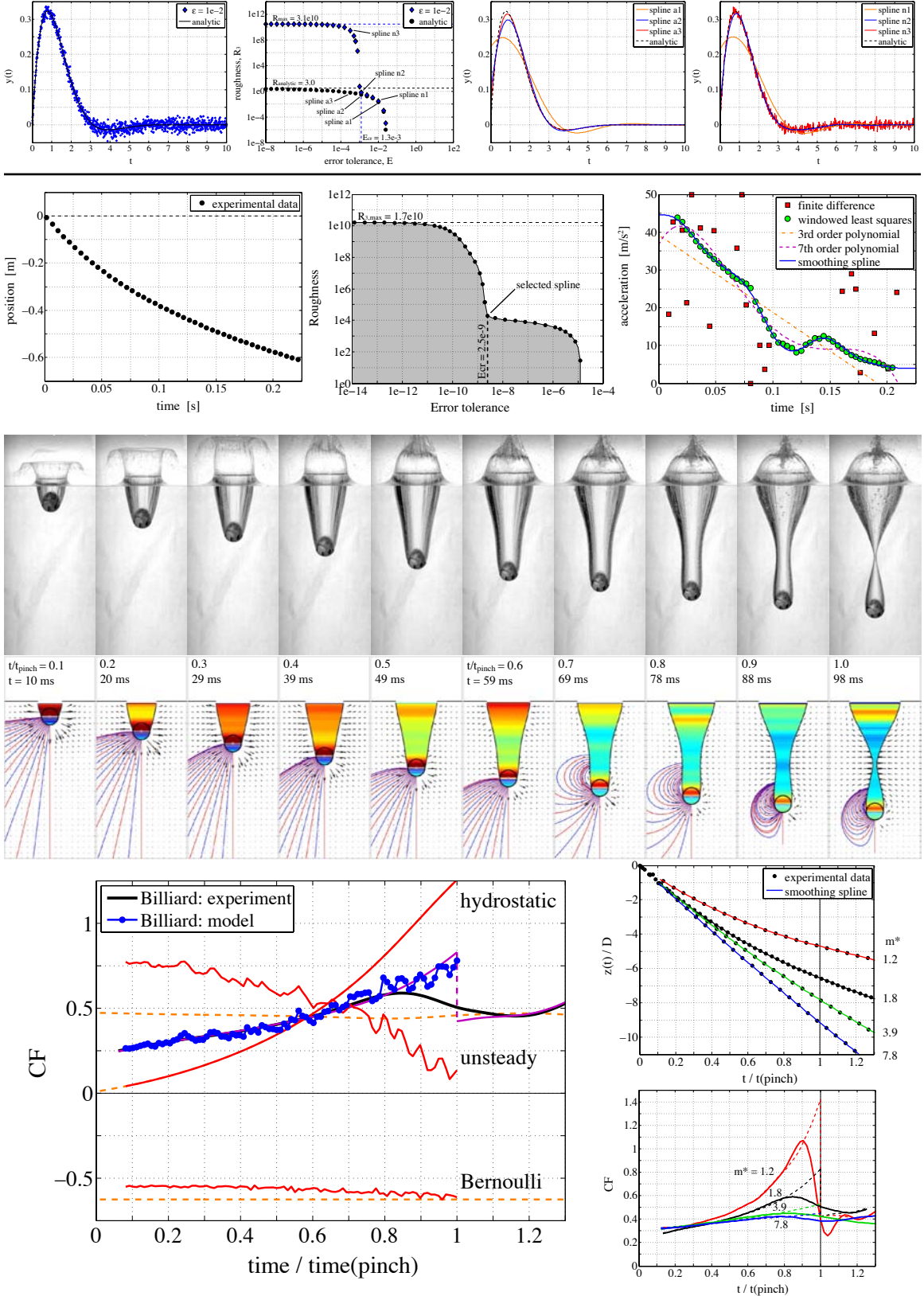
In conjunction with experimental efforts, there is a strong need to continue investigating the effects of experimental error in advanced data processing techniques. Mathematical procedures such as the singular value decomposition, Lagrangian coherent structures analysis, and even simply the calculation of fluid vorticity and strain rate tensors are powerful tools for analyzing fluid physics from high fidelity data. However, the effects of experimental error on the results of these analyses are not widely documented. It is paramount for the experimental community to be able to harness the power of these mathematical tools, despite the presence of noise in experimental data.

This thesis lays a strong foundation in classical fluid dynamics, experimental methods, and applied math that I aim to build upon to investigate propulsion and ocean energy harvesting. The overarching goal of my work is to further our understanding of fluid dynamics using both rigorous experimentation and efficient numerical simulation.

GALLERY OF FIGURES



GALLERY OF FIGURES



GALLERY OF FIGURES

